Universitat Autònoma de Barcelona

Metallic glasses and derived composite materials: a correlation between microstructure and mechanical properties

Doctoral Thesis presented by

Jordina Fornell Beringues

Bellaterra, March 2012

Departament de Física

Facultat de Ciències

Universitat Autònoma de Barcelona

Departament de Física

Grup de Física de Materials II

El Dr. Jordi Sort Viñas, director de la tesi doctoral realitzada per Jordina Fornell Beringues i que porta per títol "Metallic glasses and derived composite materials: a correlation between structural and mechanical properties",

FA CONSTATAR:

Que l'aportació del doctorand al treball que es presenta ha estat fonamental tant pel que fa al disseny experimental com a l'obtenció de les mostres, la realització d'experiments, l'anàlisi de les dades i la discussió i elaboració dels resultats presents.

I perquè així consti, a petició de l'interessat i als efectes oportuns, ho signem a Bellaterra, el 8 de Març de 2012 .

Jordi Sort Viñas

Edifici Cc (C3/202) - Campus de la UAB - 08193 Bellaterra (Cerdanyola del Vallés) – Barcelona.Spain

Tel.: 93 581 14 01 – Fax: 93 581 21 55

www.lmt.uab.es

Table of contents

Preface

Metallic glasses are amorphous metallic alloys. As the name suggests, being glasses, they do not possess long range order leading to its amorphous nature; formed by metals, they are not transparent to light. As a result, they exhibit unique chemical, physical mechanical and magnetic properties compared to the conventional crystalline metallic alloys.

Since the discovery of the first metallic glass in 1960, numerous compositions have been reported so far. However, it was not until the early 90s when metallic glasses regained extensive attention due to the fact that new glass forming compositions with dimensions up to 1 cm were casted. From this point, extensive research works have been focused on the development of new metallic glasses with ameliorated properties to be used as structural materials.

As stated, to obtain a metallic glass the formation of a periodic structure (typical of crystalline materials) must be avoided. It was observed that applying cooling rates high enough to the melted alloy, the nucleation and growth of equilibrium phases could be suppressed, obtaining as a result a highly disordered arrangement of atoms with lack of periodicity. However, not all compositions are able to be casted without crystallization; although various criteria were developed to guide researchers to find good glass former systems, the exact composition leading to metallic glasses remains unpredictable to a large extent.

Due to their structure, metallic glasses exhibit a range of interesting properties. For example, under the application of a magnetic field, they display superior soft-magnetic properties than their crystalline counterparts making them suitable materials to be used in sensors for electronic article surveillance or in cores of high-frequency transformers.

As with the magnetic properties, the mechanical properties of metallic glasses are in many cases superior to those of their crystalline counterparts. Metallic glasses exhibit outstanding strength, elastic strain and elastic energy storage that, together with their superior corrosion resistance, make them interesting candidates in many structural applications (sporting goods, precision gears, optical mirror devices, fuel cells…).

However, despite their high fracture strength, after yielding most metallic glasses tend to fracture in a brittle manner, with almost total lack of plasticity, restricting their use in many applications.

Deformation in metallic glasses does not occur through slip systems and dislocation modes as in crystalline materials. Instead, metallic glasses suffer work softening as a consequence of extreme localization of plastic strain into narrow shear bands. The formation of multiple shear bands, so that strains are not concentrated in one or few shear bands, can avoid the premature failure observed in metallic glasses.

As expected, in the last decade, many works were focused on the circumvention of this limited plasticity. Apart from some specific cases where intrinsic plasticity was observed, precipitation of a second phase was found to be the most effective way to promote multiple shear band formation and obtain both, high strength and enhanced plasticity. Many methods were developed to obtain such heterogeneous microstructure. For instance, the second phase can be physically added to the alloy prior to casting, precipitated directly from the melt or by thermal or mechanical treatments of the as-cast alloy. Following one of those procedures a microstructure composed of either a micro- or nano- sized crystalline, quasi-crystalline or non-crystalline phases embedded in an amorphous matrix can be obtained.

The structural and mechanical changes induced in metallic glasses by annealing, element addition and deformation form are the main topic of the work presented in this Thesis.

Below, there is a description of the structure of this Thesis where a summary of the main aspects that will be found in each chapter is presented:

Chapter 1 introduces some general aspects about glass formation and structural models describing metallic glasses where special attention was set into the free volume concept. Further, a brief explanation about three main routes to obtain in-situ nanocomposite is given. Finally, mechanical and corrosion properties of metallic glasses and composites are discussed and compared to those of crystalline materials.

Chapter 2 is divided in two subsections: processing techniques and characterization techniques. In the first one, the procedure to obtain a master alloy is described by two

methods, arc melting and levitation melting; the subsequent casting into rods is also explained. Finally, the specifications used to obtain the treated specimens (by annealing or deformation) are given. In the latest, the main techniques used to characterize the as-cast and treated specimens are explained. Special emphasis was given to the structural characterization techniques (electron microscopy and X-ray diffraction) as they are primarly used in this Thesis. In the mechanical characterization section, particular attention was set into the nanoindentation technique as this is one of the key techniques used in this work.

Then this Thesis includes a "results and discussion" section (**Chapter 3**) which is divided into three main subsections: (I) Devitrification-induced structural and mechanical changes in two metallic glass families (Ti-based and Fe-based), (II) the effect of Nb addition to the TiZrCuPd metallic glass alloy in terms of thermal, structural, mechanical and corrosion behavior and (III) the structural and mechanical response of three different alloys subjected to plastic deformation (indentation and compression test).

Finally, **Chapter 4** presents the main conclusions and future research works to be developed.

1. INTRODUCTION

1.1. Bulk metallic glasses

Metallic glasses are amorphous structures with unique physical, chemical and mechanical properties. These attractive qualities come from the combination of certain properties of metallic alloys together with those of conventional glasses. For example, as glasses, they exhibit a glass transition, non-crystalline structure and usually brittle behavior. Due to their metallic character, they are not transparent to light, exhibit high strength and may display excellent soft magnetic properties. However, certain properties of metallic glasses are rather far from those of oxide glasses and even further different from those of their crystalline counterparts.

The first amorphous alloy reported was in the Au-Si system produced by direct quenching from the melt (1). A very high cooling rate was required to obtain the glassy structure (around 10^6 K/s) so the samples obtained (ribbons, wires and droplets) were very small and sometimes irregular in shape. This drawback strongly restricted their possible applications as structural materials.

Some years later, in 1969, Chen et al. discovered that some systems containing noble metals such as Pd-Cu-Si (2) and Pd-Ni-P (3) required lower cooling rates to form the glassy structure and were able to cast them into the glassy state with a diameter of 0.5 mm. The vision about the synthesis of an amorphous alloy with a dimension exceeding 10 mm came true in 1984 by processing a $Pd_{40}Ni_{40}P_{20}$ alloy in a boron oxide flux (4). During the last two decades, a large variety of metallic glasses, based on different components and requiring lower cooling rates, were developed to obtain the so-called bulk metallic glasses (BMGs) by conventional casting techniques. Nowadays, BMGs have been produced at relatively low solidification rates (10^2- 10^3 K/s) and can be obtained by a wide variety of rapid solidification techniques.

To get an idea about the production of BMG, a summary of the main families developed up to date are listed in Table 1.1.

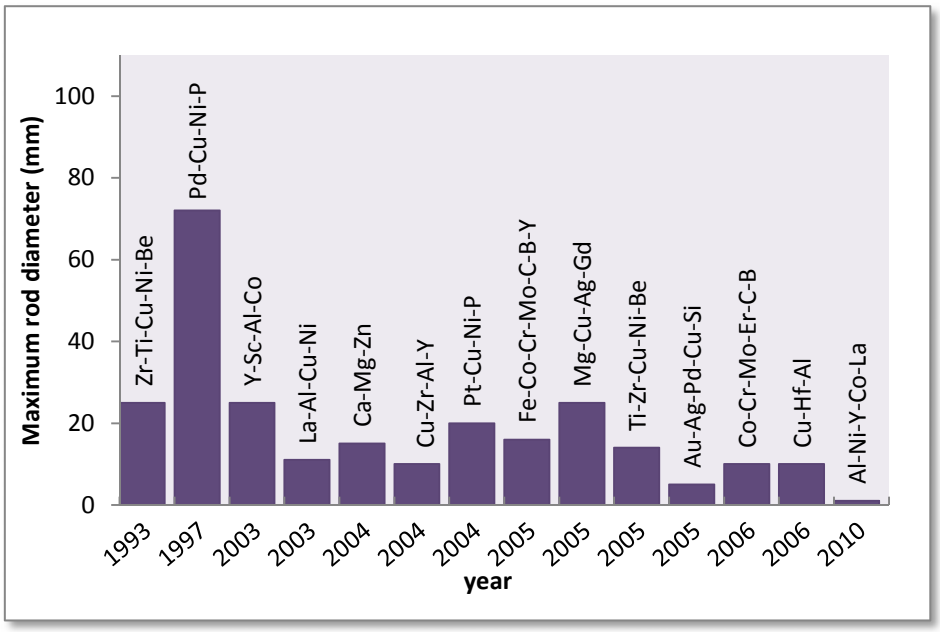

Table 1.1: Most important BMGs systems for various key elements together with their critical diameter and their publication year's.

1.1.1. Nature of a glassy structure and its formation

A glass is a solid which does not crystallize upon cooling fast enough from the melt. On cooling, a liquid must undercool below the equilibrium crystallization temperature before crystallization can begin because of the existence of an energy barrier for formation of nuclei. If the liquid is rapidly cooled, the formation of nuclei is increasingly delayed for kinetic reasons; as the cooling rate is increased, the undercooling is enhanced. Consequently, the crystallization range over which crystallization proceeds becomes lower leading to structural modifications such as a refinement of microstructure or eventually, if the cooling rate is high enough, crystallization is suppressed because of insufficient time for significant growth or nucleation. In this case, the mobility of the atoms is continuously decreased, which is reflected in the continuous increase of viscosity as shown in Figure 1.1.

Although the driving force for nucleation is continually increasing, this is opposed by the rapidly decreasing atomic mobility which, at very high undercoolings, dominates. Below the equilibrium melting temperature, the liquid, called *undercooled* or *supercooled liquid*, deviates from equilibrium and becomes homogeneously frozen at the glass transition temperature T_g. In this regime, the temperature dependence of

viscosity will change its trend (Figure 1.1). Conventionally, it is considered that the undercooled melt becomes a glass when its viscosity is about 10^{12} Pa.s. Below the glass transition, the structure remains virtually unchanged and volume and viscosity depend only slightly on temperature. The glass transition does not occur at a distinct temperature but in a temperature interval called the glass transition domain.

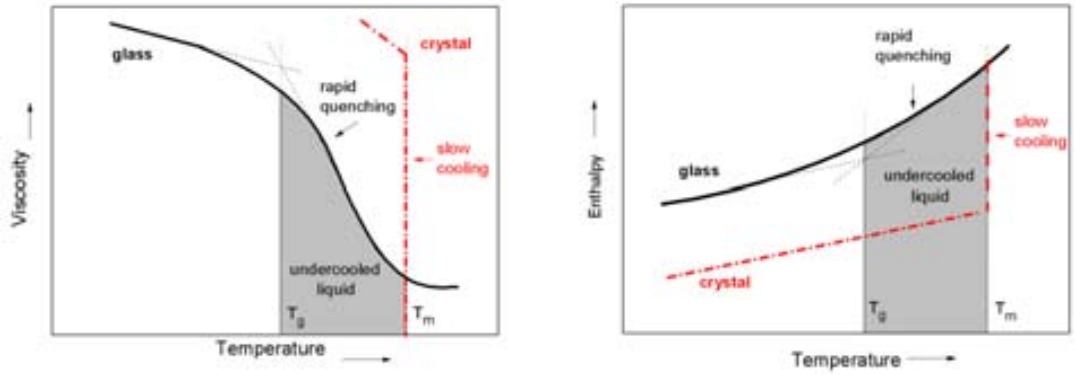

Figure 1.1: Temperature dependence of the viscosity and enthalpy corresponding to crystallization and vitrification of a metallic melt.

1.1.2. Crystallization (nucleation and growth of crystals)

Crystallization of conventional metals from the melt occurs through two processes: nucleation of stable seeds and growth of these seeds to grains. Lowering the solidifying system's free energy, ΔG, is the driving force for the whole solidification process (5; 6).

However, the formation of small particles of new phase involves the creation of an interface, and thus an increase of the free energy of the system;

$$\Delta G = -\Delta G_v + \Delta G_i = -\frac{4\pi}{3} r^3 \Delta g_v + 4\pi r^2 \gamma \qquad \text{(Eq. 1.1)}$$

Where ΔG_v is the change in the Gibbs free energy on solidification associated with the volume and ΔG_i is the Gibbs free energy associated with the interface, γ is the solid/liquid interfacial free energy and Δg_v is the difference in Gibbs free energy per unit volume of the crystal and the liquidus. Figure 1.2 shows the two contributions of Eq. 1.1 as well as the resultant ΔG as a function of the radius. Note, that ΔG shows a maximum value at a critical radius, $r^* = \frac{2\gamma}{\Delta g_v}$ meaning that, sizes below r^* are thermally unstable and will tend to dissolve in the liquid. However, the cubic dependence of ΔG_v dominates over ΔG_i and ΔG passes through a maximum at r^*. Consequently, greater

stability is achieved and growth will occur as a result of the descent of the total free energy (7; 8).

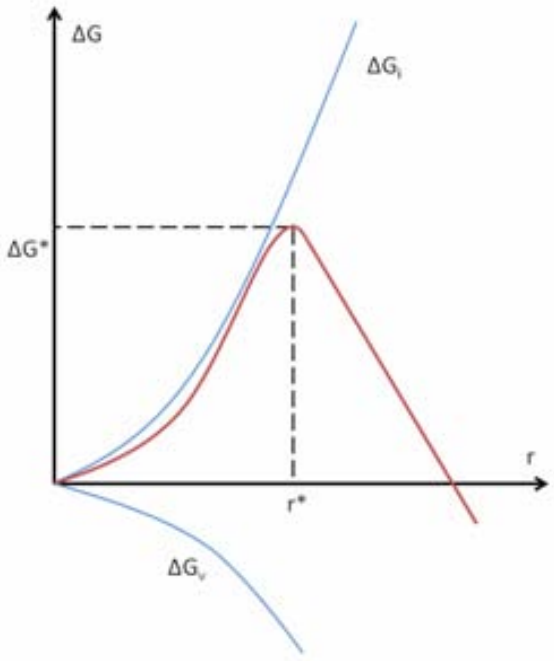

Figure 1.2: Free energy change ΔG accompanying the formation of a spherical particle of a new phase as a function of radius, r.

For homogeneous nucleation, the critical energy of activation for r^* is equal to:

$$\Delta G^* = \frac{16}{3}\pi\frac{\gamma^3}{(\Delta g_v)^2} \qquad \text{(Eq. 1.2)}$$

In the case of heterogeneous nucleation, which occurs on energetically favorable catalytic surfaces, e.g. impurities, the formation of a stable, critical nucleus may appear at a much smaller undercooling. Compared to ΔG^* (Eq. 1.2) the thermodynamic barrier to heterogeneous nucleation ΔG^*_{het} is reduced by a factor, the so-called wetting function $f(\theta) = \frac{2+\cos\theta\ (1-\cos\theta)^2}{4}$

The contact angle θ between the nucleus and the substrate can vary from 180° (non-wetting) to 0° (perfect wetting) (9). When θ = 180°, the solid does not interact, $f(\theta) = 1$ and homogeneous nucleation appears. For θ = 0°, the solid "wets" the substrate, $f(\theta) = 0$, and the value of the critical energy of activation is 0. As a consequence, the solidification process can begin instantly when the liquid cools to the freezing point (7).

A general expression for the steady state nucleation rate (nuclei formed per cm^3 per second), assuming that it follows an Arrhenius law, can be expressed as:

$$I\ T\ = \frac{K}{\eta(T)}\ e^{\frac{-\Delta G*}{k_B T}} \qquad \text{(Eq. 1.3)}$$

where $\eta(T)$ is the viscosity of the undercooled liquid, the parameter K is a proportionality constant and k_B is the Boltzmann constant. From Eq. 1.3, it can be concluded that crystal nucleation rate is a product of a thermodynamic term (probability of a fluctuation to overcome the nucleation barrier) and a kinetic part (depends on the viscosity). Considering now the formation of spherical nuclei, the homogeneous nucleation rate can be written as (10):

$$I\ T\ = \frac{K}{\eta(T)}\ e^{-\frac{16}{3}\pi\frac{\alpha^3\beta}{T_r(\Delta T_r)^2}} \qquad \text{(Eq. 1.4)}$$

where $T_r = T/T_m$ refers to the reduced temperature, $\Delta T_r = \frac{T_m - T}{T_m}$ accounts for the degree of undercooling and α and β are dimensionless parameters related, respectively, to the liquid-crystal interfacial energy and to the molar entropy of fusion.

Consequently, a related kinetic approach was taken by Uhlmann (11) for a number of non-metallic glass formers, but account was also taken of a limited degree of crystal growth; this provides a convenient and practically useful method of quantitatively estimating *T*. Following the Johnson-Mehl-Avrami treatment of transformation kinetics, the fraction of transformed phase *x* in time *t*, for small *x*, is given by:

$$x \sim \frac{\pi I\ T\ u(T)^3 t^4}{3} \qquad \text{(Eq. 1.5)}$$

where, *u(T)*, the crystal growth velocity, can be expressed as:

$$u\ T\ = \frac{kT}{3\pi\eta a_0^2}\ 1 - e^{\frac{-\Delta T_r H_f}{RT}} \qquad \text{(Eq. 1.6)}$$

where f is the fraction of sites at the crystal surfaces where atomic attachment can occur (=1 for close packed crystals and $0.2\Delta T_r$ for faceted crystals), a_0 the mean atomic diameter, ΔH_f the fusion's enthalpy and *R* the gas constant (8.314J/K.mol).

Eq. 1.5 allows us to draw the time-temperature-transformation (TTT) curve for $x \ll 1$. The time *t* being expressed as a function of T_r, to transform to a barely detectable fraction of crystal. TTT diagram shows a typical "C" shape with the "nose" of the TTT curve pointing higher transformation rates at intermediate temperatures and lower ones at higher temperatures (due to a lower driving force reducing nuclei's frequency

formation) as well as at lower temperatures due to the low atomic mobility affecting the grow velocity u.

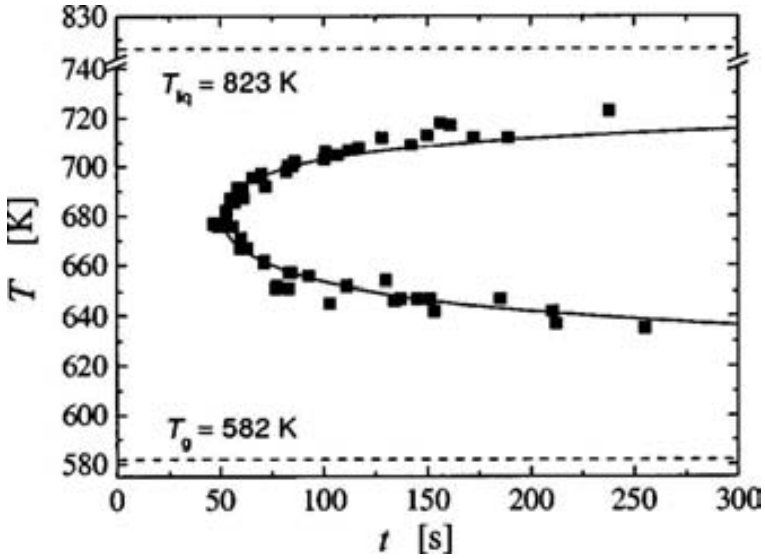

Figure 1.3: Schematic time-temperature-transformation (TTT) diagram for metallic glasses

Computed TTT curve for the $Pd_{40}Cu_{30}Ni_{10}P_{20}$ alloy is presented in Figure 1.3 for a fraction of transformed phase of $5*10^{-3}$ (12). This curve allows us to determine the critical cooling rate, R_c, to avoid crystallization. In approximate terms, R_c is given by the slope of the tangent that passes through the melting point at $t = 0$ (13).

$$R_c \approx \frac{T_m - T_n}{t_n} \qquad \text{(Eq. 1.7)}$$

Where T_n and t_n are the "nose" coordinates on the TTT curve. The nose of the curve is at 50 seconds and at 680 K obtaining a R_c around 1.5 K/s.

1.1.3. Glass forming ability

As mentioned in section 1.1.1, as the ability to obtain a glassy state is higher, the more the undercooled liquid is stabilized against crystallization; this ability is called glass forming ability (GFA). Since substances are more stable in their crystalline than in their amorphous state, thermodynamic and kinetic aspects are key parameters to understand the glass formation. Those aspects are explained in the previous section; however, for the sake of clarify, in this section the kinetics and thermodynamic requirements will be briefly enumerated. Furthermore, structural properties are also taken into account to

select good glass former systems and some criteria reported in the literature are also named.

- Thermodynamics aspects: To obtain higher undercooling and consequently larger GFA, the driving force for crystallization ΔG must be low. $\Delta G = \Delta H_f - T^*\Delta S_f$ where ΔH_f is the enthalpy of fusion and ΔS_f is the entropy of fusion. Since smaller ΔG is obtained for low ΔH_f and high ΔS_f. Low melting temperatures and therefore, compositions close to deep eutectics are suited to obtain lower ΔH_f; as well as ΔS_f is higher for alloys with many constituent elements.

- Kinetic aspects: The kinetic parameter influencing glass formation is the viscosity (or diffusion). According to Eq. 1.4, the higher viscosity is, the lower the tendency to nucleation; consequently, the GFA is higher.

  Another way of expressing the kinetics of glass formation is by means of the TTT or CCT diagrams. As mentioned in the previous section; depending on the position of the crystallization "nose" with respect to the time axis the required cooling rates to avoid crystallization can be different. The more the nose is shifter towards larger time values; the higher is the GFA of the system.

- Structural aspects: Usually, metallic glasses are multicomponent alloys, since the addition of specific elements tend to decrease the liquidus temperature and thus improve glass formation by increasing T_{rg} (T_g/T_l). Furthermore, in order to prevent rearrangements to form an ordered crystalline structure, elements chemically and topologically different (in atomic size and valence) need to be selected.

  There are diverse criteria that tackle the importance of atomic size and the critical concentration of a solute in phase transformations to predict alloy compositions with better GFA. For instance, Egami and Wasenda (14) developed a topological criterion for metallic glass formation. According to this criterion, amorphization occurs when local atomic strains generated by size differences between solute and solvent elements attain a critical level, leading a topological instability of the crystalline lattice by changing the local atomic coordination number (by means of substitutional atoms). After that, Senkov et al. (15) took into account the contribution of interstitial atoms instead of a substitutional one, modifying the topological model developed by Egami et al.

for the case when a solute is small and it can occupy an interstitial site. Lisboa et al. (16) extended to multicomponent systems the topological instability model of Egami and Wasenda introducing the "lambda criterion" according to which amorphous alloys with $\lambda > 0.1$ exhibit glassy behaviour, whereas alloys with $\lambda < 0.1$ are nanocrystalline. More generally, the efficient cluster packing model by Miracle (17), provides new analysis to predict density and packing fraction, to more completely assess short range order (SRO). This model is described for metallic glasses based on a new sphere packing scheme (the efficient filling of space by solute centered clusters).

Bearing in mind all the mentioned above theoretical contributions such as thermodynamics, kinetics and structure, Inoue et al. found out that in order to optimize the GFA of a given alloy, three empirical rules should be satisfied:

- The selected system must consist of more than three elements: increased complexity and size of the crystal unit cell reduces the energetic advantage of forming an ordered structure of longer-range periodicity than the atomic interactions.
- A significant difference in atomic size ratios above 12% among the three dominant constituents is required: This fact leads to a higher packing density and smaller free volume in the liquid state compared with metallic melts and requires a greater volume increase for crystallization.
- Heats of mixing among the three main constituent elements should be negative. Negative heat mixing increases the energy barrier at the liquid-solid interface and decreases atomic diffusivity; this retards local atomic rearrangements and the crystal nucleation rate, extending the supercooled liquid temperature range.

1.1.4. Structure of metallic glasses

A liquid can solidify to a crystalline solid or to an amorphous solid or glass. Even if these structures share essential properties of the solid state, they exhibit different atomic configuration which are the responsible of the different behaviour observed on these solids.

While crystalline solids (Figure 1.4 left) exhibit long range order (the atomic positions repeat in space in a regular array), glassy solids lack this three dimensional periodicity (Figure 1.4 right). This lack is signalled by the absence of sharp Bragg peaks when the structure of glassy materials is studied using x-ray, electron or neutron diffraction techniques.

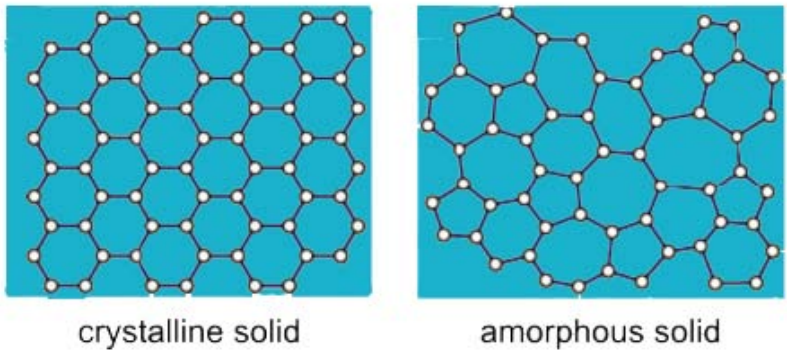

Figure 1.4: Atomic arrangements in a crystalline and an amorphous solid

However, both cases (crystalline and amorphous) exhibit the so-called short range order (SRO) or even medium range order (MRO) as a consequence of the atoms trying to find comfortable configurations to lower their energy. SRO develops above the first couple of coordination shells (typically <0.5 nm) while MRO refers to over-next neighbour arrangements and extends further to distances of beyond 1 nm. For a monolithic glass, it is the SRO and MRO that are expected to control its properties, such as the initiation of plastic flow (18).

Understanding how atoms pack in metallic glasses is not a trivial task. For years, different models were developed to understand their structure.

1.1.4.1. Structural models for metallic glasses

In the past, atomic packing in metallic glasses was explained with Bernal model (19) (20). In this theory the structure of glasses is described by a "dense random packing of spheres" where the larger atoms are randomly, but densely distributed, and the smaller (solute) atoms jammed into cavities (Bernal holes) left available by the geometry of this packing. However, these so-called Bernal holes are too small to accommodate the host solute in metallic glasses.

Based on Bernal's model, Polk (20) proposed that the small metalloid atoms, in the amorphous metal-metalloid systems, could host in the largest Bernal's holes being positioned as interstitial atoms between the metal atoms. In 1979, Gaskell (21) developed the stereochemically defined model (used for oxide glasses) based on the idea of rebuilding the structure of amorphous metal-metalloid alloys for the staking of trigonal prisms (Figure 1.5). In general trends, although the model developed by Polk-Bernal seems adequate for metalloid contents lower than 20%, the Gaskell model, which recognizes the partially covalent atomic bonds, seems to suit better to amorphous compositions close to the M_3N type, being M a metal and N a metalloid.

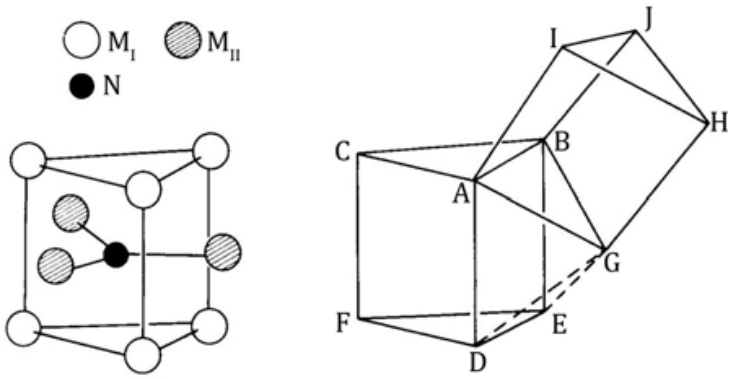

Figure 1.5: Gaskell's model: the coordination polyhedra is a trigonal prism containing six metallic atoms in a nearest neighbour sub-shell around a central non-metallic element with three further metal atoms.

However, as it is clear that dense packing is a characteristic trend of glass forming systems, the idea of random packing is certainly incorrect. Furthermore, these models failed to give an explanation why in metallic glasses atomic sizes have to be significantly different and neither do they provide an explanation about SRO and MRO.

Because of the densest possible packing of atoms of different sizes can be achieved only with well developed local order and bearing in mind that the density difference between BMGs and their crystalline counterpart is <0.5%, Miracle focuses his work on the concept of efficient filling of space (17; 22). He considered solute-centred clusters as representative structural elements. Considering these idealized clusters as spheres, a scheme (Figure 1.6) was suggested to efficiently pack these clusters to fill the space. Basically, a cluster consists of a primary solute A, which is surrounded by the solvent atoms D. Additionally, two topologically distinct solutes exist: the secondary B solute atoms (occupying the cluster-octahedral interstices) and the tertiary C solute atoms (occupying the cluster-tetrahedral interstices). This model has been termed as the

efficient cluster packing (ECP) model, in which adjacent clusters share solvent atoms in common faces, edges or vertices so that neighbouring clusters overlap in the first coordination shell leading to MRO and dense packing in three dimensional space.

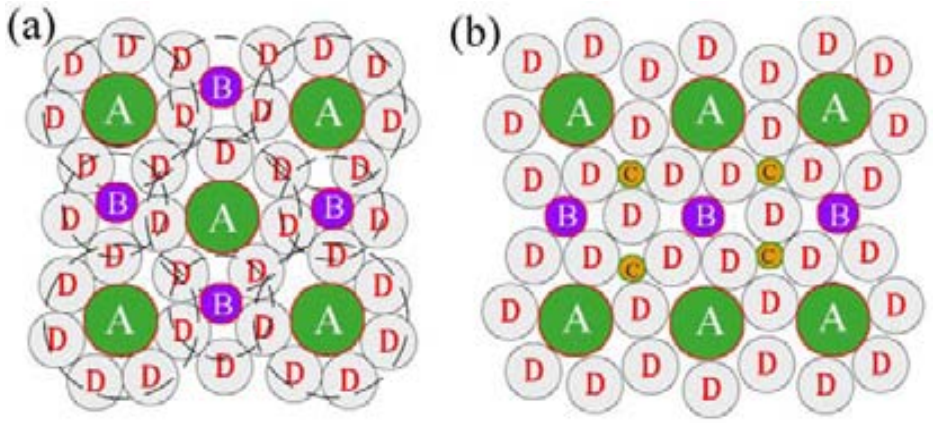

Figure 1.6: Schematic two-dimensional representation of a denser cluster-packing structure of clusters in (a) (100) plane and (b) (110). (17)

Another attempt to figure out the characteristics of MRO came from Sheng et al. (23) who establish the preference for, and dense packing of, solute-centered quasi-equivalent clusters.

From this section we could conclude that the structure of a metallic glass can be understood as a dense packing of overlapping atomic clusters. Even if there is not a complete agreement on the type of packing, in general trends, those models allow us to understand unusual properties observed on metallic glasses from a structural point of view.

1.1.4.2. Free volume

In the atomic structure of metallic glasses, besides the bonded atomic clusters defined in the previous section, free-volume also plays an important role to understand the structural properties of the glassy state.

The concept of free volume was initially developed by Cohen and Turnbull for liquids (24) and was adapted to metallic glasses by Spaepen (25).

The free volume model (FVM) describes the atomic mobility of amorphous solids in terms of the free volume available for the atoms. Atoms being surrounded by a critical

free volume v^* can perform atomic movements in their close neighbourhood. The probability for an atom being surrounded by free volume v^* is called the structural defect concentration c_f (24). The structural relaxation is identified as an approach of the amorphous solid to the quasi-equilibrium defect concentration $c_{f,e}$. By rapid solidification of liquid alloys an excess defect concentration $c_{f,0}$ is frozen into the glassy state. Upon isothermal heating the concentration $c_{f,0}$ reduces towards $c_{f,e}$. By subsequent heating of the sample to a higher temperature, the defect concentration increases until equilibrium has again been established. These processes of annihilation and creation of free volume can be experimentally determined by means of in-situ synchrotron diffraction, combination of density measurements and differential scanning calorimetry and by positron annihilation spectroscopy (26; 27).

For example, Russew and Sommer (26) measured the relative density changes and length scale changes as a function of annealing time at different temperatures in the $Pd_{40}Cu_{30}Ni_{10}P_{20}$. They established a quantitative relationship between the density changes and the length changes in metallic glass samples.

More recently, Yavari et al. (27) measured the excess free volume during heating cycles by in situ X-ray diffraction in transmission and the results are the same as those of dilatometry. They concluded that contrary to the case of vacancies in crystals, free volume in glasses can be directly measured by diffraction methods.

However, the free volume model has some limitations. For instance, it is assumed in the FVM that diffusion in metallic glasses occurs through atom jumps; however, molecular dynamics simulations revealed that diffusion is a more collective and diffusive process, where chain action occurs at many atoms linearly connected (28). Lately, by means of positron annihilation spectroscopy it was observed a distribution in sizes of open volumes rather than one macroscopic average deduced from the FVM indicating that the free volume distribution is more complex than that described by Cohen and Turnbull (29). Even if some assumptions of this model are not correct, the concept is useful and intuitive.

Besides playing a role in diffusion processes, these free volume sites, form the basis for deformation in metallic glasses at the atomic level. In this context they are referred as flow defects or shear transformation zones (30). Upon deformation, shear bands locally nucleate in regions where the deformation-induced creation of free volume cannot be

fully compensated by thermal diffusive relaxation (25). As a result, the excess free volume coalesces and the viscosity significantly reduces.

1.2. From the amorphous to the crystalline state

One of the main drawbacks of metallic glasses comes from the fact that they usually exhibit little macroscopic plasticity, limiting their use in many structural applications. In order to overcome this weakness, numerous studies were carried out in the recent years. The concept of fabricating glass-matrix composites was developed with the purpose to avoid the premature failure commonly observed in glassy alloy by means of introducing a nano/micro-sized second phase in the amorphous matrix to hinder the rapid propagation of shear bands.

Crystalline phases embedded in an amorphous metallic matrix can be obtained in different ways forming two main groups: in-situ composites or ex-situ composites (Figure 1.7).

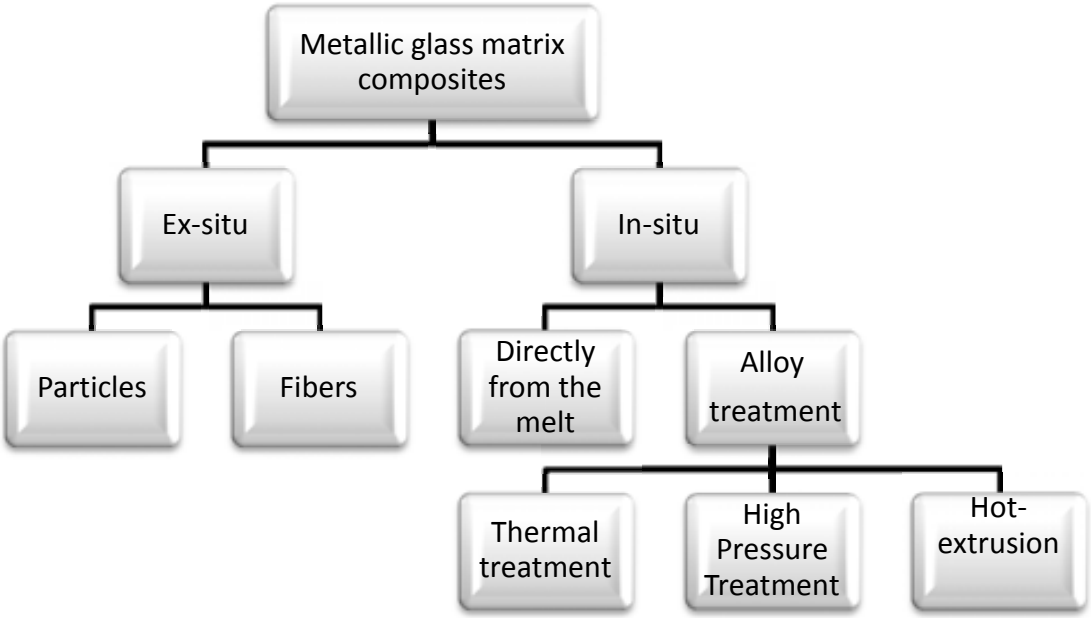

Figure 1.7: Various processing routes to obtain a metallic glass matrix composite

A composite is classified into the ex-situ composite group when the reinforcing phase is physically added to the alloy prior to the casting. Conversely, we refer to an in-situ composite when the crystalline phase is precipitated directly from the melt during cooling or by thermal or mechanical treatment of the as-cast alloy.

In this work we fabricate in-situ composites by three different processing routes: by crystalline precipitation during the cooling of the melt, by devitrification of the amorphous alloy (thermal treatment), and by deformation- induced nanocrystallization (using nanoindentation and compression test techniques).

1.2.1. In-situ composites

1.2.1.1. Precipitated from the melt during cooling

They are mainly produced by two different ways: on one side, they are obtained by adjusting the chemical composition of the alloy. The chosen composition is not exactly the one corresponding to the glass-forming alloy; consequently, the solidified phases will not be a homogeneous glassy phase. The amount of second (crystalline) phase formed can be controlled by the extent of deviation from the glass-forming composition range (31). On the other side, in-situ composites can be obtained by the addition of a high melting point element to the glass forming composition. When a high melting point element is added, the procedure to obtain the glass-matrix composite differs from the conventional one. The high melting point element is first melted together with one element of the composition and later, mixed with all the other components to obtain the master alloy. Following this procedure, the high melting point element precipitates as nano/micro-meter size particles (this is, it remains solid due to high melting point) when the alloy is melted and casted to form the amorphous matrix composite.

Following one of those procedures, we can obtain a microstructure composed of either micro- or nanometer-sized crystalline, quasi-crystalline or non-crystalline phases embedded in an amorphous matrix. In this section we will focus our attention on the crystalline BMG matrix composites.

- *Metallic glass matrix composites*

Up to now, a lot of BMG matrix composites were successfully synthesized. The first contributions come by the hand of Hays et al. (32). They tuned the Vitreloy I to obtain ductile β-Ti(Zr) dendrites in a glassy matrix (Figure 1.8a). This new alloy had a compressive plastic deformation up to 5 %. This work opened a new research area on

the development of new BMG matrix composites with the aim to improve the plasticity of the monolithic BMG. After that, many studies were done to induce in situ crystallization, first, in Zr-based BMG. Kühn et al. (33) reported the first in situ Be-free Zr-based metallic composite with glass matrix and ductile bcc precipitates.

Besides Zr-based glassy alloys, the composite structure formation was also achieved in other families of metallic glasses. For example, in a Cu-Ti-Zr-Ni-Si alloy (Figure 1.8b) the precipitation of nanoscale fcc crystals homogeneously dispersed in the glassy matrix improves the compressive strength up to 4% (34). In a Cu-Hf-Ti-Ag-(Ta) alloy (glassy matrix +Ta-enriched dendrites) a plastic strain up to 19% together with an increase of compressive strength is achieved for a tantalum content of 8% (35). He et al. (36) reported a Ti-based alloy containing dendritic hcp-Ti solid solution precipitates and a few Ti_3Sn, β-(Cu,Sn) grains dispersed in a glassy matrix with a more than 6% plastic strain under compressive stress.

Summarizing, we could conclude that the mechanical properties of metallic glasses are improved when dispersed nanocrystals or micrometer-sized ductile crystalline phases are embedded in a glassy matrix.

- *Nanostructured matrix composites*

Nanostructured materials also exhibit unique physical, chemical and mechanical properties however, these materials are often extremely hard and brittle and almost no ductility appears under tension. This behaviour is analogous to that of bulk metallic glasses.

Based in the same idea (introducing nano-micro scale precipitates in a glassy matrix) a new class of nanocomposites consisting in alloys with bimodal grain size distribution (dendrites embedded in a nanostructured matrix) was also developed. These materials are usually obtained by typical rapid solidification techniques but varying the casting conditions rather than the alloy composition. They are designed with the aim to combine the high strength of the nanostructure with the high plasticity of a ductile phase. For instance, He et al. (37) reported a new Ti-based in situ-formed nanostructured matrix/ductile dendritic phase composite (Figure 1.8c) which exhibits up to 14.5% compressive plastic strain at room temperature. The development of nanostructured materials was mostly focused in Ti-based and Zr-based alloys. One

example of Zr-based nanostructured material was reported by Das et al. (38). They obtained a novel $Zr_{73.5}Nb_9Cu_7Ni_1Al_{9.5}$ composite with bcc β-Zr dendrites embedded in a nanostructured matrix that exhibit high strength coupled with high plastic strain (up to 15%).

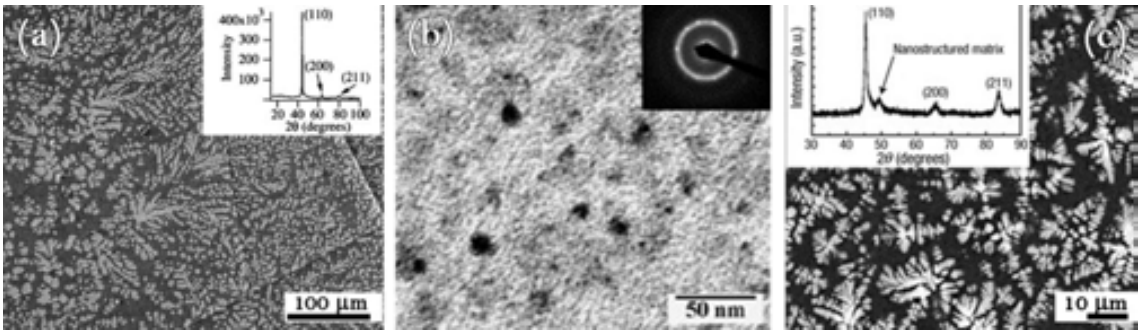

Figure 1.8: Microstructures of in-situ composites with nanocrystals/dendrites precipitates embedded in an amorphous/nanostructured matrix (a) SEM backscattered electron image for Zr-based alloy composed of β-phase dendrites embedded in an amorphous matrix (32) *(b) TEM image of $Cu_{47}Ti_{33}Zr_{11}Ni_8Si_1$ alloy composed by nanocrystals embedded in an amorphous matrix* (34) *(c) SEM backscattered electron image of in situ formed β-Ti(Ta,Sn) dendrite/ nanostructured matrix composite in a $Ti_{60}Cu_{14}Ni_{12}Sn_4Ta_{10}$ alloy* (37).

1.2.1.2. Thermally-induced devitrification of metallic glasses

Apart from the amorphous/nanostructured matrix composite material, by means of devitrification of BMGs, we can also obtain other structural morphologies such as a relaxed state or a completely crystalline alloy.

When a metallic glass is annealed, different reaction can occur in the glass. With increasing annealing temperature, the glass may exhibit structural relaxation and then crystallization. The crystalline structure obtained will show properties that are not possible to achieve from in-situ crystallization methods. In the present section, we will focus on the methodology to obtain a glass+nanocrystals, an ultrafine grained composite, or a completely crystalline material of different grain sizes by controlling the time and temperature of the annealing treatment.

Differential Scanning Calorimetry (DSC) is a commonly used method to study the crystallization behaviour of metallic glasses. It allows identifying the characteristic temperatures in which the glassy phase transforms to the crystalline state. In some cases it also permits determining the supercooled liquid region or even transformations from

metastables to other metastable phases or equilibrium ones. In Figure 1.9 a typical DSC curve, with the mentioned above transitions identified, is depicted.

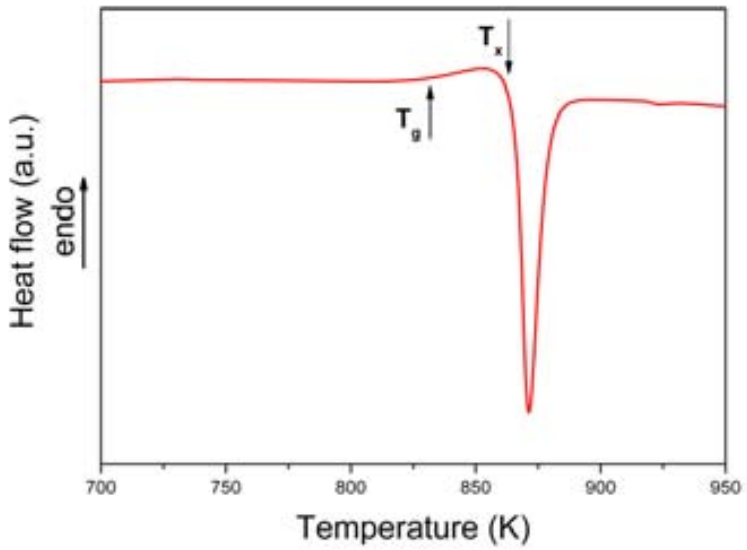

Figure 1.9:Typical DSC curve of a metallic glass material

T_g is identified by a change in the slope of the base line and, although crystallization does not occur below T_g, the glass undergoes structural relaxation. Crystallization is indicated by one or various exothermic peaks depending on the number of stages that crystallization takes place. T_x designates the onset of the first crystallization peak. For clarity, a schematic diagram about the different pathways that a metallic glass can follow when it is annealed at different temperatures is shown in Figure 1.10. The obtained structure depends on the annealing time and temperature, as well to the constituent elements of the system.

In general trends, as observed in Figure 1.10, when a metallic glass is annealed we can obtain three main different states: (a) a relaxed glass (b) Phase separation or (c) crystallization.

Phase separation is the process in which a homogeneous glassy phase of a given composition is separated into two different glassy phases of different compositions. Phase separation can be formed in the supercooled melt either during the process of solidification or during the annealing of a homogeneous glassy phase. Phase separation occurs in alloy systems whose phase diagrams feature a miscibility gap between two phases that are thermodynamically stable. Such situation arises when the two constituent elements in the binary alloy have a zero or positive heat of mixing (31).

However, in this section we will focus on the relaxed state and the crystalline one, which are the ones we have observed during our annealing treatments.

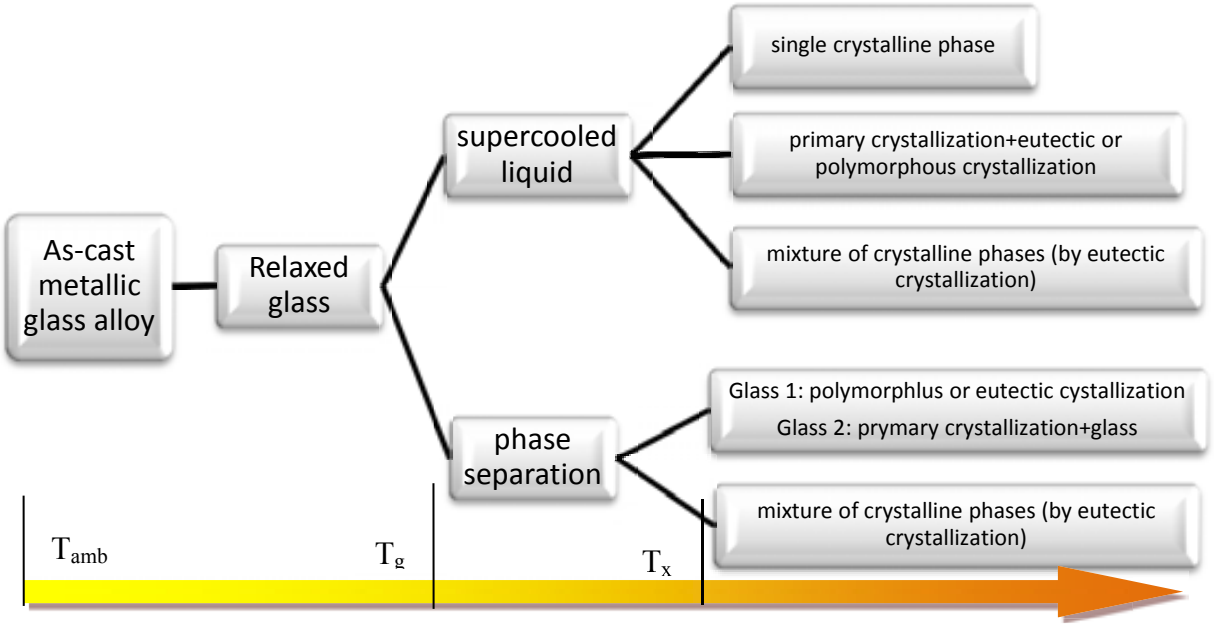

Figure 1.10: Different pathways for a metallic glass to crystallize into the equilibrium phases.

- **Structural relaxation**

Metallic glasses are in a non-equilibrium state with respect to the ideal glassy state; however, during isothermal annealing below T_g, the glass tries to reach the ideal glassy state characteristic of the annealing temperature. This process is designated as structural relaxation (39). The mechanisms by which structural relaxation occurs are believed to be the annihilation of "defects" or free volume, the recombination of the defects of opposing character or changes in the SRO (40).

Structural relaxation in metallic glasses is commonly studied in two regimes: low temperature (T_g -200 K< T_a<T_g -100 K) or high temperature ($T_a \geq T_g$ -100 K), where T_a is the annealing temperature. However, in some binary glassy ribbons (Pd-Si, Fe-B and Zr-Cu alloys) structural relaxation was reported just above room temperature; this fact is attributed to the large amount of frozen-in free volume acquired during rapid solidification methods.

Structural relaxation causes a significant change in physical and mechanical properties. In general trends, relaxed glasses exhibit a decreased specific heat, reduced diffusivity,

reduced magnetic anisotropy, increased elastic constants (by about 7%), increase of mechanical hardness, significantly increased viscosity and, in some cases, a loss of ductility. Relaxation can also change electrical resistivity, Currie temperature, enthalpy, superconductivity, and several other structure-sensitive properties (40). As mentioned in the previous section, another important parameter that changes with structural relaxation is the density. An increase about 0.1%-0.15% for BMG alloys was reported (41).

The most popular techniques to study structural relaxation in metallic glasses are DSC and electrical resistivity measurements. For instance, structural relaxation in DSC scans is indicated by an exothermic relaxation peak (loss of enthalpy).

In our work, structural relaxation was mainly investigated through a combination of hardness measurements, DSC, XRD, acoustic measurements and electron microscopy techniques.

- **Crystallization**

Theoretically, a metallic glass starts to crystallize when it is heated at T_x or above. The crystallization temperature is determined by DSC (see Figure 1.9) and it is identified as the first exothermic peak in the DSC curve. The crystallization temperature, as well as the glass transition temperature, depends on the heating rate employed in the DSC scan, so the faster is the heating rate, the higher the temperatures values. Some metallic glasses exhibit more than one exothermic peak meaning that they crystallize in various steps. Each exothermic peak corresponds to the heat released for the formation of a crystalline phase (or various phases when eutectic crystallization takes place).

However, in some metallic glasses crystallization can occur below T_x. It has been widely observed in the supercooled liquid region of the glass or at temperatures even below T_g. Supposedly, it is possible for a metallic glass to crystallize even at room temperature; however, most of metallic glasses can be considered "stable", it means that they do not undergo any transformation at room temperature. Furthermore, in the rare case that it could happen, the kinetics of crystallization will be so slow that in a reasonable amount of time will not be possible to study the crystallization behavior (31).

- Activation energy for crystallization

The activation energy is defined as the minimum energy necessary for a specific reaction to occur, consequently, to activate crystallization, such activation energy must be overcome. In other words, a thermal impulse like heating is required. As the crystallization processes of metallic glasses is a nucleation and growth transformation, the thermal fluctuations when annealing near T_g, will be high enough to overcome this energy barrier to nucleation.

There are two different methods by which the activation energy can be determined. On one hand, we have the Kissinger method (42) where the temperature corresponding to the peak of the crystallization event is supposed to be determined (instead of the peak temperature (T_p), T_x can be also used) at different heating rates. Then, using Eq. 1.8 and plotting $\ln(\frac{\beta}{T_p^2})$ against $1/T_p$, one obtains a straight line whose slope is $-Q/R$, from which the activation energy for the transformation Q can be calculated.

$$\ln \frac{\beta}{T_p^2} = -\frac{Q}{RT_p} + A \qquad \text{(Eq. 1.8)}$$

Where R is the universal gas constant, β is the heating rate and A is a constant.

It is also possible to study the kinetics of transformation by recording the isothermal DSC scans at different temperatures and using the Johnson-Mehl-Avrami (JMA) analysis (explained in section 1.1.2).

On the other hand, in the Ozawa (43) method, $\log T_x/\beta$ is plotted against $1/T_x$. The activation energy can be determined from the slope of the straight line.

The Kissinger method has been more commonly employed but both methods yield similar Q values.

- Crystallization modes

The crystalline phases formed during annealing can be either the equilibrium phases or some metastables phases usually formed in the first stages of crystallization.

On further annealing, the metastable phases may transform to the equilibrium ones or not. Depending on the composition of the alloy, the metallic glass tends to crystallize in one of the three modes described below. Figure 1.11 shows the hypothetical diagram of

the free energy curve for polymorphous, primary, and eutectic crystallizations of an amorphous alloy with constituents A and B and crystalline phases α and β.

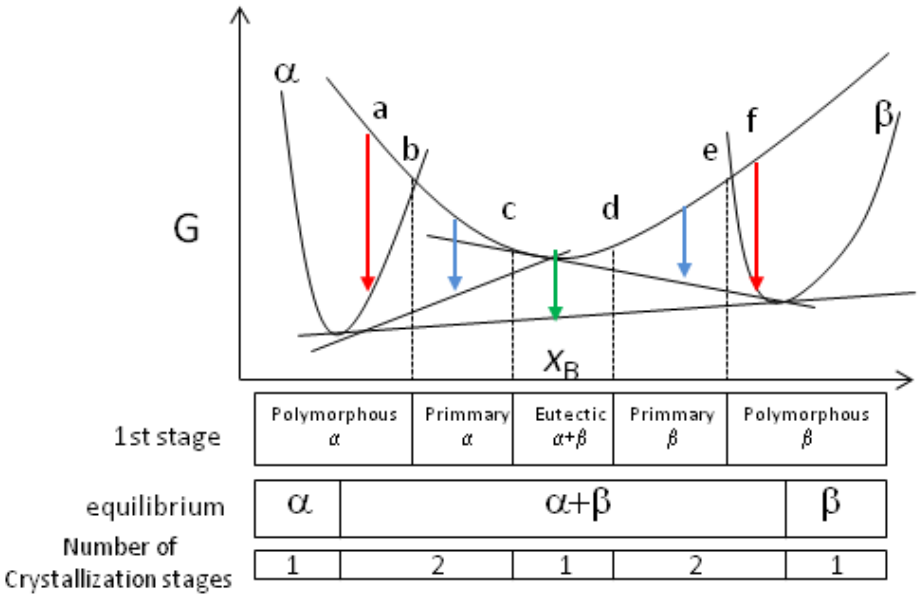

Figure 1.11: Hypothetical free energy composition diagram

- Polymorphous crystallization:

In this mode of transformation the glassy alloy will transform into a single crystalline phase without any change in the composition. This is only possible to form in the ranges where the glassy phase was formed in the composition range of a stable, metastable or an intermetallic phase. For example, in Figure 1.11, polymorphous crystallization will occur in reactions indicated with red arrows and its morphology is presented in Figure 1.12a.

- Eutectic crystallization

Contrary to the previous mode, the glassy phase transforms simultaneously into two or more phases by a discontinuous reaction. Eutectic crystallization can occur in the whole concentration ranges between two stable/metastable phases. The eutectic reaction is indicated with green arrow in Figure 1.11 and its morphology is shown in Figure 1.12b.

- Primary crystallization

This mode of crystallization is the main transformation method observed in metallic glasses. It consists in a supersaturated solid solution first formed from the glassy phase;

consequently, the remaining glassy matrix will be enriched in solvent atoms until it will further transform (later or at higher temperatures) by one of the mechanisms described above.

The morphology of the primary crystalline phase depends on composition and it ranges from a spherical to a highly dendritic structure. For example, in Figure 1.11, primary crystallization of α and β is represented by the blue arrows. Figure 1.12c illustrates a TEM image showing primary crystallization from a Fe-Co-B-Si-Nb BMG alloy obtained at heating at 1148 K.

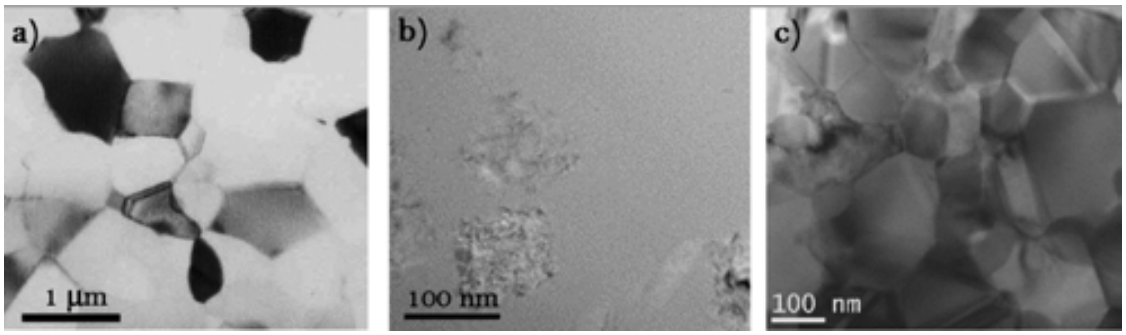

Figure 1.12: TEM micrographs showing a) polymorphous crystallization (44) *b) eutectic crystallization* (45) *c) primary crystallization* (46).

1.2.1.3. Deformation-induced nanocrystallization

Deformation-induced nanocrystallization of metallic glasses has received increasing attention during the last years. Several factors, such as temperature rise due to localized heating of shear bands, enhanced diffusion induced by the larger amounts of defects (dilatation) or growth of pre-existing nanocrystalline nuclei during deformation, can explain this effect.

A way to induce nanocrystallization in amorphous alloys is by using heavy deformation techniques, known as severe plastic deformation techniques (SPD) such as high pressure torsion (HPT) or equal chanel angular pressing (ECAP). This technique, besides inducing changes in the microstructural, thermal and mechanical properties of BMG alloys, it is widely used to refine the microstructure of crystalline materials (for example to obtain nanostructured materials), to achieve a significant increase of hardness, in accordance with the Hall-Petch relationship (47).

In the HPT technique, a sample in the form of a thin disk is subjected to a high pressure and a concurrent torsion strain. The disk deforms by pure shear through the surface frictional forces, under quasi-hydrostatic pressure, which prevents the sample from failing (48).

Focusing on the effects of HPT in amorphous materials various studies were carried out in the recent years. Boucharat et al. (49) investigated deformation-induced nanocrystallization in an Al-based glassy alloy by HPT and found out the growth of small Al nanocrystals. Nanocrystallization was also observed in other glassy systems such as Ti-based (50) and Fe-based (51) metallic glass alloys. However, nanocrystallization induced by HPT is not observed in all metallic glass systems. It is suggested that partial nanocrystallization has been observed in systems with low glass forming ability with a primary crystallization mode (52) but what is commonly accepted is that HPT always involve extensive atomic rearrangements changing their thermal as well as mechanical properties.

Besides HPT, the formation of nanocrystals in amorphous matrix has been previously observed by several other deformation techniques. In 1995 He et al. reported that ball milling for 1 minute induced the formation of nanocrystalline Al particles in an Al-based metallic glass. These results are consistent with the observation that nanocrystal formation can be induced within the shear bands of some Al-based metallic glasses after bending (53).

Nanocyrstallization has also been observed during tension and compression test in amorphous alloys. For example Gao et al. observed Al-nanocrystal precipitation in tension test within vein protrusions on fracture surfaces and along crack propagation path (54). In a Cu-Zr-Al amorphous alloy, an homogeneous precipitation of ~2 nm sized nanocrystallites was observed in the sample after being tested under uniaxial compression test. The mechanism of the deformation-induced nanocrystallization process was explained in terms of thermodynamics and the kinetics associated with the stress states imposed on the samples (55). Deng et al. presented a direct high resolution TEM observation of nanocrystallization in a Zr-Al-Ni-Cu BMG fractured under compression. In 2002, Kim et al. (56) reported for the first time nanocrystallization in bulk amorphous alloy subjected to nanoindentation. They found out that nanocrystallites nucleate inside and around shear bands produced near indents and that they are the same

crystallites formed during annealing at 783 K. In 2003, Jiang et al. confirmed that plastic deformation can induce crystallization without a heating effect (under quasistatic condition used) and they observed that the nucleation of nanocrystals is highly affected by the strain rate. As it will be explained in the results and discussion section, we reported nanocrystallization in a $Zr_{62}Cu_{18}Ni_{10}Al_{10}$ alloy subjected to compression test and nanoindentation

1.3. Properties of metallic glasses and composites

Mechanical properties play a crucial role in the application area; therefore a lot of studies were focused on improving the above-mentioned mechanical properties introducing some inhomogeneities to the glassy phase.

In this section we will compare the mechanical behavior of metallic glasses with that of nanocomposite materials as well as with their crystalline counterpart alloys.

Besides mechanical properties we will also describe in general terms thermal and corrosion properties that also play an important role in the application field.

1.3.1. Mechanical behaviour – general aspects-

1.3.1.1. Metallic glasses

Mechanical properties of metallic glasses are in many cases superior to their crystalline counterparts. Remarkably, they have very high yield strength and their elastic modulus can be up to 30 % lower than the one of the crystalline alloys; however, metallic glasses tend to fail soon after yielding without any signs of reasonable amount of plastic deformation. As shown in Figure 1.13, the yield stress of BMG is more than twice the one corresponding to the steel but it fractures much earlier than the steel alloy.

Deformation in metallic glasses does not occur through slip system and dislocation modes as in crystalline materials. Instead, deformation in metallic glasses is ascribed to the formation of shear bands, their rapid propagation and the sudden fracture of the sample leading to the typical lack of plasticity. This type of localized deformation is

known as inhomogeneous and it is observed in metallic glasses at low temperatures (lower than about $0.5T_g$) and low strain rates. Metallic glasses have been shown to exhibit strain softening, that is, an increase in strain makes the material softer and allows the material to be deformed at lower stresses and higher rates. In the opposite side, crystalline materials can show work hardening (with increasing strain the material becomes harder) which makes further deformation difficult and results in higher plasticity. Shear band deformation or shear localization has been considered a direct consequence of strain softening.

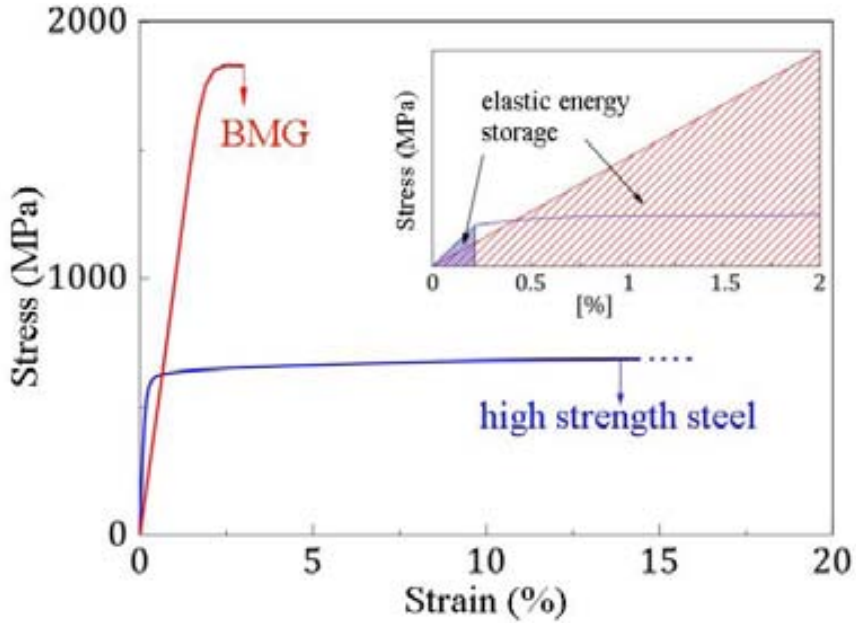

Figure 1.13: Comparison of the mechanical properties of a typical BMG (in compression) and a typical high strength steel (in tension)

Despite this lack of plasticity, restricting their use in many structural applications, metallic glasses manifest elastic deformation of more than 2% before yielding (in conventional metallic alloys this value is about 10 times lower) (inset Figure 1.13). Equally, metallic glasses can absorb up to 30 times more elastic energy, which is represented by the surface area under the curve in the elastic region (inset Figure 1.13), offering them possibilities for mechanical energy storage (57).

- **Deformation mechanisms**

Shear softening and formation of shear bands have been attributed to a local decrease in the viscosity of the glass (31). The cause of this viscosity drop is still unclear and many reasons (which can be grouped under two hypotheses) have been suggested to explain it. The first hypothesis proposed that the viscosity in shear bands decreases during deformation due to the formation of free volume and therefore its resistance to deformation. A first approach was explained by the classical "free-volume model" (58). This model views deformation as a series of discrete atomic jumps in the glass, at sites where the excess free volume is large enough, which in fact is a diffusion-like process. This model had some limitations: Egami calculated further that a dilatation of less than 10% was sufficient to change the atomic environment, instead of the 80% critical free volume suggested by the free volume model. Furthermore, the amount of free volume necessary for atoms to move in local shear transformation appears to be much smaller than the amount of free volume for diffusion (59).

Therefore, a second model, which explained deformation in terms of shear transformation zones (STZ), was developed by Argon in 1979 (60). The STZ is essentially a local cluster of atoms that undergoes an inelastic shear distortion from one relatively low energy configuration to a second low energy configuration, crossing an activated configuration of higher energy and volume. Argon demonstrated that flow localization occurs in a shear band in which the strain rate has been perturbated due to the creation of free volume.

The second hypothesis suggests that local adiabatic heating occurs in shear bands, which leads to a decrease in the viscosity (61). This adiabatic heating could lead to a substantial increase in the temperature to a level above T_g or even to the melting point of the alloy. Experimental evidence is available for both, the increase in free volume and rise in temperature in shear bands during deformation.

- **Features of metallic glasses under deformation**

As can be observed in Figure 1.14a, BMGs usually exhibit strain softening; however, some new ductile BMGs exhibit work hardening (Figure 1.14b) such as crystalline alloys. This recently developed "ductile metallic glasses" exhibit high-strength (between 1272 and 1830 GPa) and a significantly improved ductility (the total true strain can

reach up to 170% for binary $Pd_{81}Si_{19}$ alloy) (62). After the yield point, the stress level continues to increase, indicating a "workhardening-like" behavior. (63; 64; 65). This phenomenon is common to most of the BMGs exhibiting intrinsically enhanced ductility.

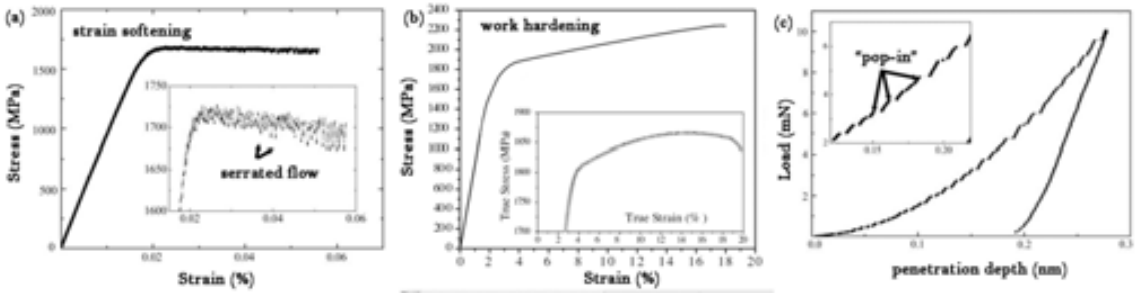

Figure 1.14: (a) Stress–strain curve of the $Ti_{40}Zr_{25}Ni_8Cu_9Be_{18}$ BMG alloy. The inset shows the occurrence of serrated flow along with a progressive mechanical softening after yielding; (b) Stress-strain compression curve of a $Cu_{47.5}Zr_{47.5}Al_5$ showing a highly "work-hardenable" metallic glass (63)*; (c) load-displacement nanoindentation curve of the $Ti_{40}Zr_{25}Ni_8Cu_9Be_{18}$ BMG alloy. The insets show the central parts of the loading curves, where some pop-ins can be easily distinguished.*

From Figure 1.14a (typical compressive strain-stress curve for BMG), it is interesting to note the sudden drops in load observed in the inset. These drops are associated with the formation and propagation of individual shear bands as a consequence of the increase of free volume during deformation in the shear bands, thereby decreasing its density and hence its resistance to deformation.

Serrated flow is also observed during nanoindentation, but only at slow loading rates. At this time, the activation of each individual shear band and the consequent sudden rise in load is known as a "pop in" event (Figure 1.14c). A single shear band can rapidly accommodate the deformation at slow loading rates; however, when the loading rate is high, there is not enough time to accommodate the strain and multiple shear bands operate at the same time resulting in a smooth load- displacement curve.

In order to overcome the limited plasticity typically observed in metallic glasses leading to a catastrophic failure after yielding, the development of amorphous matrix composites with reinforcing particles/ductile phases was widely explored.

1.3.1.2. Composite materials

In terms of mechanical properties, a second phase can be introduced in the amorphous matrix with two main goals: promoting shear band initiation (to distribute the plastic strain more broadly to avoid the catastrophic localization) and hindering shear band propagation. Such second phases can exist in many types, shapes and sizes, ranging from atomic clusters to micrometer-sized dendrites

In general trends and, as studied in section 1.2, there are two main groups of composites: in-situ and ex-situ formed composites.

Ex-situ composites contain TiC, TiB_2, WC, ZrC, ZrO_2 particles, W/steel filaments or carbon nanotubes. These reinforcing phases lead to higher fracture strength with increasing their amount; even so, the ductility is still limited to 1-5% plastic deformation (except for Zr-based BMG reinforced by W filaments, for which a strain to failure of up to 18.5% has been reported) (66).

Compared to the ex-situ composites, in-situ processing lead to a better bonding between the matrix and the crystalline phases (66). The deformation behavior of in situ composites mainly depends on the volume fraction of the crystalline phase and their nature, size and shape. The best combination of high strength and improved ductility is achieved when the reinforcement is in the form of ductile dendrites, however, when the dendritic phase has been changed into a spherical shape, the properties appear to be further improved (67) (see Figure 1.15a).

Commonly, the BMG matrix composites obtained by ***annealing*** monolithic BMG alloys exhibit (in their optimum state: the most favorable crystallite size and % of crystals) slightly higher strength and ductility than the as-cast alloy. At this time, the crystalline phase is usually nanometric and is homogeneously dispersed in the matrix. In most cases, no reliable improvements in ductility are reported by annealing treatments.

One exception, for example, is the case reported by Jun et al. (68). They found that the ductility under compression increased up to 42% without compromising the maximum strength when the alloy was annealed under T_g. They ascribed the increase of ductility to the variation of free volume caused by structural relaxation and the possible partial nano-crystallization.

Enhanced plasticity was observed when nanocrystals or phase separation was formed during ***deformation*** processes. Deformation-induced nanocrystallization is a phenomenon in which a secondary phase is precipitated during deformation within the initial glassy phase. This phenomenon has been extensively studied in the literature in several works (65; 69; 64; 70; 71; 72). In some cases, crystallization induced during compression test was considered to be correlated with the relatively low stability of the supercooled liquid phase and the high transformation rate of the primary precipitation phase (69). Other works suggest that the origin of plasticity is closely related to the short/medium-range order existing in the glassy phase (72) and other authors attributed the large plasticity to the nanocrystallization that was in-situ produced by plastic flow within the shear bands (64; 65; 71).

Another way to ameliorate the plasticity of metallic glasses by deformation techniques was reported by Cao et al. (73). They rolled at cryogenic temperature a Cu-based BMG; the crystallization was suppressed during the deformation, however, when the thickness reduction exceeds 89%, phase separation was observed and the microhardness and ductility of the alloy increased drastically.

Among the in-situ composites, ***those directly produced from the melt***, are the ones where the second phase can be precipitated in form of particles or dendrites, also their size can be more or less controlled adjusting the solidification parameters such as the cooling rate and, as mentioned before, they are the ones exhibiting better plasticity.

The first alloy composition used to produce an in-situ composite ($Zr_{56.2}Ti_{13.8}Nb_5Ni_{5.6}Be_{12.5}$) formed by dendrites embedded in the glassy matrix exhibited an improvement in ductility when compared to the monolithic BMG. To further improve the ductility, Sun et al. (74) developed a new processing technique to transform the dendritic morphology of the crystalline phase into spherical particles. The alloy heaving the spherical particles showed higher ductility (12% plastic strain) than the one with the dendritic morphology (8.8% plastic strain).

Another example of improved mechanical properties of in-situ composites is shown in Figure 1.15b. The fracture strength and plastic strain for the $Cu_{60}Hf_{25}Ti_{15}$ BMG have been measured about 2088 MPa and 1.6%, respectively. But, with the addition of 10% Nb, these values increased to 2232 MPa and 14.1%, respectively (75).

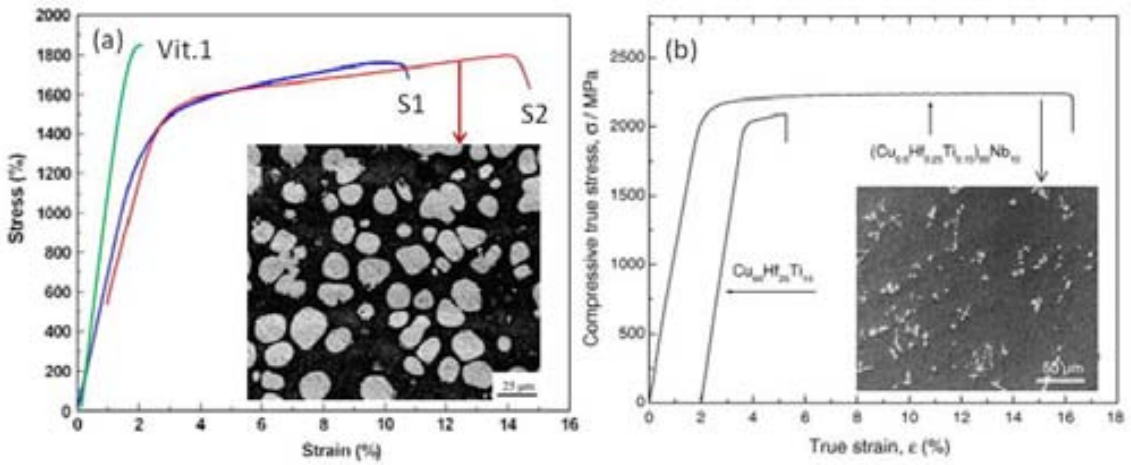

Figure 1.15: stress-strain compressive curve of amorphous and glassy-matrix composites (a) Vit 1 monolithic BMG, S1 ($Zr_{56.2}Ti_{13.8}Nb_5Cu_{6.9}Ni_{5.6}Be_{12}$ with spherical crystalline second phase) and S2 ($Zr_{60}Ti_{14.7}Nb_{5.3}Cu_{5.6}Ni_{4.4}Be_{10}$ with spherical crystalline second phase). Inset SEM image of the S2 alloy. (b) $(Cu_{60}Hf_{25}Ti_{15})_{100-x}Nb_x$ (x=0 and 10 at.%) alloys. Inset, SEM image of the sample with x=10.

- **Deformation modes in composites depending on the lengh-scale and morphology of the second phase.**

When the length scale of the second phase that precipitates is in the ***nanometer range*** (containing quasicrystals or intermetallic compounds) it typically constitutes a hard and non-deformable phase. Of course, as mentioned before, there is a critical volume fraction of crystalline phase for which a ductile-to-brittle transition is observed. This fact is attributed to the nanoscale particles free of defects that tend to strengthen the alloy. Below a critical volume fraction, the nanocrystals are isolated and homogeneously distributed in the amorphous matrix and, because their size is smaller than the shear band spacing (between 10 and 30 nm), they increase the resistance to flow deformation by increasing the viscosity inside the shear bands. The glassy matrix hardens, which leads to a higher strength and shear band propagation is retarded, thus enhancing ductility (66). The nanocrystals seem to have no effect on crack initiation, and the deformation is still controlled by the amorphous matrix.

In some cases, ***large-scale inhomogeneities*** (micrometre-sized particles or dendrites) are embedded in the amorphous matrix. Besides the dependence of the second phase size, plasticity also depends on the morphology of this second phase. It is not the same when micrometrer sized intermetallic particles (commonly brittle) precipitate during an

annealing treatment than when a ductile dendrite phase (which is usually a softer phase) is obtained from the melt.

Now, we will focus on the deformation mechanisms of BMG/ductile dendrite composites. In the first stages of deformation the ductile dendritic phase begins to yield, and part of the load is transferred to the surrounding matrix. Just after yielding, primary shear bands are initiated and propagate in the glassy matrix until they are blocked by the dendrites. The slip is transferred from the matrix to the dendrites and secondary shear bands are initiated in another direction to accommodate the strain. With further strain, multiplication of shear bands occurs. They are first hindered by the dendrites but for higher strain levels they pass through them. During this process, microcracks are nucleated around the shear bands or at the dendrite/matrix interface. The crack propagation follows the shear bands and similar phenomenon occurs (66). The macroscopic consequence of all this process is an enhanced ductility attributed to the shear band multiplication, branching and mutual interaction, within and around the shear bands. Furthermore, the intrinsic deformation behaviour of the dendrites contributes to further increase the ductility and lead to work hardening of the alloy (76).

Also in this case, there is a critical volume and size of dendrites to observe an improvement of the plasticity of the alloy.

On the other side and, as it was mentioned before, a group of BMG with intrinsic ductility has been reported in the literature. This intrinsic ductility bas been ascribed to a variety of factors such as: large Poisson's ratio (76), deformation-induced nanocrystallization (64; 55; 70), phase separation (62; 77) or intrinsic SRO/MRO (63; 78).

The intrinsic ductility of BMG ascribed to the atomic scale inhomogeneities has been observed in metallic glasses with rather poor glass forming ability. Literature data reports a special case of spatially inhomogeneous clustered glassy structure based on martensitic ingots which exhibit high compressive strength and large plastic deformation (63; 79; 80): the so-called martensite-glasses or M-glasses. In those systems, a 'stress induced displacive transformation occurs around the STZs, which release the local stress concentrations, and delocalizes the shear by forming wavy shear bands (79) thus retarding their failure. For instance, a remarkable increase of plastic

strain (18%) attributed to microstructural features at the atomic scale was observed by Das et al. in the Cu-Zr-Al system (63).

1.3.2. Corrosion behaviour

Besides magnetic, physical, mechanical and chemical properties, the corrosion behaviour of BMGs and composite materials becomes of great importance when these materials are developed to be used as structural components. For example, if they are designed to be exposed at high temperatures, oxidizing atmospheres and corrosive media or, if they are intended for biomedical or decorative applications, knowledge of the corrosion behaviour is of prime importance.

Corrosion processes are largely affected by alloy composition and its structural particularities, giving rise to a significant difference in the corrosion behaviour of amorphous and crystalline alloys.

Due to the rapid solidification of BMGs, the atoms of glassy structures are in non-equilibrium configuration; therefore metallic glasses are in a high-energy state and they need lower free energy of activation (ΔG^*) than their crystalline counterparts. This is schematically represented in Figure 1.16a. A lower free energy of activation implies a higher exchange current intensity, i_0, which in turn determines a higher corrosion current intensity, i_{corr}. Simultaneously, the corrosion potential is shifted towards less noble values (i.e., towards more anodic values) (Figure 1.16b) (81).

However, in most cases, amorphous alloys exhibit enhanced corrosion resistance than their crystalline counterparts. This is mainly attributed to the multiple crystalline phases that are usually present in the crystalline fractions of glassy alloys, which can form galvanic couples. Furthermore, contrary to the homogeneous nature of metallic glasses, crystalline alloys contain crystal defects (grain boundaries, dislocations, second-phase precipitates) which could act as galvanic cells to initiate localized corrosion. However, not all BMGs show chemical homogeneity and the presence of heterogeneities during the casting cannot be completely avoided, especially in commercial production. Some examples comprise gas pockets formed by entrapment of gas bubbles during production (82), small crystallites formed due to the presence of oxygen in the melt (83), or the gradient of MRO in the cross-section of a rod sample (84) or phase separation (85). These heterogeneities or their interface with the glassy matrix can act as nucleation sites

for pit initiation, thereby deteriorating the good corrosion properties anticipated for homogeneous glassy alloys. In any case, the corrosion behaviour of a particular system largely depends on the alloy composition and alloying elements so general rules can not be easily extracted.

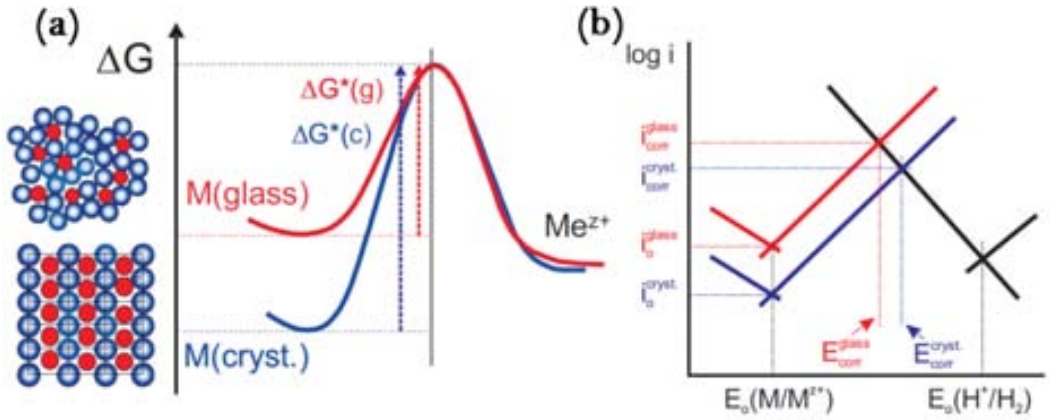

Figure 1.16: (a) Schematic representation of the free energy at the interface metal/electrolyte for crystalline and glassy alloys; (b) schematic i-E curves for glassy and crystalline alloys when ΔG is the predominant factor.*

2. EXPERIMENTAL TECHNIQUES

In this chapter the experimental procedure followed to produce the alloys will be described. In addition, a brief explanation about the characterization techniques used to explore the microstructure, mechanical and corrosion properties of the alloys will be also provided.

2.1. Processing techniques

In this work, metallic glasses and composite materials produced in-situ (directly from the melt) were obtained by arc or levitation melting and subsequent copper mould casting. This production route involves basically two steps: the production of a master alloy and its casting into rods of 2, 2.5 and 3 mm on diameter.

It is worthy to mention that the control of the synthesis atmosphere is of great importance, since lack of it can lead to some undesired mechano-chemical reactions or contamination in the obtained materials. For example, if the synthesis is performed in air, one can easily get a significant contamination from oxygen or nitrogen. To avoid undesired contamination, the master alloy was prepared under Ar atmosphere after doing at least three purgues consisting in -1 bar relative vacuum and subsequent Ar filling. The rods were also casted under Ar atmosphere.

2.1.1. Master alloy – arc melting and levitation melting-

First of all, the master alloys were prepared by melting of a mixture of high purity elements (99.9%) under a titanium-gettered argon atmosphere. The ingots were obtained either through an arc- or a levitation-melting process.

2.1.1.1. Arc-melting

An electric arc furnace is a system that heats charged material by means of an electric arc. Arc furnaces of various capacities exist: units of approximately one tone capacity

used in foundries for producing cast iron product, while e.g. in research laboratories units with a capacity as small as around 50 grams are used.

The basic set-up of an electric arc furnace consists of a furnace shell with a roof on top. The furnace shell is lined with ceramic bricks insulating the furnace from the liquid metal alloy. On the upper side walls and on the inside of the roof, water cooled elements are used instead of ceramic insulation. These water cooled panels are positioned to avoid direct contact with the liquid metal. Through the retractable roof, one or more tungsten electrodes enter the furnace. Electrodes may be pyramidal allowing the formation of an electric arc between the material and the electrode. On contact, electrical power is transformed into heat as arcing takes place between the electrodes and the solid feedstock. The material is heated both by current passing through the charge and by the radiant energy evolved by the arc.

The arc furnace described above can be used extensively for the preparation of different alloys (including systems with high-melting point elements). In order to make a master alloy as homogeneously as possible, the ingot must be remelted at least four times. Quite homogeneous melt can be made by simply distributing the elements in a random manner in the mold and repeating the arc melting several times with successive inversions of the sample (86).

2.1.1.2. Levitation melting

In a cold crucible levitation melting (CCLM) furnace, the molten metal formed in the crucible is levitated by an electromagnetic force to be in no contact with the inner wall surface of the crucible. As a result, the migration of contaminants from the crucible to the molten alloy is avoided.

With this technique, high-homogeneity alloys are obtained thanks to powerful electro-magnetic agitation. Furthermore, it is possible to melt alloys having high melting temperature (>2000ºC).

The set-up of the levitation melting crucible comprises a cylindrical main body having a closed bottom (usually made of copper), a plurality of slits defined vertically in the circumferential wall of the main body to open inward and outward at predetermined intervals in the circumferential direction and an insulating material filled in each of the

slits. Induction coils are disposed around the crucible, and when a high-frequency current is applied to these coils, a material introduced into the crucible is heated and melted. Figure 2.1a shows a schematic representation of the set-up of a CCLM. The CCLM device from OCAS used to produce part of the alloys of this work is presented in Figure 2.1b. Detail of the cold crucible and the melt during casting can be observed in the upper inset. The lower inset is a detailed view of the set-up.

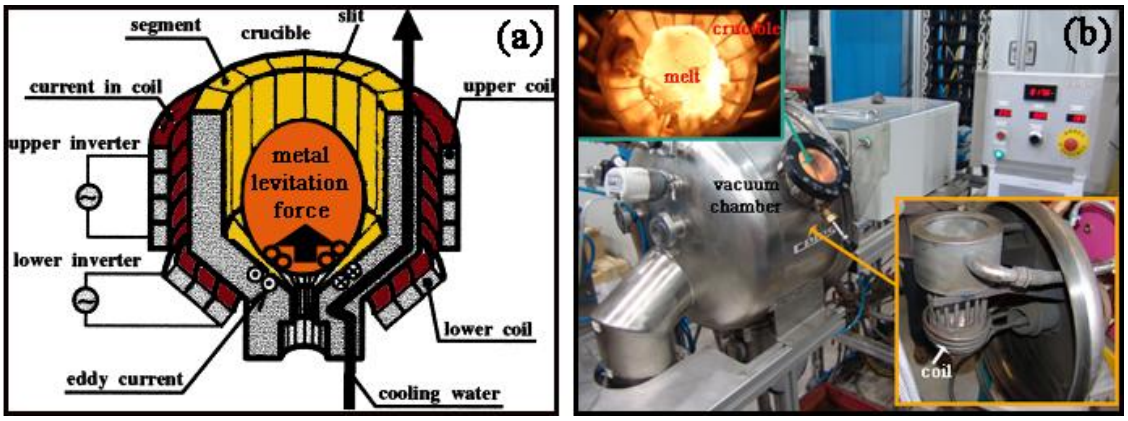

Figure 2.1: (a) schematic representation of the basic principles of CCLM. (87). *(b) General view of the CCLM device during casting. (Insets) detailed views of the melt, crucible and coil.*

2.1.2. Casting into rods: Cu mold casting

Pieces of master alloy are introduced in a crucible (quartz or graphite) or, in the case of the levitation melting the pieces are directly placed at the bottom of the cold crucible. Then, the melt is brought into a copper mold. The insertion into the Cu mold can occur by applying an overpressure in the crucible (injection casting) or by the application of a negative pressure (i.e. vacuum) at one end of a mobile copper mold (suction casting).

Optimization of the casting parameters is of importance in particular to obtain fully amorphous samples. Crucibles and chamber atmosphere are selected depending on the reactivity of the alloy with them. Once these parameters are selected, it is of vital importance to control the casting temperature and the pressure of ejection. In fact, both parameters determine the viscosity of the molten alloy, which is the most important parameter in glass forming ability.

The castings for the $Zr_{62}Cu_{18}Ni_{10}Al_{10}$, $Ti_{40}Zr_{25}Ni_8Cu_9Be_{18}$, $Cu_{46.5}Zr_{48.5}Al_5$, $Cu_{50}Zr_{50}$ alloys were done at the Anhui University of Technology (China). The $Fe_{36}Co_{36}B_{19.2}Si_{4.8}Nb_4$ alloy was prepared at the Tohoku University (Japan). In both

cases, the master alloys were prepared by arc- melting under Ar atmosphere. Rods of 2 and 3 mm diameter were obtained from the melt by copper mold casting.

$Ti_{40}Zr_{10}Cu_{38}Pd_{12}$ alloy was prepared at OCAS- Arcelor Mittal (Belgium). The master alloy was produced using a cold crucible levitation melting equipment (with a capacity of 1 kg of iron), under Ar atmosphere, after purging several times with Ar to a base pressure of 6.10^{-6} Pa. It was remelted and inverted four times to ensure chemical homogeneity.

The rods (3 mm in diameter) were injected into copper mold using a smaller levitation setup (with a capacity of 200 g of iron and a maximum achievable vacuum of 5.10^{-6} Pa).

$(Ti_{40}Zr_{10}Cu_{38}Pd_{12})_{100-x}Nb_x$ (with x =2, 3, 4) alloys were prepared under Ar atmosphere at the Universitat Autònoma de Barcelona (Spain) using an arc-melting device. Rods of 3 mm were obtained by suction the melt into Cu cold crucible molds.

2.1.3. Post-synthesis treatments

In this work, two techniques were used to tune the mechanical properties of metallic glasses. In one side, annealing treatments were carried out with the aim of strengthening the alloy; on the other, plastic deformation was applied by means of nanoindentation and compression test.

2.1.3.1. Annealing treatment

The annealing treatments of the $Fe_{36}Co_{36}B_{19.2}Si_{4.8}Nb_4$ alloy were performed in a tubular furnace under vacuum after thoroughly fluxing the oven with argon to ensure high purity atmosphere. The as-cast rods were heated at a rate of 10 K/min. Isothermal annealing was carried out at the different temperatures for 30 min and the samples were then immediately cooled to room temperature at 120 K/min.

The annealing treatments of the $Ti_{40}Zr_{10}Cu_{38}Pd_{12}$ alloy were performed in a high temperature furnace under vacuum atmosphere at a heating rate of 10 K/min in order to induce progressive devitrification of the glassy structure. All the samples were kept for 30 min at the different temperatures and then cooled at 80 K/min.

2.1.3.2. Mechanical treatments

Nanoindentation experiments with the aim to promote plastic deformation were carried out at room termperature using a Berkovich pyramidal-shaped indenter tip applying maximum loads ranging from 2 to 500 mN (with corresponding loading rate varying from 0.05 to 3.20 mN/s). A load holding period of 20 s was applied in all cases before unloading and the thermal drift was always kept below ±0.05 nm/s (see section 2.2.3.2. for further details).

Nanoindentation experiments in $Zr_{62}Cu_{18}Ni_{10}Al_{10}$ alloy indicate that deformation promotes nanocrystallization and, therefore an increase in hardness.

Nanoindentation measurements in the compressed $Zr_{62}Cu_{18}Ni_{10}Al_{10}$ alloy also show a hardness enhancement when compared to the as-cast specimen at low maximum applied loads.

Strengthening of the $Cu_{46.5}Zr_{46.5}Al_5$ alloy is also observed by nanoindentation after subjecting the alloy to compression test.

2.2. Characterization techniques

This section gives an overview of the different techniques used to characterize the as-cast materials and to study structural, thermal, mechanical and corrosion changes induced by annealing, plastic deformation and element addition to fully amorphous alloys.

First of all, Differential Scanning Calorimetry (DSC) has been used to study the thermal stability and crystallization of several metallic glasses and composite materials.

Morphological and structural changes in the materials were analyzed by means of scanning and transmission electron microscopy and X-ray diffraction. Compression tests and nanoindentation were used to study the macroscopic and microscopic mechanical behavior of the alloys. Furthermore, elastic constants were carefully determined using acoustic measurements. Corrosion characterization was carried out using potentiodynamic polarization curves

2.2.1. Thermal characterization

Thermal analysis focuses on the study of physical or chemical changes of a sample which occur as the temperature is increased or decreased. Several methods are commonly used to study the thermal behaviour of alloys. These are distinguished from one to another by the property which is measured. However, all of them have common features. The sample, positioned in an appropriate crucible (depending on the nature of the alloy that will be analyzed), is placed in a furnace and subjected to the desired temperature programme. During this procedure, one or more properties of the sample are monitored by means of suitable transducers for converting the properties to electrical quantities, such as voltages or currents.

2.2.1.1. Differential thermal analysis (DTA)

DTA is the simplest and most widely used thermal analysis technique. The difference in temperature between the sample and a reference material is recorded while both are subjected to the same heating programme.

The principle and a scheme of a DTA device are illustrated Figure 2.2. As the specimen is heated or cooled in a controlled manner, its temperature (T_s) will depart from the normal rate as it undergoes a reaction or transformation. When, for example, an endothermic event occurs in the sample, the temperature of the sample will lag behind the temperature of the reference material, which follows the programmed heating. For exothermic processes (Figure 2.2b), the response will be a faster heating. Furthermore, second order transitions characterized by for example a change in thermal conductivity or heat capacity of the sample, would give rise to a change in slope during thermal analysis and an offset of the baseline in differential thermal analysis.

The typical DTA device uses a pair of matched temperature sensors, generally thermocouples, one of them is in contact with the sample or its container and the other one is in contact with the reference material, as shown in Figure 2.2a. The output of the differential thermocouple is amplified and fed to the recorder or data acquisition system.

The use of a reference sample, besides the specimen of interest, is essential in order to eliminate disturbances in the recorded signal resulting from unintended fluctuations in

the rate of heating or cooling. This reference sample should be inert during the temperature interval of interest and should have a similar heat capacity. Since both the sample and reference material will react similarly to possible fluctuations, the final effect should be cancelled, leaving the baseline undisturbed.

A typical DTA-curve is the temperature difference between sample and reference monitored against the reference temperature, the actual sample temperature or time. Ideally, the area under the DTA peak should be proportional to the enthalpy of the process to give rise to the peak. However, changes in thermal transport properties of the system, detector sensitivity, etc. with temperature will generally decrease the response of the DTA device with increasing temperature and are not compensated for in a traditional DTA curve. To compensate those effects Differential Scanning Calorimetry (DSC) was developed.

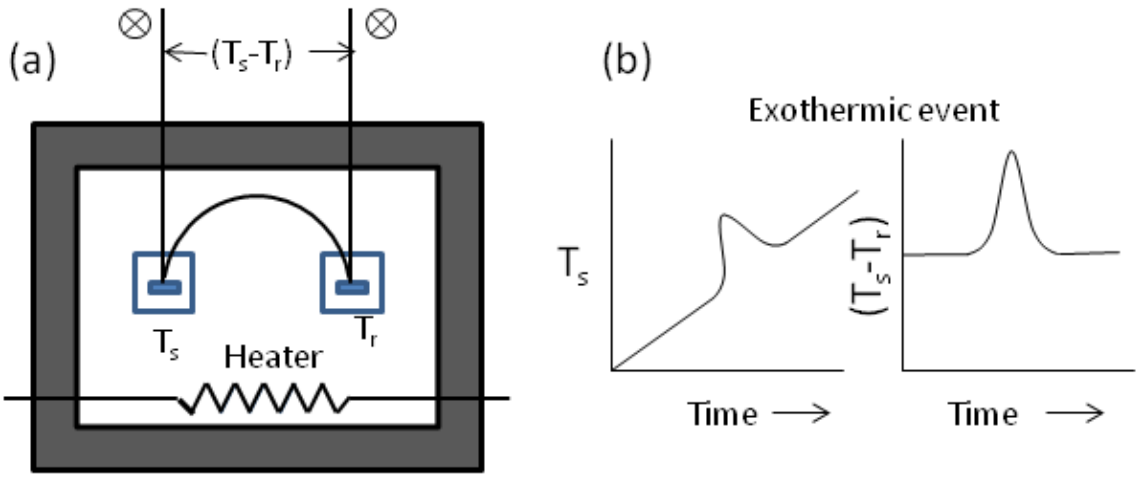

Figure 2.2: a) scheme of a DTA device b) general principle for an exothermic event where T_s is the sample temperature, T_r is the reference temperature, T_i is the initial temperature and T_f is the final temperature

DTA in this work was used to study the thermal behaviour at high temperatures of the $Fe_{36}Co_{36}B_{19.2}Si_{4.8}Nb_4$ alloy. DTA experiments were performed with a Perkin Elmer DTA at the Tohoku university at a heating rate of 40 K/min.

2.2.1.2. Differential Scanning Calorimetry (DSC)

This technique aims to maintain the sample and the reference material at the same temperature at any time during the experiment, by compensating independently the supplies of power to the sample and reference.

A schematic representation of a power compensating is shown in Figure 2.3. The inventive concept keeps the value of ΔT equal to zero by placing the temperature sensor, Pt resistance thermometers, into a bridge. Any imbalance drives a heater to compensate in the appropriate (sample or temperature) part of the cell. The power needed to the bridge circuit in balance is proportional to the change in heat capacity or enthalpy. The integral of power over the time of the total event gives the energy difference between sample and reference, which corresponds to the enthalpy difference of the process. Therefore, if power is supplied to the sample, the process is endothermic, if it is supplied to the reference side it is exothermic.

The International Union of Pure and Applied Chemistry, IUPAC, has given precise definitions of the terminology used for the interpretation of DSC curves, as illustrated in Figure 2.4:

- Baseline: part or parts of the DSC in which *dQ/dt* is nearly zero (lines AB and DE).
- Peak: part of the curve which initially goes off and later goes back on the baseline (line BCD).
- Peak width: interval of time or temperatures in which the DSC curve goes off the baseline (line B'D').
- Peak height distance, perpendicular to the time or temperature axis, between the interpolation of the baseline and the peak vertex (line CF).
- Peak area: closed area by the peak and the interpolation of the baseline (area enclosed by the lines BC, CD and BD)
- Initial temperature of transformation: temperature corresponding to the intersection point between the tangent at the maximum slope point at the beginning of the peak and the interpolation of the baseline point (point G)

- Final temperature of transformation: temperature corresponding to the intersection point between the tangent at the maximum slope point at the end of the peak and the interpolation of the baseline point (point H).

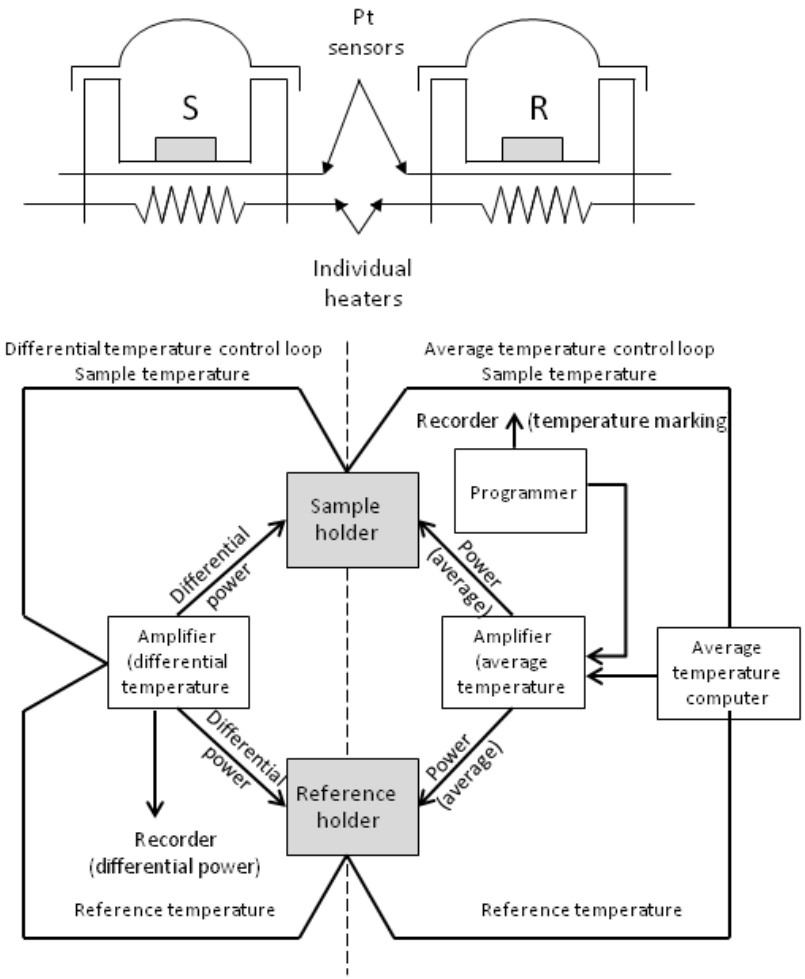

Figure 2.3: Schematic representation of a power compensating DSC instrument and its operation

DSC in this work was mainly used to study the thermal stability of the amorphous alloys. Furthermore, in some cases, it was also used to study the change in mechanical and structural properties induced by heating a metallic glass below the crystallization temperature (to induce structural relaxation) or between the various crystallization steps.

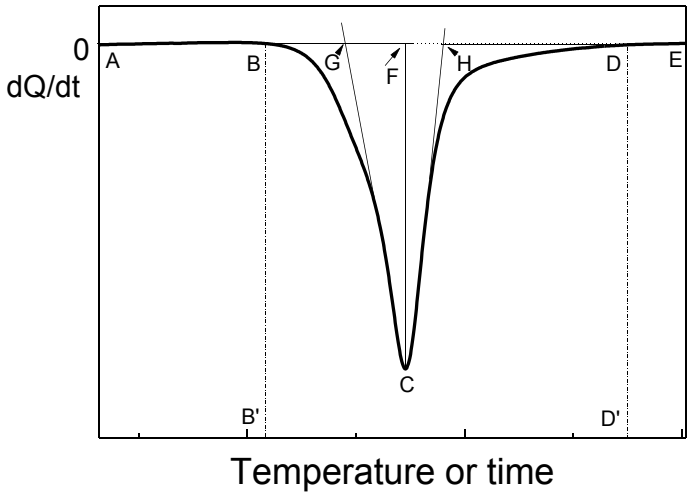

Figure 2.4: DSC curve and its interpretation following the IUPAC rules.

DSC experiments were performed with a Perkin Elmer DSC-7 at the Universitat Autònoma de Barcelona at a heating rate of 40 K/min.

All our experiments were carried out up to high temperatures. As a consequence, graphite crucibles were used as a reference holder as well as a sample holder. The reference material in all the DSC experiments was simply an empty graphite holder.

For each experiment, two consecutive scans were made: the first one to let the sample crystallize and measure its thermal properties; the second one (in the same sample) was made for baseline correction.

2.2.2. Structural characterization

Structural characterization comprises the use of scanning and transmission electron microscopy as well as X-ray diffraction.

The main characteristics of electron microscopes, compared to conventional optical microscopes, are that they use electrons instead of light and electromagnetic lenses instead of glass lenses. Under certain assumptions, electrons can be considered as waves, with wavelengths much smaller than visible light. This allows the observation of very small structures that would remain unobservable using optical microscopes.

Basically, it is possible to distinguish between: (i) transmission electron microscopy (TEM), where one can directly observe on a fluorescent screen the image obtained by

electrons that go through a thinned sample and (ii) scanning electron microscopy (SEM), where the electron beam scans over the surface of the sample, inducing electronic transitions and reemission of new electrons that can be used to form the image of the scanned surface.

2.2.2.1. Scanning electron microscopy (SEM)

When an electron beam arrives at the surface of a sample, some electrons can penetrate into it. The depth of this penetration directly depends on the atomic number of the constituents of the specimen. The electrons lose their kinetic energy as they go deeper into the sample. In the zone of penetration, a certain number of interactions between the electrons of the beam and the atoms of the sample take place. And, as a consequence, in this zone, several kinds of signals are emitted (see Figure 2.5):

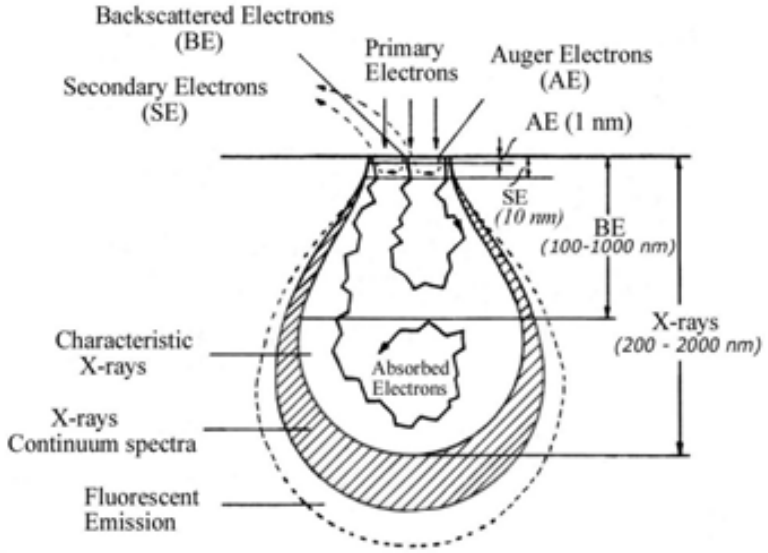

Figure 2.5: Types of electrons and radiation generated inside the sample in a scanning electron microscope.

- **Auger Electrons**: when an incident electron of the beam is able to expel out an electron of a certain atom, an electronic vacancy is created. Therefore, the "hole" will be occupied by another electron from an external shell resulting in some amount of energy, which can be transferred to another electron. If the electron leaves the sample, it is called Auger electron.

These electrons have typically low energy values and, therefore, they can only escape the sample from its surface (from a depth range between 0.5 and 2 nm), thus not giving information about more internal parts of the sample. Nevertheless, the energy of this type of electrons is characteristic of the atom that emits them. Thus, these electrons give compositional information of the specimen.

- **Secondary electrons**: these electrons originate from the impacts between high energetic incident electrons and the atoms of the specimen. If the energy of the incident electrons is large enough, the electrons of the atoms in the sample may have enough energy to be expelled out. These are the so-called secondary electrons, which have energies in the range of 0-50 eV. The secondary electrons give information about the density of the sample and the surface topography. However, all the information obtained from secondary electrons is restricted to a penetration depth of 10 nm.
- **Backscattered electrons:** these electrons are originated when the electrons of the incident beam hit the sample but are not able to penetrate it and are consequently reflected back. Therefore their energy depends very much on the energy of the primary incident beam. The information they give also depends on the atomic number of the elements on the surface and also on its topography. Hence, for example the brightness of the image will depend on the atomic number of the specimen since for higher atomic numbers a larger number of backscattered electrons will be obtained.
- **X-rays: Energy Dispersive X-ray analyses (EDX):** when an incident electron hits one atom of the sample inducing the emission of another electron, the corresponding "hole" is immediately occupied by a third electron initially located in a more external electronic shell. As a consequence, some energy in the frequency range of x-rays, is emitted. The wavelengths of the emitted x-rays are characteristic of the atoms that compose the sample. Thus, the resulting spectrum is often used to make compositional analyses of the material. This process is usually denoted as *energy dispersive x-ray analysis* (EDX). If some regions of the sample are scanned selecting the part of the x-ray spectra corresponding to one of the elements in the sample, it is possible to obtain the distribution of this element at the surface. This technique is commonly known as

x-ray mapping. Therefore, regions with higher densities of this element will appear as bright in the image, while lack of this element will result in a dark area.

The main components of a scanning electron microscope are: filament, system of electromagnetic lenses and diaphragms, sample chamber, scanning generator system, and detectors.

When the *filament* (e.g., a tungsten wire) is heated, it produces a beam of electrons, which are accelerated under application of a voltage between cathode and anode, in the range between 1 and 30 kV. Since electrons have a net charge they can be deviated by applying magnetic fields and, therefore, the beam diameter can be significantly reduced by using a system of *electromagnetic lenses*. Moreover, the beam can be further refined and homogenized by means of several metallic *diaphragms*. Furthermore, the electromagnetic lenses also contribute in accelerating the particles and, thus, they can influence the sharpness of the resultant image.

In the *sample chamber* one can find: the holder, with mechanical mechanisms to move the sample along the three spatial directions and, also, several detectors of the different types of radiation emerging from the sample (x-rays, secondary electrons, backscattered electrons, etc.).

In order to systematically scan the sample, there are two *electromagnetic spirals*, located among the electromagnetic lenses that produce oscillating magnetic fields, along the X-Y directions. This allows precise control of the scan speed.

SEM observations in this work were carried out using a JEOL JSM 6300 or a Zeiss EVO microscope; both equipped with an EDX data acquisition system (model Link Pentafet) and located at the Servei de Microscòpia of the Universitat Autònoma de Barcelona.

Before proceeding with the observations, the samples were embedded into an epoxy conductive resin for easy polishing. Samples were mechanically polished to mirror-like appearance with a final polish step using 1μm diamond paste. In some cases, to enhance microstructural features such as grain size and phase features, the samples were

chemically etched. Kroll's reagent (92 ml distilled water, 6ml HNO_3, 2ml HF) was used to etch Ti-based alloys while Cu- and Fe-based alloys were etched with distilled water (50 ml) and HNO_3 (50 ml) for 5 to 15 seconds.

The samples were basically imaged using backscattered and secondary electrons and their composition was analyzed by means of EDX.

2.2.2.2. Transmission Electron Microscopy (TEM)

In a conventional transmission electron microscope (TEM) a thin specimen is irradiated with an electron beam of uniform current density. If the penetration depth of the electrons is larger than the thickness of the sample they can go through it. The transmitted electrons are then focused onto a fluorescent screen.

TEM exploits three different interactions of electron beam-specimen; unscattered electrons (transmitted beam), elastically scattered electrons (diffracted beam) and inelastically scattered electrons.

- **Unscattered electrons:** when incident electrons are transmitted through the thin specimen without any interaciton occurring inside the specimen, then the beam of these electrons is called transmitted. The transmission of unscattered electrons is inversely proportional to the specimen thickness. Areas of the specimen that are thicker will have fewer transmitted unscattered electrons and so will appear darker, conversely the thinner areas will have more transmitted and thus will appear lighter.
- **Elastically scattered electrons**: Another part of the incident electrons, are scattered (deflected from their original path) by atoms in the specimen in an elastic fashion (no loss of energy). Elastically scattered electrons are the major source in TEM imaging and diffraction patterns.
- **Inelastically scattered electrons:** are the incident electrons that interact with specimen atoms in an inelastic fashion, loosing energy during the interaction. Historically, in operating a TEM only elastic signals were taken into account; therefore, the information about the specimen resulting from inelastic scattering was wasted (this information was obtained in related instruments such as SEM and Auger electron spectrometry). However, many of these signals can also be

detected using TEM to obtain a more complete characterization of the specimen. Furthermore, because some of the beam electrons lose energy, an extra signal related to the electron energy loss can be measured by Electron Energy Loss Spectroscopy (EELS). The EELS signal, together with X-ray signal, constitute analytical electron microscopy (AEM) (88).

- *Components and working basics*

In electron microscopy techniques, electrons are emitted from the electron gun and illuminate the specimen through a two or three stage condenser lens system. Objective lens provides the formation of either image or diffraction pattern of the specimen. The electron intensity distribution behind the specimen is magnified with a three or four stage lens system and viewed on a fluorescent screen. The image can be recorded by direct exposure of a photographic emulsion or an image plate or digitally by a CCD camera. A more detailed explanation of the main components and working principles of TEM equipment is provided in this section. In Figure 2.6 a schematic diagram illustrating the main components of a TEM is presented.

- **Electron gun:** The first and basic part of a microscope is the source of electrons. It is usually a V-shaped filament made of LaB_6 or W (tungsten) that is wreathed with Wehnelt electrode (Wehnelt Cap) shaping the beam electrostatically, i.e. reducing the crossover of the diameter of the beam optimizing its brightness. Due to negative potential of the electrode, the electrons are emitted from a small area of the filament (point source). A point source is important because it emits monochromatic electrons (with similar energy). The two usual types of electron guns are the conventional electron guns and the field emission guns (FEG).

  In conventional electron guns, a positive electrical potential is applied to the anode, and the filament (cathode) is heated until a stream of electrons is produced. The electrons are accelerated by the positive potential down the column, and because of the negative potential of cap, all electrons are repelled toward the optic axis. A collection of electrons occurs in the space between the filament tip and Cap, which is called a space charge. Those electrons at the bottom of the space charge (nearest to the anode) can exit the gun area through

the small hole (<1 mm) in the Whenelt Cap and then move down the column to be later used in imaging.

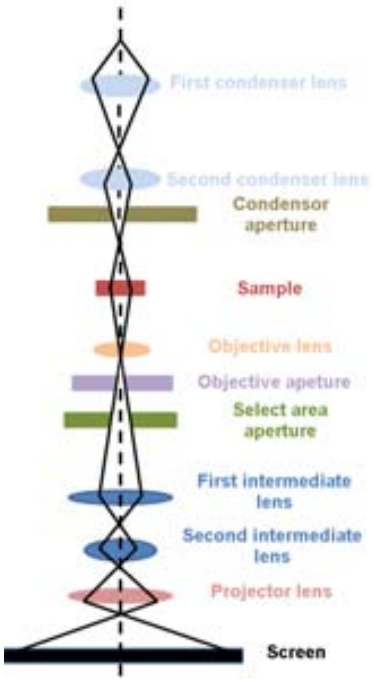

Figure 2.6: schematic diagram illustrating the main components of a TEM

A field emission gun consists of a sharply pointed tungsten tip held at several kilovolts negative potential relative to a nearby electrode, so that there is a very high potential gradient at the surface of the tungsten tip. The result of this is that the potential energy of an electron as a function of distance from the metal surface has a sharp peak (from the work function), then drops off quickly (due to electron charge traveling through an electric field). Because electrons are quantum particles and have a probability distribution to their location, a certain number of electrons that are nominally at the metal surface will find themselves at some distance from the surface, such that they can reduce their energy by moving further away from the surface. This transport-via-delocalization is called 'tunneling', and is the basis for the field emission effect. FEGs produce much higher source brightness than in conventional guns (electron current > 1000 times), better monochromaticity, but requires a very good vacuum (~10^{-7} Pa).

In Table 2.1 there is a comparison of the most important parameters characteristic of both types of electron sources.

	W	LaB_6	FEG (Schottky)
Maximum Current (nA)	1000	500	300
Normalised Brightness (-)	1	10-30	2500
Energy spread (eV)	3-4	1.5-3	0.6-1.2
Source spotsize	30-100 µm	5-50 µm	15-30 nm
Required Vacuum (Pa)	10^{-3}	10^{-5}	10^{-7}
Temperature (K)	2700	2000	1800
Life time (hr)	60-200	1000	>2000
Normalised Price (-)	1	10	100

Table 2.1: Comparison of the characteristics of electron sources: thermo-ionic (W LaB_6 filaments) and W field emission gun (FEG).

- **The condenser system:** Below the electron gun there are two or more condenser lenses. Together, they demagnify the beam emitted by the gun and control its diameter as it hits the specimen. An aperture is present between the condenser lenses (the condenser aperture) which can be used to control the convergence angle. The condenser controls can be thought as brightness controls but in fact they permit a wide range of control over the region of specimen.

  Going further insight, the first condenser lens, often labeled spot size, set the demagnification of the gun crossover. The second lenns provide control of the convergence angle of the beam leaving the condenser assembly (89).

- **The specimen chamber:** Below the condenser lies the specimen chamber. The specimen must be held in precisely the correct position inside the objective lens, but should be capable of being moved several milimiters and tilted by large angles.

- **The objectives and intermediate lenses:** The role of the objective lens is to form the first intermediate image and diffraction pattern, which are enlarged by subsequent projector lenses and displayed on the viewing screen. The first projector lens (often called intermediate or diffraction lens) can be switched between two settings. In the image mode, it is focused on the plane of the objective. Conversely, on the diffraction mode, the inermadiate lens is focused on the back focal plane of the objective and the diffraction pattern is projected onto the viewing screen.

An essential feature of the objective system is the aperture holder which enables any one of three or four small apertures to be inserted into the column in the back focal plane. Its diameter controls the resolution so, for higher resolution a large aperture will be needed. The objective aperture can also be used to control the contrast of the image.

- **The projector system**: As mentioned before, the first image is produced by the objective lens (with a magnificagtion of 50-100 times). This is further magnified by a series of intermediate and projector lenses and is finally projected onto the fluorescent screen.

  Some specialized microscopes have an energy filter below the specimen which can be tuned to allow the passage of only elastically scattered electrons. For example, this is of special interest in high resolution electron microscopy since inelastic scattering degrades image quality or in the quantitative interpretation of diffraction pattern intensities (89).

- **Other components:** In a TEM system there are various electromagnetic deflection coils placed at strategic points in the column. They are required to do minor adjustments on the alignment of electromagnetic lenses which have been previously mechanically well aligned. Further coils permit small fields to be imposed to correct for the effect of astigmatism in the condenser, objective and projector systems.

  Other important components are the detectors, to detect and record all different types of signals. In the past, images were typically recorded by an analogue camera. Nowadays, typically, CCD cameras are used to record images and diffraction in electron microscopy. Also, by combining the output from such a camera with a computer which a computer which has image processing software and control of the microscope lenses, it is now possible to perform some alignment procedures quickly and automatically (89)

- *Imaging and diffraction modes*

To operate in ***imaging mode***, suitably sized objective lens apertures (Figure 2.7) are placed in the back focal plan of the objective lens. In this way, diffracted beams can be deliberately excluded and only the central beam is allowed to pass trhough. The image

built up is called bright field image (Figure 2.7). Alternatively, a dark field image is formed by excluding all beams, except a particular diffracted beam of interest.

This dark field image reveals the regions contributing to the diffracted beam intensity selected, which can be useful in the characterization of complex microstructures. In particular, for amorphous samples, the dark field technique can be very useful to reveal (or exclude) the presence of nanocrystals. In samples with a certain contrast in bright field imaging but an apparent amorphous diffuse halo in diffraction, dark field imaging by selecting part of the diffuse halo can be useful to give the definitive answer.

The most limiting factor for the use of the dark field technique is the confined resolution caused by spherical aberration. This can be avoided in modern TEMs by tilting the illumination system so that the chosen diffracted beam is aligned accurately along the objective axis of the microscope, instead of simply positioning an objective aperture around the desired diffracted beam.

At smaller magnifications TEM image contrast is due to absorption of electrons in the material, due to the thickness and composition of the material. At higher magnifications complex wave interactions modulate the intensity of the image, requiring expert analysis of observed images. Alternate modes of use allow for the TEM to observe modulations in chemical identity, crystal orientation, electronic structure and sample induced electron phase shift as well as the regular absorption based imaging.

Resolution of electron microscopy can be expressed by the Rayleigh formula which shows that resolution increases with higher voltage and lower wavelength:

$$R = \frac{0.61\lambda}{\alpha} \quad \text{(Eq. 2.1)}$$

where R is the size of the resolved object (the smallest R, the higher the resolution), λ is the wavelength and α is the semi-angle of the objective lens aperture. However, the use of larger apertures to increase resolution is limited by several aberration errors in the lenses. As a result, an optimum aperture equilibrating minimum aberration and maximum resolution exists (90; 91).

For instance, for high resolution transmission electron microscopy (HRTEM), several beams on the back focal plane are selected, by using a large objective aperture. The image results from multiple beam interference and is based on the phase difference

between the transmitted and diffracted beams. HRTEM is often used to determine disordered and defect structures which are difficult to determine by other methods.

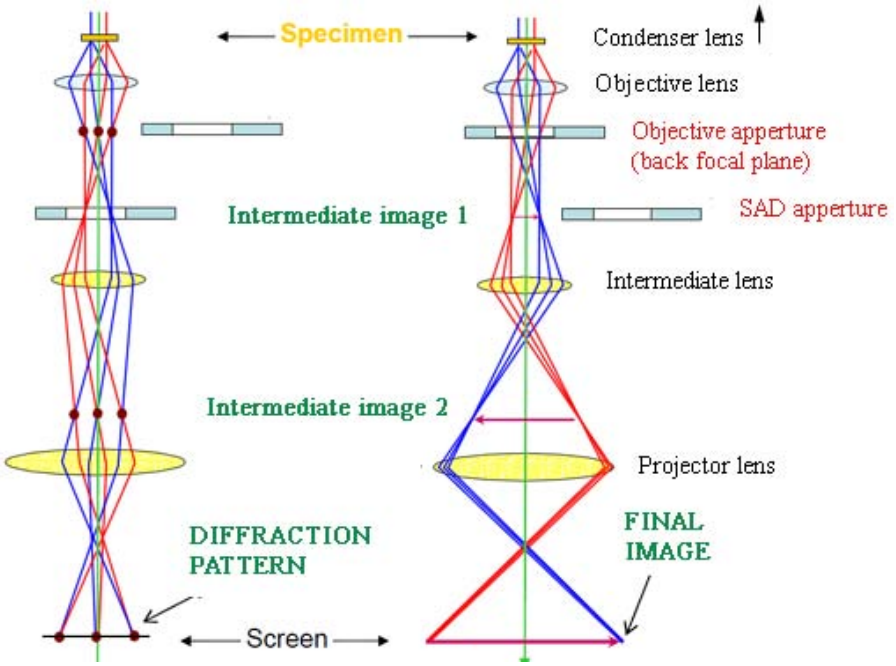

Figure 2.7: Schematic diagram illustrating the difference between operating in diffraction mode and bright field image mode.

To operate in ***diffraction mode*** no aperture is placed in the back focal plane of the objective lens, as a consequence, the diffraction pattern can be observed and recorded. By inserting an aperture at the image plane of the objective lens, the field form which the diffracted information is obtained is limited, which is referred to as selected area electron diffraction (SAED).

There are two parameters of importance in electron diffraction: the angular distribution of the scattered electrons and the intensity of the scattering. With the geometry of the diffraction pattern we can obtain information about the structure and orientation of a crystal. Furthermore, the intensity of electron scattering enable us to deduce more detailed information from a diffraction pattern and perhaps, enable us to understand and interpret the images of crystalline materials.

To interpret any diffraction pattern the Bragg's law ($2dsin\theta = n\lambda$ (Eq. 2.2)) must be fulfilled.

In electron diffraction it is conventional to consider only the first order of diffraction (n=1) and to deal with higher orders by using the corresponding multiples of the Miller

indices. Eq. 2.2 can be further simplified due to the high energy of electrons (small values of λ), the scattering angles that fulfill Bragg's law are very small and we can consider $\sin\theta=\theta$, hence equation Eq. 2.2 can be written as $\lambda = 2d\theta$ (Eq. 2.3)). This makes the geometry of electron diffraction patterns much simpler than that of X-ray diffraction patterns, for which can be very large.

On the other side, the intensity of a given diffraction spot is related to the shape, volume and perfection of the crystal and to the structure factor, *F*, for the unit cell. This structure factor is a mesure of the amplitude scattered by all the atoms in a unit cell into the reflection *hkl*.

For a primitive cell, the scattering from the whole unit cell (given by the structure factor *F*), is the same as the scattering from one single atom (given by the atomic scattering factor *f*). The scattering from each atom in the unit cell can be described as:

$$A = f exp\ i\theta \qquad \text{(Eq. 2.4)}$$

where *f* is the scattering factor for a single atom and θ is the phase of the wave with respect to the wave scattered from the origin of the cell. If diffraction occurs from the (*hkl*) plane, then the phases are such that scattering from an atom *n* at cell position *uvw* can be given by:

$$A_n = f_n \exp(2\Pi i\ hu + kv + lw\ ) \qquad \text{(Eq. 2.5)}$$

The structure factor F is given by summing the scattering from all the atoms of the unit cell.

In some cases, the individual terms can sum to zero, i.e. the planes give rise to no diffracted beam. These are known as forbidden reflections (89). The structure factor is also important since the intensity of the beam diffracted by all the atoms of the unit cell is proportional to $|F|^2$ (90). The combination of the structure factor equation and Bragg's law allows the direction of all strongly diffracted beams from a crystal to be calculated.

Coming back to the geometry of electron diffraction, let's now focus on its understanding. As can be observed in Figure 2.8, when a beam of electrons goes through a crystalline specimen, some of the electrons pass through it without interaction and hit the screen which is at a distance L from the specimen. Other electrons are diffracted through an angle 2 by the crystal planes of spacing d; so, by simple geometry, $R/L = 2\theta$ (for small angles), combining this with Eq. 2.3 we find $Rd = L\lambda$,

where $L\lambda$ is the camera constant (L is the camera length) and can be determined by a standard with known d-spacings. Therefore, R is inversely proportional to the d spacing so, by simply measuring r on the pattern d can be determined.

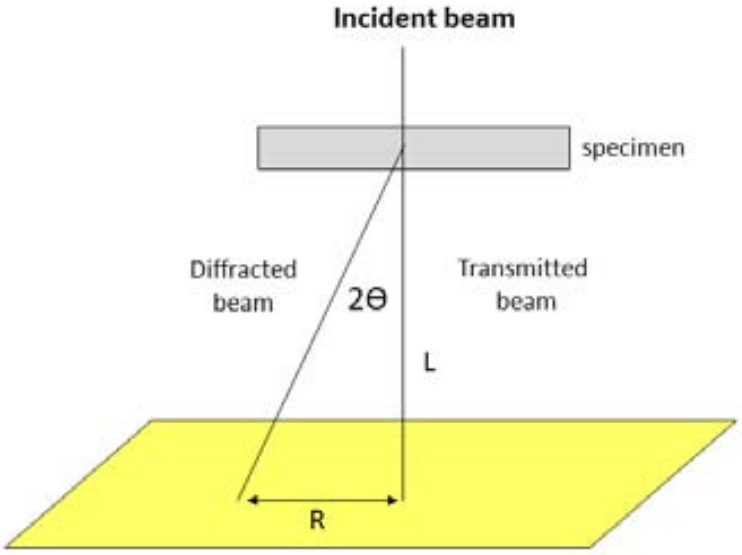

Figure 2.8: Schematic diagram showing the geometry of diffraction pattern formation

The planes lying approximately parallel to the electron beam are the ones that would diffract electrons. In Figure 2.9 various diffraction patterns for different microstructures are presented. A single crystal specimen (Figure 2.9a) will give rise to a diffraction pattern consisting of a regular array of spots. If the specimen contains several crystals of different orientations, then the diffraction pattern will be the sum of the individual pattern (Figure 2.9b). Figure 2.9c shows the case for a specimen containing very many crystals of random orientation. At this time, the spots on the rings are so close that the rings appear continuous.

Another type diffraction pattern comes from amorphous structures, i.e., metallic glasses. This time, the diffraction pattern will consist of fuzzy rings whose distances are related to the average nearest (SRO) and next-nearest (MRO) neighbor distances in the material.

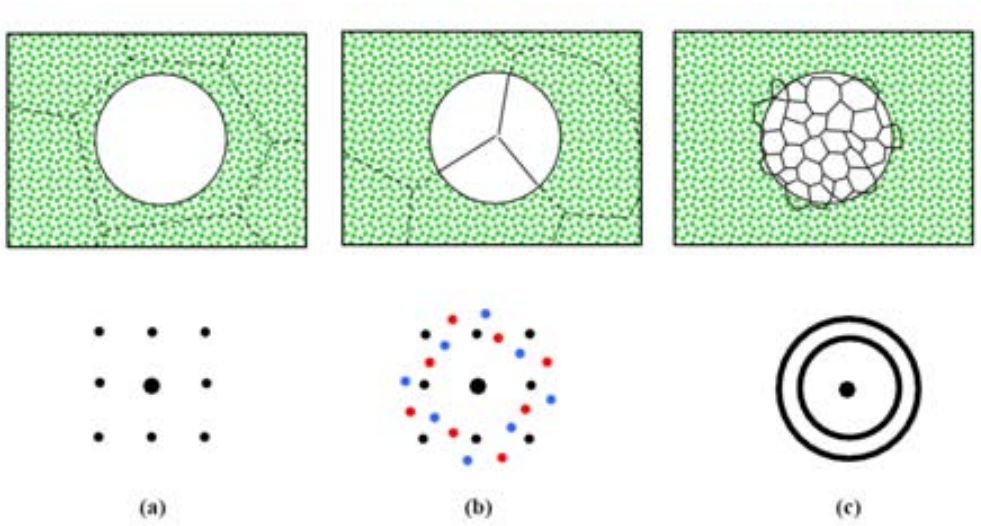

Figure 2.9: Types of diffraction pattern for (a) single crystal (b) a small number of grains (c) A large number of randomly oriented grains

In this work, TEM observations were carried out with a 200 kV JEOL-JEM-2011, located at the Servei de Microsòpia at the Universitat Autònoma de Barcelona, equipped with a LaB_6 thermo-ionic source. Indexing and crystalline phase identification from diffraction patterns was performed using the Carine simulation software together with phase identification softwars described in section 2.2.2.3.

- ***Preparation of specimens for TEM***

Before we can proceed with any observation, a specimen representative of our sample must be carefully prepared. The final specimen thickness must be of the order of nanometers and structural changes coming from the preparation have to be avoided.

The technique employed to prepare the specimen vary mostly depending on the nature of the material. Furthermore, not all the preparation methodologies are suitable for all kinds of materials; some of them involve a risk of structural and/or chemical modification in certain materials; thus, special care should be taken in the selection of the preparation technique, especially when the materials to be observed are metastable (metallic glasses and nanocomposites).

The different specimen preparation techniques can be divided into two main groups. The first group includes the techniques based in *removal* of unwanted material, by either chemical or mechanical means, until a very thin specimen is left behind. The

second group embraces the *cutting* techniques, in which the samples is either cut with a knife or sliced along crystallographic planes so that a very thin specimen is produced.

In this section we will describe a mechanical + ionic type procedure (grinding, dimpling and ion milling), which is the one we used to thin our specimens.

In this work, all the samples were obtained in form of rods of 2, 2.5 and/or 3 mm in diameter directly upon casting. First of all, disks of around 300 μm in thickness were cut using a diamond bladed saw (struers Minitom). Then, the disks were attached to a mount using low melting point thermoplastic polymer and mechanically polished with SiC paper down 80-100 μm using a Gatan Disc Grinder. The dimpling process can be accomplished without demounting the specimen.

The second step consists of thinning the center of the disk down to 15-20 μm with the aim to reduce the ion milling time. To perform this step we used a commercial mechanical dimpler consisting of two rotating systems with different diameter and with perpendicular rotating axes. The Gatan Dimple Grinder is also equipped with a dual measuring system. A digital micrometer that automatically stops the device when the desired thickness is obtained and an analog dial indicator that gives a continuous display of the dimple depth. First, the grinding wheel is lowered until the dial indicator show that it just touches the specimen mount and the digital micrometer is zeroed electronically. Second, the grinding wheel is lowered onto the specimen disc using the cam control at the base of the dimpler. When the grinding load is fully transferred to the specimen, the dial indicator reads the depth of material which is to be removed to achieve the desired dimple depth. Grinding will continue and the grinding wheel platform will slowly fall until the dial indicator reaches its zero stop. Before starting with the grinding, diamond paste is applied on the sample and on the grinding wheel at the same time than it is cooled with a refrigerant (92).

The final thinning of the disk was performed by ion milling. This process consists in bombarding the specimen with energetic ions (usually Ar^+) in order to sputter the material until it is thin enough to be studied in the TEM. The parameters to control are: the voltage, the nature of the ion and the geometry (angle of incidence and attack from the bottom or top part). Some devices also offer the possibility of cold milling with liquid nitrogen. The specimen is usually rotated at a few rpm during thinning.

The ion milling rate increases with higher etching angle and higher etching voltage; however, the sample is also more severely damaged. Therefore, the angle as well as the voltage should be kept rather low.

In this work, the amorphous and nanocrystalline samples were prepared with a GATAN polishing ion device at an incident angle of 4-4.5º from the top part and an etching voltage of 4 kV. Those values were observed to be appropriate and no structural changes were detected in the major part of our samples. However, in the harder samples (using small voltages and angles) the milling time was quite large.

2.2.2.3. X-ray diffraction

X-ray diffraction (XRD) is a versatile, non-destructive technique that reveals detailed information about the chemical composition, physical properties and crystallographic structure of natural and manufactured materials. X-ray diffraction is based on observing the scattered intensity of an X-ray beam hitting a sample as a function of incident and scattered angle, polarization, and wavelength or energy.

If one assumes that the incident x-ray beam is perfectly collimated and monochromatic (with a single wavelength λ) and makes an incident angle θ with respect to the reticular planes of the crystal, it can be demonstrated that the aforementioned Eq. 2.2. is fulfilled:

$$n\lambda = 2d\ sin\theta \qquad \text{(Eq. 2.2)}$$

where n is the reflection order and d is the interplanar distance of one family of crystallographic planes, x-rays will be completely in phase and will, therefore, give constructive interferences. This condition, known as the Bragg's law, is schematically represented in Figure 2.10 and it can be used to determine the angular positions of the XRD peaks diffracted by each family of planes (93; 94; 95).

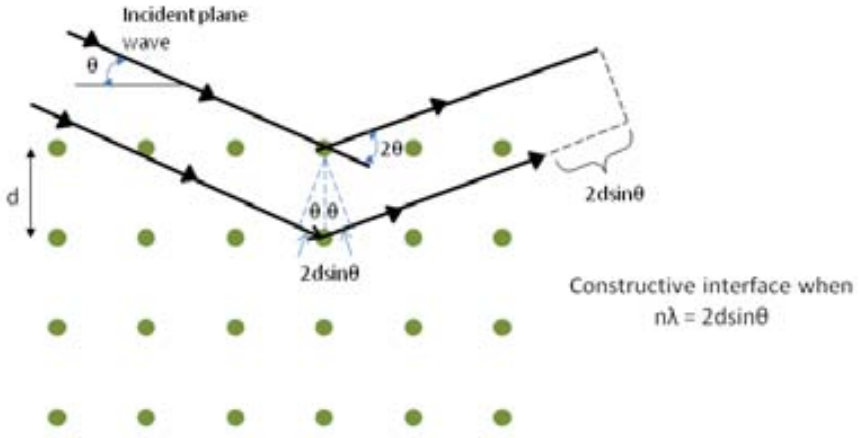

Figure 2.10: Schematic representation of the conditions for constructive interference resulting in Bragg's law.

The Bragg's law assumes the crystal is ideal (without structural defects) and the incident beam is perfectly monochromatic and collimated. These conditions are never fulfilled completely. Moreover, usually, the particles are found to be composed of several grains, with different orientation and with certain amount of defects. Each of these grains is called a *crystallite*. The size of these crystallites and the microstrains present in them can also be obtained from the XRD spectra, since both effects contribute to the width of the diffraction peaks (94; 95).

The peak shape of conventional materials can usually be fit by a simple Gaussian function:

$$X(2\theta_i - 2\theta) = \alpha \exp\left(\frac{(2\theta_i - 2\theta)^2}{\Gamma_i^2}\right) \quad \text{(Eq. 2.6)}$$

Where Γ_i is the half-width of the i^{th} reflection with center in 2θ, which on its turn can be calculated with the formula of Cagliotti:

$$\Gamma_i^2 = U\tan^2\theta_i + U\tan^2\theta_i + W \quad \text{(Eq. 2.7)}$$

With *U*, *V*, *W* the half-width parameters. However, when crystallite size drops below certain values or large strains are present, a deviation of the shape occurs from pure Gaussian to a mixture of a Gaussian and a Lorentzian function, also referred to as a pseudo-Voight function:

$$X'\ 2\theta_i - 2\theta\ = \eta L + \ 1-\eta\ G =$$
$$\eta\ \ \beta\ \ 1+\frac{(2\theta_i-2\theta)^2}{\Gamma_i^2}\ \ ^{-1} + (1-\eta)\ \ \alpha\exp\ \ \frac{2\theta_i-2\theta\ ^2}{\Gamma_i^2} \qquad \text{(Eq. 2.8)}$$

Using this formalism, the crystallite size can be deduced from the lorentzian contribution, to the integral width of the diffraction peak, Γ_{fL}, as given by the Scherrer formula:

$$\delta_{hkl} = \frac{\lambda}{\Gamma_{fL} cos\theta_B} \qquad \text{(Eq. 2.9)}$$

where θ_B is the angular position of the peak (measured in radians) and λ is the wavelength (measured in Å). The value of δ_{hkl} represents the coherent diffraction domain and is measured also in Å. Analogously, microstrains can be determined from the Gaussian contribution to the integral peak width, Γ_{fG}, using the expression:

$$e\ = \frac{\Gamma_{fG}}{4tan\theta_B} \qquad \text{(Eq. 2.10)}$$

where $<e>$ represents the upper limit of microstrains. However, it is more frequent to use the mean square root of microstrains, $<\varepsilon^2>^{1/2}$ (*rms strain*), which is related to $<e>$ in the following way: $<e> = 1.25\ <\varepsilon^2>^{1/2}$.

When a sample, composed of several phases, is analyzed by x-ray diffraction, each phase originates its own diffraction pattern. The relative intensity of the several peaks in the pattern depends on the relative concentration of the different phases. The phase identification can be carried out by comparison with *Powder Diffraction Files* databases such as PCPDFWIN, FindIt or the X'Pert HighScore program.

In general, the main components and working basics of a powder diffractometer are described here bellow:

The generation of X-ray is based on the impacts between source electrons, emitted from the cathode, and metal atoms (typical Cu, Co, Mo, Cr in the anode), which result in the emission of electrons of the metal, leaving a large number of holes inside the inner electronic shells. These holes become immediately occupied by electrons from more external shells and the excess of energy is liberated as x-ray radiation, whose energy depends on the energy difference between the energy levels of the electrons and, hence, has discrete values.

The X-ray tube is equipped with a filter with the aim to obtain maximum monochromatisation and to eliminate unwanted radiations. It also contains the soller slits, several fine metallic foils positioned very close to each and parallel to the diffraction circle plane. The soller slits are necessary to make a parallel and collimated beam, since the X-ray source emits in all directions. In front and behind these Soller slits, divergence slits are present to limit the divergence of the beam to typically limits of 1/30º to 4º. The sample placed at the center of the goniometer, rotates with an angle velocity of $\theta/\Delta t$.

The X-ray detector moves around at the circumference of the goniometer with an angle velocity of $2\theta/\Delta t$ and counts the number of photons per second. Since the detector has to follow the diffracted radiation, when the sample rotates at an angular speed θ, the detector has to rotate at 2θ with respect to the incident beam. As a consequence, this Bragg-Brentano geometry is also known as "θ-2θ scan".

Before entering the detector, the diffracted X-rays pass again through Soller and divergence slits, in order to keep the X-ray diffracted by the sample collimated and make them convergent respectively. The width of these slits determines the maximum intensity in the detector.

These different parts of the Bragg diffractometer are illustrated in Figure 2.11.

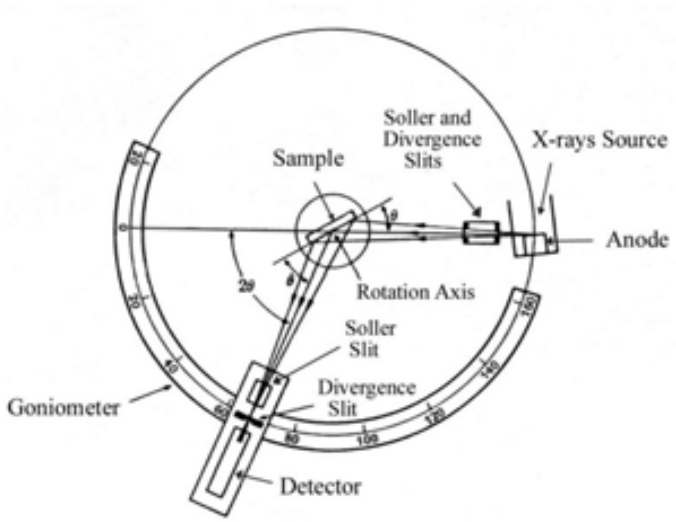

Figure 2.11: Schematic picture of an x-ray diffractometer.

XRD experiments were carried out at the Servei de Difracció at the Universitat Autònoma de Barcelona, using a Phillips X'Pert diffractometer.

The sample was stick on a circular silicon holder with plasticine or baseline. Ensuring that the sample surface covers the plasticine or the baseline (to avoid undesired diffraction peaks coming from the glue). The surface is flat and it is at the Bragg's plane of the diffractometer.

The x-ray spectra were obtained in a *step-scan* mode. This means that the sample and the detector rotated in steps instead of in a continuous way. The appropriate step size for each experiment was selected in order to have at least 10 experimental points above the half height width. Therefore, depending on the peak widths, 2θ steps of 0.02º or 0.04º were chosen. Moreover, the time for step was selected to be relatively long (around 10 s) in order to reduce the statistical error.

The powder diffractometer used in our study was set up in *Bragg-Brentano* geometry (Figure 2.11).

Some technical specifications are presented here:

Tube	**Radiaton**	**Primary beam optics**	**Secondary beam optics**
Anticatode: Cu Voltage: 40kV Current: 50 mA	Cu-K_α : $\lambda(K_{\alpha 1})$ = 1.54060 Å $\lambda(K_{\alpha 2})$ = 1.54439 Å $I(K_{\alpha 2}) / I(K_{\alpha 1})$ = 0.50	Soller slits: 0.04 mm Divergenge at the entrance:1/2º	Soller slits: 0.04 mm Divergenge at the exit:1/2º Monochromator: pyrolitic graphite

Table 2.2: Technical specifications of X-ray measurements

The fully crystalline XRD patterns were adjusted by a full-pattern fitting procedure (Rietveld method) using the Microstructural Analysis Using Diffraction (MAUD) software.

2.2.3. Mechanical characterization

Mechanical properties are those that reveal a reaction in a material, either plastic or elastic, to an applied load. Strength, hardness, toughness, elasticity, plasticity, brittleness, and ductility are mechanical properties used as measurements of how metals behave under a load enabling us to determine the range of usefulness of a material and to establish the service life that can be expected.

These properties are described in terms of the types of force or stress that the metal must withstand and how these are resisted. Common types of stress are compression, tension, shear, torsion, impact, or a combination of these stresses, such as fatigue. Many materials show marked differences when they are subjected to compression, tension or shear; therefore the type of test should be in accordance to the applied stress that the material will be subjected and, always, the type of loading used to determine a mechanical property should be stated.

It should be also noted that the mechanical properties of a material are not constant and often change as a function of temperature, rate of loading, and other conditions. For example, measurements at temperatures below room temperature generally cause an increase in strength while ductility, fracture toughness, and elongation usually are reduced. Conversely, measurements at temperatures above room temperature usually cause a decrease in the strength of the alloy.

In this work, compression test, acoustic measurements and nanoindentation were carried out to study the mechanical properties of BMGs and nanocomposite alloys. For instance, by compression test, the yield strength, the fracture strength, the Young's modulus and the plasticity can be determined; however, to determine more accurately the Young's modulus, acoustic measurements were also carried out. Besides Young's modulus, other elastic properties, like shear modulus, bulk modulus or Poisson's ratio can also be determined by acoustic measurements. Nanoindentation studies were performed with the aim to measure the hardness, which on its turn can be related to the yield stress and the reduced Young's modulus. This technique is especially useful to measure the hardness of thin films or small areas but it also allows determining parameters related to the wear resistance or to the elastic recovery.

2.2.3.1. Ultrasonic spectroscopy: Pulse-echo technique

Contrary to most spectroscopy techniques that use electromagnetic waves in analysis (UV, IR, NMR…), ultrasonic spectroscopy uses high-frequency sound waves (higher than 20 kHz, the limit of human hearing). When such a sound wave propagates in a material it forces particles to oscillate. They oscillate around their equilibrium positions with a frequency equal to that of the ultrasonic wave. The oscillations can be parallel to

the direction of propagation, so that the sound wave generates a compressional wave. If the oscillations are perpendicular to the direction of propagation, a shear wave is generated.

An ultrasonic wave is characterized by its amplitude, frequency, wavelength, and attenuation coefficient. The first two are predetermined whereas the latter two depend on the material through which the ultrasonic wave is passing. As the ultrasonic velocity is the product of wavelength and frequency, it is also characteristic of a particular material.

Attenuation is determined by the energy losses when the wave travels through the sample. The rate of dissipation increases with the frequency of the sound wave and decreases with the density of the medium.

For measurement purposes the trade-off is between attenuation and resolution, both of which are a function of sound frequency. Higher frequencies yield higher resolution but also higher attenuation. For instance, in thinner, non attenuating materials, it is suitable to use higher frequencies in order to obtain better resolution. So, depending on the nature and geometry of the material to be measured, an appropriate ultrasound transducer must be selected.

In the pulse-echo ultrasonic testing technique, a signal pulse propagates through a sample with the path length *d* and is reflected at the opposite wall of the cell producing an echo. Each echo travels a distance equal to twice the cell length d before it reaches again the transducer. By measuring the time delay between two echoes, *t*, the ultrasonic velocity *v* can be calculated according $v = 2d/t$.

To determine the elastic constants, the velocity of the longitudinal (also known as compressional) and transverse waves (shear wave) has to be measured. Using Eq. 2.11 and 2.12 the values of Young's modulus, *E*, and Poisson's ratio, *v*, can be determined (96).

$$C_L = \sqrt{\frac{E(1-\nu)}{\varphi(1+\nu)(1-2\nu)}} \qquad \text{(Eq. 2.11)}$$

$$C_T = \sqrt{\frac{E}{2\varphi(1+\nu)}} \qquad \text{(Eq. 2.12)}$$

In turn, bulk modulus, B, and shear modulus, G, can be derived using the following relations (47):

$$B = \frac{E}{3(1-2\nu)} \qquad \text{(Eq. 2.13)}$$

$$G = \frac{E}{2(1-\nu)} \qquad \text{(Eq. 2.14)}$$

In this work, samples of 2, 2.5 and 3 mm in diameter and about 2 mm on length were tested, after polishing them to perfect orthogonal geometry. Their densities have been determined by the Archimedes method and the sample dimensions were measured with a digital caliper.

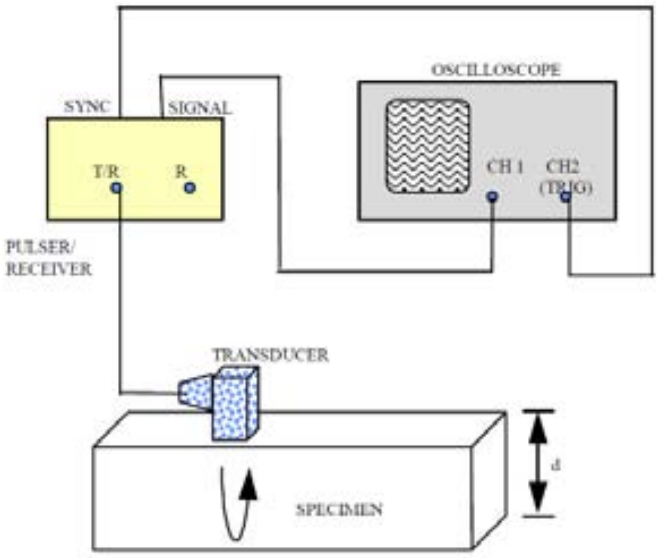

Figure 2.12: Schematic diagram of the components of the ultrasonic testing device.

A normal incidence shear wave transducer (V222-BB-RM from Olympus) with a frequency of 20 MHz was used to generate transverse waves. The longitudinal waves were produced with a Delay line transducer (V208-RM from Olympus) also with a frequency of 20 MHz. The transducers were employed with a panametric pulser-receiver (5072 PR from Olympus) and a digital oscilloscope as shown in Figure 2.12. The pulser produces an electrical pulse to excite a transducer that converts the electrical input to mechanical energy creating an ultrasonic wave. To provide acoustic coupling between the transducer and the material to be tested, a couplant is almost always necessary.

Finally, the transversal and longitudinal signals were recorded and treated using a home-made Labview program. Subsequently, the elastic constants were automatically calculated.

2.2.3.2. Nanoindentation

In general terms, nanoindentation technique consists in touching a material whose mechanical properties such as hardness and Young's modulus are unknown with another material whose properties are known. Nanoindentation is simply an indentation test at which the length scale of the penetration is measured in nanometers rather than microns or millimeters and the applied load is in the order of μN and mN rather than N as the conventional hardness measurements.

Nanoindentation is considered as a depth-sensing indentation techniques as the penetration depth is continuously monitored as a function of the load during the test. Contrary to the conventional methods, where just the hardness of the specimen was measured, this technique can also be used to calculate elastic modulus, strain-hardening exponent, fracture toughness and viscoelastic properties.

The test procedure involves a loading sequence followed by an unloading (Figure 2.13a). The loading part usually consists of an initial elastic contact, followed by plastic flow, or yield, within the specimen at higher loads. Upon loading, if yielding has occurred, the load-displacement data follows a different path until at zero applied load, a residual impression is left in the specimen surface. The maximum depth of penetration for a particular load, together with the slope of the unloading curve measured at the tangent to the data point at maximum load, lead to a measure of hardness and Young's modulus. For a viscoelastic material, the relationship between load and depth is not linearly dependent so, for a given load, the resulting depth of penetration may depend upon the rate of application of load as well as the magnitude of the load itself. For such materials, the indentation test will be accompanied by "creep" and this manifests itself as a change in depth for a constant applied load (97).

It is interesting to note that the validity of nanoindentation data depends largely upon the analysis procedure used to process the raw data. Such procedures are concerned not

only with the extraction of modulus and hardness, but also with correcting the raw data for various systematic errors that will be later discussed.

- *Tip geometry*

Nanoindentation tests can be performed with a wide variety of tips chosen in function of the material to be tested or the data that is required. Usually they are made with spherical or pyramidal indenters; for instance, the Berkovich indenter, the most widely used in nanoindentation, is generally employed in small-scale studies and has the advantage that the edges of the pyramid are more easily constructed to meet a single point, rather than the inevitable line that occurs in the four-sided Vickers pyramid, thus ensuring a more precise control over the indentation process. The original Berkovich indenter was designed to have the same ratio of actual surface area to indentation depth as a Vickers indenter and had a face angle of 65.0333º. Since it is usual to use the mean contact pressure as a definition of hardness in nanoindentation, Berkovich indenters used in nanoindentation work are designed to have the same ratio of projected area to indentation depth as the Vickers indenter in which case the face angle is 65.27º.

The Knoop indenter (four sided pyramid indenter) is useful to investigate anisotropy of the surface of the specimen by measuring the unequal lengths of the diagonals of the residual impression. It was originally developed to measure the hardness of very hard materials using moderate loads in microhardness measurements. Because one axis is longer than the other, the length of the long axis can be more accurately determined compared to a conventional Vickers impression.

The spherical indenter provides a smooth transition from elastic to elastic-plastic contact and it is particularly suitable for measuring soft materials and for replicating contact damage in in-service conditions. In this work, all the nanoindentation experiments were carried out with a diamond Berkovich nanoindenter tip.

- *Analysis of nanoindentation data for a Berkovich indenter*

The hardness (H) and reduced elastic modulus (E_r) values were derived from the load-displacement curves at the beginning of the unloading segment using Oliver and Pharr's method (98). Form the initial unloading slope (see Figure 2.13a), the contact stiffness, S, was determined as:

$$S = \frac{dP}{dh} \qquad \text{(Eq. 2.15)}$$

Where P and h denote, respectively, the applied load and the penetration depth during nanoindentation. The elastic modulus was evaluated based on its relationship with the contact area, A, and stiffness:

$$S = \beta \frac{2}{\sqrt{\pi}} Er\sqrt{A} \qquad \text{(Eq. 2.16)}$$

Where β is a correction factor that depends on the geometry of the indenter, 1.034 for a Berkovick type, and Er is the so-called reduced Young's modulus defined as follows:

$$\frac{1}{E_r} = \frac{1-\nu^2}{E} + \frac{1+\nu_i^2}{E_i} \qquad \text{(Eq. 2.17)}$$

The reduced modulus takes into account the elastic displacements that occur in both the specimen, with Young's modulus E and Poisson's ratio ν, and the indenter, with elastic constats E_i and ν_i. Note that for diamond, E_i= 1140 GPa and ν_i=0.07. Finally, Hardness, H, is calculated from the following expression:

$$H = \frac{P_{max}}{A} \qquad \text{(Eq. 2.18)}$$

Where P_{max} is the maximum load applied during nanoindentation. As can be observed from Eq. 2.18, the determination of the contact area is of prime importance to calculate H and E values.

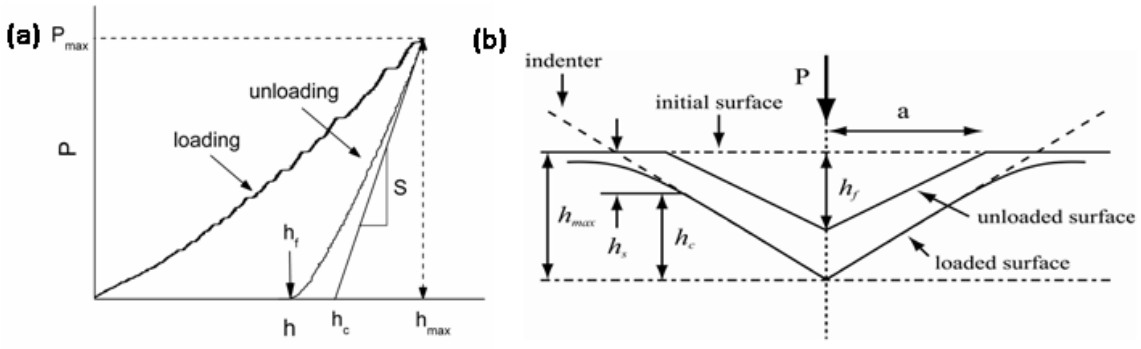

Figure 2.13: (a) Typical load-displacement nanoindentation curve. (b) Schematic illustration of the indenter and specimen surface at full load and unload and the parameters characterizing the contact geometry.

In a first approximation, A, can be equal to the one for a perfect indenter; for instance, for a Berkovich indenter, which has a face angle of $\theta = 65.27$, the relationship between the contact area A of the indentation and the depth h_c is given by:

$$A = 3\sqrt{h_c^2}tan^2 65.27 = 24.5h_c^2 \qquad \text{(Eq. 2.19)}$$

where the contact depth, h_c is:

$$h_c = h_{max} - \varepsilon\frac{P_{max}}{S} \qquad \text{(Eq. 2.20)}$$

where the parameter ε depends again on the shape of the indenter ($\varepsilon = 0.75$, for a Berkovich tip).

In conventional indentation tests, the area of contact between the indenter and the specimen at maximum load is usually calculated from the diameter or size of the residual impression after the load has been removed. However, in nanoindentation tests, the size of the residual impression is on the order of microns and too small to be conveniently measured directly. Consequently, the area is calculated by measuring the depth of penetration of the indenter into the specimen surface as stated from Eq. 2.19. However, there are various errors associated to this procedure. Some of them arise from environmental changes during the test and the non-ideal shape of the indenter. Furthermore, there are the material related issue such as the indentation size effect or the pile-up.

The most commonly encountered measurements artifacts are briefly explained just below. Those errors must be corrected to obtain consistent nanoindentation values.

- Thermal drift: There are two types of drift behaviour that can be detected during nanoindentation experiments: the first is creep within the material as a result of the plastic flow; it can be observed when the load is held constant and the penetration depth increases. The second one (virtually indistinguishable from specimen creep) is a change of the instrument due to thermal expansion or contraction of the apparatus. Thermal drift, is usually increasing or decreasing but can be also oscillating if T oscilates in a non-monotonous manner. It may be measured by indenting the specimen with a known, constant force and monitoring the displacement signal.

If the thermal drift rate is a constant then is it possible to correct the experimental data by the drift rate to compensate. To correct for the thermal drift, a hold series of data points at the maximum load or at the end of unloading can be designed.

- Initial penetration depth: before proceeding with a nanoindentation test, it is necessary to detect the specimen's surface. For this purpose an initial contact force on the order of 0.02 mN is applied. However, there is a small penetration of the indenter beneath the surface so, in all the subsequent displacement measurements this initial penetration depth has to be added.
- Instrument compliance: The compliance of the system, $C = C_f + C_s$, is made up of the load frame compliance C_f and the specimen compliance $C_s = \frac{1}{S}$, which is the inverse of the stiffness as defined above. Consequently, system calibrations are based on the relation:

$$C = C_f + \frac{\sqrt{\pi}}{2E}\frac{1}{\sqrt{A}} \qquad \text{(Eq. 2.21)}$$

Once A is known, Eq. 2.19 can be plotted as C vs $A^{-1/2}$, and the intercept will give the load compliance.

- Indenter shape correction: Eq. 2.19 assumes that the geometry of the indenter is ideal; however a Berkovich indenter is blunted rather than sharper than the ideal geometry, which means that at a given contact depth h_c, the actual area of contact A is larger than that calculated upon the basis of a perfect geometry A_i. The correction for indenter shape takes the form of a ratio of the actual area over the ideal area A/A_i. This correction becomes of prime importance at small penetration depths, where the area ratio may be as high as 50:1 due to tip rounding. In our equipment, the area correction function is obtained by performing indentations at different loads on a specimen of known modulus (fused silica in our case).

In our nanoindentation data, corrections for the mentioned above errors were applied; however, other phenomena must be taken into account:

- Piling-up: The elastic equations of contact assume that the contact circle is beneath the specimen surface. Depending on the ratio E/H of the material,

instead of sinking-in, a material may be pushed upwards and be "piled-up" around the edges of the indentation. When this happens, more material is supporting the indenter load than is assumed by the contact equations. As a result, the specimen appears stiffer (higher modulus) and harder than it really is. However, there are no corrections that account for the pile up. The best way to avoid the effect is to measure the contact area with an AFM or SEM. However, in metallic glasses or nanocomposites, pile-up is usually not pronounced.

- Indentation size effect (ISE): is referred to the variation of hardness and/or modulus with indentation depth. ISE has been ascribed to a variety of factors. It can arise from the presence of very thin oxide films in the surface, the presence of residual stresses, strain-hardening occasioned during sample preparation, to the friction between the indenter and the specimen or in crystalline materials, to the strain gradient hardening. This later considers that, as a result of the shear field created by the indenter, the crystal lattice becomes distorted and (extra) geometrically necessary dislocations have to be created, besides the statistically stored dislocations present in crystalline materials; for larger indentations loads, the strain variations between two extremes is more gradual and statistically stored dislocations can easily accommodate the shear stress without the need of geometrically necessary dislocations, thus reducing strain gradient effects. In metallic glasses ISE can appear as a consequence of the deformation-induced free volume.
- Surface Roughness: The contact area between the indenter and the specimen depends on the penetration depth; as a consequence, surface finishing is of vital importance to avoid errors in the penetration depth measurements.

Due to all these factors, it is essential to clearly specify the nanoidentation conditions of the test. The maximum applied load, the geometry of the tip, the strain loading/unloading rate, the holding segment (if present) and the surface finishing of the specimen should be mentioned for any nanoindentation test.

Nanoindentation experiments were carried out with an UMIS nanoindenter from Fischer-Cripps laboratories. All experiments were performed at room temperature, in load control mode using a Berkovich indenter tip.

Prior to nanoindentation, the samples were carefully polished to a mirror-like appearance using diamond paste. The maximum applied loads ranged from 1 to 500 mN and a holding segment of 20 s was added in all the measurements. Thermal drift was always kept bellow ± 0.05 nm/s. The maximum applied loads ranged from 1 to 500 mN and at least 25 indentations for each loading condition were performed to verify the accuracy of the indentation data. Nanoindentation values were evaluated at the beginning of the unloading segment using the method of Oliver and Pharr.

The set-up is equipped with an optical microscope which permits us to select a suitable site for indentation and even observe the indentations for intermediate applied loads.

2.2.3.3. Compression test

In a compression test a specimen is subjected to a continuous compressive force until it fractures. As a result, the displacement and the applied force are recorded and consequently, the stress-strain curve can be calculated taking into account that the stress is defined as the force acting per unit area (F/A_0) and the strain is defined as the change in dimensions per unit length ((l_0-l)/l_0).

Up to certain loads, a solid will recover its original dimensions when the load is removed, which is known as elastic behavior. The critical stress value needed to initiate plastic deformation is defined as the elastic limit of the material. After this limit, the specimen undergoes plastic deformation, it means that the body will show permanent deformation after the load is removed.

From the stress-strain curve parameters such as the elastic modulus, the yield strength and the ultimate strength can be obtained. The modulus of elasticity, or Young's modulus (E), is the slope of the stress-strain curve in the elastic region. This relationship between stress and strain in the elastic region is known as the Hooke's law: E= stress/strain (99).

The determination of the exact elastic limit depends strongly on the sensitivity of the instrument measuring the displacement. For engineering purposes, the limit of elastic behavior is therefore described by the yield strength. The yield strength is defined as the stress which will produce a small amount of permanent deformation, generally equal to 0.002 or 0.2%.

The maximum stress on the engineering stress strain-curve is commonly known as the ultimate compressive strength. Beyond that value, the diameter of the specimen begins to decrease rapidly and the load required drops off.

To calculate the engineering stress-strain curve the original area is used; however, this is not precise because the area continually changes; with this purpose the true stress-strain curve is usually defined. At this time the true stress is calculated with the instantaneous area (F/A_i) to obtain a more direct measure of the material's response in the plastic flow range. The true strain takes the increment of strain to be the incremental increase in displacement *dL* divided by the current length and can be calculated as $ln(l/l_0)$. Contrary to the engineering curve, the stresses increase continuously up to fracture.

Plastic deformation is known as the ability of a material to be permanently deformed without breaking when force is applied. As mentioned before, one of the main goals in the development of metallic glasses is to improve the ductility so, compression test is a useful tool to study it.

Macroscopic compression tests were carried out using an Instron 8562 testing machine at a strain rate of $1*10^{-4}s^{-1}$ at room temperature located at the IFW Dresden. The compression test samples were prepared according to ASTM standards to a perfectly orthogonal geometry with an aspect ratio of 2:1.

2.2.4. Corrosion properties

The corrosion behaviour of alloys is usually evaluated using weight-loss and/or the electrochemical techniques. In this work it has been studied by the latest one, so in this section, we will focus on the understandings of basic terminology of the electrochemical technique; particularly, on the understandings of potentiodynamic polarization curves.

2.2.4.1. Electrochemical method

All corrosion type event is an electrochemical process involving oxidation and reduction reactions. As corrosion occurs, electrons are released from the metal (oxidation) and gained by another entity (reduction) in the corroding solution. Because there is a flow of electrons (current) as a result of the corrosion reaction, the corrosion rate can be measured and controlled electronically. Therefore, controlled

electrochemical experimental methods can be used to characterize the corrosion properties of metallic materials in combination with various electrolyte solutions.

In a corrosion experiment, a polarization cell is a setup consisting of the electrolyte solution, the reference electrode, the counter electrode and the working electrode (the sample of interest) as schematized in Figure 2.14. The electrodes are placed in the electrolyte solution and connected to the potentiostat.

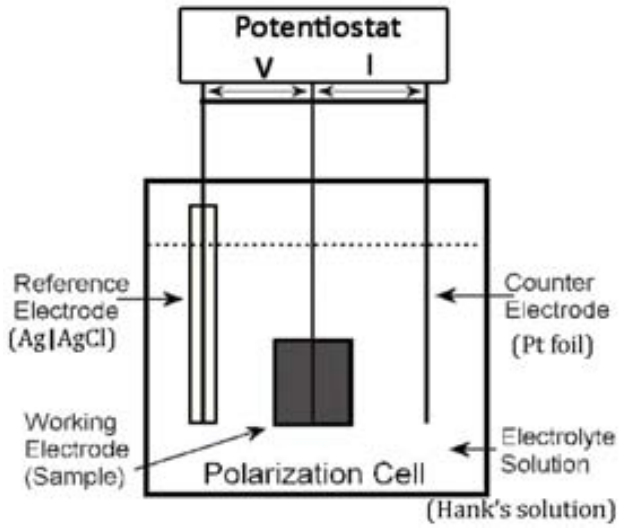

Figure 2.14: Schematic representation of a three electrode set-up to perform corrosion experiments.

There are several types of electrochemical corrosion experiments that measure and/or control the potential and current of oxidation/reduction reactions. Most of them impose a potential on the working electrode and measure the resulting current. For instance, a potentiostatic experiment imposes a constant potential on the working electrode for a specific time period. The measured current is plotted versus time. On the other side, in a potentiodynamic experiment the applied potential is increased with time while the current is constantly monitored. The current (or current density) is plotted versus the potential. After the potential is scanned to a predetermined current density or potential, the potential scan may be reversed while the current continues to be measured. An example of a typical cyclic anodic polarization curve is shown in Figure 2.15. On it, values such as the corrosion current density (j_{corr}) and the corrosion potential (E_{corr}) can be easily calculated using the Tafel method.

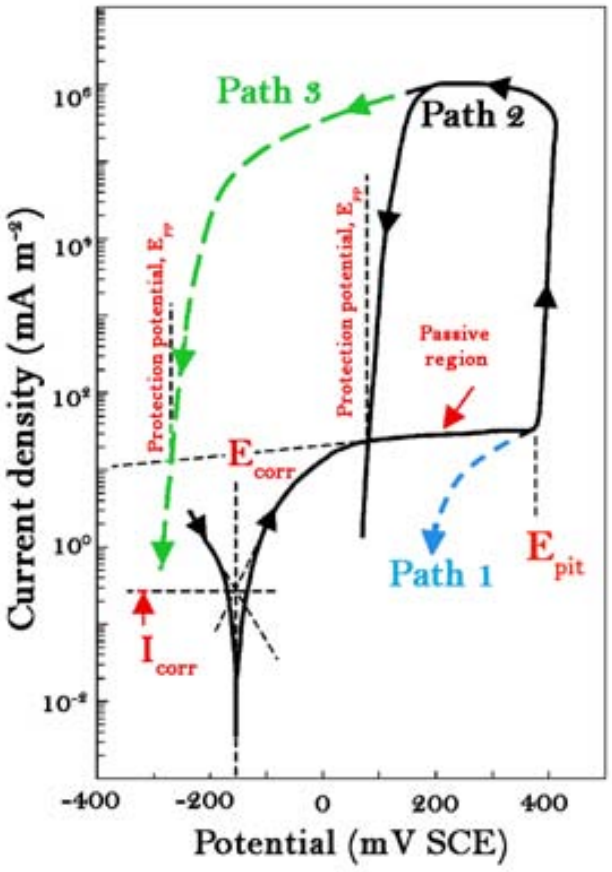

Figure 2.15: Schematic representative cyclic polarization curve of a material that is susceptible to pitting corrosion (100).

As can be observed in Figure 2.15 the current density first decreases, reaches a minimum (E_{corr}) and then starts increasing again. At some point, the current density remains constant, suggesting that the alloy was already passivated. When the alloy is not spontaneously passivated, the current density increases until a maximum point (passivation potential) and then decreases until reach the stability (passivation zone). The passivation process consists on the formation of a thin oxide/hydroxide protective layer on the specimen's surface protecting the material from ongoing corrosion. The wider is the passive region, together with low current densities, the more resistant is the sample against corrosion. With continued increase of potential, the passive layer breaks down and the current density suddenly increases. This is known as the pitting potential (E_{pit}). If we wish to obtain information about the repassivation of the material, cyclic anodic polarization curves must be carried out. As signaled in Figure 2.15 the potential at which the current density returns to the passive value is known as the repassivation potential or protective potential, E_{pp}. Between E_{pit} and E_{pp} pits will initiate and

propagate. In path 2, at E_{corr}, pits will not initiate; however, in path 3 the material will undergo pitting corrosion at surface defects or after incubation time periods at E_{corr} (31). That is, higher positive values of E_{pit}-E_{corr} and E_{pp}-E_{corr} are desirable for improved corrosion resistance of material.

In our work, the electrochemical measurements were carried out with an Autolab electrochemical interface connected to a cell with a three electrode arrangement. The reference electrode consisted of a double junction Ag|AgCl electrode filled with 3 M KCl inner solution and 1 M NaCl interchangeable outer solution. A platinum foil acted as the counter electrode. The specimens were immersed in aerated Hank's balanced salt solution (HBSS) - (purchased from Sigma-Aldrich) at 310 K. Before each polarization scan, the sample was immersed in the electrolyte and left for potential stabilization until the fluctuations became lower than 0.01V/h. The stabilized value was considered to be the open-circuit potential (OCP). Subsequently, the potential was swept anodically at a scan rate of 0.1 mV/s, starting from 300 mV below the OCP.

Prior to measurement, slices from the 2 mm diameter rods were carefully grinded with SiC paper at 1200 grit, degreased in acetone and finally cleaned with distilled water. The area of the specimen that was in tontact with the media was measured with the purpose to determine the corrosion current density.

3. RESULTS AND DISCUSSION

3.1. Devitrification-induced enhanced mechanical properties

Some properties of BMGs can be improved by partial devitrification of the glassy structure. In terms of mechanical properties, higher strength is usually observed in BMGs in their relaxed state or when they are partially or fully crystallized. However, crystallization tends to induce brittleness. Nevertheless, some recent studies report that annealing near the supercooled liquid region and for an optimum annealing time can significantly enhance plasticity (101; 68). They attribute this behavior to the relative effect of free volume and nanocrystallization.

From a tribological point of view, it has been shown that the wear resistance is also enhanced by nanometer-scale dispersion of crystallites or quasi-crystallites in the amorphous matrix (102).

In this section, the structural changes occurring upon annealing are correlated with the evolution of the elastic, mechanical and corrosion properties of two systems of metallic glasses: a Ti-based (with potential applications in the biomedical field) and a Fe-based (to be used in magnetic applications) amorphous alloys.

3.1.1. Characterization of $Ti_{40}Zr_{10}Cu_{38}Pd_{12}$ after annealing treatments

Owing to their excellent mechanical strength and resilience, metallic materials show a great potential for load-bearing orthopedic applications and are superior in many aspects to alternative biomaterials such as polymers and ceramics. To assure long life-time of the bone implant, biomaterials need to combine high strength with relatively low Young's modulus (as close as possible to the Young's modulus of bone). This avoids loosening of the implant, a biomedical incompatibility known as "stress shielding effect". In addition, biomaterials should not contain toxic or non-biocompatible elements (e.g., Be, Al, Ni, Co or Cr) and should possess high corrosion and wear

resistance. These parameters are especially important because they determine the useful life-time of the implant. Finally, it is essential to achieve a good integration of the implant with the bone. In this sense, surface chemistry, surface roughness and surface topography play an important role in the development of good osseo-integration (103).

Pure Ti and Ti-6Al-4V (composed of a mixture of α+β phases) alloys are currently the most widely used structural biomaterials for the replacement of hard tissues in artificial joints. Although pure Ti has acceptable mechanical properties, in most applications titanium is alloyed with small amounts of aluminum and vanadium, typically 6 wt% and 4wt% respectively, with the aim of inducing precipitation strengthening and stabilization of the β-phase, which exhibits lower Young's modulus than the α-phase. However, recent studies have shown that the release of both V and Al ions from the Ti-6Al-4V alloy to the human body might cause long-term health problems, such as peripheral neuropathy, osteomalacia, and Alzheimer disease (104). For this reason, there is an increasing demand for new types of metallic biomaterials. Elements like Nb, Zr, Mo or Ta are the safest elements that can be alloyed with titanium. Therefore, crystalline alloys with the compositions Ti-Zr-Nb-Ta-Pd, Ti-Nb-Ta-Zr, Ti-Sn-Nb or Ti-Mo-Zr-Fe have been developed during the last decade, constituting the so-called "second generation biomaterials" (103; 105; 104). In addition, Ti-based bulk metallic glasses have also attracted huge interest in recent years since they show higher strength, lower Young's modulus and often better corrosion and wear resistance than their crystalline counterparts (106). Since 1994, when Perker and Johnson (107) reported the synthesis of the first Ti-based BMG, several investigations have focused on the fabrication of new Ti-based BMG free from harmful elements (108; 109; 110; 111; 112). Indeed, although early studies showed that Ti-rich BMG exhibit high glass-forming ability and good mechanical properties, most compositions contained the presence of toxic elements, like Ni, Al or Be, which improved the glass-forming ability but restricted their use in biomedical applications (113; 106). Amongst biocompatible BMG, Ti-Zr-Cu-Pd-Sn, Ti-Zr-Pd-Cu-Sn-Ta, Ti-Zr-Pd-Cu-Sn-Nb or Ti-Zr-Cu-Pd-Ca alloys stand out from the rest due to the combination of high yield stress and good corrosion resistance (109; 108; 110; 114; 112; 111).

It should be noticed that some of the properties of BMG can be improved by partial devitrification of the glassy structure. Indeed, the formation of nanocrystals embedded in the amorphous matrix has been shown to often result in an increase of hardness and

plasticity (46). Moreover, in some compositions, precipitation of such dispersed nanoparticles causes chemical modifications in the surrounding glassy matrix that favor the formation of a protective passive film, thus improving the overall corrosion resistance (108; 110). It is well-known that cell-substrate adhesion is enhanced in nanocrystalline materials as compared to micro- or coarse-grained structures. This has been ascribed to the larger amount of grain boundaries and the increase in the total surface area, which results in an enhancement of the grain boundary energy. In presence of a liquid or wetting media, since the grains are in a high-energy state, they tend to release their excess energy in every possible way, in particular by increasing the interaction between the material surface and the given liquid or wetting media (115). Remarkably, detailed studies on the structure evolution of Ti-Zr-Cu-Pd metallic glasses during thermal annealing and the concomitant enhancement in some of their properties are still lacking.

In this context, this work focuses on the study of the devitrification behavior of Ti-Zr-Cu-Pd bulk metallic glass, with the aim of correlating the thermally-induced structural changes with the resulting mechanical and corrosion properties.

3.1.1.1. Thermal and structural characterization

From the DSC curve (Figure 3.1) various exothermic peaks corresponding to the crystallization processes are identified. The first peak (T_{x1} ~ 720 K) is attributed to the primary crystallization event while the other peaks are ascribed to the crystallization of the remaining amorphous matrix. Note that mainly two exothermic peaks are visible between 800 and 825 K, indicating that probably more than one phase crystallize in this temperature range. The glass transition temperature (T_g) can be clearly identified at T_g ~ 685 K and the supercooled liquid region is therefore $\Delta T = T_{x1} - T_g$ = 35 K.

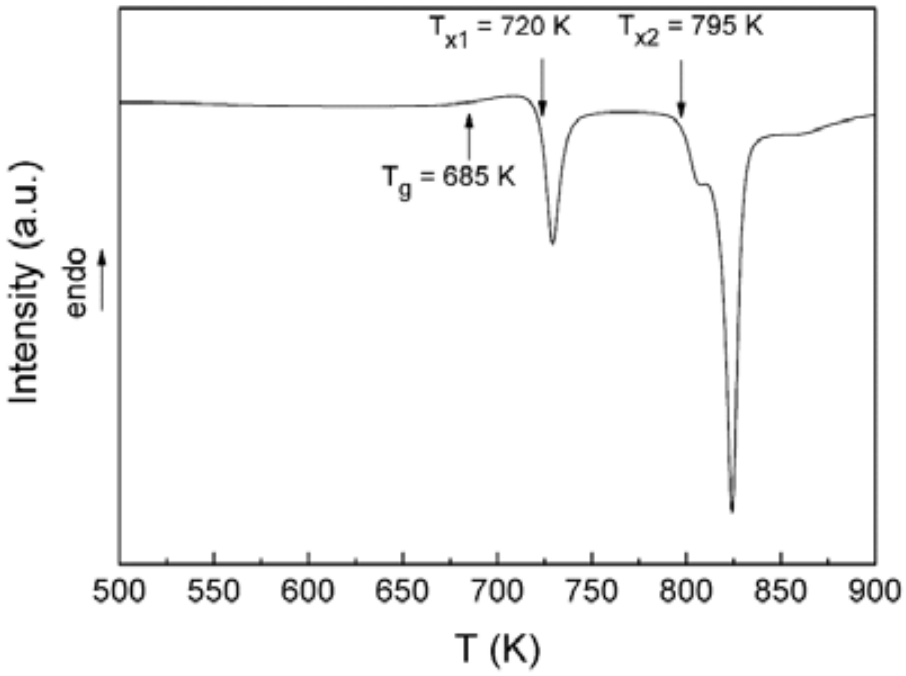

Figure 3.1: DSC curve of the as-cast alloy. The values of the glass transition temperature, T_g, and the temperature onsets of the two first crystallitzation events, T_{x1} and T_{x2}, are indicated in the figure.

The amorphous character of the sample is confirmed by the absence of well-defined peaks and the presence of two broad halos in the XRD pattern of the as-cast alloy (Figure 3.2a). Further evidence for the amorphous character of the sample is obtained from the TEM image and the corresponding SAED pattern (Figure 3.3a). However, after annealing the sample for 30 min at 738 K (above the first crystallization peak) the XRD pattern (Figure 3.2a) shows the appearance of some additional diffuse peaks superimposed to the characteristic amorphous halos, indicating the precipitation of a crystalline phase during this heat treatment. Due to the large width and weak intensity of these peaks, together with the amorphous nature of the matrix, the phases could not be easily identified by XRD. However, the corresponding TEM image shows some dispersed nanocrystals (with sizes between 5-10 nm) embedded in the glassy matrix (Figure 3.3b). Indeed, the related SAED pattern reveals that the observed nanocrystallites belong to the CuTi phase (space group P4/nmm).

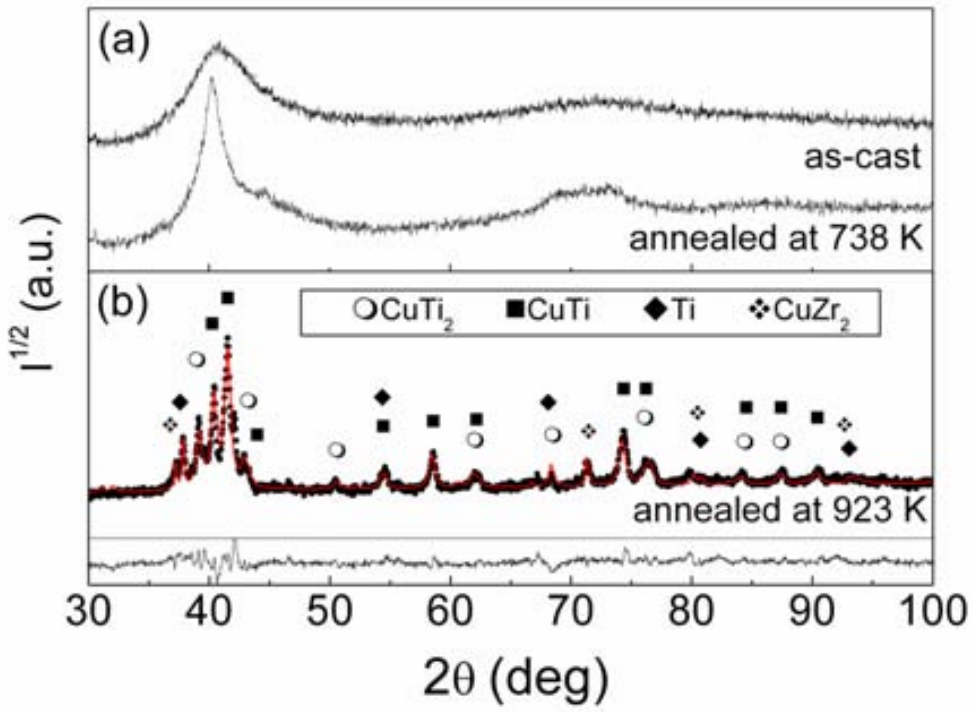

Figure 3.2: XRD patterns corresponding to: (a) as-cast alloy and specimen annealed for 30 min at 738 K; (b) sample annealed for 30 min at 923 K. The XRD pattern adjusted using the MAUD software (Rietveld method) is also shown in (b), together with the difference between the experimental and calculated profiles.

Finally, the phases that precipitate in the sample annealed at 923 K (above T_{x2}) have been identified by XRD (Figure 3.2b). Besides the CuTi phase, which was already found after annealing at 738 K, additional phases, like $CuTi_2$ and $CuZr_2$ (both with space group I4/mmm), β-Ti (space group $Im\bar{3}m$) and Pd_3Zr (space group $P6_3/mmc$) are now identified. The volume percentages, crystallite sizes and cell parameters of the different phases are listed in Table 3.1. Microstrains are always kept below 8.10^{-4}. For comparison, the tabulated cell parameters for each phase are also listed. As has been noted by other authors (116; 117) small discrepancies between the values obtained here and those reported in the literature for Cu-Ti phases are sometimes encountered. This is usually observed in multicomponent alloys where atoms of different species can act as substitutional atoms. For instance, as can be observed in Table 3.1, the phases containing Ti exhibit a computed cell parameter, after MAUD refinement, slightly larger than the tabulated one. This can be attributed to the partial substitution of Ti for

Zr or Pd which, due to their larger atomic size, cause an increment in the lattice parameter.

Phases	**%**	**Cell parameter (Å)**		**Grain**
		a	b	**size (nm)**
$CuTi_2$ (I4/mmm)	16	2.98 (2.94)	10.83 (10.78)	28
CuTi (P4/nmm)	56	3.15 (3.108)	5.99 (5.887)	29
Ti (Im3m)	3	3.36 (3.306)		50
$Pd_3Zr(P6_3/mmc)$	2	5.58 (5.612)	9.23 (9.235)	62
$CuZr_2$ (I4/mmm)	23	3.16 (3.22)	11.21 (11.18)	39

Table 3.1: Summary of the volume phase percentages, crystallite sizes and cell parameters of the different phases present in the sample annealed at 923 K, obtained after Rietveld refinement of the XRD data. Indicated in parenthesis are the tabulated values of cell parameters for the different phases (PCPDFWIN, 1998)

As can be observed in the TEM image of the sample annealed at 923 K (Figure 3.3c), the fully crystallized sample is composed of grains of different phases with sizes ranging between 30 and 100 nm. These grain sizes are slightly larger than the values evaluated by means of XRD (listed in Table 3.1). The discrepancies between TEM and XRD results can be attributed to the presence of structural defects (i.e. stacking faults or low-angle grain boundaries) and the disordered character of grain boundaries, which reduce the average coherently diffracting domain size (118; 119). A high resolution TEM image of the specimen annealed at 923 K is shown in Figure 3.3d. A selected square including part of a nanocrystal has been digitally analyzed to obtain the fast Fourier transform (FFT) as shown in the inset of Figure 3.3d. The diffraction spots fit the CuTi (012), (113) and (101) planes along the [121] zone axis.

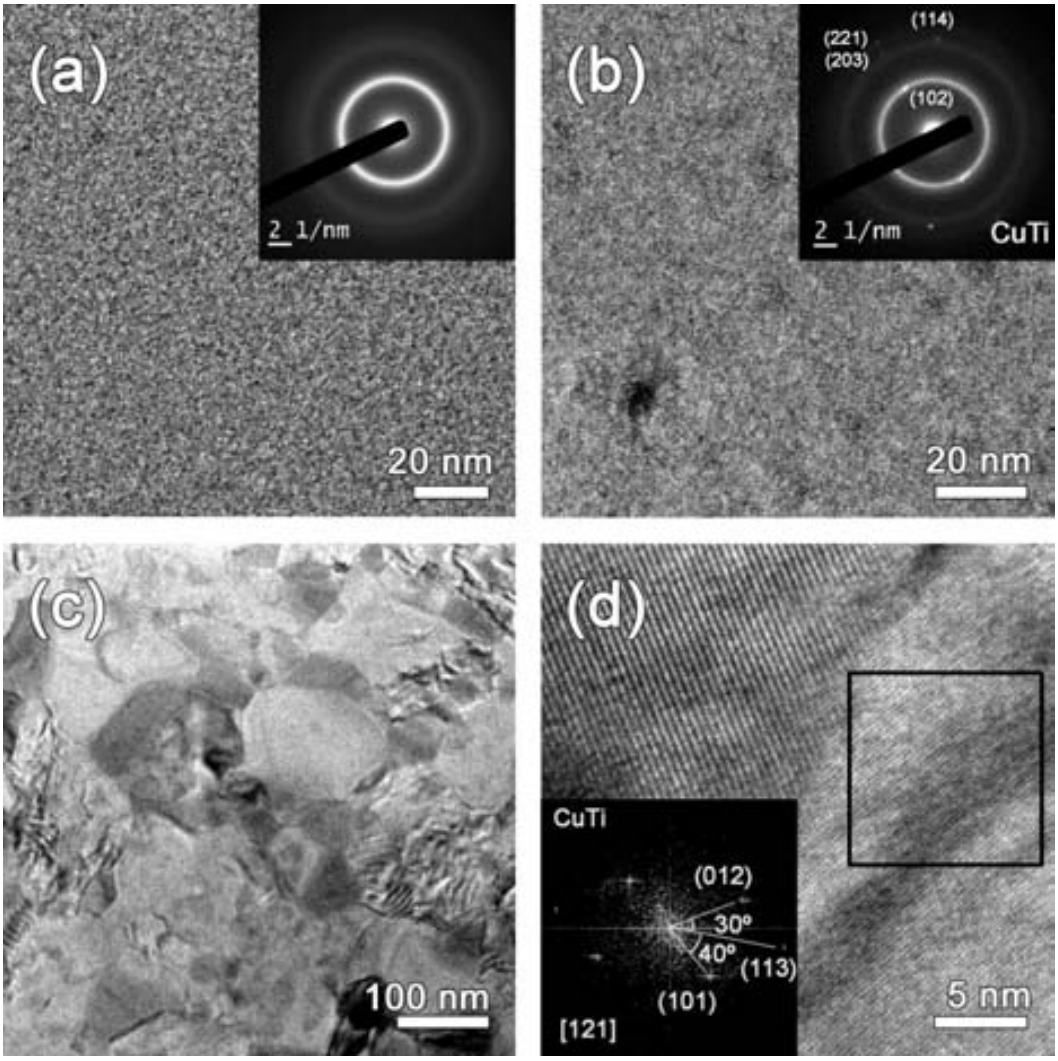

Figure 3.3: TEM images of: (a) the as-cast $Ti_{40}Zr_{10}Cu_{38}Pd_{12}$ alloy (b) the sample annealed at 738 K, (c) the sample annealed at 923 K. The insets in (a) and (b) are the corresponding selected area electron diffraction patterns. Shown in (d) is a high-resolution TEM image of the sample annealed at 923 K. The inset in (d) is the FFT of the region indicated with a square, which contains part of a nanocrystal of CuTi phase observed along the [121] zone axis.

3.1.1.2. Elastic properties

The dependence of the elastic constants (Young's modulus *E*, bulk modulus *K* and shear modulus *G*, evaluated from acoustic measurements) and the Poisson's ratio, *v*, of the $Ti_{40}Zr_{10}Cu_{38}Pd_{12}$ alloy with the annealing temperature is presented in Figure 3.4. For comparison, the elastic constants of the commercial Ti-6Al-4V alloy were also evaluated. Remarkably, the Young's modulus of Ti-6Al-4V is 110 GPa, thus higher than the Young's modulus of the Ti-Zr-Cu-Pd amorphous and partially crystallized

samples. It should be noted that the lowest Young's modulus values reported for metallic biomaterials are around 50 GPa and correspond to Ti-Nb-Ta-Zr and NiTi systems but, in these cases, other important parameters, such as the yield strength or the corrosion resistance, are clearly worse than for Ti-6Al-4V alloy (103).

The Poisson's ratio of the as-cast Ti-based BMG is relatively high and it is close to the value reported for other Ti-based BMGs (113; 120). As shown in Figure 3.4, the value of ν decreases after annealing in the supercooled liquid region and it is further reduced upon crystallization of the metallic glass. The reduction of ν with temperature is in agreement with the behavior observed in many other metallic glasses (Zr-based, Cu-based, Mg-based) (121; 122; 123). Namely, prior to crystallization, ν decreases as a result of the atomic reordering associated with the annihilation of free volume frozen in the amorphous structure during the casting process, i.e., structural relaxation.

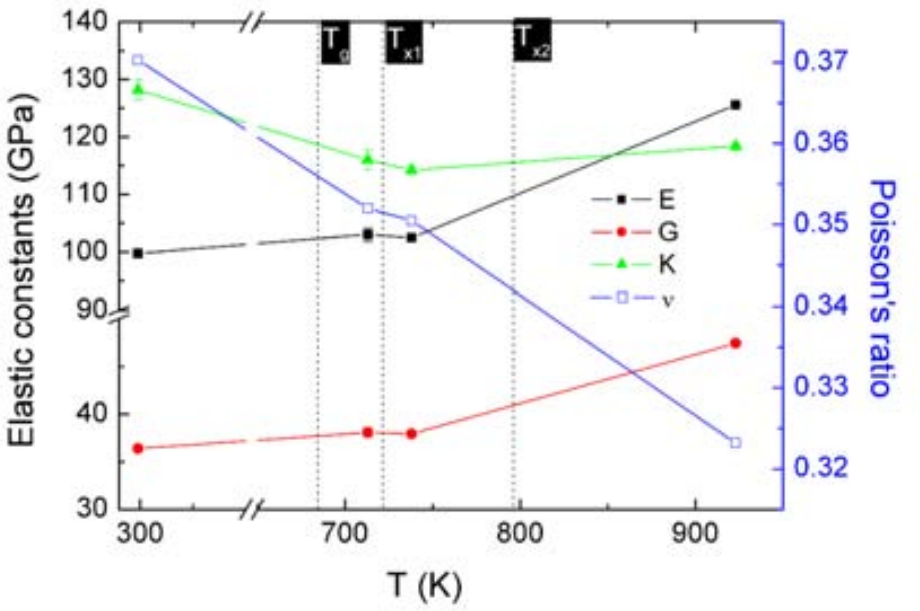

Figure 3.4: Dependence of the elastic constants (Young's modulus, E, bulk modulus, K, and shear modulus, G) and Poisson's ratio, ν, of the $Ti_{40}Zr_{10}Cu_{38}Pd_{12}$ alloy, evaluated from acoustic measurements, on the annealing temperature. Note that the glass transition, T_g, and crystallization temperatures, T_{x1} and T_{x2}, are indicated in the figure.

Typically, the bulk modulus in metallic glasses is about 6% smaller in the amorphous state as compared to crystalline alloys with similar composition (124). In our case, *K* decreases by 8.2% when the sample is annealed at T_{x2}. Since *K* is essentially related to the short range order of the alloy and the cohesive forces are not significantly different

between the two structures no large differences in K are expected upon crystallization. In contrast, the response of metallic glass to shear stresses (represented by G and E) is quite different than in their crystalline counterparts. Indeed, G and E are usually about 30% smaller in the amorphous structures than in the fully devitrified states (125; 126; 124; 127; 128). Our results show an increase of about 27 % and 25 % in G and E, respectively, when comparing the as-cast glassy alloy with the fully crystallized specimens. These effects are related to the so-called "elastic softening" of metallic glasses which is in part due to the slightly larger average interatomic spacing exhibited by BMG as compared to crystalline alloys, owing to the existence of free volume (129; 130). However, it was reported that the density difference between amorphous and crystalline alloys is not sufficient to account for the observed large variations in elastic constants (129; 130; 128; 131). Thus, additional mechanisms need to be considered. More recently, elastic softening has been ascribed to anharmonic vibrations resulting from the chemical and topological disorder of the glassy structure and also to the highly cooperative atomic diffusion that occurs in amorphous metals under the action of shear stresses (129; 130; 131). Indeed, in a metallic glass atoms exist in a range of local atomic environments. Consequently, not all atoms experience the same displacement during elastic deformation (130). Upon application of small stresses (i.e., within the elastic regime), topological atomic rearrangements occur, in which atoms can exchange some of their near-neighbors with other atoms located in the second near-neighbor shell, thus resulting in larger elastic strains (132). If the elastic deformation was only limited to the first near-neighbor shell, then the elastic moduli of metallic glasses would be comparable to those of crystalline materials with similar composition. However, in metallic glasses the entire structure gets the benefit of the added deformation due to the atomic rearrangements within the first and subsequent atomic shells and, therefore, the elastic constants are effectively reduced.

3.1.1.3. Mechanical properties

Figure 3.5 shows the dependence of hardness, H, and reduced Young modulus, E_r, on the annealing temperature for the as-cast and heat-treated $Ti_{40}Zr_{10}Cu_{38}Pd_{12}$ specimens. For comparison, the H and E_r values corresponding to the Ti-6Al-4V alloy are also indicated in the figure. The largest hardness in the $Ti_{40}Zr_{10}Cu_{38}Pd_{12}$ alloy ($H \approx 9.5$ GPa)

is achieved after annealing at 713 K (which is above T_g but below the first crystallization event). Usually, metallic glasses show an increase of hardness when annealed to progressively larger temperatures (133) but this also depends on the phases that form during crystallization. Actually, a more dense randomly packed structure with stronger bonding between atoms is obtained in the sample annealed in the supercooled liquid region due to the annihilation of free volume, hence leading to an increase in hardness. Sometimes, this enhancement of hardness can be also affected by formation of fine clusters resulting from thermally-induced phase separation within the amorphous structure (134).

An unexpected decrease of hardness is observed when the sample is annealed at 738 K.

As has been evidenced by TEM, the only phase that crystallizes at this temperature is CuTi, hence suggesting that this phase is softer than the as-cast alloy. An analogous behaviour was reported by Wang J. et al. (135) in the Ti-Zr-Cu-Ni system, where the hardness was reduced for increasingly larger amounts of CuTi crystallites formed within the amorphous matrix. However, when the annealing temperature is increased beyond T_{x2}, H increases again. This strengthening behavior is probably linked to the appearance of new phases, such as β-Ti, Pd_3Zr and intermetallic $CuTi_2$ and $CuZr_2$ phases, which are known to possess large hardness values (136). Moreover, as realized from the cell parameters values obtained by the MAUD refinement of the XRD data (Table 3.1), Ti can be partially substituted for Zr and Cu for Pd during thermal treatments. This effect can induce an enhancement of hardness via the so-called solid solution hardening mechanism. The reduced Young's modulus values obtained from nanoindentation tests (Figure 3.5) follow a similar trend with the annealing temperature as the Young's modulus determined from acoustic measurements.

Besides hardness and Young's modulus, nanoindentation is also useful to obtain other important parameters to predict the service life of a component or device. One of these parameters is the so-called wear resistance which is related to the ratio H/E_r (137; 138). Our results (listed in Table 3.2) reveal that the H/E_r ratio slightly increases when nanocrystallites become embedded in the amorphous matrix during annealing. This trend has been observed in other families of metallic glasses, for example in Zr-based ones, where it was claimed that samples having a structure consisting of an amorphous matrix with dispersed nanocrystalline particles exhibited the best wear performance

(102). Another parameter related to the wear characteristics is $\frac{H^3}{E_r^2}$, which is indicative of the resistance of the material to plastic deformation in loaded contact, i.e., the so-called yield pressure (47; 139). Again, the $\frac{H^3}{E_r^2}$ ratio is also maximum for intermediate annealing temperatures. Hence, nanoindentation results point out that the wear resistance is optimized in partially crystallized $Ti_{40}Zr_{10}Cu_{38}Pd_{12}$. Interestingly, the wear resistance for both amorphous and crystalline $Ti_{40}Zr_{10}Cu_{38}Pd_{12}$ alloys is always better than in the commercial Ti-6Al-4V system. This is in agreement with in-vitro wear studies on several Ti-based teeth prostheses, where the presence of intermetallic Ti-Cu phases in some of the compositions improved the wear resistance with respect to pure Ti or Ti-6Al-4V alloys (140).

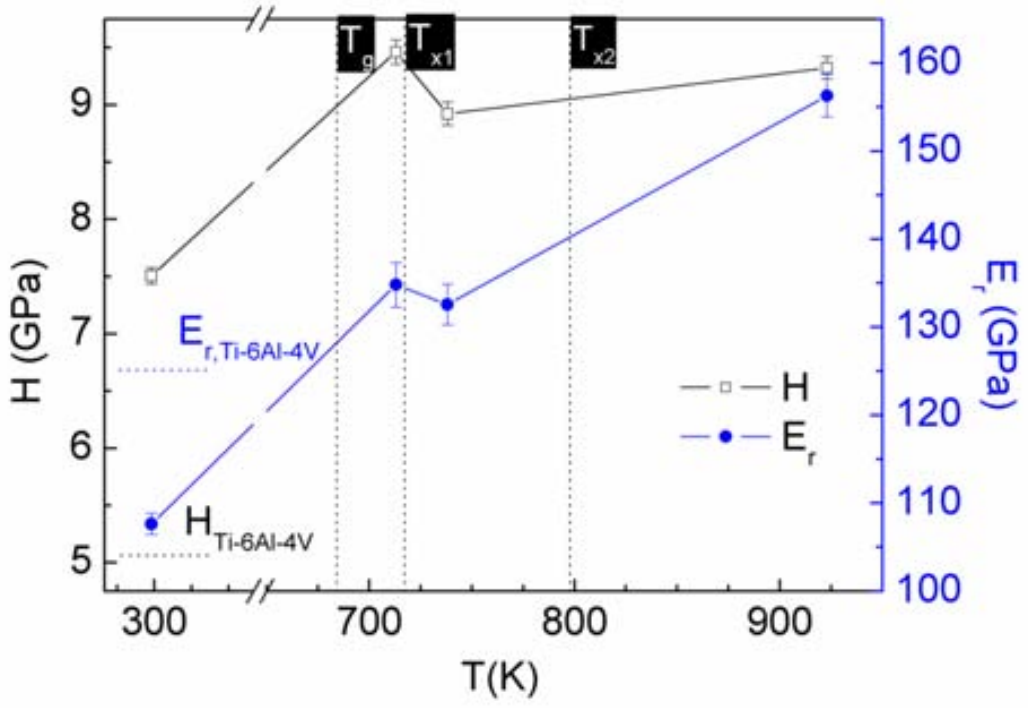

Figure 3.5: Dependence of hardness, H, and reduced Young's modulus, E_r, on the annealing temperature for the $Ti_{40}Zr_{10}Cu_{38}Pd_{12}$ alloy. For comparison, the H and E_r values of commercial Ti-6Al-4V alloy, measured using the same nanoindentation conditions, are also indicated.

The elastic recovery, related to U_{el}/U_{tot} (where U_{el} and U_{tot} are the areas between the unloading and loading indentation curves and the displacement axis, respectively) is of particular interest in applications such as impact loading since it indicates how much

energy is released from the material after being loaded. As it has been demonstrated in the literature (139) there is no general correlation between hardness and elastic recovery. In our case, the highest hardness value corresponds to the sample annealed at 923 K while the highest elastic recovery is achieved for the sample annealed at 713 K. The values of U_{pl}/U_{tot} shown in Table 3.2 are close to those reported for $Zr_{50}Cu_{40}Al_{10}$ (U_{pl}/U_{tot} ~ 0.6 (141)) and $Cu_{46.25}Zr_{45.25}Al_{7.5}Er_1$ BMG (U_{pl}/U_{tot} ~ 0.7 (142)) and clearly larger than for brittle Fe-based BMG (U_{pl}/U_{tot} ~ 0.37) (46)). Remarkably, most brittle materials (like ceramics) show relatively low U_{pl}/U_{tot} values (around 0.3-0.4 in SiC or Al_2O_3), whereas ductile metals (like Cu or Al) can show U_{pl}/U_{tot} values larger than 0.9 (143).

sample	H/E_r	H^3/E_r^2	U_{total}	U_{el}/U_{total}	U_{pl}/U_{total}
As-cast	0.069	0.063	126.99	0.379	0.621
Annealed at 713 K	0.070	0.075	111.96	0.393	0.607
Annealed at 738 K	0.067	0.091	114.19	0.379	0.621
Annealed at 923 K	0.059	0.085	109.36	0.354	0.646
Ti-6Al-4V	0.040	0.008	139.55	0.256	0.747

Table 3.2: Summary of the values of H/E_r, H^3/E_r^2, U_{total}, U_{el}/U_{total} and U_{pl}/U_{total} (where H, E_r, U_{el}, U_{pl} and U_{tot} denote hardness, reduced Young's modulus, elastic energy, plastic energy and total energy during indentation, respectively) for the as-cast, annealed specimens and the Ti-6Al-4V alloy

3.1.1.4. Corrosion properties

The potentiodynamic polarization curves of the as-cast and annealed $Ti_{40}Zr_{10}Cu_{38}Pd_{12}$ samples in Hank´s solution at 310 K are shown in Figure 3.6. For the aim of comparison, the data corresponding to the commercial Ti-6Al-4V alloy is also included. The corrosion potential (E_{corr}), the corrosion current density (j_{corr}) and the polarization resistance (R_p) extracted from the polarization curves are listed in Table 3.3. The nanocrystalline sample annealed at 923 K displays better anticorrosion properties, i.e., higher R_p values and lower j_{corr} than the as-cast alloy. However, the E_{corr} is slightly more cathodic in the partially or completely crystalline specimens than in the amorphous sample, although the differences in E_{corr} values cannot be considered to be significant. Nevertheless, taking into account the significant and progressive decrease in

j_{corr} with annealing temperature, one might conclude that the corrosion resistance tends to ameliorate as the annealing temperature is increased. As the commercial Ti-6Al-4V alloy is concerned, the j_{corr} is lower than in any of the investigated Ti-Zr-Cu-Pd alloys. However, if the current density at high potential (over +500 mV) is taken for comparison, the samples annealed at 738 and 923 K exhibit lower values than in Ti-6Al-4V. The rather low values of current density in the anodic region suggest the existence of a wide passive region related to the formation of a protective passive film, as commonly observed in this type of alloys (144). No breakdown potentials are observed in these samples below +500 mV, which suggests that the susceptibility to pitting corrosion is low within this potential range (145).

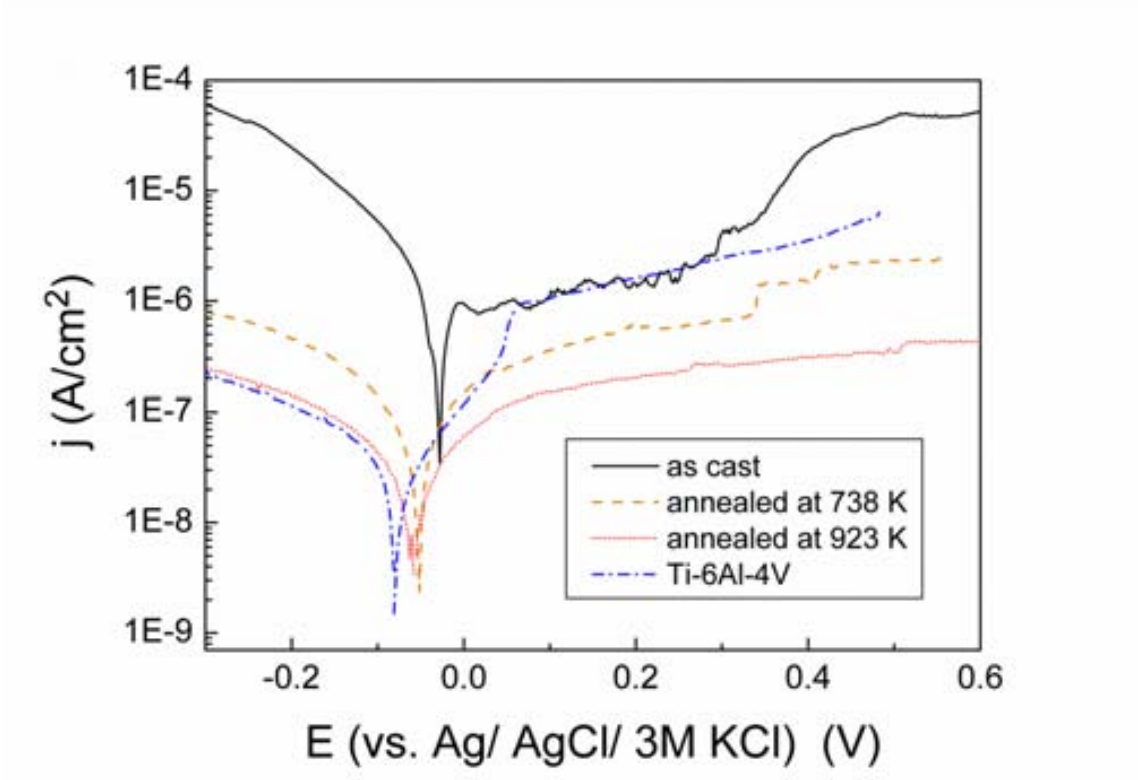

Figure 3.6: Polarization curves of the as-cast and annealed $Ti_{40}Zr_{10}Cu_{38}Pd_{12}$ alloys and of the Ti-6Al-4V alloy in naturally aerated Hank's solution.

These results also suggest that the high corrosion resistance shown for the Ti-Zr-Cu-Pd system not only depends on the composition but also on its microstructure. Typically, the high corrosion resistance of Ti-based alloys is attributed to the rapid formation (within ms) of very stable, continuous, highly adherent, self-rehealed and protective oxide films (mainly TiO_2) on metal surfaces in a wide range of corrosive media at any pH value (144).

It should be noted than in BMG materials, every system shows different tendencies in the corrosion behavior depending on the elements composing the alloy. For instance, in the Cr-Zr system, the precipitation of hcp-Zr nanoparticles increase the corrosion resistance due to the enrichment in Cr in the residual amorphous matrix (146) while in several Fe-based systems a decreased corrosion resistance was attributed to the formation of α-Fe nanoparticles (147). Usually, the completely crystallized sample is believed to show worse corrosion resistance than the fully amorphous one. For example, Ong et al. (148) attributed the deleterious corrosion resistance of Mg-Ni and Mg-Cu alloys to the galvanic coupling between the crystallized Mg and Mg_2Ni or Mg_2Cu phases. Yet, several examples of lower j_{corr} (e.g. Zr-Cu-Ni-Ti-Al alloy) have been reported in the literature for the completely crystalline counterpart when compared to the amorphous state (149). In our case, it can be concluded that the devitrification process in Ti-Zr-Cu-Pd alloy improves the corrosion resistance of the material. This behavior is likely to be related to the crystallization of intermetallic TiCu and Ti_2Cu phases, which are known to show low corrosion current densities (150; 151).

sample	**R_p (Ωcm^2)**	**E_{corr} (V)**	**j_{corr} (A/cm^2)**
As-cast	$1.26 \cdot 10^4$	-0.031	$4.36 \cdot 10^{-7}$
Annealed at 738 K	$3.63 \cdot 10^5$	-0.053	$3.38 \cdot 10^{-8}$
Annealed at 923 K	$9.63 \cdot 10^5$	-0.061	$2.01 \cdot 10^{-8}$
Ti-6Al-4V	$1.19 \cdot 10^6$	-0.076	$1.72 \cdot 10^{-8}$

Table 3.3: Summary of the electrochemical parameters obtained for the different investigated alloys, where R_p, E_{corr} and j_{corr} denote the polarization resistance, the corrosion potential and the corrosion density, respectively.

3.1.1.5. Summary

In summary, this section reveals that the $Ti_{40}Zr_{10}Cu_{38}Pd_{12}$ bulk glassy alloy exhibits large hardness (much higher than in commercial Ti-6Al-4V), relatively low Young's modulus, good wear resistance and excellent corrosion behavior. A further increase of hardness is observed in the sample annealed at 713 K, which can be attributed to the annihilation of free volume accompanying structural relaxation. Nanoindentation tests also indicate that the optimized wear performance is obtained after annealing at

intermediate temperatures, in particular after the first crystallization event, where the alloy shows a structure consisting of nanocrystals (about 5-10 nm in size) embedded in the amorphous matrix. The devitrification process of the $Ti_{40}Zr_{10}Cu_{38}Pd_{12}$ glass also ameliorates its corrosion resistance in Hank's solution. Namely, a decrease in the corrosion current density is progressively observed with the annealing temperature, together with an increase in the polarization resistance. This work demonstrates that with the aim of enhancing the properties of metallic glasses for load-bearing applications, partial devitrification of the amorphous structure can be beneficial both from mechanical and corrosion points of view. These alloys with tunable microstructure and properties could thus constitute a new generation of metallic materials for orthopedic implants, surpassing the versatility of conventionally-used Ti-6Al-4V and other fully-crystalline Ti-based alloys.

3.1.2. Characterization of $Fe_{36}Co_{36}B_{19.2}Si_{4.8}Nb_4$ after annealing treatments

Since 1995, when a ferromagnetic Fe-(Al,Ga)-metalloid bulk glassy alloy was synthesized for the first time (152), Fe-based metallic glasses have attracted huge interest in the scientific community mainly due to their good soft magnetic properties. Compared to other bulk metallic glasses, (Fe-Co)-based amorphous alloys are also particularly attractive for engineering applications due to their combination of ultrahigh strength (the highest reported in the literature) (153), superior wear resistance, good glass forming ability and rather low cost. In some systems, nanocrystallization has been shown to be beneficial from magnetic and mechanical points of view (154). Namely, eddy currents are minimized in partially devitrified soft magnetic metallic glasses, thus enhancing their applications in transformers. Furthermore, nanocomposites obtained from partial devitrification of glassy alloys typically exhibit larger strength and plasticity than the pristine monolithic BMGs. From a tribological viewpoint, it has been shown that the wear resistance is also enhanced by nanometer-scale dispersion of crystallites or quasicrystallites in the amorphous matrix (155). It is noteworthy that although the magnetic properties of glassy and crystallized Fe-Co-Si-B-Nb alloys have been recently investigated (156; 157; 158), few studies have reported on the mechanical properties (hardness, Young's modulus or wear resistance) of this system. In particular,

in spite of the ultra-high hardness exhibited by Fe-Co-Si-B-Nb BMGs, the effect of crystallization on the mechanical properties of these alloys remains virtually unexplored.

Due to the lack of plasticity of Fe-based amorphous alloys, nanoindentation turns out to be a very suitable technique to evaluate the mechanical properties of these systems. This technique provides information about the hardness, *H*, of the alloy, its reduced Young's modulus, *Er*, and the wear resistance. It should be noted that the wear resistance of a system not only depends on *H*, as considered by classical theories of wear (159), but also on the reciprocal of *Er*. Indeed, the so-called 'plasticity index', which is the ratio between *H* and *Er*, is widely quoted as a valuable measure in determining the limit of elastic behavior in a surface contact. This parameter is thus important to study the wear behavior of materials (160). Other important near-surface material properties such as the yield pressure (i.e. resistance to plastic deformation) can be estimated by the ratio H^3/E_r^2 (139). The interest in the tribological properties of metallic glasses is prompted by their potential applications as audio/video recording heads, foil bearings, electric razors and razor blades (161). Nanoindentation also gives a measure of the ratio between the elastic and total indentation energies, i.e., the so-called elastic recovery, U_{el}/U_{tot}. This parameter indicates how much energy is released from the material after being loaded and it is of particular interest in applications involving impact loading (139). Remarkably, most of these properties have not been assessed for Fe-Co-B-Si-Nb alloys prior to the current work.

In this work, we perform a detailed investigation of the devitrification process of Fe-Co-B-Si-Nb bulk metallic glass. The structural changes occurring upon annealing are correlated with the evolution of the elastic and mechanical properties of the system. Formation of dispersed ultrafine quasicrystals and crystalline phases embedded in the amorphous matrix is observed for intermediate annealing temperatures, whereas a polycrystalline microstructure is obtained after heating to sufficiently high temperatures. Although the as-cast amorphous alloy is already very hard (amongst the highest BMGs reported in the literature) further increase of hardness (accompanied with a decrease of the Young's modulus and an enhancement of the wear resistance properties) is observed in the partially or fully crystallized states. The significant impact of partial devitrification on the mechanical properties has been identified and related to the controlling microstructure based mechanisms.

3.1.2.1. Thermal Characterization

The DTA curve shown in Figure 3.7 reveals the existence of two exothermic peaks corresponding to various crystallization processes. The first peak (T_{x1} ~ 865 K) is attributed to the primary crystallization phases while the second one (T_{x2} ~ 1047 K) is ascribed to the crystallization of the remaining amorphous matrix and some phase transformations (as will be described in detail in section 3.1.2.2). The melting and liquidus temperatures are T_m = 1300 K and T_l = 1680 K, respectively. The glass transition temperature (T_g = 833 K) can be determined from the DSC curve of the as-cast sample (inset Figure 3.7). Also shown in the inset of Figure 3.7 is the DSC curve of the sample annealed at 820 K, where a decrease in the crystallization enthalpy (evaluated from the area of the first crystallization peak) is clearly observed (from ΔH = -59.31 J/g in the as-cast sample to ΔH = -16.14 J/g after annealing at 820 K). This suggests that annealing at 820 K could possibly induce the primary crystallization, a hypothesis which will be further discussed in section 3.1.2.2.

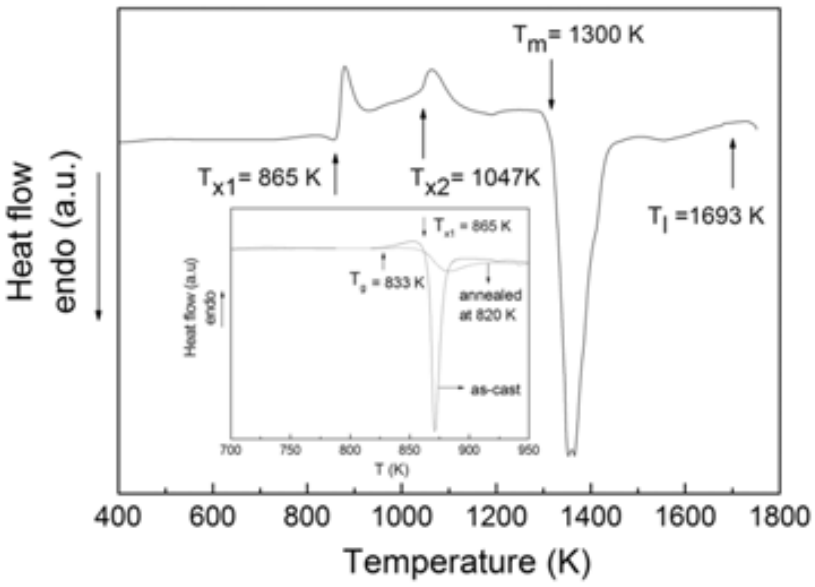

Figure 3.7: DTA curve of the as-cast $Fe_{36}Co_{36}B_{19.2}Si_{4.8}Nb_4$ metallic glass alloy performed at a heating rate of 40 K/min. The inset shows DSC curves of the as-cast alloy and a sample annealed at 820 K, acquired at a heating rate of 40 K/min. Note that the discontinuous arrows in the DTA curve indicate the heating and cooling directions.

The Curie temperatures of the magnetic phases were determined by magnetic thermo-gravimetry (MTG). In the heating MTG curve (see Figure 3.8), an abrupt drop in magnetic weight is observed when temperature reaches 687 K. This corresponds to the

Curie temperature of the amorphous matrix ($T_{c,am}$). The magnetization becomes nearly zero until temperature surpasses 860 K. At this point an increase in magnetic weight is observed, which could be ascribed to the appearance of magnetic crystalline phases. Afterwards, a sharp increase of magnetization is observed at 1040 K, corresponding to the second crystallization step. The Curie temperatures of the magnetic crystalline phases can be identified from the cooling MTG curve. Magnetic transitions are detected at 1190, 1159, 890 and 687 K. A precise correlation between each magnetic transition and the corresponding crystalline phase will be described in section 3.1.2.2. At 698 K a decrease in magnetization is also observed. This anomalous effect could be caused by an antiferromagnetic coupling between different magnetic constituents of the annealed sample and is currently being further investigated.

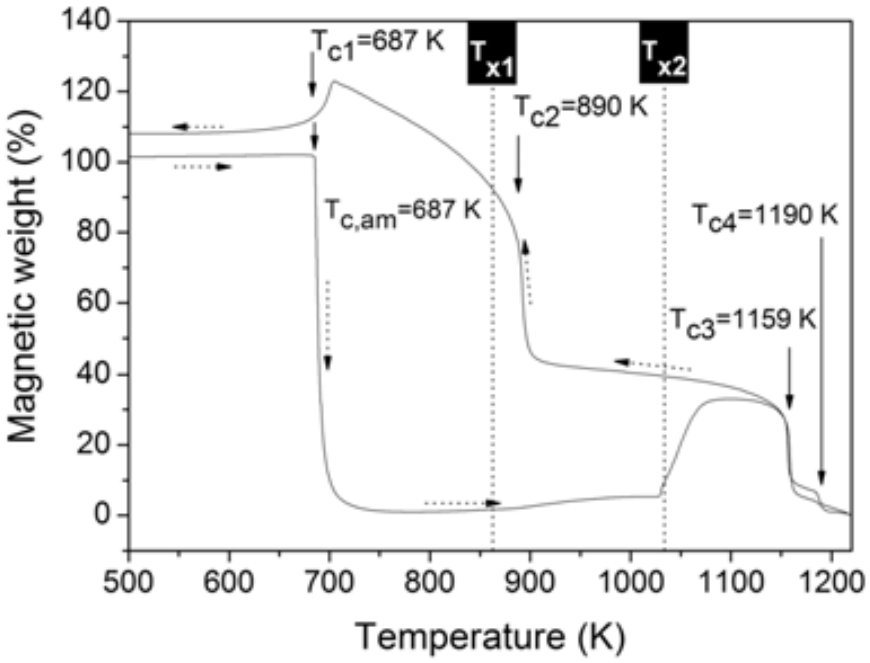

Figure 3.8: MTG curve of the as-cast sample. The dashed arrows indicate the heating and cooling directions. Note that the crystallization and Curie temperatures of the amorphous glass as well as the crystalline phases are indicated in the figure.

3.1.2.2. Structural characterization

The The XRD pattern of the as-cast alloy (Figure 3.9) reveals the presence of broad halos without well-defined peaks, suggesting that the sample is amorphous. TEM images and the corresponding SAED patterns confirm the amorphous character of the

as-cast alloy (Figure 3.10). After annealing the sample for 30 minutes at 820 K no detectable changes are observed by XRD (Figure 3.9a). However, when the HRTEM micrographs are carefully examined (Figure 3.11), some dispersed atomic clusters with an average size of 5 nm are encountered (Figure 3.11a). A selected square containing one of these clusters has been digitally analyzed to obtain the Fast Fourier Transform (FFT), as shown in the inset of Figure 3.11a. The FFT shows ten strong diffraction spots located at a distance of 2.03Å from the center. This pseudotenfold symmetry is related to a quasicrystal-like structure with a close relationship to the $Fe_{23}B_6$ phase as has been shown Hirata and al., who reported that the pseudotenfold symmetry can be understood from a combination of three types of tiles found in the $Fe_{23}B_6$ structure. This pseudotenfold quasicrystal-like structure with no icosahedral atomic arrangement can be considered as an intermediate state appearing prior to nanocrystallization of $Fe_{23}B_6$ (162). The quasicrystal-like structure is also related to the medium range order (MRO) locally forming the glassy state since the strong diffraction spots are found only in the position of the first amorphous halo ring (163).

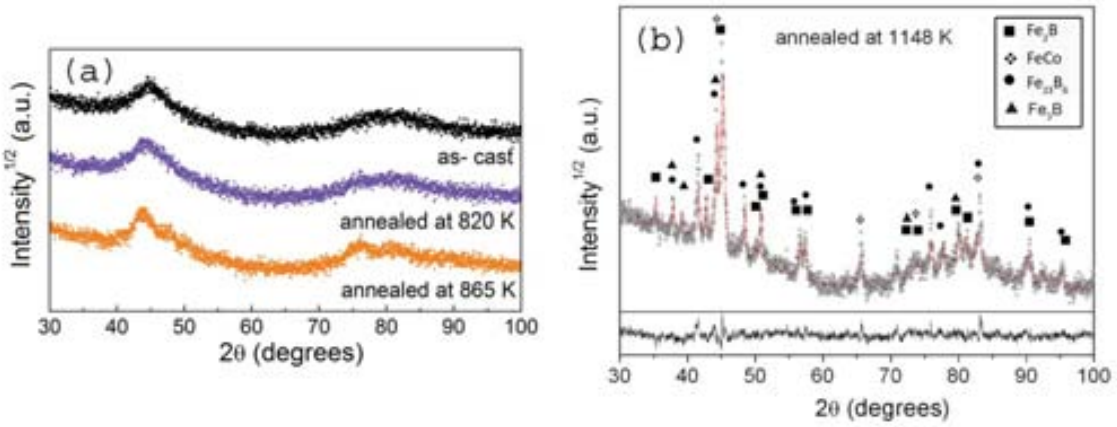

Figure 3.9: XRD patterns corresponding to: (a) as- cast alloy and specimens annealed for 30 min at 820 K and 865 K; (b) sample annealed at 1148 K. The XRD pattern calculated using the MAUD software (Rietveld method) is also shown in (b), together with the difference between the experimental and calculated profiles.

A HRTEM image of another part of the sample is presented in Figure 3.11b. After analyzing the FFT (Figure 3.11c) of the selected square in Figure 3.11b it was found to belong to the $Fe_{23}B_6$ phase (space group Fm-3m). At first glance this structure seemed to be a single crystallite but when the FFT is carefully analyzed (Figure 3.11d) three different zone axes are observed, indicating that, in fact, this region is formed by the overlapping of at least three differently-oriented crystallites. For clarity, the FFT has

been separated into the 3 diffraction patterns along the different zone axes (Figure 3.11e) and the observed planes are indicated in it.

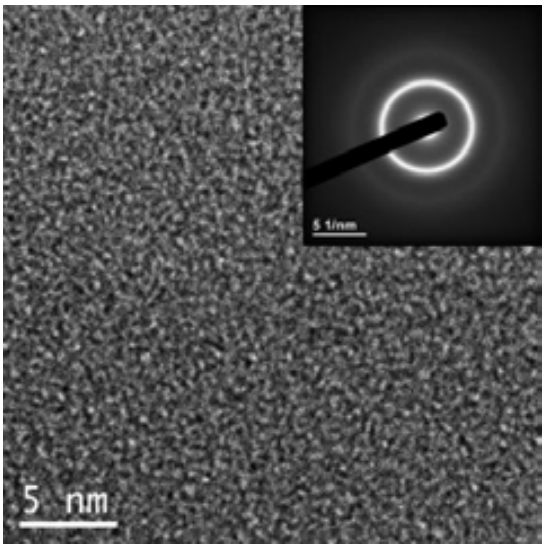

Figure 3.10: HRTEM image of the as-cast $Fe_{36}Co_{36}B_{19.2}Si_{4.8}Nb_4$ metallic glass. The inset displays the corresponding selected area electron diffraction (SAED) pattern.

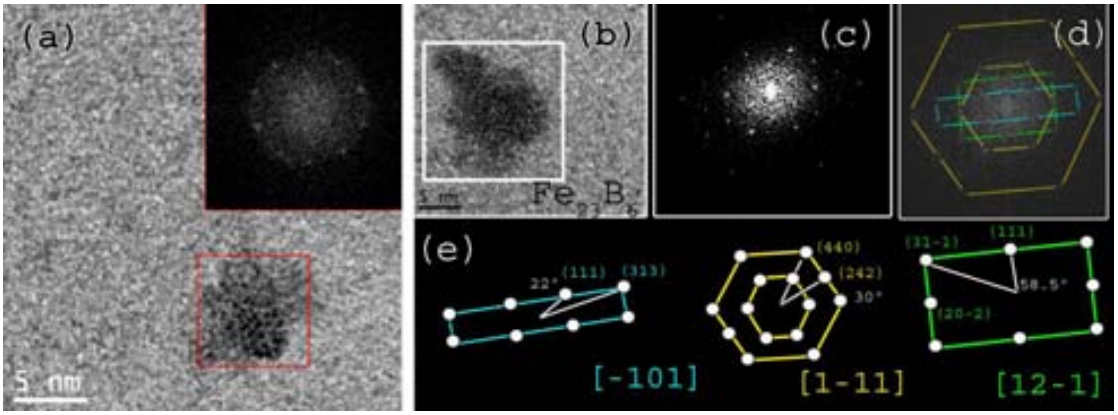

Figure 3.11: (a), (b) HRTEM images of the sample annealed for 30 min at 820 K (i.e., below T_{x1}). The inset in (a) corresponds to the FFT of the selected square containing the quasicrystal. The FFT of the square indicated in (b) is presented in (c). (d) and (e) are detailed analyses of the FFT (of panel c), separating it into three diffractions along different zone axes.

The XRD pattern of the sample annealed for 30 min at 865 K (Figure 3.9a), shows the characteristic amorphous halos and the appearance of some additional diffuse peaks, indicating the precipitation of crystalline phases during this heat treatment. Due to the large width and weak intensity of these peaks, together with the amorphous nature of the matrix, the phases could not be easily identified by XRD. Also in this case, the TEM

analysis (Figure 3.12) proved to be very useful to identify the several phases composing the alloy. Figure 3.12a shows that after annealing at 865 K the microstructure of this sample consists of crystallites of ~ 7 nm in size and a sparkle phase surrounding the grains corresponding to the remaining amorphous matrix. While in the sample annealed at 820 K, the only crystalline phase was $Fe_{23}B_6$, this time the Fe_3B phase (space group Pnma) is also encountered, as confirmed by the FFT image-analysis (inset Figure 3.12b). The diffraction spots fit to the Fe_3B (102) plane (2.03Å) and to the (220) plane (2.10Å) forming an angle of 73º along the [221] zone-axis. It should be noted that Nb addition to Fe-B based alloys has been reported to favor the eutectic crystallization of Fe_3B and $Fe_{23}B_6$ phases (164).

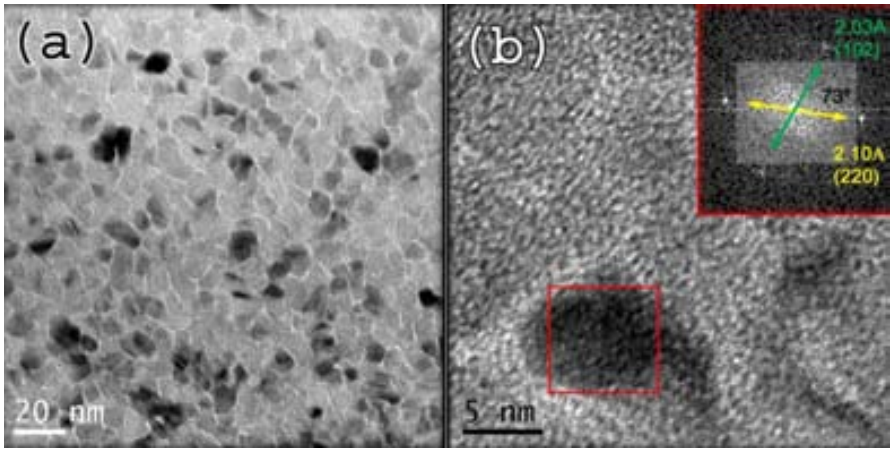

Figure 3.12: TEM images of the $Fe_{36}Co_{36}B_{19.2}Si_{4.8}Nb_4$ alloy after annealing at 865 K. (a) is the bright field TEM image. (b) is a HRTEM image. The inset in (b) is the FFT of the selected nanocrystal corresponding to the Fe_3B phase with zone axis [-2,2,1].

Finally, the phases that precipitate in the sample annealed at 1148 K have been identified by XRD (Figure 3.9b). Besides the cubic $Fe_{23}B_6$ and orthorhombic Fe_3B phases (which were already found after annealing at T_{x1}), additional phases, like tetragonal Fe_2B (space group I42m) and cubic Fe-Co solid solution (space group Pm-3m) are now identified. The volume percentages, crystallite sizes and cell parameters of the different phases are listed in Table 3.4. The Fe_2B phase probably forms by the partial transformation of the metastable $Fe_{23}B_6$ and Fe_3B phases into Fe_2B and cubic Fe-Co, as has been noted by other authors (164; 165; 166). Actually, long-term annealing (i.e., 10 h – Figure 3.13) at 1148 K resulted in the disappearance of $Fe_{23}B_6$ and Fe_3B phases and the formation of Fe_2B and cubic Fe-Co stable phases, together with

crystallization of FeB –space group Pbnm– (not observed in the rod annealed for 30 min), thus corroborating the decomposition of the metastable phases into the stable ones.

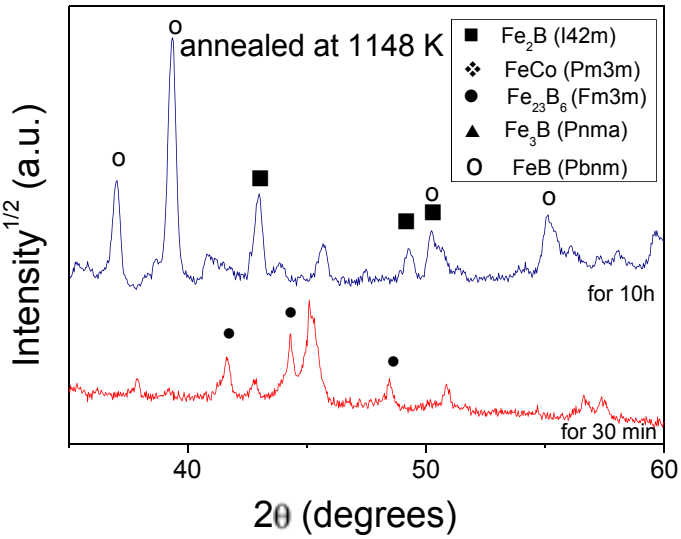

Figure 3.13: XRD pattern corresponding to the sample annealed at 1148 K for 30 min and 10 hours. Note that the range of the XRD pattern was cut from 35 to 60º in order to obtain better resolution.

Bearing in mind the formation of all these phases, the different magnetic transitions observed by MTG while cooling can be interpreted as follows: T_{c4} = 1190 K can be ascribed to the Curie temperature of α-(Fe,Co), since values between 1000 K and 1250 K have been reported in the literature for this solid solution (167); T_{c3} = 1159 K probably corresponds to the ferromagnetic Fe_2B phase (168); T_{c2} = 890 K corresponds to the Curie temperature Fe_3B (169); finally, T_{c1} = 687 K is likely to be the Curie point of the remaining $Fe_{23}B_6$ (some authors have reported a T_c value of 698 K for this phase (170; 171). Small discrepancies between the values obtained here and those reported in the literature for Fe-B phases could be due to the partial substitution of Fe for Co or Nb.

It is noteworthy that from the cell parameter of the Fe-Co solid solution (Table 3.4) it can be inferred that the solid solution in our case is near the 1:1 stoichiometry since, according to the Powder Diffraction Files Database, the 7:3, 1:1 and 3:7 Fe:Co ratios lead to a = 2.864 Å, 2.857 Å and 2.8417 Å, respectively. Moreover, the cell parameter of $Fe_{23}B_6$, obtained from the fit of the XRD data (see Table 3.4) is a bit smaller than the tabulated value (10.760 Å, from JCPDS-PDF-47-1332). This reduction of lattice

parameter can be understood from the presence of Co in the $Fe_{23}B_6$ phase, as has been recently reported in the literature (172). The lattice parameters of the Fe_2B phase, obtained by XRD (see Table 3.4), are close to the tabulated ones (a = 5.099 Å and c = 4.240 Å, from JCPDS-PDF-75-1062). The small discrepancies could be due to some incorporation of Nb, Co or Si into the boride phase, although from our data this effect is difficult to quantify. Finally, the lattice constants of Fe_3B, obtained from the fit of the XRD data (Table 3.4) differ, to a certain extent, from the tabulated ones (a = 5.430 Å, b = 6.660 Å and c = 4.450 Å, from JCPDS-PDF-34-1198). Although full understanding of this anisotropic lattice distortion is complicated, the variations in lattice parameters are probably linked to Nb and Si incorporation into the Fe_3B phase (173).

Phases	Volume fraction (%)	Crystallite size (nm)	Cell parameter a (Å)	Cell parameter b (Å)	Cell parameter c (Å)
Fe_3B (Pnma)	10	11.8	5.460	6.720	4.330
FeCo (Pm3m)	19.59	34.1	2.850		
Fe_2B (I-42m)	37.18	46.8	5.093		4.227
$Fe_{23}B_6$ (Fm3m)	33.23	53.4	10.630		

Table 3.4: Summary of the volume phase percentages, crystallite sizes and cell parameters of the different phases present in the sample annealedfor 30 min at 1148 K, obtained after Rietveld refinement of the XRD data.

As can be observed in the TEM images (Figure 3.14), the sample annealed at 1148 K is composed of grains of different sizes (ranging from 20 to 300 nm). Furthermore, large amounts of stacking faults (marked by arrows in Figure 3.14a) are observed. In fact, stacking faults and other defects could be one reason for the larger grain sizes obtained from TEM imaging, as compared to those evaluated by means of XRD (listed in Table 3.4). Indeed, stacking faults are able to reduce the average coherently diffracting domain size in an analogous way as high-angle grain boundaries. The selected area electron diffraction pattern (SAED) presented in Figure 3.14b2 (obtained from the crystal in Figure 3.14b1) corresponds to a FeCo solid solution. The angle measured between (110) and (211) is 30º (zone axis [111]). Finally, a SAED pattern corresponding to the Fe_2B phase is presented in Figure 3.14c2. Along the [110] zone-axis, angles of 31º between the (002) and (112) planes or 91º between the (002) and (110) planes are calculated.

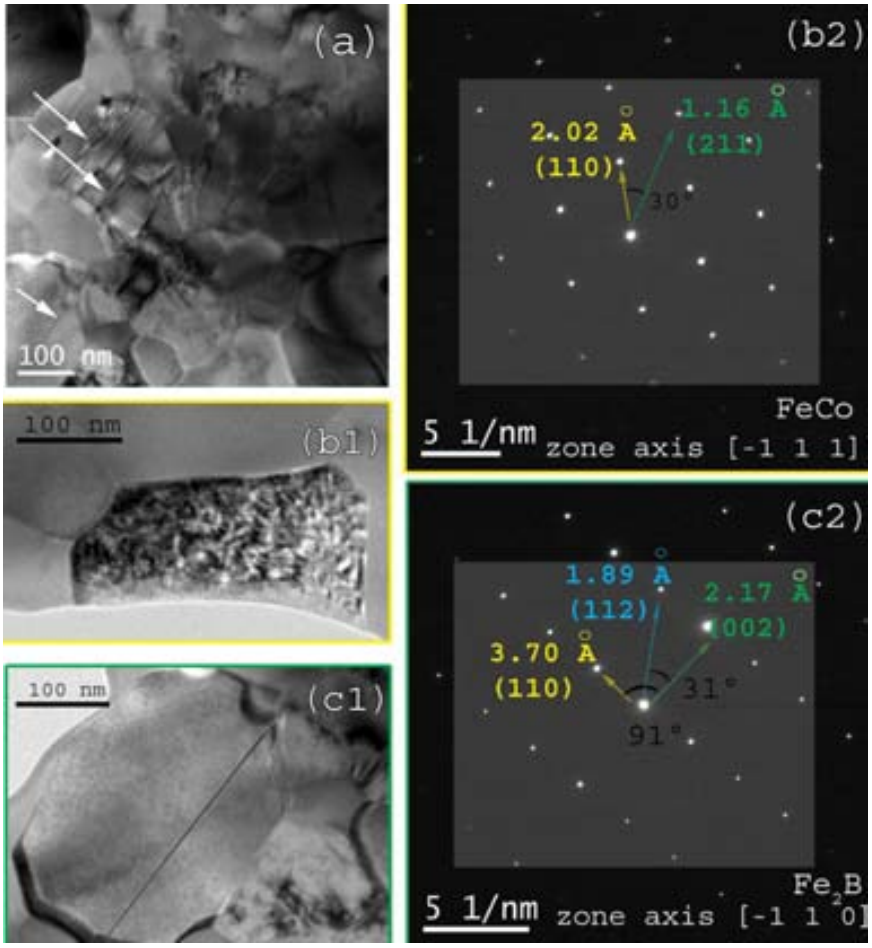

Figure 3.14: Bright field TEM images of the $Fe_{36}Co_{36}B_{19.2}Si_{4.8}Nb_4$ alloy after annealing at 1148 K. The arrows indicate stacking faults. (b2) SAED pattern corresponding to the crystal in (b1), belonging to the FeCo phase. (c2) SAED pattern corresponding to the crystal in (c1), related to the Fe_2B phase.

3.1.2.3. Elastic Properties

The dependence of the elastic constants (Young's modulus E, bulk modulus K and shear modulus G) and the Poisson's ratio, ν, of the $Fe_{36}Co_{36}B_{19.2}Si_{4.8}Nb_4$ alloy with the annealing temperature is presented in Figure 3.15. Compared to other families of metallic glasses (particularly those showing reasonable compressive plasticity), the Poisson's ratio of the as-cast Fe-based BMG is relatively low (121) and is close to the value reported for other Fe-based BMGs (174). The value of ν becomes even lower after annealing near T_g and it is further reduced upon crystallization of the metallic glass.

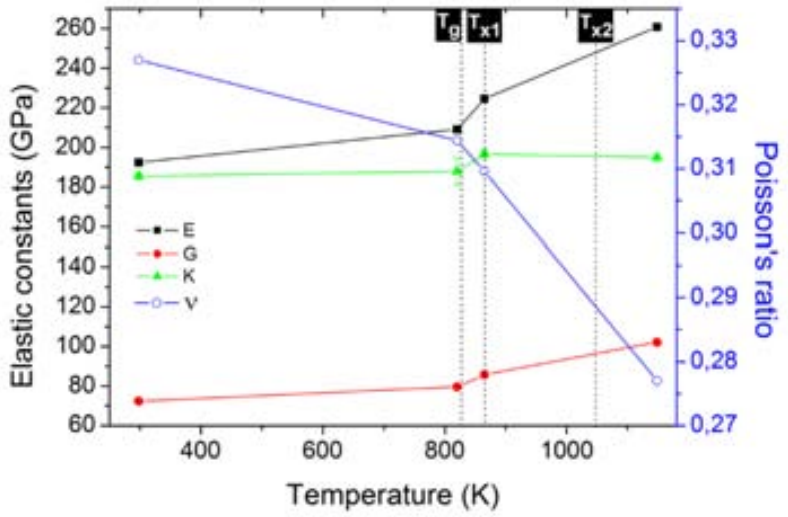

Figure 3.15: Dependence of the elastic constants (Young's modulus, E, bulk modulus, K, and shear modulus, G) and Poisson's ratio, ν, of the $Fe_{36}Co_{36}B_{19.2}Si_{4.8}Nb_4$ alloy on the annealing temperature. The glass transition, T_g, and crystallization temperatures, T_{x1} and T_{x2}, are indicated in the figure.

The reduction of ν with temperature is in agreement with the behavior observed in many other metallic glasses (Zr-based, Cu-based, Mg-based) (121; 122; 123). Before the onset of crystallization, ν decreases as a result of the atomic reordering associated with the annihilation of free volume frozen in the amorphous structure during the casting process, i.e., structural relaxation (175). This also results in an increase of *K*, *G* and *E*. Such trends become exacerbated when the annealing temperature exceeds T_{x1}. Heat treatments at higher temperatures promote progressive crystallization of the Fe-based glassy alloy. The sample annealed at 1148 K is essentially fully crystalline and, in this case, an enhancement of *E* and *G* is observed, whereas the increase in *K* is less pronounced. Similar results have been obtained in the literature (176; 177; 130), where the bulk modulus of BMGs is typically found to be around 6% smaller than for crystalline alloys with analogous composition, whereas this difference can reach 30% in the shear modulus (123). In turn, the Poisson's ratio markedly decreases after crystallization (since ν is inversely proportional to the ratio *G/K*). These effects are related to the so-called elastic softening of metallic glasses, which has been described in detail in section 3.1.1.2.

In addition to crystallization, the grain growth that occurs during the annealing treatments is also likely to play an important role in the evolution of the elastic constants. Indeed, nanostructured materials often exhibit lower elastic constants than the

equivalent coarse-grained ones (178; 179). This is due to the large amounts of interfaces in nanocrystalline metals, where different types of defects can form, thus leading to a local reduction of the average atomic coordination number, an increase of topological disorder and a concomitant reduction of the elastic constants (180). At the nanoscale, size effects often become prominent due to the higher surface-to-volume ratio (181). Hence, in the alloys annealed at intermediate temperatures, the elastic properties are particularly governed by the interfaces. In these nanocomposites, the Young's modulus is determined by the contributions from the nanocrystals, the interface regions and the amorphous matrix. As a first approximation, the Young's modulus of the composite can be expressed using a simple rule of mixtures (182; 183):

$$E = E_{cryst}V_{cryst} + E_{interf}V_{interf} + E_{am}V_{am} \qquad \text{(Eq. 3.1)}$$

where V_{cryst}, V_{interf} and V_{am} are the volume fractions of crystals (excluding grain boundaries), interfaces and amorphous matrix, respectively, while E_{cryst}, E_{interf} and E_{am} are the corresponding Young's modulus of each region constituting the composite (in which it can be assumed that $E_{am} < E_{interf} < E_{cryst}$ (123; 179; 180)). Similar expressions would apply for the shear and bulk moduli. As described in section 3.1.2.2, the grain size in the sample annealed at 865 K is about 7 nm; this value significantly increases when the samples are annealed at 1148 K. As the grain size is progressively increased the ratio V_{interf}/V_{cryst} decreases and since $E_{interf} < E_{cryst}$, this also contributes to the observed increase in Young's modulus after the annealing treatments.

3.1.2.4. Mechanical Properties

Figure 3.16a shows the dependence of hardness on the maximum nanoindentation load for the as-cast and annealed specimens. Generally, the hardness is found to decrease with increasing indentation loads. This effect is commonly known as the indentation size effect (ISE) and is usually observed in crystalline materials but it can also be found in metallic glasses. In crystalline materials the ISE has been ascribed to a variety of factors, such as surface effects (184), friction between the indenter and the sample (185) or, more recently, strain gradient hardening (186; 187). The latter considers that, as a result of the shear field created by the indenter, the crystal lattice becomes distorted and (extra) geometrically necessary dislocations, besides the statistically stored ones, have to be created to account for the large shear strains. For large indentations, the strain

variation between two extremes is more gradual and the statistically stored dislocations can easily accommodate the shear stress without the need of geometrically necessary dislocations, thus reducing strain gradient effects. In metallic glasses, where dislocations cannot form, the ISE is believed to be related to deformation-induced excess free volume (113; 188) which is created in addition to the free volume typically trapped in the material upon quenching (for further details see section 3.3.1.2). Figure 3.16a reveals the existence of an ISE in all the investigated samples, either in the as-cast (amorphous) or in the annealed (partially/fully crystalline) states.

The morphology of the indents performed at P_{max} = 500 mN was investigated by SEM. Clear differences are observed between the amorphous state corresponding to the as-cast sample and the crystalline state corresponding to the sample annealed at 1148 K. Indentations carried out in the as-cast condition (Figure 3.16b) show semi-circular surface steps, produced by the propagation of shear bands towards the unconstrained free surface. These shear bands can be observed in the amorphous sample and also in the partially crystallized ones. Actually, using atomistic simulations some common aspects in the process of shear localization have been established between bulk amorphous metals and nanocrystalline metals (189). Namely, when the grain size approaches the amorphous limit, the deformation mechanisms are accompanied by much localized shear banding, as commonly observed in metallic glasses (190; 191). Moreover, from the loading part of the indentation curves (not shown) serrations are clearly visible, indicating the propagation of discrete shear bands. A clear reduction of the shear band activity can be ascertained in the indentations performed in the crystallized condition (Figure 3.16c); accordingly, no pop-in events are observed in the corresponding indentation curves.

It is worth mentioning that Fe-based systems are amongst the hardest BMG materials hitherto manufactured. The as-cast Fe-Co-B-Si-Nb system investigated here exhibits H = 14 GPa at P_{max} = 500 mN. When the sample is crystallized at 1148 K, hardness values over 18 GPa are obtained for P_{max} = 500 mN. From compression tests, carried out at room temperature at a rate of $5x10^{-4}s^{-1}$, no plasticity is observed, which is not surprising bearing in mind the low Poisson's ratio of this alloy. As it is known Fe-based metallic glasses possess ultrahigh yield strength (192; 193). In our case, compression tests reveal that the yield strength is over 4 GPa. The constraint factor, calculated as the ratio between hardness and compressive yield strength, is C = 3.5 for the as-cast sample

(taking H = 14 GPa). This value is close to typical values obtained in crystalline metals (C = 3) and is similar to the values reported for Ni-based, Pd-based (194) and some Zr-based BMGs (195).

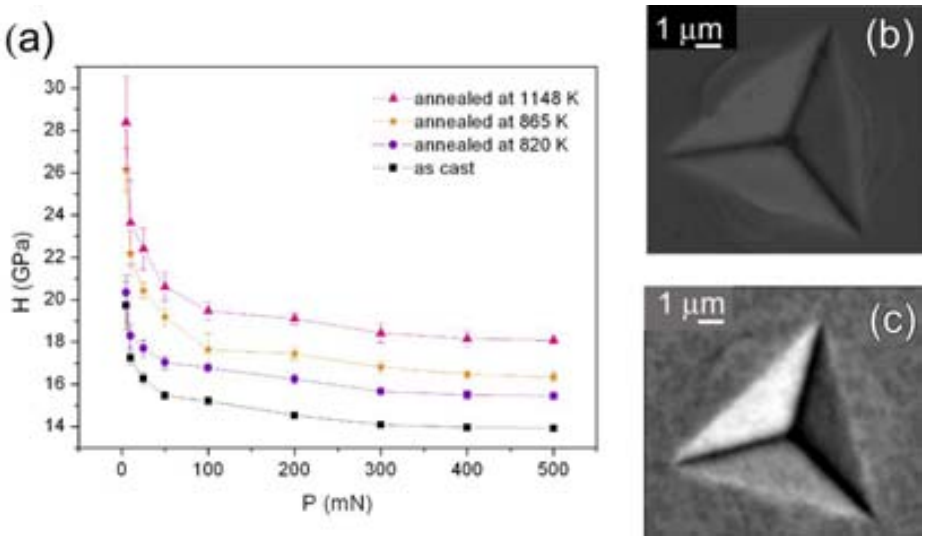

Figure 3.16: Dependence on hardness on the maximum nanoindentation load for the as-cast alloy and the different annealed samples. (b) SEM image of an indentation performed in the as-cast specimen using a maximum load of 500 mN. (c) SEM image of an indentation performed in the specimen annealed at 1148 K using a maximum load of 500 mN.

There are several effects that can contribute to the ultrahigh hardness of the as-cast and annealed specimens. First, the high strength of the as-cast alloy is interpreted as a result of the strong bonding between the constituent elements, as is expected from the large negative mixing enthalpy values (-9, -11, -16, -18, -21, -25, -39 kJ/mole for the Co-B, Fe-B, Fe-Nb, Fe-Si, Co-Si, Co-Nb, B-Nb pairs, respectively) (196). It can be seen that the mixing enthalpies with the highest negative values correspond to the pairs containing Nb and Si, thus indicating that addition of Nb and Si contributes to the super-high fracture strength of the Fe-based metallic glass. Then, as it can be observed in Figure 3.16a, the hardness further increases as the annealing temperature is progressively increased. The $Fe_{23}B_6$ structure (the first one to crystallize) is a metastable complex-cubic phase reported to be associated to a network-like structure, in which distorted trigonal prisms consisting of Fe and B are connected to each other through glue atoms of Nb, leading to the precipitation of a metastable $(Fe,Co,Nb)_{23}B_6$ structure which possesses large hardness (196). In the partially crystallized samples, hardness can be enhanced by other additional mechanisms. For example, the alloying of Fe with Co is an example of substitution solid solution, which may lead to an enhancement of

hardness (i.e., the so-called solid solution hardening) although it is generally accepted that solid solution hardening by substitutional atoms is much smaller than that by interstitial atoms (197). In addition, due to the already large hardness of $Fe_{23}B_6$, the partial substitution of Fe by Co does not probably cause a significant effect in the alloy strength. In the sample annealed at 820 K, the formation of quasicrystals could be also responsible for the increase in hardness. This effect has been reported in the literature for various systems, for example in a Fe-based alloy where the precipitation of quasicrystalline particles was used to increase the tensile strength of the alloy (198).

It should be noted that the increase of H with the annealing temperature does not necessarily occur in all families of metallic glasses since the lack of atomic ordering in the amorphous structure precludes dislocation activity, thus often resulting in larger H values in the glass when compared to crystalline phases with analogous compositions. However, it is known that Fe-B phases are particularly brittle and therefore possess an ultrahigh resistance against plastic deformation (196; 197). Bearing in mind that Fe-B are the main phases in the sample annealed at 1148 K, it is thus understandable that a very high hardness value is obtained in this case. Furthermore, as shown in Figure 3.14, the crystallized sample contains several twins. In this case, work hardening may occur via the interaction of dislocations with twin boundaries and with other defects acting as barriers for their propagation through the lattice (198). Nevertheless, due to the high temperatures used to crystallize the alloy, the amount of structural defects is rather limited and, consequently, work hardening is probably not a major hardening mechanism in the investigated system.

It is remarkable that for the as-cast $Fe_{36}Co_{36}B_{19.2}Si_{4.8}Nb_4$ sample a good agreement is observed between the Young's modulus obtained from compression test (201±10 GPa) and acoustic measurements (192±0.5 GPa), although the acoustic measurements are generally assumed to be more precise. Note that the elastic regime during compressive loading is often identified only with difficulty. Moreover, surfaces that are not perfectly flat and parallel can cause a curvature or changes in the slope in the linear elastic part of the compression test curve. Although care was taken to minimize these issues, these effects cause a relatively larger error in the determination of the Young's modulus, which is expected to be around ±10 GPa. Furthermore, the reduced Young's modulus, E_r, for the as-cast and annealed samples obtained from nanoindetation (listed in Table

3.5) are also in good agreement with the values obtained from acoustic measurements (Figure 3.15).

Besides hardness and Young's modulus, nanoindentation is also useful to obtain other important parameters to predict the service life of a component or device. As already described (section 3.1.1.3) one of these parameters is the so-called wear resistance which is related to the ratio H/E_r (138; 137). Our results (Table 3.5) reveal that the H/E_r ratio increases when nanocrystallites or quasicrystallites become embedded in the amorphous matrix. This trend has been observed in other families of metallic glasses; for example in Zr-based ones, where Wang et al. claimed that samples having a structure consisting of an amorphous matrix with dispersed nanocrystalline particles exhibited the best wear performance (102). Table 3.5 shows that the H/E_r parameter is somewhat larger in the "fully-crystallized" sample than in the amorphous condition, however, it is lower than in the "partially-crystallized sample".

Sample	E_r **(GPa)**	H/E_r	H^3/E_r^2 **(GPa)**	U_{total} **(nJ)**	U_{el}/U_{total}	U_{pl}/U_{total}
As-cast	205	0,067	0,063	259,5	0,373	0,627
Annealed at 820 K	221,6	0,070	0,075	247,6	0,384	0,616
Annealed at 865 K	219	0,075	0,092	245,5	0,404	0,596
Annealed at 1148 K	263,7	0,069	0,085	228,9	0,393	0,606

Table 3.5: Summary of the values of H/E_r, H^3/E_r^2 , U_{total}, U_{el}/U_{total} and U_{pl}/U_{total} (where H, E_r, U_{el}, U_{pl} and U_{tot} denote hardness, reduced Young's modulus, elastic energy, plastic energy and total energy during indentation, respectively) for the as-cast and annealed specimens.

Similarly, the H^3/E_r^2 ratio indicates that annealing at intermediate temperatures (e.g. 865 K, where nanoparticles are embedded in the amorphous matrix) results in optimized wear performance.

The dependence of the elastic recovery, U_{el}/U_{tot} , is of particular interest in applications such as impact loading since it indicates how much energy is released from the material after being loaded. As it has been demonstrated in the literature (139) there is no general correlation between hardness and elastic recovery. In our case, the highest hardness value corresponds to the sample annealed at 1148 K while the highest elastic recovery is achieved for the sample annealed at 865 K.

It is noteworthy that in spite of the brittle behavior of Fe-based systems, the ultrahigh hardness and good wear resistance make them promising materials for technological applications where plasticity is not an issue. For example, multi-component Fe-based alloys may become good candidates for the implementation of micro-electro-mechanical systems (MEMS), particularly magnetic ones, or coatings, since embrittlement becomes less significant in devices of reduced dimensions. Indeed, it has been suggested that if the sample size is smaller than the so-called process zone size, d (which is the ultimate size of the plastic zone at the tip of a sharp crack), plastic flow may occur without fracture (199). Another interesting sample size effect has been predicted by Shimizu et al (200), where an incubation length scale is defined as the length scale necessary for the propagation of embryonic shear bands, typically of the order of 100 nm. In samples smaller than this length, propagation of shear bands would be inhibited and the sample would deform in an overall homogeneous manner.

3.1.2.5. Sumary

Our results reveal that $Fe_{36}Co_{36}B_{19.2}Si_{4.8}Nb_4$ bulk glassy alloy exhibits ultra-large hardness, high Young's modulus and good wear resistance. The high strength of the as-cast specimen is mainly associated to the strong bonding between the constituent elements, particularly in the atomic pairs containing Nb and Si. The hardness and elastic properties are enhanced by annealing treatments whereas the Poisson's ratio is found to progressively decrease. In the sample annealed below T_g, mechanical hardening is attributed to the precipitation of quasicrystalline particles and the formation of the metastable complex cubic phase $Fe_{23}B_6$, which is known to possess large hardness. For the partially and fully crystalline samples the enhancement on hardness is ascribed to other additional mechanisms, such as solid solution hardening or the interaction between dislocations and twin boundaries and other defects. Concerning wear properties, the best wear resistance is obtained for the sample showing a structure consisting of nanocrystals embedded in an amorphous matrix (i.e., after annealing at intermediate temperatures, between T_g and T_{x2}). All these properties make these materials promising candidates for technological applications like micro-electro-mechanical systems, where embrittlement is less significant than for bulk specimens.

3.2. In-situ nanocomposite formation

Besides annealing treatments at intermediate temperatures, another way to ameliorate the mechanical properties of BMGs is via the precipitation of crystalline particles within the metallic-glass-matrix during casting. This can be achieved by designing suitable alloy compositions or through the mixing of a good glass former composition with a high melting point element, which will undergo precipitation as a second phase (201).

In this section, the influence of Nb addition on the microstructure of the Ti-Zr-Cu-Pd alloy is correlated with the changes in mechanical properties, Young's modulus and corrosion behavior.

3.2.1. Characterization of $(Ti_{40}Zr_{10}Cu_{38}Pd_{12})_{100-x}Nb_x$ (x = 0, 2, 3, 4)

Up to now, Ti-6Al-4V alloy remains the most widely used structural metallic biomaterial for the replacement of hard tissues in artificial joints. However, the Ti-Zr-Cu-Pd BMG exhibits higher strength (almost twice) and lower Young's modulus than commercial Ti-6Al-4V (202). In section 3.1.1, we have observed that annealing treatments to the Ti-Zr-Cu-Pd metallic glass alloy tend to ameliorate its mechanical properties; unfortunately, devitrification often induces embrittlement of the alloy. The addition of specific elements to the Ti-based BMG composition (such as Si (203), Sn (204) or Nb (205)) have been found to result in enhanced mechanical properties. For instance, Zhu et al. (204) reported that addition of 2% of Sn to a Ti–Zr–Cu–Pd metallic glass increases the plasticity (around 3 %) without compromising neither the strength nor the glass forming ability of the resulting alloy. However, the most convenient element to be added has been shown to be Nb. This element is tougher than Sn, it is biocompatible, and it can enhance the plasticity of BMGs by (i) in-situ formation of ductile bcc phase (37; 206), (ii) formation of quasicrystals (207) or medium range ordered (MRO) clusters (208) and (iii) nano-particles embedded in the glassy matrix (209).

Concerning the corrosion behavior in artificial body fluid, there are several studies that investigate the effect of Nb addition. For example Qiu et al. (207) found out that Nb addition to Zr-based BMG greatly enhanced the corrosion resistance in simulated body

fluid (SBF). Furthermore, the Nb-bearing BMG exhibited much higher pitting potential with respect to the Nb-free BMG. For Ti-based BMGs, Oak et al. reported similar values of passive current densities and corrosion resistance for the Nb-free and Nb-bearing BMGs; however, more anodic corrosion potentials were achieved in the Nb-containing sample (108).

3.2.1.1. Thermal Characterization

The DSC curves corresponding to the $(Ti_{40}Zr_{10}Cu_{38}Pd_{12})_{100-x}Nb_x$ with x = 0, 2, 3, 4 alloys are shown in Figure 3.17. A similar thermal behaviour is observed in the x = 0 and x = 2 alloys; they exhibit a distinct glass transition temperature (T_g), followed by a supercooled liquid region and various exothermic transformations indicating multi-stage crystallization events. The T_g and the onset of the first crystallization peak (indicated with arrows in Figure 3.17) are 680 and 721 K, respectively, for the x = 0 alloy, and 631 and 702 K for the x = 2 alloy. As a result, the supercooled liquid region ($\Delta T = T_{x1} - T_g$) is evaluated to be 41 K for x = 0 and 71 K for x = 2. A large supercooled liquid region implies that the supercooled liquid has a high resistance against crystallization leading to a large glass forming ability and enabling the production of bulk glassy rods with larger diameters. However, a decrease in the enthalpy of the first crystallization peak is observed (from ΔH = 24 J/g in the sample with x = 0 to ΔH = 17 J/g in the sample with x = 2), suggesting that the alloy with 2 % of Nb was not completely amorphous and some nanocrystallites could have become embedded in an amorphous matrix during casting.

For the sample with x = 3, T_g cannot be easily determined and also the crystallization enthalpies are further reduced when comparing with the amorphous sample (x = 0), suggesting that crystallization again took place during casting. Finally, for the sample with x = 4 two crystallization peaks are detected but their enthalpy energies are much lower than for the other compositions, indicating a clear crystallization process during the fabrication. Hence, from the DSC measurements it can be concluded that the glass forming ability tends to decrease when the Nb content increases.

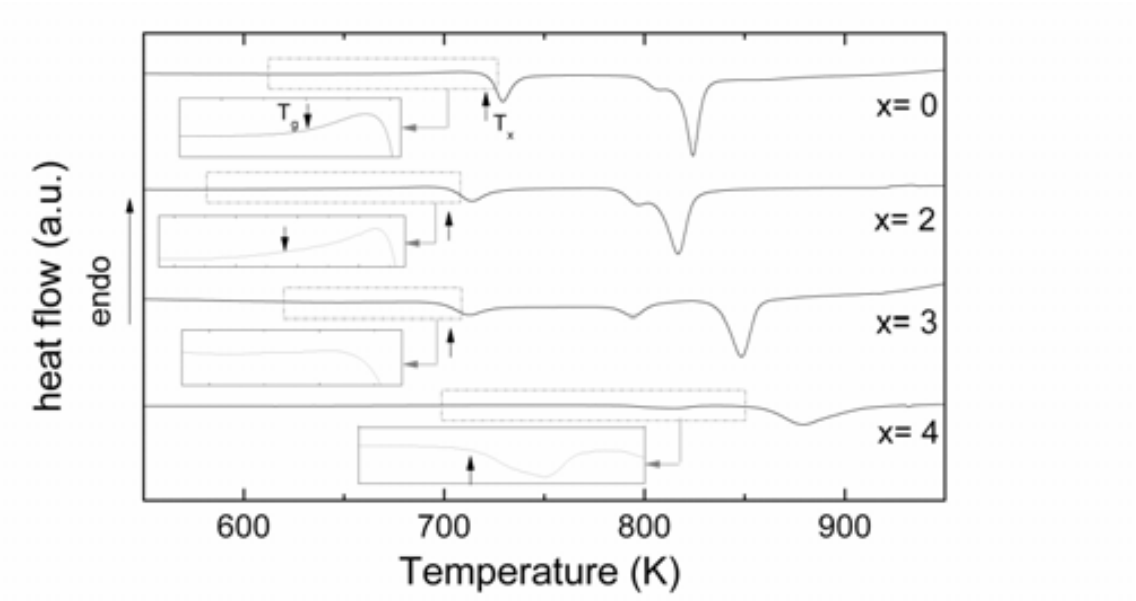

Figure 3.17: DSC curves of the Ti-based alloys, where the glass transition temperature, T_g, and the onset of the first crystallization temperature, T_x, are indicated. The insets are enlarged views around T_g and T_x, shown for clarity.

3.2.1.2. Structural Characterization

Figure 3.18 shows the X-ray diffraction patterns of the $(Ti_{40}Zr_{10}Cu_{38}Pd_{12})_{100-x}Nb_x$ alloys with x = 0, 2, 3, 4. The XRD pattern of the sample with x = 0 consists of only two broad halos, without well-defined diffraction peaks, suggesting that this alloy is amorphous. Further evidence of the amorphous character of this sample is obtained from the TEM image and the corresponding SAED pattern (Figure 3.19a). Conversely, even if not well-defined XRD peaks are observed in the samples with x = 2 and 3, a sharper XRD halo is detected as the Nb content is increased, indicating precipitation of some crystalline phase. This result is corroborated by the TEM observations of the sample with x = 3 (presented in Figure 3.19b), where tiny nanocrystallites dispersed in the amorphous matrix can be observed.

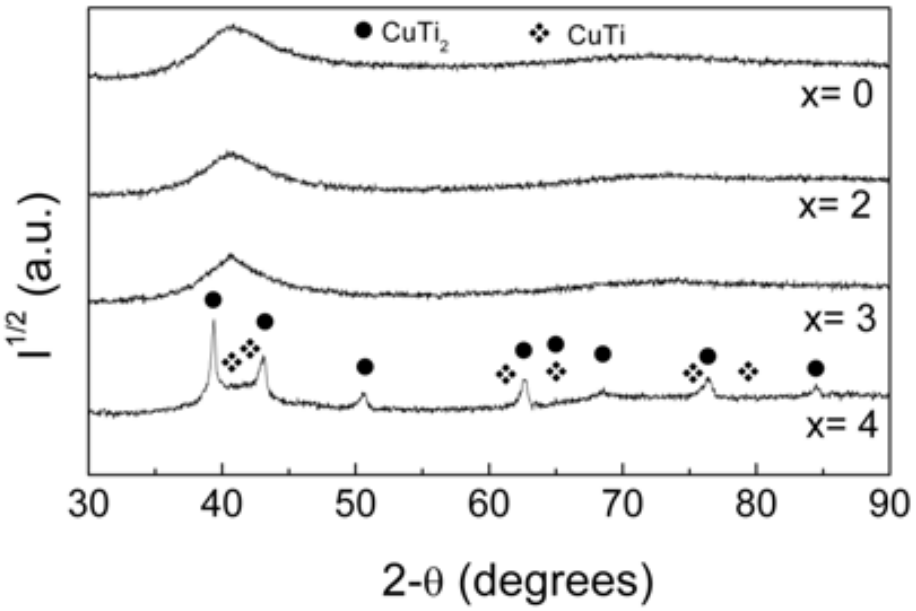

Figure 3.18: XRD patterns corresponding to the $(Ti_{40}Zr_{10}Cu_{38}Pd_{12})_{100-x}Nb_x$ alloys with x = 0, 2, 3, 4.

Clear XRD peaks superimposed to low-intensity amorphous halos are observed for the sample with x = 4. Besides the remaining amorphous phase, the main XRD peaks correspond to the tetragonal $CuTi_2$ (space group I4/mmm) and, in fewer amount, to tetragonal CuTi (space group P4nmm) phases. Figure 3.19c shows a SEM image of the central region of the rod. The microstructure is composed of two crystalline phases (labeled as B and C). Zone A (inset Figure 3.19c) belongs to the amorphous structure located mainly in the outer part of the rod (surrounding the crystalline phases) where the cooling rate is higher and thereby crystallization is precluded. The corresponding energy dispersive X-ray (EDX) analysis results are listed in Table 3.6. Note that the composition of the amorphous zone is almost the nominal one, evidencing that this zone is not enriched in any element. The darker zone (B), enriched in Ti, corresponds to the $CuTi_2$ phase and the C zone can be identified as the CuTi phase. Note that Zr, Pd and Nb are also present in the crystalline phases as substitutional elements or forming solid solutions.

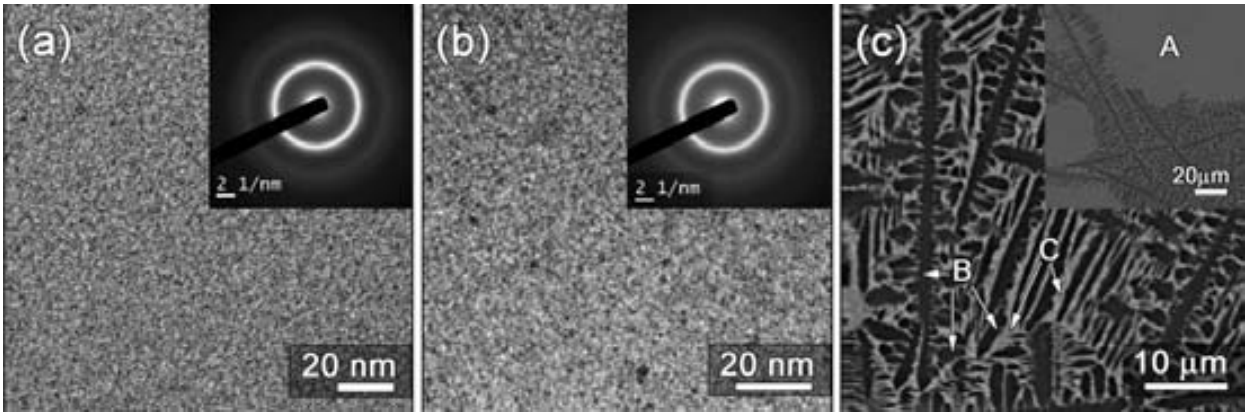

Figure 3.19: TEM images of the $(Ti_{40}Zr_{10}Cu_{38}Pd_{12})_{100-x}Nb_x$ alloys with (a) x= 0, (b) x= 3. Panel (c) is a SEM image for the sample with x= 4 (center of the rod). The insets in (a) and (b) are the corresponding selected area electron diffraction patterns. The inset in (c) is a SEM image showing the coexistence of amorphous and crystalline phases at the peripherical part of the rod.

% at.	Ti	Cu	Zr	Nb	Pd
A	45.3	35	9.1	3.6	7.0
B (CuTi2)	53.0	29.4	7.0	4.0	6.6
C (CuTi)	35.4	43.0	12	3.0	6.6

Table 3.6: EDX compositional analyses corresponding to the different regions (A, B and C) indicated in Fig.19c).

3.2.1.3. Mechanical Characterization

Typical compressive stress-strain curves of the $(Ti_{40}Zr_{10}Cu_{38}Pd_{12})_{100-x}Nb_x$ alloys are shown in Figure 3.20. Remarkably, the yield stress of the amorphous and partially nano-crystalline samples (with x = 0, 2 and 3) is rather high, around 1.9 GPa. However, the sample with x = 4 fractures before yielding, indicating a brittle behavior. An increase in the total strain (ε_{total}) is achieved with minor additions of Nb. Namely, the values of ε_{total} increase from 0.027 (x = 0) to 0.132 (x = 3). Serrated flow is observed after yielding, as typically encountered in many metallic glasses, indicating that abundant shear bands are activated during plastic flow. BMGs usually fracture in a brittle manner with plastic strains < 2%. This is attributed to the inhomogeneous plastic flow characteristic of amorphous materials where deformation proceeds via formation and rapid propagation of shear bands (210; 211).

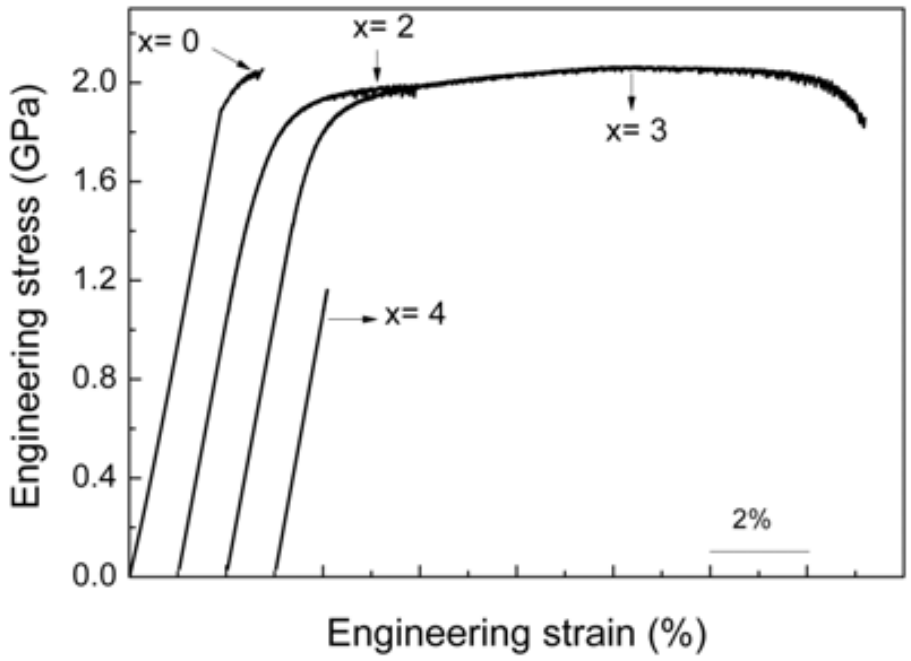

Figure 3.20: Compressive stress-strain curves for the $(Ti_{40}Zr_{10}Cu_{38}Pd_{12})_{100-x}Nb_x$ alloys with x = 0, 2, 3, 4.

The increase of plasticity in the sample with x = 3 can be therefore attributed to the aforementioned formation of nanocrystals in the glassy matrix, which hinder the propagation of shear bands and facilitate their uniform initiation and branching. The Young's modulus values obtained by compression tests (E_{compr} = 100, 103, 104 and 106 GPa for the samples with x = 0, 2, 3 and 4, respectively) are in good agreement with the values obtained from acoustic measurements (see Figure 3.21). Further evidence for the deformation behavior of these alloys can be obtained by imaging the fracture surface of the compressed specimens using SEM (Figure 3.22). Note that the brittle sample (with x = 4) fractured before yielding in a large amount of small pieces; as a result, no SEM observation could be performed in this case. In all the other samples, SEM imaging reveals vein-like pattern morphology, as commonly observed in the fracture surface of relatively tough metallic glasses under compression, i.e., when they exhibit certain plasticity (212). In the insets of Figure 3.22, the compression fracture angles of the alloys with x = 0, x = 2 and x = 3 are indicated. In all cases, the fracture angles are lower than 45º (the value obtained in most polycrystalline metallic specimens, where yielding is governed by the von Mises or Tresca criteria). The obtained values are within the range of fracture angles typically reported for BMGs deformed under

compression (213). The low fracture angles values indicate that yielding in this material is influenced by local normal stresses acting on the shear plane. This effect is described by the Mohr-Coulomb yield criterion (113).

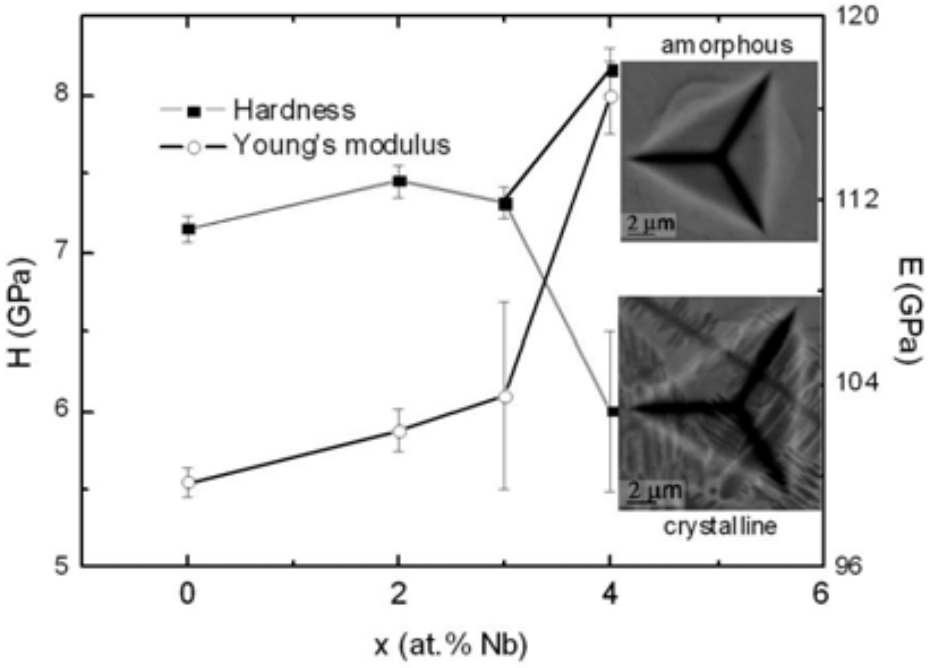

Figure 3.21: Dependence of hardness (measured by nanoindentation) and Young's modulus (measured by acoustic measurements) on the atomic % of Nb addition. Insets show the SEM images of the indents performed in the amorphous and crystalline regions in the sample with x = 4.

As shown in Figure 3.21, hardness values measured at P_{max} = 250 mN are found to be up to 7 GPa for the samples with x = 0, 2 and 3 suggesting that, as it was observed in the compression tests, the strength of the sample is not enhanced when nanocrystallites are embedded in the amorphous matrix. However, for the sample with 4 at. % Nb, nanoindentation experiments indicate that the hardness in the amorphous part increases to 8 GPa, whereas in the crystalline regions the hardness is around 6 GPa. Insets of Figure 3.21 show the SEM images of the indents performed in the amorphous and crystalline regions of the sample with x = 4. Note that the indent corresponding to the amorphous part is much smaller than the one performed in the crystalline phase, evidencing the harder nature of the material in the amorphous state. Furthermore, in the indent performed in the amorphous part, shear bands surrounding the indent are easily observed. These shear bands are attributed to the accommodation of plastic flow and, whereas in the compression curve they manifest as sudden load drops, in the indentation curves they appear as pop-in events in the loading part of the curves. The Young's

modulus, *E*, (calculated from acoustic measurements) tends to slightly increase with 2 and 3 at. % of Nb addition but higher increase is noticed for the sample with x = 4. Such an increase may be attributed to the change in the microstructure since metallic glasses often suffer from the so-called elastic softening effects due to quenched-in free volume in the glass structure as well as anharmonic vibrations resulting from structural disorder (129; 131). Similar trends are observed for the shear and bulk moduli, i.e., values of *G* and *K* range from 36.3 to 37.8 GPa and from 128 to 134 GPa, respectively, for the samples with x = 0, 2, 3. Conversely, an increase of both constants, around 15 %, is detected in the almost fully crystalline sample (x = 4).

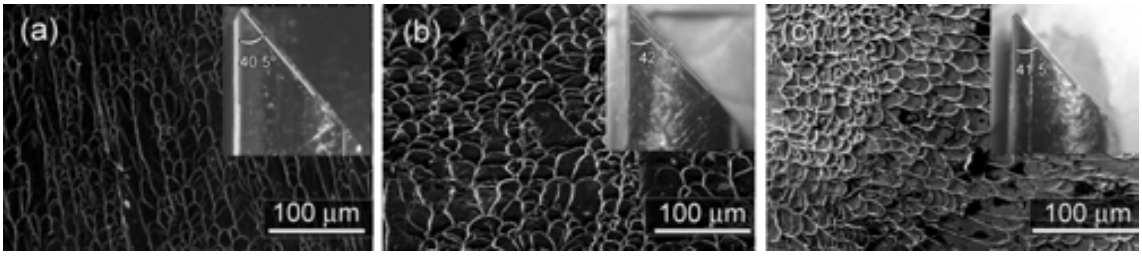

Figure 3.22: SEM images of the fracture surfaces of the $(Ti_{40}Zr_{10}Cu_{38}Pd_{12})_{100-x}Nb_x$ alloys with (a) x= 0, (b) x= 2 and (c) x= 3. The insets in (a), (b) and (c) are optical micrographs showing the fracture angle of the corresponding alloys.

3.2.1.4. Corrosion Properties

The potentiodynamic polarization curves of the $(Ti_{40}Zr_{10}Cu_{38}Pd_{12})_{100-x}Nb_x$ with x = 0, 2, 3, 4 samples in HBSS medium at 310 K are shown in Figure 3.23. The corrosion potential (E_{corr}), the pitting potential (E_{pit}) and the corrosion current density (j_{corr}) extracted from the polarization curves are listed in Table 3.7. The samples with x = 0, 3 and 4 display an E_{corr} slightly more anodic than the sample with x = 2. Actually, for x = 2, the E_{corr} is more cathodic than for the Nb-free alloy. The crystalline sample (x = 4) displays the lowest corrosion current density and also the lowest passive current density. Nevertheless, all the samples show rather low corrosion current densities, likely due to the rapid formation (within ms) of very stable, continuous, highly adherent, self-rehealed, and protective oxide films (mainly TiO_2) on metal surfaces in a wide range of corrosive media at any pH value (144). Even though the samples are spontaneously passivated, passivity breakdown occurred upon sweeping the potential towards more

anodic values, suggesting a certain degree of susceptibility to pitting corrosion. However, before the occurrence of pitting (up to +0.45V), a current step at ~0.1 V is observed, which would fit to the dissolution regime of Cu and the subsequent change of the composition of the passivation layer, as noticed in Zr/Ti-Cu-based glasses and composites in near-neutral pH media (214). Larger E_{pit} - E_{corr} ranges were observed in the samples with 2 and 3 at. % of Nb (Table 3.7). A SEM image of a highly pitted region on the $Ti_{40}Zr_{10}Cu_{38}Pd_{12}$ alloy after polarization to approximately 0.4 V is provided in Figure 3.24 (top left). An elemental EDX mapping (Figure 3.24) of the pitted region shows the distribution of Ti, Zr, Cu, Pd, C, O and Cl elements. Regions with clear tonality indicate that they are rich in the corresponding element. The heavily corroded part is depleted in Zr and Ti, whilst it is enriched in Cu, Pd, O and Cl. This might be ascribed to the preferential dissolution of Ti and Zr over Cu and Pd, which can be understood by considering their standard potentials:

$$(0.91\ \text{V}\ E^0_{Pd^{2+}/Pd^0} > 0.34\ \text{V}\ E^0_{Cu^{2+}/Cu^0} > -1.35\ \text{V}\ E^0_{Ti^{3+}/Ti^0} > -1.45\ \text{V}\ E^0_{Zr^{4+}/Zr^0})$$

Furthermore, Pourbaix diagrams are also useful in predicting potential-pH domains where corrosion is precluded. According to Pourbaix diagrams, Zr precipitates into ZrO at neutral pH. Metallic Cu should first undergo oxidation to Cu^+ (-0.1 V< Cu^+ <0.18 V) and later to Cu^{2+} (for potentials larger than +0.18 V). It has been observed that Cu corrosion is strongly influenced by chloride anions. Indeed, copper dissolutions proceeds via formation of CuCl and $CuCl_2^-$ species at chloride concentrations lower than 1M (215; 216), which is in agreement with our EDX data, where the pits are enriched in Cu and Cl. Pd remains metallic within nearly all the working potentials, but at around +0.4 V it precipitates in the form of PdO and PdO_2. Since Pd and O are also observed in the corroded area, it might be possible that PdO compounds form at the pitted surface. Concerning Ti, its Pourbaix diagram depicts a wide region where the passive TiO_2 oxide film is supposed to be stable (from -0.4 to 0.8 V approximately) (217).

The addition of Nb could affect the corrosion response in two different ways. On one hand, Nb can enhance the pitting resistance due to an improvement of the passive layer properties for near-homogenous alloys (this would apply for x = 0 and also for x = 2 and 3 since the length scale of precipitates is very small). Actually, this behaviour was detected in Zr-based metallic glass containing small amounts of Nb, where an increased

pitting resistance was associated with Nb addition (218). On the other hand, in those cases where Nb induces crystallization, a reduction of the pitting resistance was observed due to the generation of grain boundaries defects and phases with different compositions, eventually rendering galvanic couples which could promote pitting corrosion. This mechanism could be plausible in our case in the almost crystalline sample (x = 4).

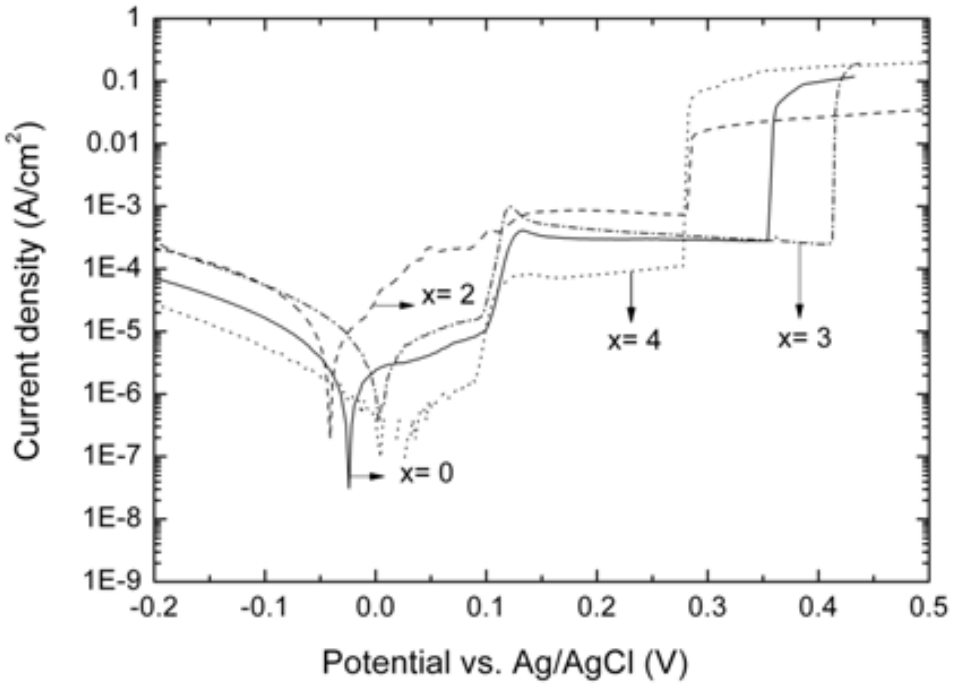

Figure 3.23: Polarization curves of the $(Ti_{40}Zr_{10}Cu_{38}Pd_{12})_{100-x}Nb_x$ in naturally aerated Hank's solution.

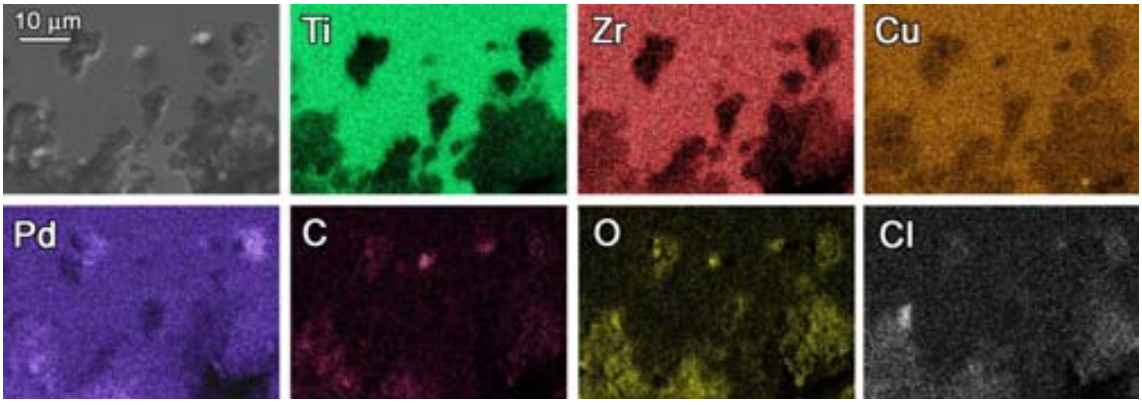

Figure 3.24: SEM image of a highly pitted region on the $Ti_{40}Zr_{10}Cu_{38}Pd_{12}$ alloy (top left), together with element distribution of Ti, Zr, Cu, Pd, C, O and Cl.

% at. Nb	j_{corr} (A/cm^2)	E_{corr} (V)	E_{pit} (V)	E_{pit} - E_{corr} (V)
0	$1.33 \cdot 10^{-6}$	-0.023	0.353	0.376
2	$5.93 \cdot 10^{-6}$	-0.041	0.282	0.323
3	$3.77 \cdot 10^{-6}$	0.007	0.412	0.405
4	$3.17 \cdot 10^{-7}$	0.019	0.270	0.251

Table 3.7: Summary of the electrochemical parameters obtained for the different investigated alloys, where j_{corr}, E_{corr} and E_{pit} denote the corrosion density, the corrosion potential and the pitting potential.

3.2.1.5. Summary

The influence of Nb addition on the microstructure, thermal, mechanical and corrosion properties of $Ti_{40}Zr_{10}Cu_{38}Pd_{12}$ bulk glassy alloy has been investigated. Our results reveal that $Ti_{40}Zr_{10}Cu_{38}Pd_{12}$ sample exhibits large hardness, relatively low Young's modulus and excellent corrosion resistance. The addition of Nb in the amorphous alloy reduces the glass forming ability and, in accordance with TEM images, favors the formation of tiny disperse nanocrystals embedded in the amorphous matrix. These nanocrystals could be responsible for the observed increase of plasticity; for instance, an increase above 10 % of plastic strain is obtained when a 3 at. % of Nb is added to the amorphous composition. Remarkably, the strength of the alloys is not compromised by the addition of Nb. However, a brittle behavior is observed if the Nb content is exceedingly high (4 at. %), where a large fraction of crystalline phases is obtained after casting. All the alloys exhibit competitive anticorrosion properties with low current densities and good corrosion potentials. Owing to all these results (low Young's modulus, high strength, large plasticity and excellent corrosion response), the $(Ti_{40}Zr_{10}Cu_{38}Pd_{12})_{97}Nb_3$ alloy is a potential candidate to be used as structural biomedical material.

3.3. Deformation-induced structural changes

In this section, the structural and mechanical changes observed in three different systems, ranging from completely amorphous to mainly crystalline alloys, subjected to nanoindentation and/or compression tests are studied by means of DSC, X-ray diffraction and TEM:

1. Mechanical softening is observed during nanoindentation in the Ti-Zr-Cu-Ni-Be metallic glass alloy, i.e. a reduction of hardness as deformation proceeds. This fact is attributed to an increase of free volume as larger loads are applied.
2. Crystallization is observed in a Zr-Cu-Ni-Al metallic glass alloy upon compression test and nanoindentation. Superplasticity and strain hardening observed in the compression test and nanoindentation experiments respectively, are likely to be related to deformation-induced nanocrystallization.
3. Finally, Cu-Zr-(Al) systems (nanostructured alloy and amorphous matrix+crystalline phases) exhibit a martensitic phase transformation after being subjected to compression test.

3.3.1. Structural characterization and nanoindentation response of $Ti_{40}Zr_{25}Ni_8Cu_9Be_{18}$ metallic glass

Plastic flow in BMGs is accompanied by dilatation, i.e., net creation of free volume (25; 219). This results in a decrease of viscosity and a concomitant strain softening. In nanoindentation experiments, this softening can manifest by the occurrence of an indentation size effect (ISE), i.e. a progressive decrease of hardness as the indentation proceeds (220; 221; 222). However, it should be noted that the ISE is typically rather pronounced in crystalline materials, due to a variety of factors, as described in section 3.1.2.4.

Plastic flow in BMGs is (at room temperature and moderate strain rates) typically inhomogeneous and proceeds via formation and propagation of shear bands (210; 211; 123). These bands locally nucleate in regions where the deformation-induced creation of free volume cannot be fully compensated by thermal diffusive relaxation (25). As a result, the excess free volume coalesces and the viscosity significantly reduces. Consequently, shear bands manifest as sudden load drops in macroscopic compression curves or pop-in events in nanoindentation experiments.

Another peculiarity of MGs is that yielding cannot be simply described by the usual von Mises or Tresca criteria, as for crystalline metals, since normal stress components acting on the shear plane and/or hydrostatic pressure also play a role at the onset of plasticity (223; 224; 225). The dependence of yielding on normal stresses seems to be related to atomic friction and the dilatation events that occur during plastic flow in MGs (224;

226). To account for the normal-stress or pressure dependence of the shear stress, both the Mohr-Coulomb (226; 224) and the Drucker-Prager (227; 228; 229) yield criteria have been used in the literature.

In this work, the mechanical properties of Ti-based metallic glass deformed by compression tests and nanoindentation (i.e., in geometrically constrained specimens) are comprehensively investigated and compared with those of other MG families. Influence of local normal stresses acting on the shear plane is evidenced by the fracture angle ($\approx$ 39.5º). This effect is incorporated in the finite-element simulations of the nanoindentation curves, which include the Mohr-Coulomb yield criterion. Furthermore, comparative studies involving compression tests and nanoindentation reveal the occurrence of shear banding and a concomitant mechanical softening, which manifests in a so-called indentation size effect, i.e., an overall decrease of hardness with the indentation penetration depth. This effect is discussed within the context of the free volume model.

3.3.1.1. Thermal, Structural and Elastic Characterization

The XRD pattern recorded for the Ti-based MG is shown in Figure 3.25a. The pattern consists of broad halos with absence of well-defined peaks, indicating that the rods are amorphous without detectable crystalline phases. Further evidence for the amorphous character of the sample is obtained from the DSC scans, as the one shown in Figure 3.25b. The curve reveals the existence of a broad exothermic peak at low temperatures, which corresponds to the enthalpy release during structural relaxation. For the heating rate of 40 K/min, the glass transition temperature is T_g = 610 K. Furthermore, two crystallization peaks are observed at T_{x1} = 668 K and T_{x2} = 783 K, rendering a supercooled liquid region $\Delta T = T_{x1} - T_g$ = 67 K. The crystallization enthalpies, evaluated from the areas of the first and second crystallization peaks, are ΔH_1 = -38 J/g and ΔH_2 = -21 J/g, respectively, in good agreement with other amorphous alloys with similar composition reported in the literature (230; 231).

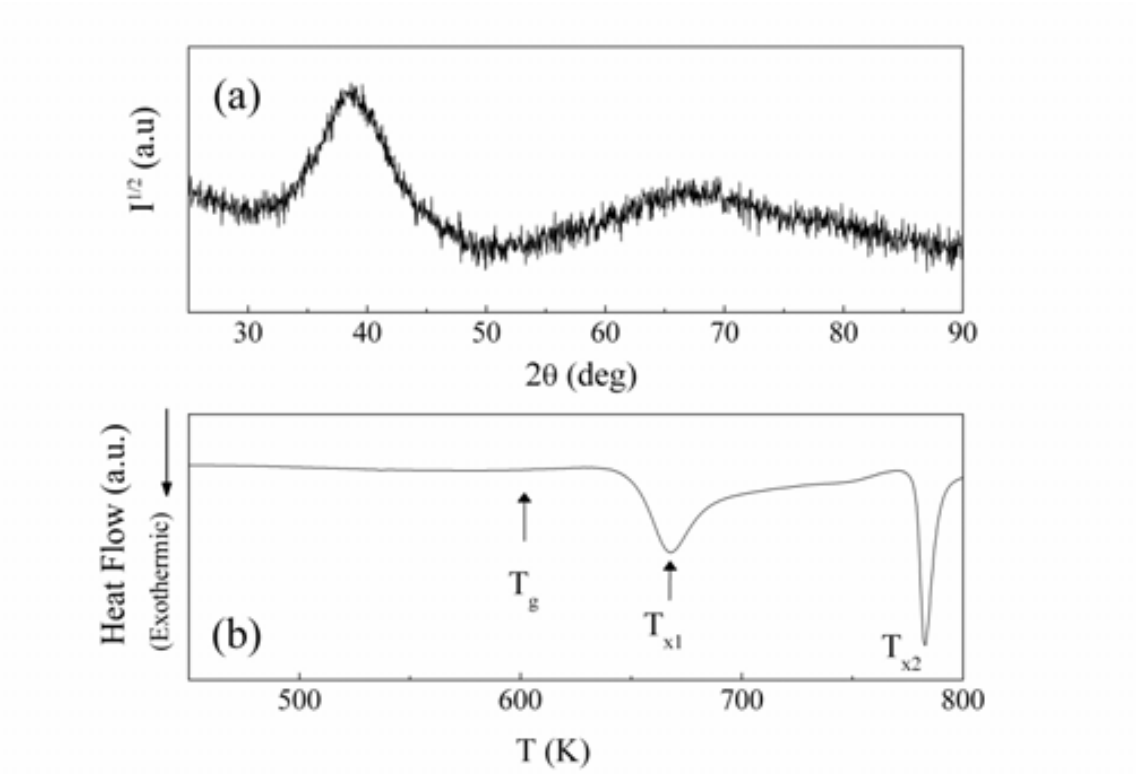

Figure 3.25: (a) X-ray diffraction pattern of the as-cast $Ti_{40}Zr_{25}Ni_8Cu_9Be_{18}$ alloy, showing the absence of sharp, crystalline peaks; (b) differential scanning calorimetry curve of the Ti-based alloy.

The values of density and elastic constants of this alloy are presented in Table 3.8. It is noteworthy that the Ti-based amorphous alloys are lighter than most families of MGs. For instance, the density of the investigated $Ti_{40}Zr_{25}Ni_8Cu_9Be_{18}$ MG is 15% - 20% lower than for Zr-based (232) and rare-earth (233) MGs, 30% lower than for $Cu_{47.5}Zr_{47.5}Al_5$, about 55% lower than for some Pd-based MGs (232; 234) and more than 60% lower than for Pt-based MGs (234). Also remarkable is that the Young's modulus displayed by this alloy is higher than for most rare-earth MGs – which exhibit E around 30 GPa (233) –, Cu-based ($E \approx 85$ GPa) or Au-based ($E = 70$ GPa) MGs (234) and similar to Zr-based, Pd-based or Pt-based MGs (233; 232).

It has been recently suggested that the mechanical toughness of these materials can be correlated with the ratio between the elastic shear modulus and the bulk modulus, G/K. Namely, alloys with low G/K ratios (like Zr-based, Pt-based or Pd-based glasses) are relatively tough, while those with larger G/K ratios (like Mg-based, Nd-based or Ce-based) tend to fracture in a brittle maner. In our case, G/K, is higher than for Pd-based and Pt-based MGs ($G/K \approx 0.18$) but lower than for some (more brittle) rare earth-based MGs ($G/K \approx 0.43$ for Mg-based and Ce-based MGs) or oxide glasses ($G/K > 0.7$) (235).

φ (g/cm3)	v	E_{Acoust} (GPa)	G (GPa)	K (GPa)	G/K
5,60	0,358	95	34	108	0,314

Table 3.8: Summary of the elastic properties (v, G, B and E_{Acoust} denote the Poisson's coefficient, shear modulus, bulk modulus and Young's modulus, respectively) of the as-cast $Ti_{40}Zr_{25}Ni_8Cu_9Be_{18}$ alloy The density of this alloy, φ, determined using the Archimedes' technique, is also presented.

3.3.1.2. Mechanical Characterization

a) Compression test

A typical true stress –strain curve obtained during uniaxial compression of the as-cast $Ti_{40}Zr_{25}Ni_8Cu_9Be_{18}$ alloy, carried out at room temperature at a rate of 1.8 x 10^{-4} s^{-1}, is shown in Figure 3.26. The obtained Young's modulus is E_{compr} = 98 GPa, the yield stress is σ_y = 1.72 GPa and the total strain is ε_{tot} = 0.056. Concerning the elastic strain, the obtained value (2.2 %) is not far from the universal value reported for most MGs (ε_e = 0.026) (234). After yielding, clear serrations in the compression curve are observed, as can be seen in the inset of Figure 3.26. The occurrence of inhomogeneous plastic flow indicates the formation of shear bands (123). Some of these shear bands can be observed at the outer surface of the deformed specimen (see Figure 3.27a). In these shear bands there is a sudden decrease of viscosity (25), which brings about load drops and a concomitant mechanical softening. In fact, an overall mechanical softening of the Ti-based BMG takes place as deformation proceeds, as can be also seen in the inset of Figure 3.26.

Fracture occurs after a plastic strain, ε_p, of around 0.034. The fracture angle, θ_C = 39.5 ± 1º (see Figure 3.27a), is lower than the value obtained in most polycrystalline metallic specimens (θ_C = 45º) but is within the range of fracture angles typically reported for MGs deformed under compression (213; 236).

This is an indication that yielding is influenced by the internal pressure and/or local normal stresses acting on the shear plane (237; 123). This effect is captured by the Mohr-Coulomb yield criterion, which can be expressed as follows:

$$\tau_y = c - \beta_{M-C}\sigma_n \qquad \text{(Eq. 3.2)}$$

where τ_y is the shear stress on the slip plane at yielding, c is the shear strength in pure shear (also termed cohesion), β_{M-C} denotes the internal friction coefficient of the glass and σ_n is the normal stress acting on the shear plane. Using a geometrical reasoning it is easy to demonstrate that the fracture angle can be related to β_{M-C} as follows:

$$\beta_{M-C} = \frac{\cos 2\theta_C}{\sin 2\theta_C} \qquad \text{(Eq. 3.3)}$$

From this equation, the friction coefficient, β_{M-C}, for the investigated $Ti_{40}Zr_{25}Ni_8Cu_9Be_{18}$ alloy is estimated to range between 0.23 and 0.15, which is in agreement with values evaluated from other studies of yielding in BMGs (224).

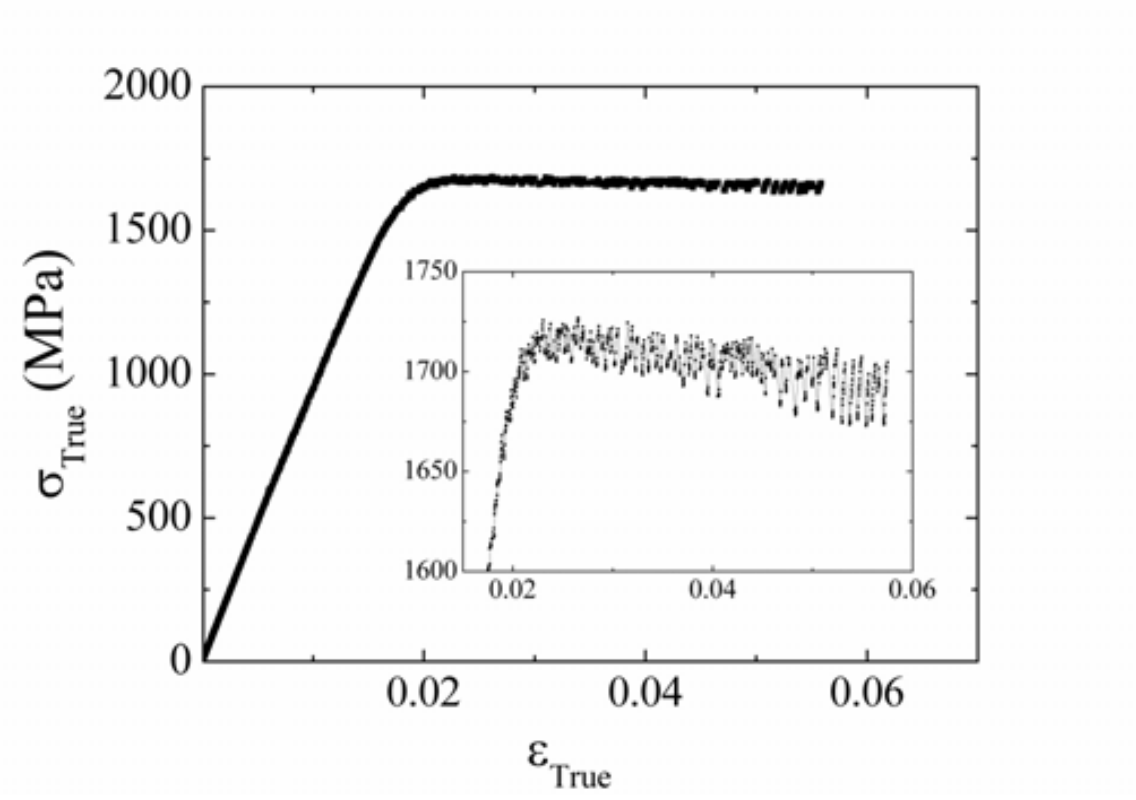

Figure 3.26: Stress-strain curve obtained during compression of the as-cast $Ti_{40}Zr_{25}Ni_8Cu_9Be_{18}$ alloy. The inset shows the occurrence of serrated flow along with a progressive mechanical softening after yielding.

Some insight into the mechanisms responsible for mechanical failure can be obtained by imaging the fracture surface of the deformed specimen using SEM. The observations reveal that vein-like patterns form at the fracture surface (see Figure 3.27b), suggesting that local heating accompanies shear during mechanical failure. In the investigated

alloy, the width of the dimples (or the wavelength of the vein features) ranges between 5 μm and 10 μm. This type of morphology is frequently encountered in BMGs deformed under compression, particularly when they exhibit significant plasticity (212). Conversely, a so-called river-like pattern is usually observed at the fracture surface of brittle BMGs and is associated with a much faster fracture. Actually, it has been recently claimed that the river-like fracture surface of brittle BMGs is also constituted of multiple dimples, similar to those observed in vein-like morphologies, but with much smaller sizes (238), suggesting that plasticity is very short-ranged in those systems. Indeed, the size of the dimples seems to be indicative of the extent of the plastic zones in the BMG, i.e., the size of regions below which it is likely to have plastic flow without premature fracture (239). Hence, as expected, the dimples in the $Ti_{40}Zr_{25}Ni_8Cu_9Be_{18}$ alloy are indeed much larger than in brittle Ce-based or Mg-based BMGs (238).

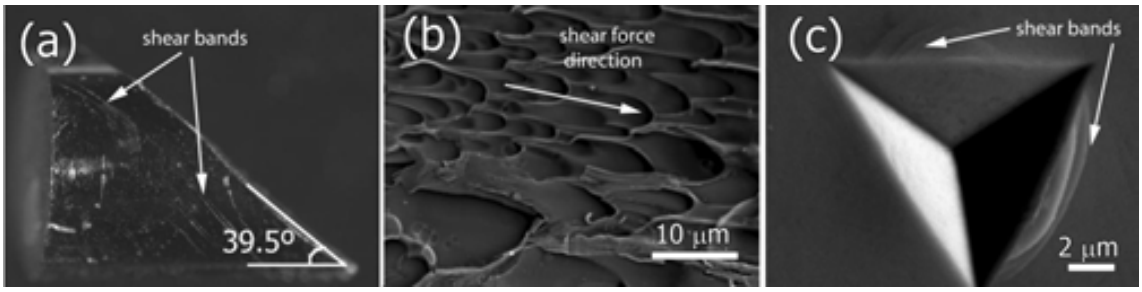

Figure 3.27: (a) Optical micrograph showing the fracture angle of the as-cast $Ti_{40}Zr_{25}Ni_8Cu_9Be_{18}$ alloy; (b) SEM image of the fracture surface of this amorphous alloy; (c) SEM image of an indent performed on the as-cast $Ti_{40}Zr_{25}Ni_8Cu_9Be_{18}$ alloy applying a maximum load of 450 mN.

b) Nanoindentation

Typical load (P) – displacement (h) curves obtained by nanoindentation performed under quasi-static conditions, using maximum loads of 10 and 100 mN, are shown in Figure 3.28a and b, respectively. Similar to compression tests, serrated plastic flow also occurs during depth-sensing nanoindentation experiments and manifests as pop-in events in the indentation loading curves. These serrations are less clearly seen for larger maximum applied load (e.g. 100 mN), mainly because of lack of resolution of the experimental setup (note that the pop-in events represent discontinuous displacements of the order of tens of nm or less).

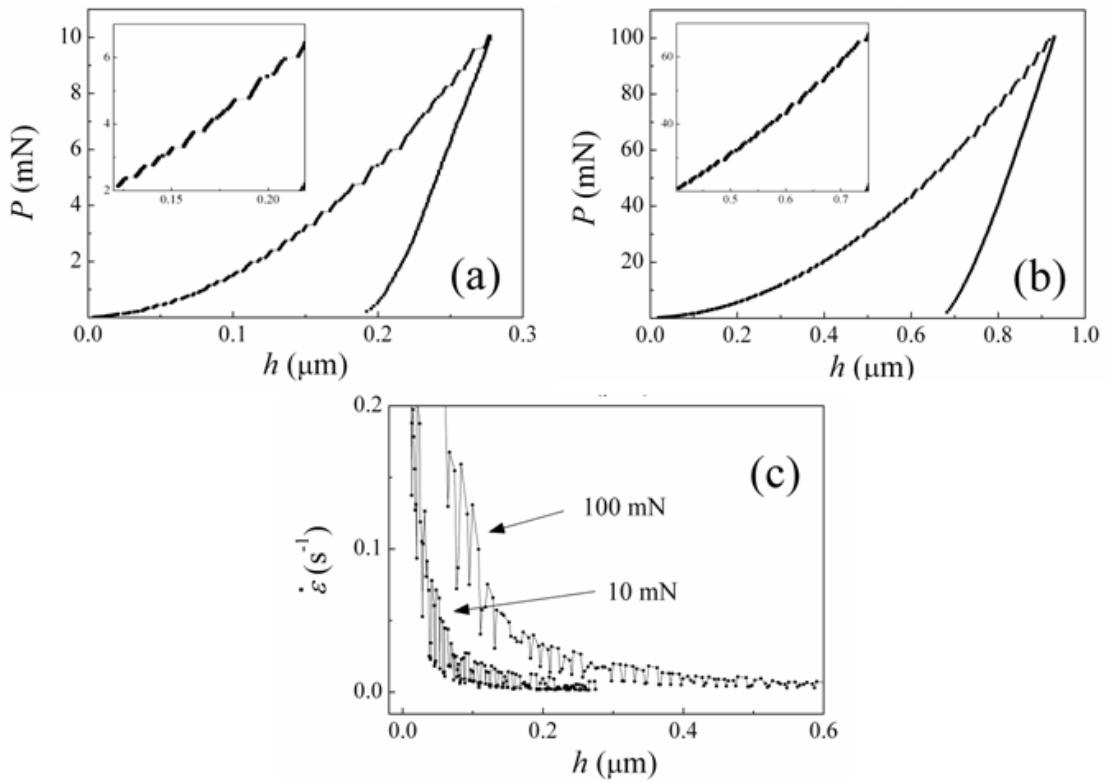

Figure 3.28: Load (P) – displacement (h) nanoindentation curve obtained using a maximum force, P_{max},(a) 10 mN; (b) 100 mN; (c) dependence of the indentation strain rate on the indentation time, corresponding to the loading segments of the indentation curves shown in (a) and (b). The insets in (a) and (b) show the central parts of the loading curves, where some pop-ins can be easily distinguished (particularly for P_{max} = 10 mN).

The pop-in events can be also visualized if the indentation strain rate is plotted as a function of the indentation time (see Figure 3.28c). The indentation strain rate is calculated as:

$$\dot{\varepsilon}_i = \frac{1}{h}\frac{dh}{dt} \qquad \text{(Eq. 3.4)}$$

where h is the penetration depth into the specimen (223; 220). As it typically occurs in nanoindentation experiments, $\dot{\varepsilon}_i$ at the beginning of the loading segments is relatively high (in our case $\dot{\varepsilon}_i > 0.2\ s^{-1}$) and it progressively decreases as the indentation proceeds ($\dot{\varepsilon}_i \approx 2 \times 10^{-3}\ s^{-1}$ at the end of the loading segments). The indentation strain rate is, in fact, multiaxial but it can be related to the effective uniaxial strain rate by $\dot{\varepsilon}_u = 0.09\dot{\varepsilon}_i$

(223). It is interesting to remark that, with the chosen indentation conditions, the uniaxial strain rate at sufficiently long indentation times (i.e., in the steady state), tends to level off at $\dot{\varepsilon}_u \approx 1.8 \cdot 10^{-4} s^{-1}$, similar to the uniaxial strain rate used for the compression tests.

In turn, the estimated uniaxial strain rate during nanoindentation is proportional to the effective shear strain rate governing deformation, $\dot{\gamma}$, roughly by a factor $\sqrt{3}$, i.e. $\dot{\gamma} = 0.16\dot{\varepsilon}_i$ (223). It should be noted that for the conditions of our experiments $\dot{\gamma}$ during indentation loading segments tends to approach a value of about 3.2 x 10^{-4} s^{-1}. For this effective shear strain rate, the deformation map developed by Schuh et al. (223) predicted that plastic deformation during nanoindentation at room temperature should be inhomogeneous, as it is indeed observed experimentally. Also noteworthy is that from these quasistatic indentation experiments with maximum loads of 10 mN and 100 mN the calculated hardness is H = 6.9 GPa and H = 6.3 GPa, respectively, whereas the Young's modulus is $E_{nanoind} \approx$ 110 GPa, not much different than the value obtained from the compression tests.

The dependence of hardness on the maximum indentation load can be studied in detail using the continuous stiffness method (CSM). With this method, the nanoindenter applies a load to the indenter tip to force the tip into the surface while simultaneously superimposing and oscillating force with a force amplitude generally several orders of magnitude smaller than the nominal load; as a result, the CSM method provides an accurate measurement of the location of initial surface contact and continuous measurement of the contact stiffness as a function of depth or frequency, thus eliminating the need of unloading cycles. From a total of ten CSM curves measured up to 450 mN, the dynamic hardness, H_d, has been evaluated as a function of the applied load. The average H_d (plotted in Figure 3.29a as a function of the penetration depth) is found to progressively decrease as the indentation proceeds, i.e., from about 7.8 (at 1 mN) to 6.3 GPa (at 450 mN). The decrease of hardness with the penetration depth is often referred to as the "indentation size effect" (ISE) and is, in fact, well-known in crystalline metals (221) but not so often reported for BMGs (220; 221; 222). In BMGs, this effect has been ascribed to the overall strain softening that occurs during plastic deformation (220). A detailed discussion of this effect within the framework of the free volume model is presented here below. Finally, it should be noted that although no clear

pop-in events are observed in the CSM nanoindentation experiments, shear bands surrounding each of the indents obtained by this method are easily observed by SEM (see Figure 3.27c). Again, this is in agreement with the deformation map proposed by Schuh et al. (223) since although these indentations are carried out using a dynamic approach, the average steady state value of the shear strain rate (for sufficiently long indentation times) is found to be around 4.4 x 10^{-3} s^{-1}, still within the inhomogeneous region of the plastic flow map. The absence of serrations in the CSM curve shown in Figure 3.29a is mainly due to the lack of experimental resolution to resolve them and the fact that the presented curve is actually the average of the ten CSM curves and pop-in events are localized at different penetration depths in each of them.

- ***Mechanical softening and indentation size effect:***

The nanoindentation experiments, both in quasistatic (Figure 3.28) and dynamic (Figure 3.29) regimes, show that H decreases as the indentation load is increased. In general, this reduction of hardness can be rather pronounced in single crystalline materials and has been ascribed to a variety of factors, such as surface effects (184), friction between the indenter and the sample (240) or, more recently, strain gradient hardening (186). The latter considers that, as a result of the shear field created by the indenter, the crystal lattice becomes distorted and, in order to form the residual indentation imprint, the so-called geometrically necessary dislocations have to be created. For large indentations, the strain variation between two extremes is more gradual and the statistically stored dislocations can easily accommodate the shear stress without need of the geometrically necessary dislocations, thus reducing strain gradient effects. In spite of the lack of dislocations in BMGs, the ISE has been also occasionally reported in these materials (220; 221; 222). Its origin is, however, still not fully understood. Nevertheless, it is known that flow events in BMGs are accompanied by dilatation, i.e., creation of free volume (25). This mechanism results in strain softening during plastic deformation (as it is also evidenced in the compression tests (Figure 3.26)) and, hence, it is likely to play a role in the ISE. The ISE can be quantified using a power law of the type $H = c \cdot h^{-m}$, where c is a constant and m denotes the ISE index (221). Plotting log(H) as a function of log(h) an ISE index m = 0.072 is obtained (Figure 3.29c), which is smaller than the

values reported for most crystalline materials (221). This indicates that the ISE in MGs, although clearly measurable, it is still less significant than for crystalline metals.

The ISE in MGs can be examined, in a semi-quantitative manner, by using the free volume concept. It has been argued that in MGs a certain amount of flow defects inherently exist, which are sites where the net free volume per atom, v_f, exceeds a threshold value, v^*, defined as the effective hard sphere size of the atom (25). The flow defect concentration is given as (241):

$$c_f = \exp(-1/x) \qquad \text{(Eq. 3.5)}$$

where $x = \langle v_f \rangle / \gamma v^*$, being $\langle v_f \rangle$ the average free volume per atom and γ a geometrical factor comprised between 0.5 and 1. In turn, the flow equation that governs the shear strain rate in MGs can be expressed as (25; 220):

$$\dot{\gamma} = 2\Delta f c_f k_{f,0} \left(\frac{\varepsilon_0 v_0}{\Omega} \right) \sinh\left(\frac{\tau \varepsilon_0 v_0}{2 k_B T} \right) \exp\left(\frac{-\Delta F_0}{k_B T} \right) \qquad \text{(Eq. 3.6)}$$

Here Ω is the atomic volume (approximately $1.5 \cdot 10^{-29}$ m^3 in our case), ε_0 is the local strain of a flow event, v_0 is the volume of a locally sheared region, k_B is the Boltzmann constant, τ is the shear stress, $k_f = k_{f,0} \exp\left(\frac{-\Delta F_0}{k_B T} \right)$ is a temperature-dependent rate constant of plastic flow (in which $k_{f,0}$ is proportional to the Debye frequency and ΔF_0 is the Helmholtz free energy required to operate a shear flow) and Δf is the volume fraction of flow units. The hyperbolic function results from subtracting the backward flux due to thermal fluctuations from the net forward flux of atoms in the direction of the stress. This equation was originally derived for high temperature viscous flow where shear transformation zones are rather spherical and uncorrelated (homogeneous flow). However, the main change when plastic flow becomes inhomogeneous is that the value of Δf changes, from being close to 1 in homogeneous flow to a lower value in low-temperature inhomogeneous flow (25).

For our Ti-based MG hardness is proportional to the shear stress by $H = 8\tau$. Then Equation 3.6 can be rewritten to:

$$H = \frac{16 k_B T}{\varepsilon_0 v_0} \sinh^{-1}\left(\frac{\dot{\varepsilon} \Omega}{2 \varepsilon_0 v_0 c_f \Delta f k_{f,0}} \exp\left(\frac{\Delta F_0}{k_B T} \right) \right) \qquad \text{(Eq. 3.7)}$$

The inverse hyperbolic sine function can be simplified using that $\sinh^{-1}(y) = \ln(y + \sqrt{y^2 + 1}) \approx \ln(2y)$ for $y >> 1$. Filling in $\dot{\varepsilon} \approx 10^{-2}$ s^{-1} (as obtained experimentally), and representative orders of magnitude for $\frac{\Omega}{\varepsilon_0 v_0} \approx 0.1$, $\Delta f \approx 0.8$, $c_f \approx 10^{-8}$, $\exp(\frac{\Delta F_0}{k_B T}) \approx 10^{25}$ and $k_{f,0} \approx 10^{24}$ s^{-1} (Table 3.9) (223; 242; 243), this simplification is found to be valid and it leads to the following expression for *H*:

$$H = \frac{16 k_B T}{\varepsilon_0 v_0} \left(\frac{\Delta F_0}{k_B T} + \ln(\frac{\dot{\varepsilon} \Omega}{\varepsilon_0 v_0 \Delta f k_{f,0}}) - \ln(c_f) \right) \qquad \text{(Eq. 3.8)}$$

Equation 3.8 predicts that for a given strain rate the hardness will decrease with increasing free volume and flow defect concentration. In other words, accumulation of free volume brings about a mechanical softening of the metallic glass.

If one assumes that each flow event, on average produces a certain amount of free volume, i.e., $dx = a_x d\varepsilon$, where a_x is the proportionality factor which a priori can be temperature dependent (242) then a free volume production term, *P*, can be readily obtained:

$$\left. \frac{dc_f}{dt} \right)_{def} = P = a_x \dot{\varepsilon} \, c_f \ln^2 c_f \qquad \text{(Eq. 3.9)}$$

During the indentation process, the change in free volume in the specimen may be approximated by (244):

$$\frac{dc_f}{dt} = -k_r c_f (c_f - c_{f,eq}) + a_x \dot{\varepsilon} \, c_f \ln^2 c_f \approx a_x \dot{\varepsilon} \, c_f \ln^2 c_f . \qquad \text{(Eq. 3.10)}$$

where k_r is a temperature-dependent rate constant for structural relaxation and c_{fe} is the equilibrium flow defect concentration. Neglecting the first term implies that the production term $P = a_x \dot{\varepsilon} \, c_f \ln^2 c_f$ is the dominant factor in the kinetics of structural relaxation at temperatures far below T_g. This is plausible since the value of k_r decreases very rapidly with decreasing temperature. Furthermore, it is believed that the duration of the local temperature rise associated with shear band formation is very short compared with the overall time scale of the nanoindentation experiment (245).

Figure 3.28c shows that, for a given h, the strain rate is higher for 100 mN than for 10 mN. According to Equation 3.10, this means that, at a certain indentation depth, the production of free volume is more pronounced for larger maximum applied loads. As a result, a lower H will be obtained for indentations performed up to higher P_{max} (220).

Combining Eqs. 3.4 and 3.10, the change in free volume as a function of indentation depth can be expressed as:

$$\ln(c_f) = \left[\frac{1}{\ln(c_{f,ini})} - a_x \ln\left(\frac{h}{h_{ini}}\right) \right]^{-1} \qquad \text{(Eq. 3.11)}$$

where $c_{f,ini}$ is the concentration of defects present in the material before deformation and h_{ini} the initial indentation depth.

Since H is continuously measured in CSM experiments, these types of curves are very suitable to investigate the ISE. In fact, the obtained data can be used to estimate the amount of free volume locally generated in the metallic glass during the indentation test. It turns out that the shear strain rate in CSM experiments is roughly constant ($\dot{\gamma}$ =4.5·10^{-3} s^{-1}) in the depth range between 0.2 and 2 μm (see Figure 3.30a). Bearing in mind that the pressure-sensitivity in this alloy results in $H \approx 8\tau_y$, it is possible to use Equation 3.6 to evaluate the change in c_f that is required to cause the softening (and concomitant ISE) observed during the course of the CSM indentation experiments. The depth dependence of $2\Delta f c_f k_f \left(\frac{\varepsilon_0 v_0}{\Omega}\right)$, calculated from Equation 3.6 using the estimated values of $\dot{\gamma}$, $\varepsilon_0 v_0$ and τ is shown in Figure 3.30b. Since the degree of inhomogeneity in plastic flow of BMGs depends on the strain rate (223; 123) and $\dot{\gamma}$ is rather constant once the steady state is achieved (i.e., for 0.1 μm < h < 2 μm), it is likely that Δf does not vary significantly within this penetration depth range. Analogously, $\left(\frac{\varepsilon_0 v_0}{\Omega}\right)$ and k_f should remain essentially constant during the steady state of CSM experiments. Then Figure 3.30b indicates that $c_{f,(h\,=\,2\mu m)} \approx 9 \cdot c_{f,(h\,=\,0.1\ \mu m)}$. Taking characteristic values of reduced free volume frozen during the as-cast procedure, $\langle v_f \rangle / v^* \approx 0.05$ (246; 247), such an increase in c_f is equivalent to an increase of reduced free volume of around 10 %. Interestingly, this value is of the same order of magnitude as the free volume

increase (≈ 4.4 %) reported for a Zr-Cu-Ni-Al-Nb amorphous alloy subjected to cold rolling to a thickness reduction of 32% (248).

Furthermore, substituting $ln(c_f)$ in Eq. 3.8 by its expression in Eq. 3.11 results in a relationship between H and the indentation depth h that can be used to fit the experimental variation of hardness with the penetration depth. Using the measured values of $\dot{\varepsilon}$ and τ and plausible values for $\frac{\Omega}{\varepsilon_0 v_0}$, Δf, $\exp(\frac{\Delta F_0}{k_B T})$ and $k_{f,0}$ from the literature (60; 223; 242; 243) (see Table 3.9), the experimental variation of H vs. h can be fitted with accuracy, as it is shown in Figure 3.30c. As a result of the fit, the obtained initial penetration is h_{ini} = 8 nm, the amount of reduced free volume at the beginning of the indentation tests is $\langle v_f \rangle / \gamma v^* = -(\ln (c_{f,ini}))^{-1} = 0.055$ and $a_x = 0.006$. It should be noted that varying the value of Δf within a reasonable range, e.g. between 0.5 and 1, also allows proper fitting of the experimental data and does not result in significant variations in the fitted values of h_{ini}, $c_{f,ini}$ and a_x. The fitted value for h_{ini} is reasonable since in the first nanometers of indentation the response of a flat specimen under an indenter is fully elastic. In turn, the obtained initial amount of reduced free volume is also in good agreement with the estimations made on other families of as-cast BMGs (246; 247). Finally, it is worth mentioning that, based on Spaepen's original model for the plastic flow of BMGs (25), the creation of free volume for deformations under high stresses can be expressed as:

$$\left.\frac{dv_f}{dt}\right)_{creation} = \frac{\gamma v^*}{v_f}\frac{k_B T}{S}\frac{\Omega}{\varepsilon_0 v_0}\dot{\varepsilon} \qquad \text{(Eq. 3.12)}$$

By combining Equations 3.9 and 3.12 it is possible to correlate a_x with the stiffness of the BMG, S, as follows:

$$a_x \approx \frac{k_B T}{S}\frac{\Omega}{\langle v_f \rangle \varepsilon_0 v_0} \qquad \text{(Eq. 3.13)}$$

Using a value for $S = \frac{2}{3}\mu\frac{1+\nu}{1-\nu}$ equal to 48 GPa (as calculated from the elastic constants reported in Table 3.8) and considering that $\gamma v^* \approx 0.8\,\Omega$ (25) a value for a_x around 0.008 is obtained, which is in rather good agreement with fitted value for this parameter obtained from the indentation data.

Parameter	Value	Reference
$\boldsymbol{\varepsilon}$	$\frac{1}{h}\frac{dh}{h}$ s^{-1}	Calculated
Ω	$1.5 \cdot 10^{-29} m^3$	Calculated
$\varepsilon_0 v_0$	$2 \cdot 10^{-28} m^3$	(242)
Δf	0.8	(60)
ΔF_0	1.5 eV	(60; 123)
$k_{f,0}$	10^{24} s^{-1}	(243)
$\tau(h)$	$H(h)/8$	Calculated
h_{ini}	8 nm	Fitted
$-(\ln(c_{f\,ini}))^{-1}$	0.055	Fitted
a_x	0.006	Fitted

Table 3.9: *Parameters used to fit the experimentally observed variation of hardness with the penetration depth (Figure 3.30(c)). Some of the parameters have been calculated from the experimental data while others (as indicated) have been taken from the literature. The fitted values for h_{ini}, $-(\ln (c_{f,ini}))^{-1}$ and a_x are also given in the table.*

It should be noted that our analysis is, in fact, representative of the average behaviour of the system. The local strain rate within shear bands is much larger than in the surrounding matrix (123); therefore only an average shear strain rate is evaluated from the CSM curves. Furthermore, a slight reduction of ΔF_0 may be expected in the previously deformed regions beneath the indenter both because of the local temperature increase within shear bands and the fact that consecutive activation of flow events requires each time a lower energy due to the presence of local strain fields and the progressive creation of free volume. In this sense, it is possible that the estimated deformation-induced average excess free volume evaluated from our analysis could be, to a certain extent, overestimated and should be rather regarded as an upper limit.

Despite these shortcomings, the presented interpretation of the ISE in MGs is derived here for the first time and it demonstrates that the free volume concept can give a good estimate of the ISE in MGs. More complex models may be elaborated in the future to incorporate other effects, such as an eventual strain rate sensitivity or plastic anisotropy induced by deformation.

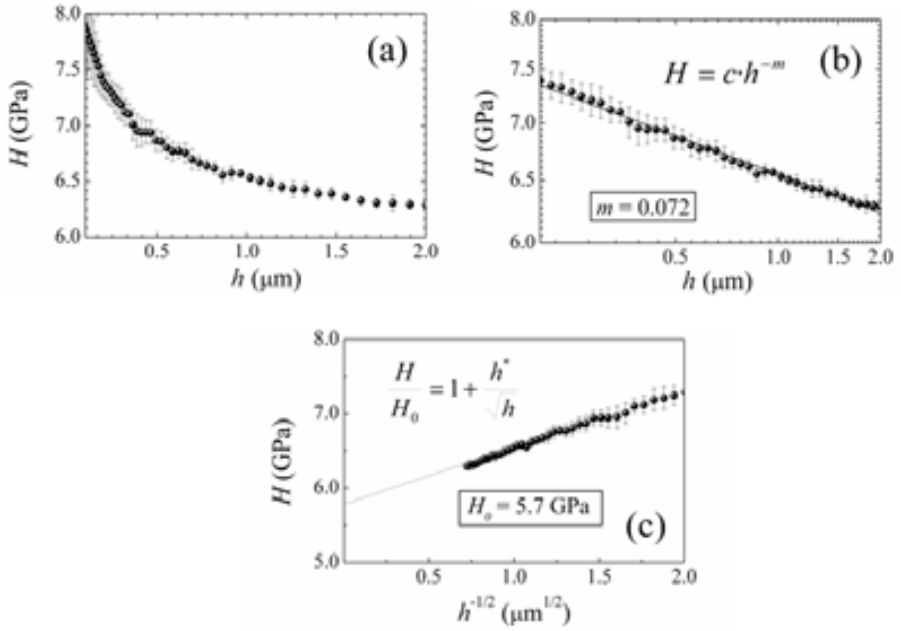

Figure 3.29: (a) Dependence of H_d on h during nanoindentation measurements carried out on the as-cast $Ti_{40}Zr_{25}Ni_8Cu_9Be_{18}$ alloy using the CSM method up to a maximum load of 450 mN; (b) Log (H) – log (h_t) plot, showing a linear fit of the experimental data, from which the indentation size effect exponent, m, can be evaluated; (c) dependence of H on $h^{-1/2}$ and linear fit of the data (discontinuous line) from where the value of H_0 can be evaluated.

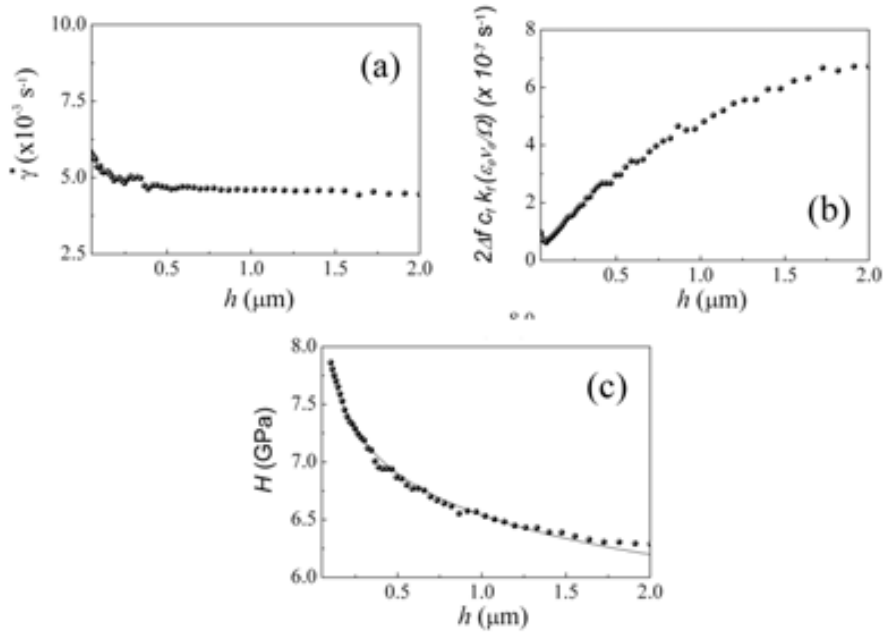

Figure 3.30: (a) Dependence of (a) the shear strain rate, $\dot{\gamma}$, and (b) $2\Delta f c_f k_f \left(\frac{\varepsilon_0 v_0}{\Omega}\right)$ on the penetration depth during the CSM mode indentation experiments. Shown in (c) is the dependence of H on h. The line in (c) is a fit of the experimental data using Equations 3.8 and 3.11 (see text).

- ***Pressure-sensitive yielding***

From compression test it was already noticed that yielding was influenced by internal pressure and/or local normal stresses acting on the shear plane; further evidence of this effect is obtained from numerical simulations of the load-displacement nanoindentation curves. As shown in Figure 3.31, the indentation loading curve calculated using the elastic Hertz theory deviates significantly from the experimental one. Also a disagreement is encountered between the experimental curve and the simulated one using the elastic-perfectly plastic formalism with a pressure-independent (Tresca) yield criterion. In this case, for a given load, the corresponding calculated penetration depth is larger than the experimental one. Conversely, the overall load-displacement indentation response is well reproduced if the Mohr-Coulomb yield criterion with the pressure index estimated from the compression experiment (i.e., β_{M-C} = 0.194) is introduced in the simulations (see Figure 3.31). Hence, the simulations reveal that the indentation load at a given indentation depth increases when a pressure-sensitivity index is introduced, a result which confirms the analysis, performed by Narasimhan, based on expanding cavity model, of the stress and displacement fields in a hollow sphere subjected to internal pressure (249).

It should be noticed that our simulation results are also in agreement with other works in the literature that have shown the influence of pressure on the indentation behaviour of Zr-based MGs, either by introducing the Mohr-Coulomb (237) or the Drucker-Prager (227) yield criterion in the finite-element simulations. In fact, the Mohr-Coulomb and Drucker-Prager pressure-dependent criteria have the same similarities and differences as the Tresca and von Mises pressure-independent criteria (195). Therefore, both yield criteria can be used to properly capture the pressure-sensitivity features of MGs.

Further outcome from the numerical simulations can be obtained by plotting the displacement and stress (in this case $\sigma_{\theta\theta}$ component) contour mappings. The contour mappings corresponding to maximum load are shown in Figure 3.32. Remarkably, both types of plots suggest that, although the maximum depth of the indenter into the specimen is larger when the Tresca criterion is employed (see also Figure 3.31), the extent of the plastic zone underneath the indenter is actually larger for the simulations using the Mohr-Coulomb criterion. This result, which has been obtained by a few authors (227; 249), is the consequence of the combined action of hydrostatic pressure

and normal stresses acting on the shear plane upon yielding. Also worth mentioning is that, as the plastic zone boundary is approached, $\sigma_{\theta\theta}$ becomes slightly tensile (rather than compressive) and then progressively decreases again with further increase in distance. Remarkably, the peak value of this tensile strength is reduced in the Mohr-Coulomb simulations (i.e., when a pressure-sensitivity index is incorporated), as predicted by Narasimhan (249).

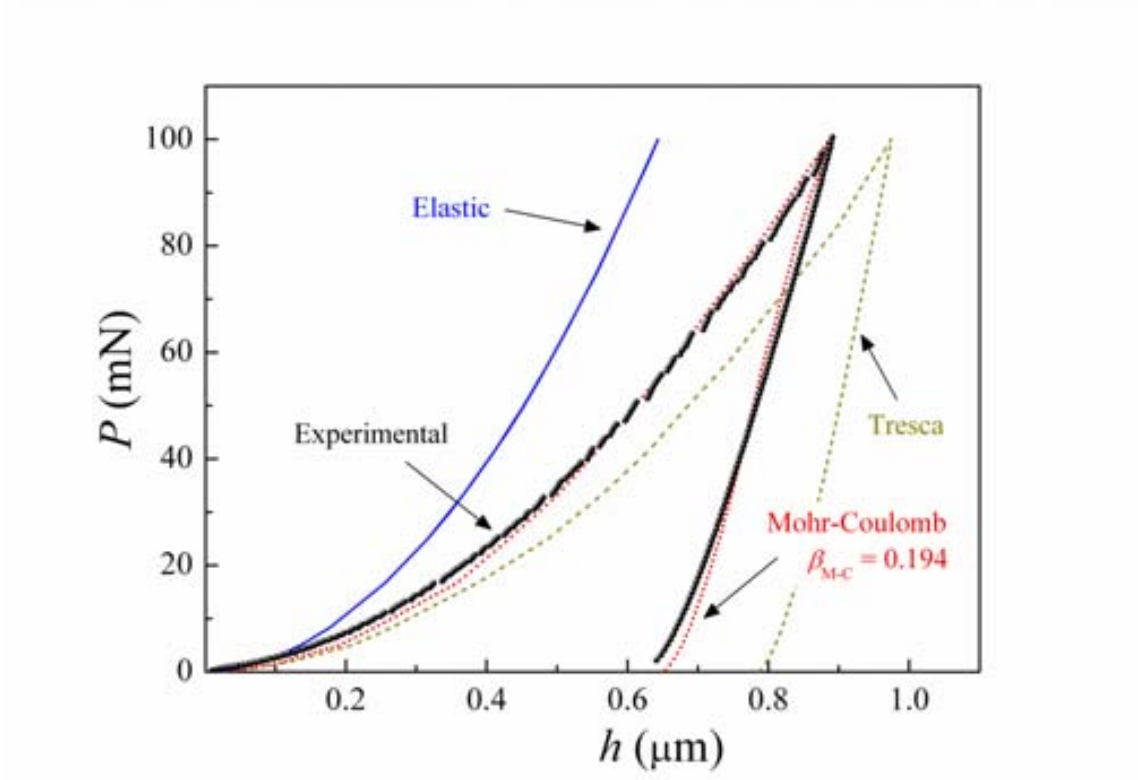

Figure 3.31: Experimental and computed load-unload nanoindentation curves of the Ti-based amorphous alloy measured to a maximum load of 100 mN. Thee different numerically simulated P-h curves are shown, using the elastic (Hertz) model, an elastoplastic deformation model based on the conventional Tresca yield criterion and an elastoplastic model based on the Mohr-Coulomb yield criterion.

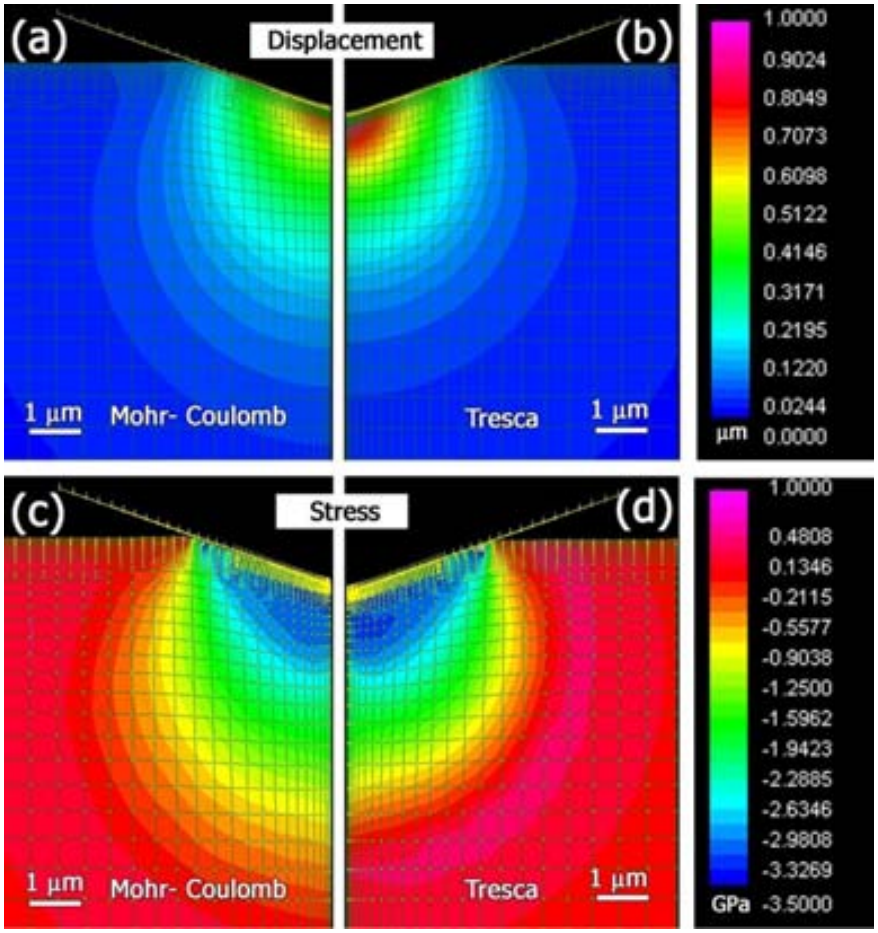

Figure 3.32: (a) Displacement contour underneath the indenter (with respect to the initial position of the region of material that gets first in contact with the indenter), plotted in the r-z plane, corresponding to P_{max} = 100 mN obtained via finite element simulations using the elasto-plastic Mohr-Coulomb yield criterion; (b) displacement contour beneath the indenter obtained using the conventional Tresca yield criterion. (c) Circumferential stress ($\sigma_{(\theta\theta)}$) contour in the r-z plane developed beneath the indenter for P_{max} = 100 mN, obtained using the Mohr-Coulomb yield criterion; (d) circumferential stress contour analogous to (c) but using the Tresca yield criterion (with $\beta_{M\text{-}C}$ = 0.194); Note that the overall mesh distribution (nodes and plates) and also the rigid indenter are displayed in the images.

3.3.1.3. Summary

The mechanical properties of an amorphous $Ti_{40}Zr_{25}Ni_8Cu_9Be_{18}$ alloy have been systematically investigated by means of two complementary techniques: macroscopic compression tests and depth-sensing nanoindentation. This study contributes to shed light on some of the fundamental issues regarding yielding and plastic deformation of metallic glasses and reveals that deformation modifies the glassy structure of the glass,

in particular by increasing the amount of free volume. The main results from our work can be summarized as follows:

1. The relatively high compressive yield stress and reasonable plasticity of the investigated alloy correlate well with the rather low ratio between the shear and bulk elastic moduli.

2. As a result of the significant plasticity, the fracture surface exhibits vein-like pattern morphology. From the relatively large size of the dimples it can be suggested that premature fracture may be circumvented in specimens with sizes smaller than 5-10 μm. Hence, this alloy may have potential applications in sub-10 μm micro- / nano-electro-mechanical systems (MEMS/NEMS).

3. Yielding is influenced by normal stresses acting on the shear plane. This causes the fracture angle to deviate towards values smaller than 45º. Consequently, the pressure-insensitive von Mises or Tresca yield criteria are found to be inadequate to describe the onset of plasticity. Alternatively, other criteria, which take normal stresses and pressure effects into account (e.g.. the Mohr-Coulomb or Druker-Prager), are invoked to properly describe the mechanical behaviour of the glass.

4. Finite element simulations of nanoindentation curves reveal that the extent of the plastic zone underneath the indenter is larger when the Mohr-Coulomb criterion is used instead of the pressure-independent Tresca criterion.

5. Plastic flow in this alloy is inhomogeneous, as it corresponds to the range of strain rates employed in this study. Moreover, shear band activity is accompanied by a local mechanical softening, which brings about sudden load drops in the compression tests and pop-in events in the indentation loading curves.

6. An overall mechanical softening is observed during the course of the nanoindentation experiments, which causes a progressive reduction of hardness as deformation proceeds, i.e., an indentation size effect. This indentation size effect is modeled, in a semi-quantitative manner, using the free volume concept. An average increase of free volume of around 10 % is estimated within the indentation plastic zone in experiments performed using the continuous stiffness method.

3.3.2.Characterization of $Zr_{62}Cu_{18}Ni_{10}Al_{10}$ metallic glass subjected to indentation and compression tests.

As explained in the previous sections, BMG usually fracture in a brittle manner with plastic strains < 2%. However, in some cases values of more than 80% of plastic deformation have been achieved. A high plastic strain has been reported, for example, in Pd-based BMG (62) where the authors attributed this result to a nanoscale phase separation which hinders the propagation of shear bands facilitating their uniform initiation and branching. An improvement of plasticity has also been reported in a Zr-based BMG annealed below T_g (57). This improvement is caused by its tendency towards chemical decomposition, i.e. phase separation that leads to the development of nanoscale compositional inhomogeneities (Cu clusters). Similar results have been found in other Zr-based BMG without evidence for the presence of nanocrystals or phase separation (250). In this case, superplasticity was ascribed to intrinsic material properties. Indeed, it is claimed that plasticity in BMG can be enhanced with an appropriate choice of composition using Poisson's ratio strategies; i.e., a larger Poisson's ratio (v) promotes a larger toughness (121). In some cases the ductility of BMG (Zr- and Cu- based) has been increased by nanocrystallization caused by deformation (63; 251; 252). An exceedingly high degree of crystallization leads to embrittlement of the alloy but in the case when the crystallites are only of nanometer size, the resulting amorphous-nanocrystalline composite exhibits more plasticity than the original material (53). All these BMG systems exhibiting large plasticity deform via formation of numerous shear bands throughout the compressed specimen. The local structural inhomogeneities favor multiple branching of these bands, which interact with each other. As a result, catastrophic failure caused by rapid propagation of a single shear band is avoided. Hence, a high-density of shear bands, often with a wavy trajectory (due to the local inhomogeneities that hinder their immediate and straight propagation) is expected in these systems.

The present work is focused on the study of the unusual mechanical behavior of a Zr-based BMG. This alloy exhibits superplasticity during compression tests (deformation strains up to 120% before fracture). In addition, strain hardening is observed during nanoindentation at low applied forces, whereas mechanical softening occurs when the applied maximum load is larger than 100 mN. Superplasticity and strain hardening are

likely to be related to deformation-induced nanocrystallization which is investigated in detail by transmission electron microscopy.

3.3.2.1. Thermal Characterization

The glass transition temperature (T_g), the crystallization temperature (T_x) and the supercooled liquid region (ΔT) were determined from the DSC curve (Figure 3.33) and the obtained values were T_g = 670 K, T_x = 768 K and ΔT = 98 K, in agreement with the literature (250). There is a tendency for the glass forming ability (GFA) to augment with increasing ΔT (253); therefore, it is important to search for glassy alloys with high ΔT values, like the Zr-based one investigated here.

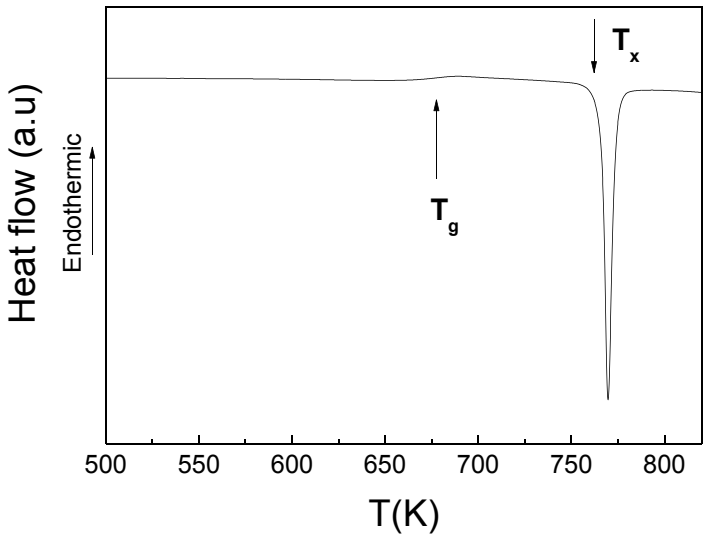

Figure 3.33: DSC curve of the Zr-based alloy where T_g and T_x are indicated.

3.3.2.2. Correlation Structural and Mechanical Properties

Figure 3.34 shows the peculiar true stress-strain curve obtained under uniaxial compression test of the $Zr_{62}Cu_{18}Ni_{10}Al_{10}$ alloy. Remarkably, the sample was compressed without fracture up to 120% strain deformation. The compression curve shows a temporary load drop until 15% true strain followed by continuous hardening until 45% deformation and subsequent softening. The final part of the curve appears to exhibit a strong work hardening. Inset (b) of Figure 3.34 shows the serrated flow

behavior typically found in metallic glasses implying that abundant shear bands are activated during plastic flow. An example of such shear bands is shown in inset (a) of Figure 3.34. Note that shear bands form along various directions, sometimes bifurcating and crossing each other. Furthermore, some shear bands exhibit wavy trajectories. This indicates that during their propagation, these bands encounter harder regions and are forced to deviate. This avoids premature fracture of the specimen due to the rapid propagation of a single shear band.

From the compression tests, the yield stress, σ_y, and Young's modulus, E, were determined: σ_y = 1.55 GPa and E = 86 GPa (note that a similar Young's modulus was also obtained from acoustic measurements). It is noteworthy that previous works have reported similar apparent softening/hardening-like behavior during compression tests in some Zr-based metallic glasses (250; 254; 255). From all these studies it is clear that the "unexpected work hardening" found in the latest stages of deformation is not real and has to be attributed to an artifact caused by the increase of friction between the sample and the tungsten carbide plates (256) due to the reduction of the length/width aspect ratio of the specimen. It should be noted that the final cross-sectional area of the compressed specimen is much larger than the initial one (but the two surfaces of the disk-shaped specimen remain parallel to each other after compression (inset (c) in Figure 3.34)). Hence, due to this friction effect, any clear conclusion about an overall softening or hardening eventually induced by compression is essentially precluded and, therefore, other complementary techniques (e.g., nanoindentation) need to be used to investigate this issue.

In turn, the great plasticity observed in this material may be ascribed to deformation-induced nanocrystallization or be due to intrinsic material properties such as a large Poisson's ratio (ν= 0.3786). Actually, in Cu-Zr based BMG, chemical heterogeneities and Cu-rich nanocrystals are considered to be the cause of the large plasticity (63; 257). However, Liu et al. (250) claim that the superplasticity of a Zr-based BMG, very similar to ours, is not a result of the stress-induced nanocrystallization but, instead, is an intrinsic property of the material.

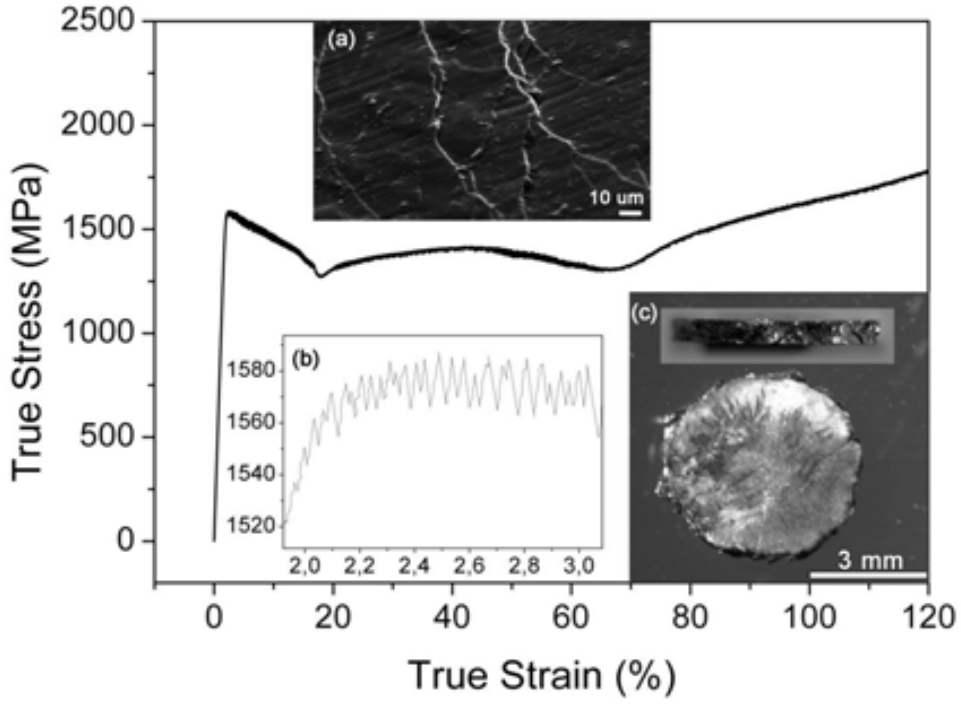

Figure 3.34: The true strain–stress curve obtained from the uniaxial compression test of the as-cast $Zr_{62}Cu_{18}Ni_{10}Al_{10}$. Inset (a) is a scanning electron microscopy image showing the shear bands formed at the outer lateral surface of a compressed specimen. Inset (b) shows a magnified view of the serrated flow region of the compression test. Inset (c) shows optical microscopy images of the compressed specimen (cross sectional and lateral views).

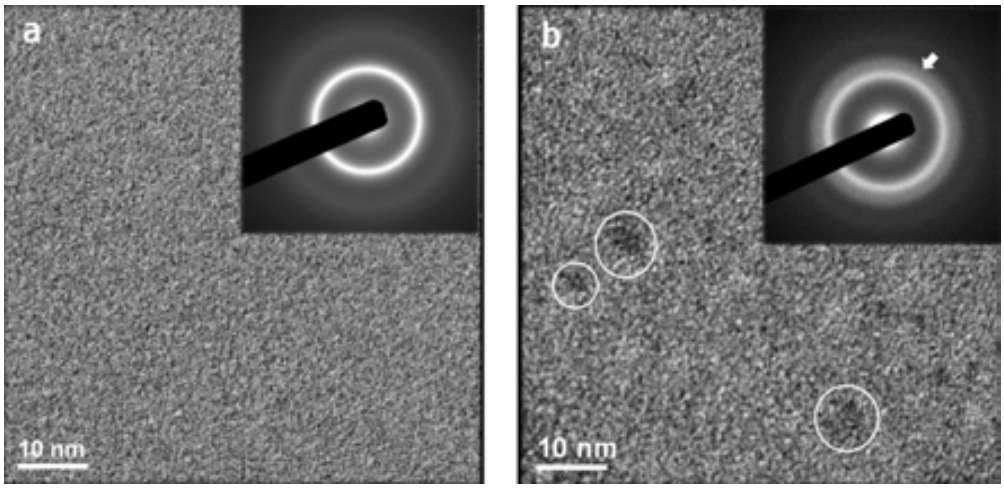

Figure 3.35: Microstructural features in the as-cast (a) and compressed sample (b), observed by TEM, revealing the amorphous nature of the as-cast sample and the appearance of some nanocrystallites (marked by circles) when the sample is compressed. The corresponding SAED patterns are shown in the insets.

To shed light on this issue, TEM imaging was performed on the as-cast and compressed spcimens. Figure 3.35a shows that, as expected, the as-cast BMG does not contain nanocrystals. The fully amorphous structure of this specimen is confirmed by the lack of lattice fringes in the high resolution TEM image and by the selected area electron diffraction (SAED) pattern (inset Figure 3.35a), where only the amorphous halos were detected. However, the TEM image of the compressed specimen (Figure 3.35b) shows the presence of some nanocrystallites with less than 10 nm in size embedded in the amorphous matrix. The second ring in the SAED pattern, marked with an arrow (inset Figure 3.35b), indicates the formation of a crystalline phase that may be the tetragonal Zr_2Ni (space group I4/mcm, a= 0.649 nm and c= 0.527 nm). Therefore, our results indicate that deformation promotes nanocrystallization. It should be noted that Deng et al. (258) also presented a direct high resolution TEM observation of nanocrystallization in a Zr-Al-Ni-Cu BMG fractured by compression test. They suggested that, due to the concentration of plastic flow, the local atomic neighbor distance increases producing nanocrystallization in the amorphous structure. Other authors have obtained evidence for nanocrystallization in shear bands (56; 259). The temperature increase associated with deformation is claimed to play a role on the formation of nanocrystals.

In order to better understand the deformation behavior in this metallic glass, nanoindentation tests were performed at different maximum loads (P_{max}) both in the as-cast and the compressed specimen. Generally, in bulk metallic glasses, hardness is expected to decrease when the indentation depth increases. As early stated in this Thesis, this effect is usually referred to as the indentation size effect and is attributed to the softening caused by deformation-induced creation of free volume. In the present study (Figure 3.36), the hardness of the as-cast alloy is found to decrease for P_{max} larger than 100 mN. However, it is interesting to remark that an increase of hardness is observed when indentations were performed at lower loads (Figure 3.36a).

To elucidate the physical origin of this mechanical hardening, TEM specimens from the as-cast alloy, containing an array of nanoindents, were prepared. Figure 3.37a is a SEM image showing a hole (created during ion milling of the TEM sample preparation) surrounded by an array of P_{max} = 100mN indentations separated by 20 μm from each other. The inset of Figure 3.37a is a small hole corresponding to one of the indents.

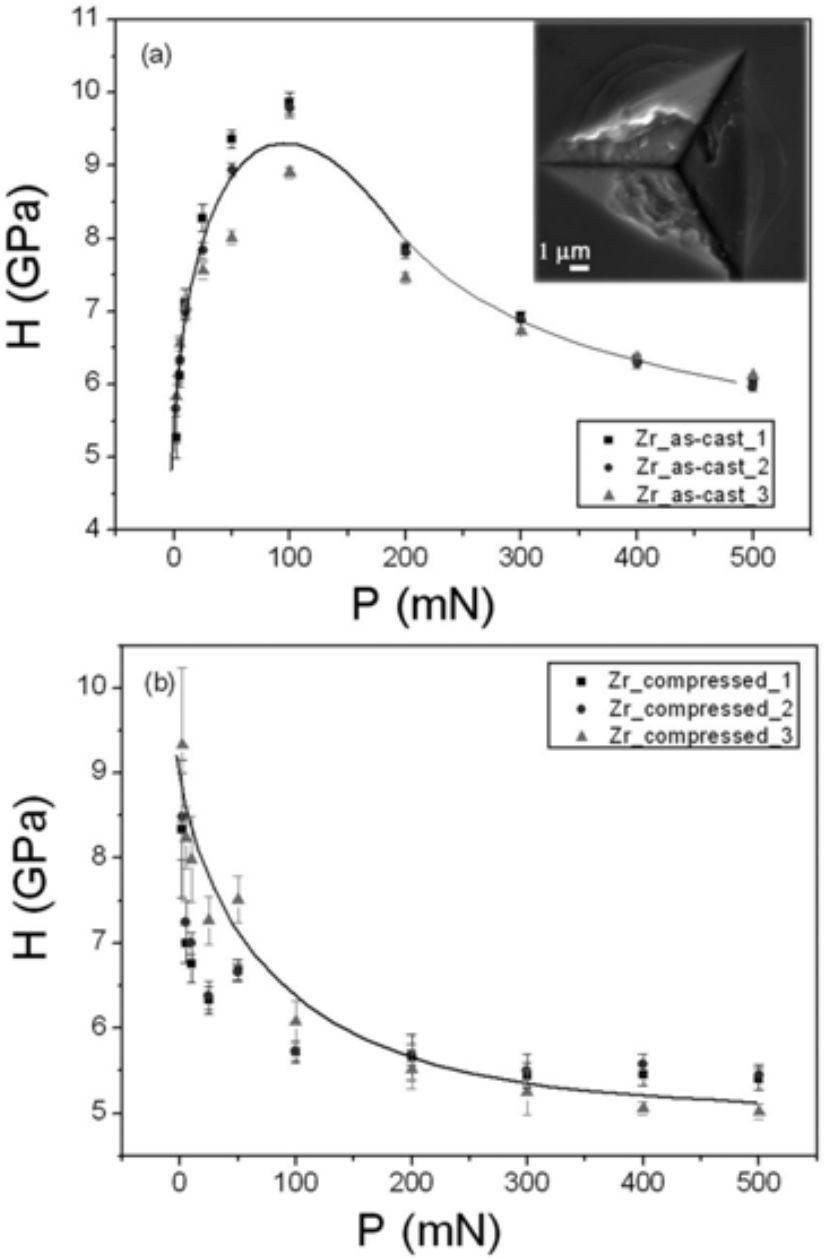

Figure 3.36: Dependence of hardness on the nanoindentation maximum load for (a) several pieces of the as-cast sample and (b) several pieces of the compressed specimen. The inset in (a) is a scanning electron microscopy image of an indentation performed on the as-cast specimen using a maximum load of 500 mN.

Figure 3.37b, which is a zoom of the square indicated in the inset of Figure 3.37a, reveals the existence of nanocrystals with an average size below 7 nm near the indent. The corresponding SAED pattern confirms the presence of a crystalline phase. The same preparation procedure was used to observe nanoindents performed at a maximum load of 10 mN. In this case, the observed nanoindent (inset Figure 3.37c), which was not perforated during the thinning process, again contained several nanocrystals.

Nanocrystallization is also evidenced in Figure 3.37d which is a dark-field TEM image from the diffraction spot highlighted in the inset, corresponding to an interplanar distance of d = 0.204± 0.01 nm. The deformation-induced nanocrystals seem to be Zr_2Ni, the same phase as in the sample subjected to compression test. Our results are in agreement with some other recent reports from the literature where nanocrystallization was related to work hardening phenomena in metallic glasses during nanoindetation (56; 259). Jiang et al. (259) observed that the obtained phases coincide with those of samples (with the same composition) subjected to ball milling (260) and bending (53). Remarkably, as evidenced by TEM imaging, the nanocrystallization of the alloy investigated in this work already occurs during the first stages of deformation (Figure 3.37c). At low indentation depths, the induced hardening counterbalances the softening effect typically found in metallic glasses. However, when the maximum applied load is larger than 100 mN the softening predominates over hardening probably due to deformation-induced increase of free volume, which is more pronounced for higher loading rates (220). Also note that shear band activity is observed inside and around the indented regions by SEM (see inset in Figure 3.36a).

Finally, indentations using the same conditions were also carried out in the compressed specimen and the resulting hardness was evaluated as a function of the applied load. The compressed specimen was indented in its central part. As shown in Figure 3.36b, no hardening is observed in this case; only the expected softening behaviour is found. However, note that when the maximum applied load is 2 mN the hardness in the compressed specimen is already 62% larger than in the as-cast. In agreement with the literature (53; 261; 262), this hardness enhancement is attributed to the existence of some nanocrystals embedded in the amorphous matrix formed during the compression test, as shown in Figure 3.35b.

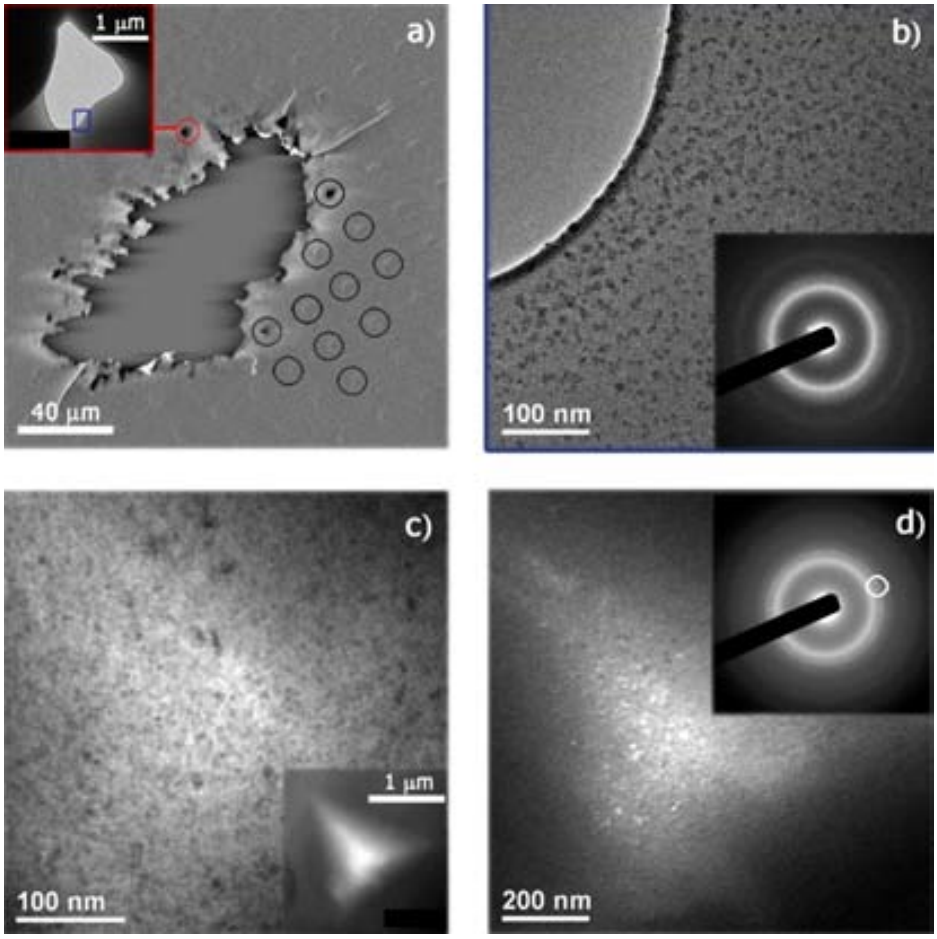

Figure 3.37: Microstructural features in the samples indented at a maximum force of 100 mN [panels a) and b)] and at 10mN [panels (c) and d)]. Shown in a) is the SEM image displaying an array of indentations (indicated by circles) prepared for subsequent TEM observation. The inset is a TEM bright-field image of an indentation which was perforated during ion milling. Shown in b) is a zoom corresponding to the square drawn in the inset in a), indicating the presence of nanosized crystals embedded in an amorphous matrix. The corresponding SAED pattern confirms the presence of the crystalline phase. Panel c) shows a zoom of a 10mN indentation (displayed in the bottom right corner) revealing the presence of a high amount of nanocrystals inside the indent. Panel d) is a TEM dark field image obtained on the diffraction ring marked on the inset SAED pattern confirming the existence of nanocrystallites in the amorphous matrix.

3.3.2.3. Summary

$Zr_{62}Cu_{18}Ni_{10}Al_{10}$ metallic glass alloy was compressed without fracture up to 120% true strain deformation. Images of the compressed specimen, obtained by TEM, confirmed the formation of some nanocrystals during compression tests which could be responsible for the observed superplasticity.

Nanoindentation measurements were also performed at different maximum loads with the aim of understanding the deformation behavior of this metallic glass. In the as-cast alloy, hardness was found to increase until P_{max}= 100 mN and decreased for higher loads. By means of TEM the formation of nanocrystals inside and around the indents was observed, which presumably explains the hardening phenomenon. In the compressed specimens, nanoindentation at low applied loads also reveals a strengthening behavior, which is likely to be related to deformation induced nanocrystallization occurred during compression tests.

3.3.3. Influence of the deformation-induced martensitic transformations on the mechanical properties of nanocomposite Cu-Zr-(Al) systems

Hardness in nanocrystalline materials is enhanced when the size of the crystals is decreased, since this favors accumulation of dislocations at grain boundaries, leading to the so-called Hall-Petch relationship (47). In addition to crystallite size refinement, some phase transformations can also contribute to increase hardness. For example, the deformation-induced martensitic transformation in austenitic stainless steel or NiTi alloys has established itself as one of the traditional strengthening methods in these materials (47). Besides the intrinsically harder nature of the martensitic phase, as compared to austenite, the microstructural changes accompanying this transformation (i.e., the formation of mechanical twins and concomitant stacking faults) not only increase the hardness but also contribute to the overall plasticity of these systems (263).

In recent years, the binary Cu-Zr system has triggered a great interest due to its tunable microstructure and reasonable plasticity during compression (63; 264). The glass forming ability in Cu-Zr has been found to be enhanced with the addition of some ternary elements like Al, Y or Ti (265; 266; 267). Moreover, apart from generating glassy structures, Cu-Zr can also solidify in the form of glass-matrix and martensitic composites, which show different mechanical properties compared with common Cu-Zr BMG. In fact, the microstructure and phase distribution in these materials not only depends on the composition but also on the preparation conditions (e.g. casting temperature or cooling rate) (268). In addition to their reasonably good mechanical

properties, Cu-based alloys are relatively low-cost, thus being attractive for engineering applications.

In this section, we perform a detailed investigation of the microstructure and mechanical properties of suction-cast $Cu_{50}Zr_{50}$ and $Cu_{46.5}Zr_{48.5}Al_5$ alloys. Despite their similar composition and identical preparation conditions, these materials exhibit very different microstructure. Namely, while $Cu_{50}Zr_{50}$ is composed of nanostructured martensitic phases, $Cu_{46.5}Zr_{48.5}Al_5$ consists of micrometer-sized dendrites (mainly of austenitic phase) embedded in an amorphous matrix. Particular emphasis is given in this work to the martensitic phase transformations that occur in these alloys during plastic deformation, which in turn are found to play a significant role on the measured mechanical properties.

3.3.3.1. Thermal Characterization

The DSC measurements (Figure 3.38) show that the $Cu_{46.5}Zr_{48.5}Al_5$ alloy exhibits an obvious glass transition T_g (see inset for details) followed by one exothermic reaction corresponding to the crystallization temperature (T_x).

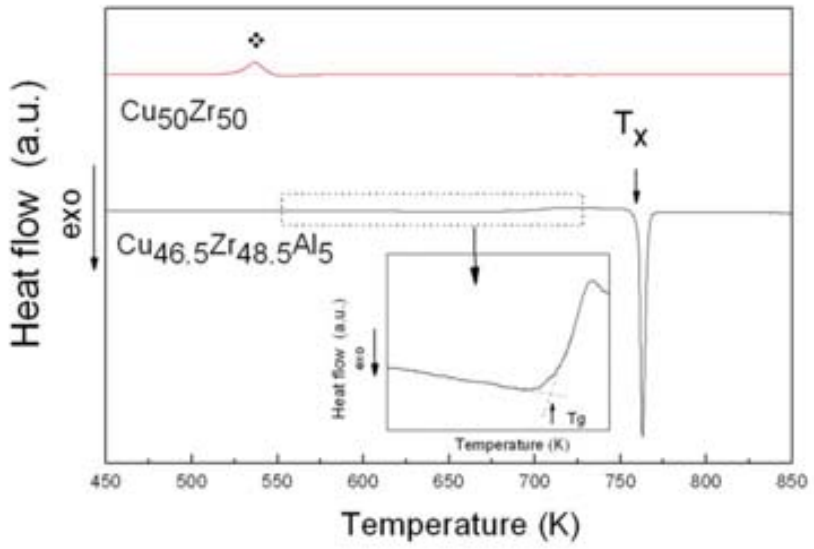

Figure 3.38: DSC curves for the $Cu_{50}Zr_{50}$ and the $Cu_{46.5}Zr_{48.5}Al_5$ alloys. The $Cu_{50}Zr_{50}$ curve shows an endothermic event (❖) which corresponds to a thermally-induced martensitic-to-austenite transformation. The inset is an enlargement of the central part of the DSC curve of the $Cu_{46.5}Zr_{48.5}Al_5$ alloy. Note that the glass transition and crystallization temperatures $Cu_{46.5}Zr_{48.5}Al_5$ alloy (T_g and T_x, respectively) are also indicated in the figure.

3.3.3.2. Structural Characterization

Figure 3.39 shows the XRD patterns of the as-cast and compressed $Cu_{46.5}Zr_{48.5}Al_5$ and $Cu_{50}Zr_{50}$ specimens. In the case of the as-cast $Cu_{46.5}Zr_{48.5}Al_5$ alloy, some Bragg reflections corresponding to the B2 CuZr austenite structure (Pm3m space group) and few traces of the CuZr martensite phases embedded in two broad halos, characteristic of the amorphous structure, are identified. The XRD pattern of the as-cast $Cu_{50}Zr_{50}$ (Al free) alloy indicates the presence of two martensitic phases and some traces of the retained B2 CuZr austenitic phase. No clear amorphous halos are observed. The two martensites have monoclinic symmetry and correspond to the basic structure ($P2_1/m$ space group) and the superstructure (Cm space group), respectively. The lattice parameters and atomic positions used to identify the martensitic phases agree with the ones suggested by Schryvers et al. (270). It should be noted that the occurrence of these martensitic phases has to be ascribed to the fast cooling rates achieved during the casting conditions. Otherwise, for sufficiently slow cooling rates, the high-temperature CuZr austenite phase would transform into $Cu_{10}Zr_7$ (orthorhombic structure) and $CuZr_2$ (tetragonal structure) which, according to the phase diagram, are the stable equilibrium phases at room temperature for this system (269).

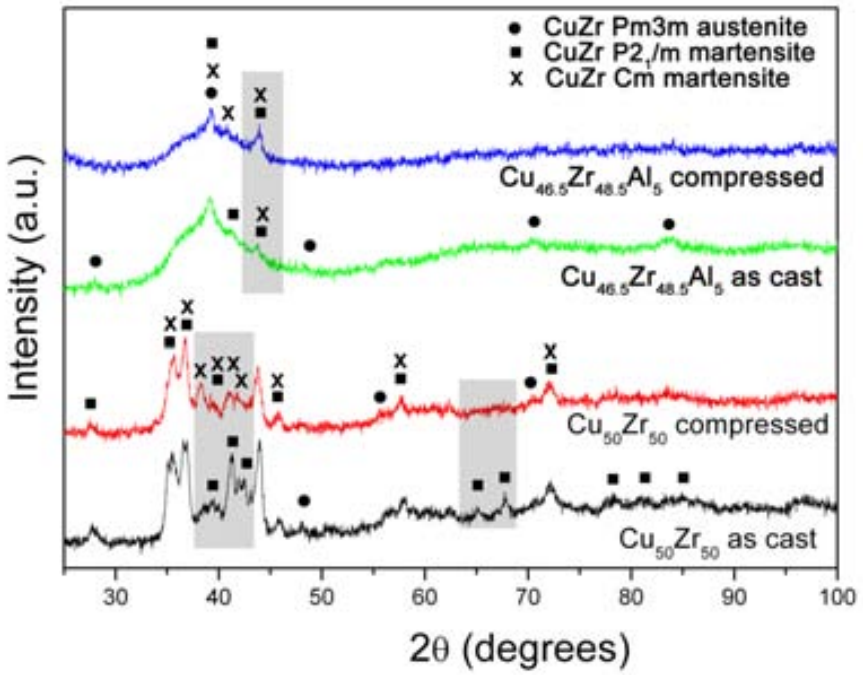

Figure 3.39: XRD patterns of the as-cast and compressed $Cu_{46.5}Zr_{48.5}Al_5$ and $Cu_{50}Zr_{50}$ alloys. Shadowed regions indicate the 2θ ranges where most prominent changes in the XRD patterns between the as-cast and compressed specimens are observed.

In order to elucidate whether structural changes occur in these alloys when being subjected to plastic deformation, XRD patterns of the deformed samples (compressed until fracture) are also presented in Figure 3.39. The diffraction peaks corresponding to the martensitic phase in the $Cu_{46.5}Zr_{48.5}Al_5$ specimen increase in intensity after compression, whereas those of the austenite tend to disappear, indicating that deformation induces a martensitic phase transformation in this alloy. This was actually observed also by Pauly et al., (264) who used in-situ high-energy X-ray synchrotron diffraction to monitor the structural changes occurring during deformation of a $Cu_{47.5}Zr_{47.5}Al_5$ sample.

Some clear differences are also observed by XRD between the as-cast and compressed $Cu_{50}Zr_{50}$ alloy. While the XRD pattern of the as-cast sample indicates the presence of monoclinic CuZr $P2_1/m$ and CuZr Cm martensites (together with some traces of cubic CuZr Pm3m austenite phase), the amount of monoclinic CuZr $P2_1/m$ phase decreases after deforming the alloy until fracture. Note that, for example, the two diffraction peaks located between 65º and 70º, corresponding to the CuZr $P2_1/m$ phase, even disappear completely after compression, while the monoclinic superstructure CuZr Cm reflections (e. g., the peak located at 38º) become more visible and intense. It should be noted that high strain levels seem to promote this martensitic superstructure transformation, as has been reported by other authors (271).

Figure 3.40 shows the OM images taken from the cross-section of the as-cast $Cu_{46.5}Zr_{48.5}Al_5$ (panel (a)) and $Cu_{50}Zr_{50}$ (panel (b)) alloys. Although the two specimens are only slightly different in composition and were prepared using exactly the same experimental procedure, their microstructures are found to be distinctly different. On one side, the microstructure of the $Cu_{46.5}Zr_{48.5}Al_5$ alloy consists of dispersed micrometer-sized dendrites embedded in the glassy matrix; the compositions of the different phases were evaluated by EDX and no perceptible differences were found between the crystalline and glassy counterparts. On the other side, the $Cu_{50}Zr_{50}$ alloy is composed of multiple thin strips (100 nm in width and several μm in length –see TEM image in the inset). This microstructure originates from the large density of twin boundaries typically encountered in martensite phases.

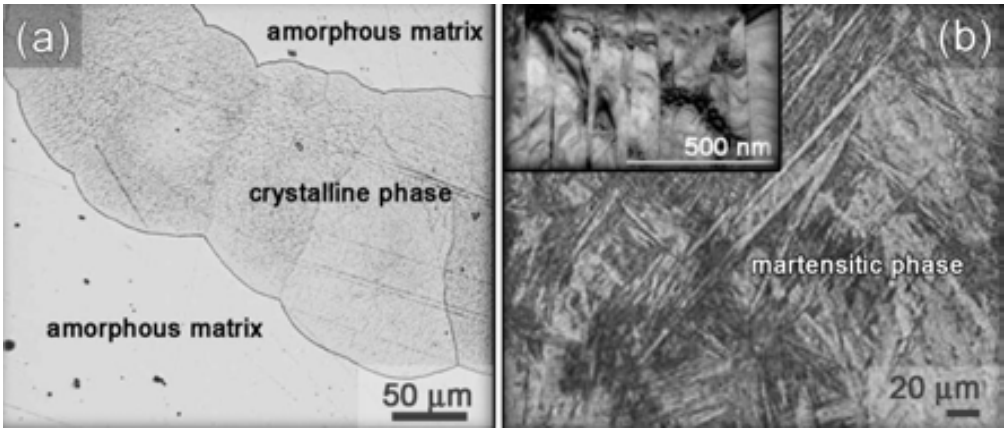

Figure 3.40: Optical micrographs of: a) $Cu_{46.5}Zr_{48.5}Al_5$ alloy and b) $Cu_{50}Zr_{50}$ alloy. The inset in (b) is a TEM image showing the CuZr martensitic plates.

3.3.3.3. Mechanical Characterization

The compression test curves of the $Cu_{50}Zr_{50}$ and $Cu_{46.5}Zr_{48.5}Al_5$ alloys are presented in Figure 3.41. These tests show a drastic difference in the mechanical behavior of both samples, even if their composition is similar. The $Cu_{46.5}Zr_{48.5}Al_5$ exhibits a certain degree of plastic deformation (up to 11% total strain), higher than for many metallic glasses. The yield stress, Young's modulus and fracture strength are 1598 MPa, 77 GPa and 1900 MPa, respectively. The plastic deformation is accompanied with work hardening and clear serrations are observed in the final stages of the compression curve. Such serrations are associated with the formation of shear bands, which are indicative of the occurrence of inhomogeneous plastic flow in the amorphous matrix. Some of these shear bands are observed at the outer surface of the compressed specimen (see inset in Figure 3.41). Deformation in this composite material is likely to be controlled by a synergetic effect arising from (i) the interaction between shear bands and the micrometer-sized CuZr B2 dendrites and (ii) the martensitic transformation occurring within the dendrites during deformation, as evidenced by XRD. Both effects have been actually claimed to enhance the plasticity and hardness of this type of material (272; 273; 274).

At first glance, the stress-strain curve of $Cu_{50}Zr_{50}$ exhibits a strange behavior, with lack of clear yielding, which can be attributed to work hardening behavior already from the first stages of deformation. Similar strain-stress curves have been reported in the literature in several martensitic alloys, including CuZr (275; 276; 277) and their peculiar

shape has been ascribed to a variety of factors, such as stress-induced detwinning or dislocations rearrangements at the twin boundaries (271). In fact, as shown in inset a) of Figure 3.41 several deformation bands, interacting with the martensitic phase, form at the outer surface of the $Cu_{50}Zr_{50}$ compressed specimen. This deformation mode allows $Cu_{50}Zr_{50}$ to deform up to almost 12% total strain with a fracture stress of 1700 GPa. Nevertheless, the lack of a clear yielding precludes the determination of Young's modulus from the compression tests. In fact, the Young's modulus of martensitic phases is quite often underestimated in the literature when evaluated from compression tests (271; 277).For this reason, the elastic constants of both $Cu_{46.5}Zr_{46.5}Al_5$ and $Cu_{50}Zr_{50}$ have been determined with accuracy using acoustic measurements. The Young's modulus has also been evaluated by nanoindentation in both samples (listed in Table 3.10). Good agreement between the *E* values obtained by nanoindentation and acoustic measurements is observed. Nevertheless, the *E* value obtained for the $Cu_{50}Zr_{50}$ alloy is lower than the one for the $Cu_{46.5}Zr_{48.5}Al_5$ alloy. This is in agreement with what is qualitatively seen from compression tests (Figure 3.41). This suggests that, also in this case, the indentation stress can cause certain detwinning or dislocations rearrangements in the $Cu_{50}Zr_{50}$ alloy (but in less extent than during compression tests) resulting in a reduction of *E*.

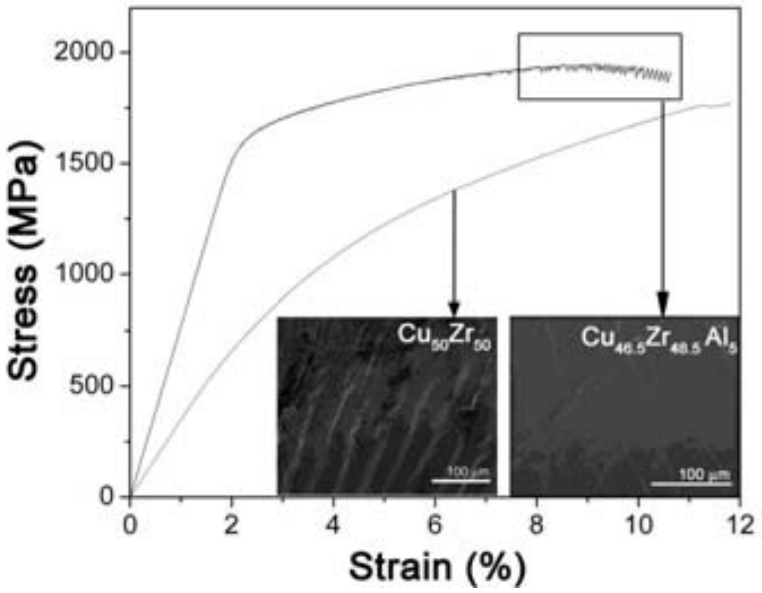

Figure 3.41: stress-strain curves of $Cu_{46.5}Zr_{48.5}Al_5$ and $Cu_{50}Zr_{50}$ alloys. Indicated with a box is the serrated plastic flow occurring in $Cu_{46.5}Zr_{48.5}Al_5$ at the final stages of compression. images of the outer surfaces of the compressed $Cu_{46.5}Zr_{48.5}Al_5$ and $Cu_{50}Zr_{50}$ samples. a) SEM image of the outer surface of the compressed $Cu_{50}Zr_{50}$ sample. b) SEM image of the outer surface of the compressed $Cu_{46.5}Zr_{48.5}Al_5$ sample.

As listed in Table 3.10 the Young's, shear and bulk moduli, and also the Poisson's ratio, are nearly the same for both samples. Usually, the Young's modulus of the BMG is lower than in their crystalline counterparts (106). This is due to the larger average interatomic spacing exhibited by BMG resulting from the existence of free volume. This phenomenon is often referred to as elastic softening (129). The Cu-Zr system seems to be an exception of this trend, as has been noted by other authors (269). It is worth mentioning that for the $Cu_{46.5}Zr_{48.5}Al_5$ sample, a good agreement is observed between the Young's modulus obtained by compression test and acoustic measurements, although the acoustic measurements are generally assumed to be more precise. Also note that the large Poisson's ratio of the nanocomposite $Cu_{46.5}Zr_{48.5}Al_5$ probably contributes to the large observed plasticity in this alloy, as it is the case in other BMG with large ν (121).

Alloy composition	***v***	***G***	***K***	***E*** **Acoustic measurements**	***E*** **Compression test**	***E*** **Nanoindentation**
$Cu_{46.5}Zr_{48.5}Al_5$	0.374	31.1	112.7	85.4	77	74.5
$Cu_{50}Zr_{50}$	0.384	31.0	123.2	85.7	-	67.2

Table 3.10: Summary of the elastic properties, determined from acoustic measurements, of the $Cu_{46.5}Zr_{48.5}Al_5$ and $Cu_{50}Zr_{50}$ as-cast systems. The Young's modulus calculated from compression test of the $Cu_{46.5}Zr_{46.5}Al_5$ alloy and the values of E calculated from nanoindentation are also given for comparison.

Since the crystalline CuZr B2 phase is clearly distinguishable from the amorphous matrix, depth sensing nanoindentation technique was used to assess the mechanical behavior of both the austenite and the amorphous matrix constituting the as-cast $Cu_{46.5}Zr_{48.5}Al_5$ alloy. The results were compared with those of the martensitic structure of the $Cu_{50}Zr_{50}$ alloy and the martensite formed in $Cu_{46.5}Zr_{48.5}Al_5$ after compression. Representative indentation curves from the different phases indented at P_{max} = 5 mN are presented in Figure 3.42. The loading segment of the amorphous matrix in the $Cu_{46.5}Zr_{48.5}Al_5$ shows serrated flow, as it has been reported in various families of metallic glasses. These pop-in events result from the propagation of discrete shear bands during inhomogeneous plastic flow (analogously to what is observed during compression experiments – inset in Figure 3.41). The SEM image of an indentation

performed on the amorphous matrix (Figure 3.42c) confirms the formation of these shear bands. In contrast, no pop-ins are observed in the loading segments of the crystalline phases, neither shear bands are found in the corresponding SEM images (Figure 3.42b and d).

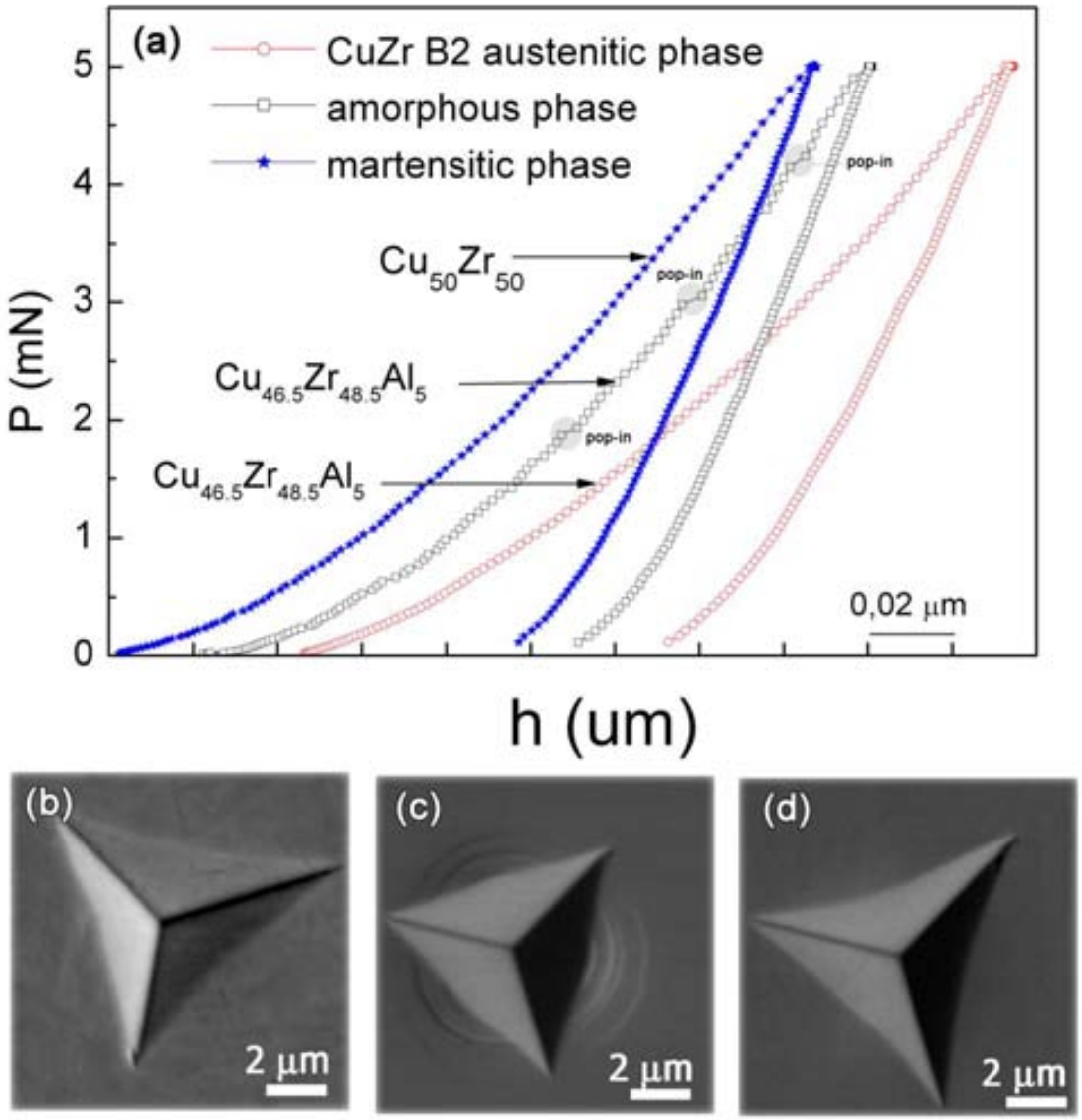

Figure 3.42: (a) Load (P)-displacement (h) indentation curves at P_{max} = 5 mN for the $Cu_{50}Zr_{50}$ alloy (martensitic phase) and the $Cu_{46.5}Zr_{48.5}Al_5$ (amorphous matrix and austenitic phase). Note that for sake of clarity, the nanoindentation curves have been shifted in h. Panels (b), (c) and (d) are SEM images of the indents performed at P_{max} = 500 mN for the martensitic phase, amorphous matrix and austenite phase, respectively.

From the nanoindentation experiments, large hardness values (between 8 and 10 GPa) are obtained at low loads for all the constituent structures of the Cu-Zr-(Al) specimens

(see Figure 3.43a). The large hardness in the austenite and martensite phases is probably related to their nanocrystalline nature. Moreover, the large amount of twin boundaries in the martensite phase can also contribute to the hardness. Indeed, twin boundaries can act in an analogous manner as high-angle grain boundaries in terms of disrupting dislocation motion and have been shown to be particularly effective in impeding the propagation of single dislocations, thus enhancing the material strength (278).

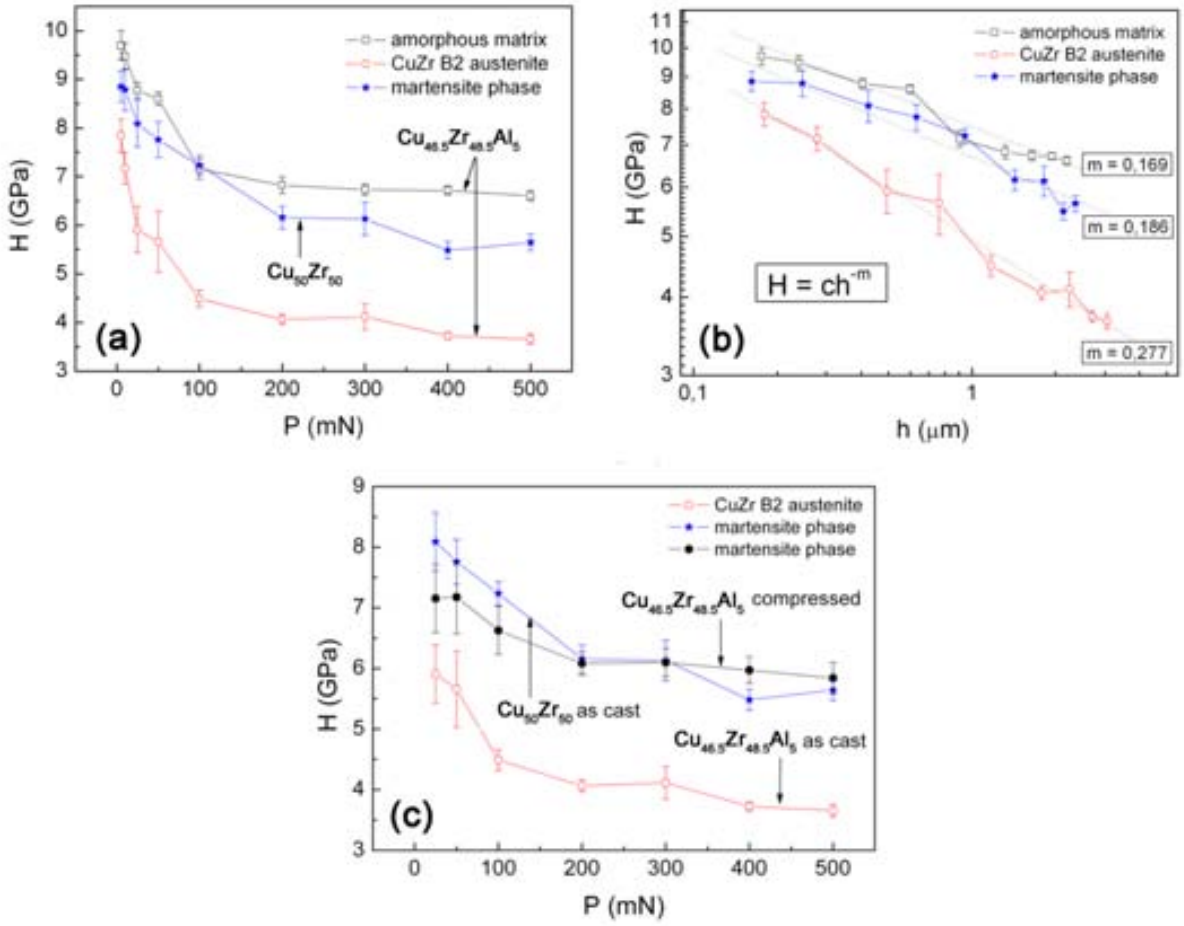

Figure 3.43: a) Dependence of hardness, H, on the maximum applied load, P_{max}, estimated from indentations measurements performed in the $Cu_{50}Zr_{50}$ alloys (martensitic phase) and in the $Cu_{46.5}Zr_{48.5}Al_5$ (amorphous matrix and austenitic phase) at maximum applied loads ranging from 5 mN to 500 mN; b) log (H) - log (h) plot, showing a linear fit of the experimental data, from which the indentation size effect exponent, m, can be evaluated; c) dependence of H on P_{max} for the austenite phase in the as-cast $Cu_{46.5}Zr_{48.5}Al_5$ specimens, the martensite phase in a compressed $Cu_{46.5}Zr_{48.5}Al_5$ rod and the martensite phase in as-cast $Cu_{50}Zr_{50}$.

The hardness as a function of the maximum applied load (Figure 3.43a) is found to decrease with increasing indentation loads. This effect is commonly observed in crystalline materials and is usually referred to as the indentation size effect (ISE) (221).

In spite of lack of dislocations in metallic glasses, the ISE has also been occasionally reported in these systems (279; 280; 281) and, in fact, it is observed in the amorphous matrix of the $Cu_{46.5}Zr_{46.5}Al_5$ composite investigated here. The origin of this effect is believed to be related to deformation-induced excess free volume (113; 188) which forms in addition to the free volume typically trapped in the material upon quenching. The ISE can be quantified using a power law of the type $H = ch^{-m}$ where c is a constant and m denotes the ISE index (221). By plotting log(H) as a function of log(h) (see Figure 3.43b) the ISE index for the three different structures can be determined. An ISE index m = 0.169 is obtained for the amorphous structure. This value is smaller than those corresponding to the crystalline counterparts (m = 0.186 and m = 0.277 for the CuZr B2 austenitic CuZr martensitic phase, respectively). This indicates that the ISE in CuZr glassy structure is less pronounced than in the crystalline phases, as often reported in the literature (221). Furthermore, a larger ISE is found for the CuZr austenite phase, possibly due to its lack of twin boundaries, which aid to accommodate plastic strains in the martensite CuZr phase, thus resulting in a reduced ISE in that case (221).

Remarkably, the hardness values measured in the crystalline regions of the compressed $Cu_{46.5}Zr_{48.5}Al_5$ sample resemble those of the martensite in the $Cu_{50}Zr_{50}$ alloy (see Figure 3.43c). This is expectable in view of the martensitic transformation that occurs in $Cu_{46.5}Zr_{48.5}Al_5$ during plastic flow. Finally, concerning the Young's modulus evaluated from nanoindentation, a value around 110 GPa was obtained with a maximum indentation load of 5 mN, both for the amorphous and the martensite, whereas a slightly lower value (80 GPa) was obtained for the austenite. However, the use of nanoindentation to determine the Young's modulus of austenite and martensitic phases has been shown to be questionable, particularly when large indentation loads are employed (282). In our case, a decrease of E was observed, both for the austenite and the martensite, with values as low as 35 and 70 GPa, respectively, for maximum loads of 500 mN. It is worth mentioning that this apparent progressive reduction of E is also evident from the shape of the compression test of the $Cu_{50}Zr_{50}$ sample (Figure 3.41) and has been studied in detail in austenite/martensite NiTi alloys (283). Variation in E can occur during nanoindentation due to partial stress-induced martensitic transformation, followed by martensite variant rearrangement (284) which upon unloading have been shown to be reversible to a certain extent.

3.3.3.4. Summary

This section shows that addition of a small amount of Al into the Cu-Zr binary system drastically changes the microstructure of the resulting as-cast alloys, leading to either a metallic glass composite ($Cu_{46.5}Zr_{48.5}Al_5$) or a martensitic nanocomposite ($Cu_{50}Zr_{50}$). The concomitant differences in mechanical properties depending on the alloy microstructure have been investigated in detail. Both samples exhibit large plastic deformation during compression (total strain beyond 10 %) and work hardening ability. The strengthening behavior during deformation in the $Cu_{46.5}Zr_{48.5}Al_5$ alloy is ascribed to an austenite-to-martensite phase transformation whereas the hardening and plasticity in $Cu_{50}Zr_{50}$ are governed by the large amounts of twin boundaries and a deformation-induced phase transformation within the already existing martensitic phase. The hardness values in the different phases have been determined by nanoindentation tests. The amorphous matrix is found to be harder than the crystalline phases and an indentation size effect (i.e., progressive reduction of hardness as the indentation load increases) is always observed. This effect is particularly pronounced in the CuZr B2 (austenitic phase). Nanoindentation measurements also confirm that the B2 austenite phase in the $Cu_{46.5}Zr_{48.5}Al_5$ alloy undergoes a martensitic phase transformation during compression.

4. Conclusions

Structural changes in metallic glasses induced by devitrification, element addition and deformation have been characterized in this Thesis by calorimetry, X-ray diffraction and transmission electron microscopy; furthermore, the influence of these structural modification on the mechanical and corrosion behaviour was investigated through compression test and nanoindentation techniques and polarization scans, respectively.

The "results and discussion" section was divided into three main groups depending on the origin of these structural changes in metallic glasses. For clarity, the main conclusions of each section are listed below:

4.1. Structural and mechanical changes upon annealing

In this section two BMGs were investigated: a $Ti_{40}Zr_{10}Cu_{38}Pd_{12}$ alloy and a $Fe_{36}Co_{36}B_{19.2}Si_{4.8}Nb_4$ alloy, both annealed at $T<T_g$, $T_g<T<T_{x1}$ and $T>T_{x1}$ (being T the annealing temperature).

Upon annealing around T_g, changes on the short/medium range order were encountered in both systems. In the Fe-based alloy, disperse clusters with an average size of 5 nm were detected. Some of them are related to a pseudotenfold quasicrystal-like structure (considered as an intermediate state appearing prior to nanocrystallization of the metastable $Fe_{23}B_6$ phase) while some others are related to the already formed $Fe_{23}B_6$ structure. In this case, an increase in hardness (compared to the as-cast state) is associated to the precipitation of the metaestalbe network-like $Fe_{23}B_6$ stucture which is known to possess large hardness. In absence of clusters, the largest hardness observed in the Ti-based alloy is attributed to the more dense randomly packed structure with stronger bondings between atoms due to the annihilation of free volume. Despite the different structure evolution, in both cases wear characteristics and the elastic recovery as well as hardness are enhanced at annealing temperatures around *Tg*.

Upon annealing at temperatures $\geq T_{x1}$, the microstructure of the Fe-based alloy consists of crystallites of $Fe_{23}B_6$ and Fe_3B metastable phases of ~ 7 nm in size surrounded by an amorphous matrix. In this case, the enhanced hardness is mainly attributed to the ultra high hardness of the Fe-B phases as well as to the substitution solid solution. In the Ti-

based alloy, annealing above T_{x1} results in a few dispersed CuTi nanocrystals embedded in the glassy matrix. An increase of hardness is detected when compared to the as-cast state; however smaller hardness value than the sample annealed around T*g* is attributed to the softer nature of the CuTi pahse. Concerning wear characteristics and elastic recovery, the Fe-based alloy displays the best values between all the thermal treatments.

Finally, upon annealing beyond T_{x2}, a completely crystalline structure is achieved with large hardness values but decreased wear and elastic recovery behaviour. The strengthening behaviour is linked to the appearance of new intermetallic phases and to the so-called solid solution hardening.

In few words, from this section it could be pointed out that annealing treatments around T_g, when disperse nanacrystallites are embedded in an amorphous matrix, results in enhanced mechanical properties. Furhtermore, special attention was taken to the Young's modulus evolution and corrosion properties of the Ti-based alloy, as they are important parameters for the applicability in the biomedical field. As a result, the more competitive characteristics were obtained in the partial devitrified alloys.

It is also interesting to notice the differences on nucleation and growth of crystals between the two different amorphous alloys. In Fe-based BMG crystallization starts much earlier than in Ti-based BMG. This fact could be ascribed to the formation of metastable phases in the Fe-based BMG while in the Ti-based BMG no metastable phase formation was detected.

4.2. Structural and mechanical changes produced by element addition

It is well-known that a successful way to produce a composite material is by switching the chemical composition of a good glass forming system by adjusting the composition of the present elements or by minor addition of a new one.

Although a small decrease of enthalpy of the first crystallization peak is observed through DSC, suggesting crystallization, no visible structural changes are detected by XRD and TEM by 2 % of Nb addition to the amorphous $Ti_{40}Zr_{10}Cu_{38}Pd_{12}$ alloy. However, its influence on mechanical behaviour, particularly plasticity under compression, is great.

3% of Nb addition results in tiny nanocrystallites dispersed in the amorphous matrix. These nanocrystals are supposed to be the responsible of the increase above 10% of plastic strain.

However, a brittle behaviour is observed if the Nb content is exceedingly high (4%). In this case, the alloy is composed of two crystalline phases (CuTi and $CuTi_2$) surrounded by an amorphous structure mainly located in the outer part of the rod.

Acoustic measurements reveal a slight increase of Young's modulus in the alloys with 2 and 3% of Nb addition; however, *E* is still lower than the reported for the commercial Ti-6Al-4V alloy. On the other hand, potentiodynamic polarization curves in simulated body fluid reveal that Nb addition does not severely affect the corrosion response and all the alloys exhibit competitive anticorrosion properties.

Lack of pronounced plasticity is one of the main disadvantages of metallic glasses, limiting their overall application; this drawback is overcome for the $(Ti_{40}Zr_{10}Cu_{38}Pd_{12})_{97}Nb_3$ which, together with low Young's modulus it exhibits also high strength and excellent corrosion response, thus turning out to be a potential candidate to be used as structural biomedical material.

4.3. Structural and mechanical changes upon deformation

Dissimilar effects can be experienced by metallic glasses upon the same deformation treatments. While strain softening in the $Ti_{40}Zr_{25}Ni_8Cu_9Be_{18}$ metallic glass alloy takes place as deformation proceeds (by means of compression test as well as during nanoindentation), in the $Zr_{62}Cu_{18}Ni_{10}Al_{10}$ BMG the opposite effect, strain hardening, is observed.

Plastic flow in the $Ti_{40}Zr_{25}Ni_8Cu_9Be_{18}$ is inhomogeneous. Flow events are usually accompanied by dilatation, i.e., creation of free volume which results in strain softening during plastic deformation; in nanoindentation, this effect is referred as the indentation size effect. A calculated ISE index of 0.072 indicates that the ISE in the $Ti_{40}Zr_{25}Ni_8Cu_9Be_{18}$ MGs is less significant than for most crystalline materials.

An opposite effect is observed from the nanoindentation curve of the $Zr_{62}Cu_{18}Ni_{10}Al_{10}$ metallic glass alloy. At low applied loads, an increase of hardness is detected; the origin of this mechanical hardening could be the deformation-induced nanocrystals formation

which, at low indentation depths counterbalances the softening effect typically found in metallic glasses. However, at larger applied loads the softening predominates over hardening probably due to deformation-induced increase of free volume, which is more pronounced at higher loading rates. Furthermore, this alloy was compressed without fracture up to 120% true strain deformation; also in this case, the formation of some nanocrystals induced during deformation could be responsible of the observed superplasticity.

Finally, martensitic phase transformations, detected during deformation in the $Cu_{50}Zr_{50}$ and $Cu_{46.5}Zr_{48.5}Al_5$ composite alloys, were thought to be responsible for the large plastic deformation during compression (total strain beyond 10 %) and work hardening ability.

Aside from the fact than deformation can induce phase transformation, from this work, it is also interesting to note than despite their similar composition and identical preparation conditions, $Cu_{50}Zr_{50}$ and $Cu_{46.5}Zr_{48.5}Al_5$ alloys exhibit different microstructures. Furthermore, the same compositions were reported to be amorphous in the literature. This is a good example from what is commonly known: i.e., small changes in the casting conditions can drastically change the structure and properties of glassy alloys. To obtain reproducible alloys, systematic castings, taking special care on the control of temperature and pressure, should be performed.

4.4. Future trends

The work presented in this Thesis has shed light on the influence of structural modifications (i.e. changes in the SRO/MRO, micro and nanometric size inhomogeneities) on the mechanical behaviour of various families of metallic glasses; particularly in their hardness and plasticity, the latter being the main factor limiting their applicability as structural materials.

In order to have a more complete understanding of the mechanical and corrosion behaviour of the different bulk glassy alloys investigated in this work and, to better assess their applicability, additional structural investigations should be conducted; for instance, to further study the structural changes upon annealing the Ti-based glassy alloy at low temperatures, a proposal to the ALBA synchrotron was already submitted to use the non-crystalline diffraction beam line to perform experiments with

SAXS/WAXS (small/large angular x-ray scattering) with the aim to study the changes in the short and medium range order.

As mentioned, Ti-Zr-Cu-Pd-(Nb) alloys are potential candidates to be used in the biomedical filed; for this reason, elastic properties, corrosion behaviour in simulated body fluid and cytotoxicty tests are of special interest. Young's modulus and corrosion studies have been already reported in this Thesis but cytotoxicity experiments are still rather limited. With this purpose, cytotoxicity tests are planned to be assessed using a live/dead viability/cytotoxicity test with mouse preosteoblasts in the next months.

It is also worth nothing that several papers directly or indirectly related to the presented work have been published in international journals. The papers are listed below:

1. J. Sort, J. Fornell, W.Li, S. Suriñach, M.D. Baró; *Influence of the loading rate on the indentation response of Ti-based metallic glass*; Journal of Materials Research, 24 (2009) 918.
2. J. Fornell, A. Concustell, S. Suriñach, W.H.Li, N. Cuadrado, A. Gebert, M.D. Baró, J. Sort; *Yielding and intrinsic plasticity of Ti-Zr-Ni-Cu-Be bulk metallic glass*; International Journal of Plasticity; 25 (2009) 1540.
3. J. Fornell, S. Suriñach, M. D. Baró, J. Sort; *Unconventional elastic properties, deformation behaviour and fracture characteristics of newly developed rare earth bulk metallic glasses*; Intermetallics 17 (2009) 1090.
4. A. Concustell, J. Sort, J. Fornell, E. Rossinyol, S. Suriñach, A. Gebert, J. Eckert, M.D. Baró; *Work-hardening mechanisms of the $Ti_{60}Cu_{14}Ni_{12}Sn_4Nb_{10}$ nanocomposite alloy*; Journal of Materials Research, 24 (2009) 3146.
5. J. Fornell, E. Rossinyol, S. Suriñach, M.D. Baró, W. Li, J. Sort; *Enhance mechanical properties in a Zr-based metallic glass caused by deformation-induced nanocrystallization*; Scripta Materialia 62 (2010) 13.
6. J. Sort, J. Fornell, S. Suriñach, M.D. Baró; *Evolution of the mechanical properties of Ti-based metallic glass during depth-sensing load-unload nanoindentation cycles*; Nanoscience and Nanotechnology Letters 2 (2010) 298.

7. J. Fornell, S. González, E. Rossinyol, S. Suriñach, M.D. Baró, D.V. Louzguine-Luzgin, J.H. Perepezko, J. Sort, A. Inoue; *Enhanced mechanical properties due to structural changes induced by devitrification in Fe-Co-B-Si-Nb bulk metallic glass*; Acta Materialia 58 (2010) 6256.
8. J. Fornell, M.D. Baró, S. Suriñach, A. Gebert, J. Sort; *The Influence of the deformation-induced martensitic transformation on the mechanical properties of nanocomposite Cu-Zr-(Al) systems*; Advanced Engineering Materials 13 (2012) 57.
9. F.S. Santos, J. Sort, J. Fornell, M.D. Baró, S. Suriñach, C. Bolfarini, W.J. Botta, C.S. Kiminami; *Mechanical behavior under nanoindentation of a new Ni-based glassy alloy produced by melt-spinning and copper mold casting*; Journal of Non-Crystalline Solids 356 (2010) 2251.
10. J. Fornell, S. Suriñach, M.D. Baró, J.Sort; *Indentation plastic work and large compression plasticity in in-situ nanocrystallized $Zr_{62}Cu_{18}Ni_{10}Al_{10}$ metallic glass*; Journal of Alloys and Compounds 509S (2011) S87.
11. J. Fornell, N. Van Steenberge, A. Varea, E. Rossinyol, E. Pellicer, S. Suriñach, M.D. Baró, J.Sort; *Enhanced mechanical properties and in vitro corrosion behavior of amorphous and devitrified $Ti_{40}Zr_{10}Cu_{38}Pd_{12}$ metallic glass*; Journal of the Mechanical Behavior of Biomedical Materials 4 (2011)1709.
12. S. González, E. Pellicer, J. Fornell, A. Blanquer, L. Barrios, E. Ibáñez, P. Solsona, S. Suriñach, M.D. Baró, C. Nogués, J. Sort; *Improved mechanical performance and delayed corrosion phenomena in biodegradable Mg–Zn–Ca alloys through Pd-alloying*; Journal of the Mechanical Behavior of Biomedical Materials; 6 (2012) 53.
13. J. Fornell, S. González, E. Pellicer, N. Van Steenberge, P. Pérez, S. Suriñach, M.D. Baró, J. Sort; *Deformation and fracture behavior of corrosion-resistant, potentially biocompatible, $Ti_{40}Zr_{10}Cu_{38}Pd_{12}$ bulk metallic glass*; Journal of Alloys and Compounds; doi:10.1016/j.jallcom.2011.10.057.
14. J. Fornell, N. Van Steenberge, S. Suriñach, M.D. Baró, J. Sort; *Influence of the Si content on the microstructure and mechanical properties of Ti–Ni–Cu–Si–Sn nanocomposite alloys*; Journal of Alloys and Compounds; doi:10.1016/j.jallcom.2011.12.002.

15. J. Fornell, E. Pellicer, N. Van Steenberge, S. Gonzalez, A. Gebert, S. Suriñach, M.D. Baró and J. Sort; *Improved plasticity and corrosion behavior in Ti-Zr-Cu-Pd metallic glass with minor additions of Nb: an alloy composition intended for biomedical applications*; submitted.
16. A. Hynowska, E. Pellicer, J. Fornell, S. González, N. Van Steenberge, S. Suriñach, J. Eckert, M. D. Baró, J.Sort; *Nanostructured β-phase Ti-31.0Fe-9.0Sn and Ti-39.3Nb-13.3Zr-10.7Ta alloys for biomedical applications: microstructure benefits on the mechanical and corrosion performances*; submitted.
17. B.B. Madeiros, M.M. Madeiros, J. Fornell, E. Pellicer, J. Sort, S. Suriñach, M.D. Baró, C.S. Kiminami, W.J. Botta, C. Bolfarini; *Nanoindentation response of Cu-Ti based metallic glasses: comparison between as-cast, relaxed and devitrified states*; submitted

Bibliography

1. *Non-crystalline structure in solidified gold-silicon alloys.* **Klement, W., R.H. Willens, and P. Duwez,.** 187 1960, Nature, p. 869.

2. *Formation, stability and structure of palladium-silicon based alloy.* **Chen, H.S. and D. Turnbull.** 17 1969, Acta Materialia, p. 1021.

3. *Thermodynamic considerations on formation and stability of metallic glasses.* **Chen, H S.** 22 1974, Acta Metallurgica, p. 1505.

4. *Formation of bulk metallic glass by fluxing.* **Kui, H W, Greer, A L and Turnbull, D.** 45 1984, Applied Physics Letters, p. 615.

5. **Boettinger, W J, et al.** *Rapidly solidified crystalline alloys.* s.l. : The metallurgical society Inc., 1985. p. 21.

6. **Polk, D E and Giessen, B C.** *Metallic glasses.* [ed.] J J Gilman and H J Leamy. Ohio : ASM, Metals Park, 1976.

7. **Biloni, H and Boettinger, W J.** *Solidification, in physical metallurgy.* [ed.] R W Cahn and P Hassen. Amsterdam : s.n., 1996.

8. **Askeland, D R and Phulé, P P.** *The science and Engineering of Materials.* USA : Thomson Brooks/Cole, 2003.

9. *Thermodynamic properties of amorphous solids-glass formation and transition-(Overview).* **Fecht, H J.** 1995, Materilas Transactions JIM, Vol. 36, p. 777.

10. *Under what conditions can a glass be formed).* **Turnbull, D.** 1969, Contemporary physics, Vol. 10, p. 473.

11. *A kinetic treatment for glass formation.* **Uhlmann, D R.** 1972, Journal of non-crystalline solids, Vol. 7, p. 337.

12. *Time-temperature-transformation diagram and microstructure of bulk glass forming* $Pd_{40}Cu_{30}Ni_{10}P_{20}$. **Loffler, J F, Schroers, J and Johnson, W L.** 77, 2000, Applied Physics Letters, p. 681.

13. *The effect of fusion volume on the kinetics of formaion of metallic glasses by liquid-quencing.* **Yavari, A R, Hicter, P and Desre, P.** 1982, Journal De Chimie Physique Et De Physico-Chimie Biologique, Vol. 79, p. 579.

14. *Atomic size effect on the formability of metallic glasses.* **Egami, T and Waseda, Y.** 1984, Journal of Non-Crystalline Solids, Vol. 64, p. 113.

15. *Topological criterion for metallic glass formation.* **Senkov, O N and Miracle, D B.** 2003, Materials Science and Engineering A, Vol. 347, p. 50.

16. *Topological instability as a criterion for design and selection of aluminium based glass former alloys.* **Sa Lisboa, R D, et al.** 2005, Applied Physics Letters, Vol. 86, p. 211904.

17. *The efficient cluster packing model - An atomic structural model for metallic glasses.* **Miracle, D B.** 2006, Acta Materialia, Vol. 54, p. 4317.

18. *Bulk metallic glasses: At the cutting edge of metals research.* **Greer, A L and Ma, E.** 2007, MRS Bulletin, Vol. 32, p. 611.

19. *Geometry of the structure of monatomic liquids.* **Bernal, J D.** 1960, Nature, Vol. 185, p. 68.

20. *Strucutral model for amorphous metallic alloys.* **Polk, D E.** 1970, Acta Metallurgica, Vol. 4, p. 117.

21. *New structural model for amorphous transition-metal silicides, borides, phosphides and carbides.* **Gaskell, P H.** 1979, Journal of Non-Crystalline Solids, Vol. 32, p. 207.

22. *A structural model for metallic glasses.* **Miracle, D B.** 2004, Nature Materials, Vol. 3, p. 697.

23. *Atomic packing and short-to-medium-range order in metallic glasses.* **Sheng, H W, et al.** 2006, Nature, Vol. 439, p. 419.

24. *Molecular transport in liquids and glasses.* **Cohen, M and Turnbull, D.** 1959, Journal of chemical physics, Vol. 31, p. 1164.

25. *A microscopic mechanism for steady state inhomogeneous flow in metallic glasses.* **Spaepen, F.** 1977, Acta Metallurgica, Vol. 25, p. 407.

26. *Length and density changes of amorphous $Pd_{40}Cu_{30}Ni_{10}P_{20}$ alloys due to structural relaxation.* **Russew, K and Sommer, F.** 2003, Journal of Non-Crystalline Solids, Vol. 319, p. 289.

27. *Excess free volume in metallic glasses measured by X-ray diffraction.* **Yavari, A R and et al.** 2005, Acta materialia, Vol. 53, p. 1611.

28. *Diffusion in metallic glasses and supercooled melts.* **Faupel, F and al., et.** 2003, Review of Modern Physics, Vol. 75, p. 237.

29. *Sub-nanometer open volume regions in a bulk metallic glass investigated by positron annihilation.* **Flores, K M, et al.** 2007, Acta Materialia, Vol. 55, p. 3403.

30. *Structural aspects of metallic glasses.* **Miracle, D, et al.** 2007, MRS Bulletin, Vol. 32, p. 629.

31. **Suryanarayana, C and Inoue, A.** *Bulk metallic glasses.* 6000 Broken Sound Parkway, NW, Boca Raton : Taylor & Francis group, 2011.

32. *Microstructure controlled shear band pattern formation and enhanced plasticity of bulk metallic glasses containing in situ formed ductile phase dendrite dispersions.* **Hays, C C, Kim, C P and Johnson, W L.** 2000, Physical Review Letters, Vol. 13, p. 2901.

33. *ZrNbCuNiAl bulk metallic glass matrix composites containing dendritic bcc phase precipitates.* **Kühn, U, et al.** 2002, Applied Physics Letters, Vol. 80, p. 2478.

34. *Improved mechanical behavior of Cu-Ti-based bulk metallic glass by in situ formation of nanoscale precipitates.* **Calin, M, Eckert, J and Schultz, L.** 2003, Scripta Materialia, Vol. 48, p. 653.

35. *Cu-Hf-Ti-Ag-Ta bulk metallic glass composites and their properties.* **Bian, Z, et al.** 2005, Acta Materialia, Vol. 53, p. 2037.

36. *Enhanced plasticity in a Ti-based bulk metallic glass-forming alloy by in situ formation of a composite microstructure.* **He, C, et al.** 2002, Journal of Materials Researh, Vol. 17, p. 3015.

37. *Novel Ti-base nanostructure–dendrite composite with enhanced plasticity.* **He, G, et al.** 2003, Nature Materials, Vol. 2, p. 33.

38. *Effect of casting conditions on microstructure andmechanical properties of high-strength $Zr_{73.5}Nb_9Cu_7Ni_1Al_{9.5}$ in situ composite.* **Das, J, et al.** 2003, Scripta Materialia, Vol. 49, p. 1189.

39. *Glassy metals.* **Chen, H S.** 1980, Reports in Progress in Physics, Vol. 43, p. 353.

40. **Chen, H S.** Structural relaxation in metallic glasses. [ed.] F E Luborsky. *In amorphous metallic alloys.* London : Butterworths, 1983, pp. 169-186.

41. *High packing density of Zr- and Pd-based bulk amorphous alloys.* **Inoue, A, et al.** 1998, Materials Transactions, JIM, Vol. 39, p. 318.

42. *Reaction kinetics in differential thermal analysis.* **Kissinger, H E.** 1957, Analytical chemistry, Vol. 29, p. 1702.

43. *Kinetic analysis of derivative curves in thermal analysis.* **Ozawa, T.** 1970, Journal of thermal analysis, Vol. 2, p. 301.

44. *Crystallization behavior of $Ti_{50}Ni_{25}Cu_{25}$ amorphous alloy.* **Louzguine, D V and Inoue, A.** 2000, Journal of Materials Science, Vol. 35, p. 4159.

45. *Crystallization behavior of the cobalt based metallic $Co_{65}Si_{15}B1_4Fe_4Ni_2$.* **Li, H F and Ramanujan, R V.** 2004, Materials Science and Engineering A, Vol. 375, p. 1087.

46. *Enhanced mechanical properties due to structural changes induced by devitrification in Fe–Co–B–Si–Nb bulk metallic glass.* **Fornell, J, et al.** 2010, Acta Materialia, Vol. 58, p. 6256.

47. **Dieter, G E.** *Mechanical Metallurgy.* 3rd ed. New York : McGraw-Hill, 1986.

48. *Experimental parameters influencing grain refinement and microstructural evolution during high-pressure torsion.* **Zhilyaev, A P; Nurislamova, G V; Kim, B - K; Baró, M D; Szpunar, J A; Langdon, T G;.** 2003, Acta Materialia, Vol. 51, p. 753.

49. *Nanocrystallization of amorphous $Al_{88}Y_7Fe_5$ alloy induced by plastic deformation.* **Boucharat, N, et al.** 2005, Scripta Materialia, Vol. 53, p. 823.

50. *Paradoxes of severa plastic deformation.* **Valiev, R Z.** 2003, advanced engineering materials, Vol. 5, p. 293.

51. *Cold-consolidation of ball-milled Fe-based amorphous ribbons by high pressure torsion.* **Sort, J, et al.** 2004, Scripta Materialia, Vol. 50, p. 1221.

52. *Structural rejuvenation in a bulk metallic glass induced by severe plastic deformation.* **Dmowski, W, et al.** 2010, Acta Materialia, Vol. 58, p. 429.

53. *Deformation-induced nanocrystal formation in shear bands of amorphous alloys.* **Chen, H, et al.** 1994, Nature, Vol. 367, p. 541.

54. *Deformation-induced nanocrystal precipitation in Al-based metallic glasses.* **Gao, M C, Hackenberg, R E and Shiflet, G J.** 2001, Materials Transactions, Vol. 42, p. 1741.

55. *Mechanism of the deformation-induced nanocrystallization in a Cu-based bulk amorphous alloy under uniaxial compression.* **Lee, S- W, et al.** 2006, Vol. 54, p. 1439.

56. *Nanocrystallization during nanoindentation of a bulk amorphous metal alloy at room temperature.* **Kim, J- J, et al.** 2002, Science, Vol. 295, p. 654.

57. *Study of structural changes of Zr-based bulk metallic glasses upon annealing and deformation treatments.* **Van Steenberge, N.** April 2008, Doctoral thesis.

58. *A microscopic mechanism for steady state inhomogeneous flow in metallic glasses.* **Spaepen, F.** 1977, Acta Metallurgica, Vol. 25, p. 407.

59. *Formation and deformation of metallic glasses: Atomistic theory.* **Egami, T.** 2006, Intermetallics, Vol. 14, p. 882.

60. *Plastic deformation in metallic glasses.* **Argon, A S.** 1979, Acta Metallurgica, Vol. 27, p. 47.

61. *Plastic flow and fracture of metallic glasses.* **Leamy, H J, Chen, H S and Wang, T T.** 1972, Metallurgical Transactions, Vol. 3, p. 699.

62. *Sueprductile bulk metallic glass.* **Yao, K F, Ruan, U Q and Chen, N.** 2006, Applied Physics Letters, Vol. 88, p. 122106.

63. *"Work-hardenable" ductile bulk metallic glass.* **Das, J, et al.** 2005, Physics Review Letters, Vol. 94, p. 205501.

64. *Nanoscale multistep shear band formation by deformation-induced nanocrystallization in Zr–Al–Ni–Pd bulk metallic glass.* **Saida, J, et al.** 2005, Applied Pysics Letters, Vol. 87, p. 151907.

65. *Extraordinary plasticity of ductile bulk metallic glasses.* **Chen, M, et al.** 2006, Physical Review Letters, Vol. 96, p. 245502.

66. *Mechanical properties of bulk metallic glasses and composites.* **Eckert, J, et al.** 2007, Journal of Materials Research, Vol. 22, p. 285.

67. *Comparison of microstructures and properties of Zr-based bulk metallic glass composites with dendritic and spherical bcc phase precipitates.* **Sun, G Y, Chen, G and Chen, G L.** 2007, Intermetallics, Vol. 15, p. 632.

68. *Ductility enhancement of a Ti-based bulk metallic glass through annealing treatment below the glass transition temperature.* **Jun, H- J, et al.** 2012, Intermetallics, Vol. 20, p. 47.

69. *Deformation-induced structural transformation leading to compressive plasticity in* $Zr_{65}Al_{7.5}Ni_{10}Cu1_{2.5}M_5$. **Setyawan, A, et al.** 2010, Journal of Materials Research, Vol. 25, p. 1149.

70. *Mechanically-assisted nanocrystallization and defects in amorphous alloys: A high-resolution transmission electron microscopy study.* **Jiang, W H and Atzmon, M.** 2006, Scripta Materialia, Vol. 54, p. 333.

71. *Crystallization-induced plasticiy of Cu-Zr containing bulk amorphous alloys.* **Lee, S W, et al.** 2006, Acta Materialia, Vol. 54, p. 349.

72. *Deformation behavior of Zr- and Ni-based bulk glassy alloys.* **Louzguine, K V, et al.** 2007, Jouranl of Materials Research, Vol. 22, p. 1087.

73. *Mechanically driven phase separation and corresponding microhardness change in* $Cu_{60}Zr_{20}Ti_{20}$ *bulk metallic glass.* **Cao, Q, et al.** 2005, Applied Physics Letters, Vol. 86, p. 081913.

74. *Innovative processing and property improvement of metallic glass based composites.* **Sun, G Y, et al.** 2006, Scrpita Materialia, Vol. 55, p. 375.

75. *A novel Cu-based BMG composite with high corrosion resistance and excellent mechanical properties.* **Qin, C L, et al.** 2006, Acta Materialia, Vol. 54, p. 3713.

76. *Lattice distortion/disordering and local amorphization in the dendrites of a* $Ti_{66.1}Cu_8Ni_{4.8}Sn_{7.2}Nb_{13.9}$. **Kim, K B, et al.** 2005, Applied Physics Letters, Vol. 86, p. 201909.

77. *Phase separation in $Cu_{43}Zr_{43}Al_7Ag_7$ bulk metallic glass.* **Oh, J C, et al.** 2005, Scripta Materialia, Vol. 53, p. 165.

78. *enhanced plastic strain in Zr-based bulk amorphous alloys.* **Xing, L Q, et al.** 2001, Physics Review B, Vol. 64, p. 180201.

79. *Ductile metallic glasses in supercooled martensitic alloys.* **Das, J, et al.** 2006, Materials Transactions, Vol. 47, p. 2606.

80. *Impact of microstructural inhomogenities on the ductility of bulk metallic glasses.* **Eckert, J, et al.** 2007, Materials Transactions, Vol. 48, p. 1806.

81. *Kinetics and mechanisms of the anodic dissolution of metallic glasses.* **Heusler, K E and Huerta, D.** 1989, Journal of the Electrochemical Society, Vol. 136, p. 65.

82. *Corrosion behaviour of rapidly solidified $Zr_{76}Ni_{16}Fe_8$ alloy in chloride environments.* **Dutta, R S, Savalia, R T and Dey, G K.** 1995, Scripta Metallurgica et Materialia, Vol. 32, p. 207.

83. *Effect of oxygen on phase formation and thermal stability of slowly cooled $Zr_{65}Al_{7.5}Cu_{7.5}Ni_{10}$ metallic glass.* **Gebert, A, Eckert, J and Schultz, L.** 1998, Acta Materialia, Vol. 46, p. 5475.

84. *Effect of structural defects, surface irregularities, and quenched-in defects on corrosion Zr-based metallic glasses.* **Vishwanadh, B, et al.** 2009, Metalurgical and Materials Transactions A-Pysical Metallurgy and Materials Science, Vol. 40A, p. 1131.

85. *Mechanical properties of a two-phase amorphous Ni-Nb-Y alloy studied by nanoindentation.* **Concustell, A, et al.** 2006, Scripta Materialia, Vol. 56, p. 85.

86. *Plasma arc melting of titanium alloys.* **Blackburn, M J and Malley, D R.** 1993, Materials & Design, Vol. 14, p. 19.

87. *Alloying titanium and tantalum by cold crucible levitation melting (CCLM) furnace.* **Morita, A, et al.** 2000, Materials Science and Engineering A, Vol. 280, p. 208.

88. **Williams, D B and Carter, Barry C.** *Transmission electron microsopy: A textbook for materials science.* New York : Plenum Press, 1996.

89. **Goodhew, J Peter, Humphreys, J and Beanland, R.** *Electron microscopy and analysis.* [ed.] Taylor& Francis. London : s.n., 2001.

90. **Goodhew, P, et al.** www.matter.org.uk. [Online]

91. **Thomas, G and Goringe, M J.** *Transmission electron microscopy of materials.* s.l. : John Wiley and Sons, 1979.

92. www.gatan.com. [Online]

93. *The diffraction of short electromagenetic waves by a crystal.* **Bragg, W L.** 1913, Proceedings of the Cambridge Philosophical Society, Vol. 17, p. 43.

94. **Cullity, B D.** *Elements of X-ray diffraction.* 3rd. Boston : Addison-Wesley Publishing Company, 1978.

95. **Klug, H P and Alexander, L E.** *X-ray diffraction procedures.* New York : Wiley, 1974.

96. **Schreiber, D.** *Elastic constants and their measurements.* New York : McGraw-Hill, 1973.

97. **Fischer-Cripps, A.** *Nanoindentation.* New York : Springer-Verlag, 2004.

98. *An improved technique for determining hardness and elastic-modulus using load and displacement sensing indentation experiments.* **Oliver, W C and Pharr, G M.** 1992, Journal of Materials Research, Vol. 7, p. 1564.

99. **Askeland, D R and Phulé, P P.***The science and engineering of materials.* USA : Thomson Brooks/Cole, 2003.

100. *Localized corrosion behavior of a zirconium-based bulk metallic glass relative to its crystalline state.* **Peter, W H, et al.** 2002, Intermetallics, Vol. 10, p. 1157.

101. *The effect of nanocrystallization and free volume on the room temperature plasticity of Zr-based bulk metallic glasses.* **Mondal, K, et al.** 2008, Acta Materialia, Vol. 56, p. 5329.

102. *Nano-scratch behavior of a bulk Zr–10Al–5Ti–17.9Cu–14.6Ni amorphous alloy.* **Wang, J G, et al.** 2000, Journal of Materials Research, Vol. 15, p. 913.

103. *Ti based biomaterials, the ultimate choice for orthopaedic implants-A review.* **Geetha, M, et al.** 2009, Progress in Materials Science, Vol. 54, p. 397.

104. *Recent research and development in titanium alloys for biomedical applications and healthcare goods.* **Niinomi, M.** 2003, Science and Technology of Advanced Materials, Vol. 4, p. 445.

105. *The influence of heat treatment and role of boron on sliding wear behavior of b-type Ti-35Nb-7.2Zr-5.7Ta alloy in dry condition and in simulated body fluids.* **Majumdar, P, Singh, S B and Chakraborty, M.** 2011, Journal of the Mechanical Behavior of Biomedical Materials, Vol. 4, p. 284.

106. *Stabilization of metallic supercooled liquid and bulk amorphous alloys.* **Inoue, A.** 2000, Acta Materialia, Vol. 48, p. 279.

107. **Perker, A and Johnson, W L.** *Be bearing amorphous metallic alloys. Patent US5288344* US, 1993.

108. *Investigation of glass-forming ability, deformation and corrosion behaviour of Ni-free Ti-based BMG alloys designed for application as dental implants.* **Oak, J J, Louzguine-Luzgin, D V and Inoue, A.** 2009, Materials Science and Engineering C, Vol. 29, p. 322.

109. *Formation, mechanical properties and corrosion resistance of Ti-Pd base glassy alloys.* **Oak, J J and Inoue, A.** 2008, Journal on Non-Crystalline Solids, Vol. 354, p. 1828.

110. *Microstructure and Corrosion Resistance of Ti-Zr-Cu-Pd-Sn Glassy and Nanocrystalline Alloys.* **Quin, F, et al.** 2007, Materials Transactions, Vol. 48, p. 167.

111. *New TiZrCuPd quaternary bulk glassy alloys with potential for biomedical applications.* **Zhu, S L, et al.** 2007, Materials Transactions, Vol. 48, p. 2445.

112. *Effects of Si addition on the glass-forming ability and crystallization behaviours of Ti40Zr10Cu36Pd14 bulk glassy alloys.* **Zhu, S L, et al.** 2008, Intermetallics, Vol. 16, p. 609.

113. *Yielding and intrinsic plasticity of Ti-Zr-Ni-Cu-Be bulk metallic glass.* **Fornell, J, et al.** 2009, International Journal of Plasticity, Vol. 25, p. 1540.

114. *Bioactive titanate nanomesh layer on the Ti-based bulk metallic glass by hydrothermal–electrochemical technique.* **Sugiyama, N, et al.** 2009, Acta Biomaterialia, Vol. 5, p. 1367.

115. *In vitro biocompatibility of equal Channel angular processed (ECAP) titanium.* **Kim, T N, et al.** 2007, Biomedical Materials, Vol. 2, p. S117.

116. *Structure, composition and microhardness of (Ti,Zr)N and (Ti,Al)N coatings prepared by DC magnetron sputtering.* **Ramana, J V, et al.** 2004, Materials Letters, Vol. 58, p. 2553.

117. *Microstructure identification of devitrified Cu–Ti–Zr–Ni bulk amorphous alloy.* **Yang, Y J, et al.** Journal of Alloys and Compounds : s.n., 2009, Vol. 480, p. 329.

118. *Microstructural aspects of the hcp–fcc allotropic phase transformation induced in cobalt by ball milling.* **Sort, J, et al.** 2003, Philosophical Magazine, Vol. 83, p. 439.

119. *Influence of stacking fault energy on the minimum grain size achieved in severe plastic deformation.* **Zhao, Y H, et al.** 2007, Materials Science and Engineering: A, Vol. 463, p. 22.

120. *Ductile-to-brittle transition in a Ti-based bulk metallic glass.* **Poon, S J, Shiflet, G J and Lewandowski, J J.** 2009, Scripta Materialia, Vol. 60, p. 1027.

121. *Intrinsic plasticity or brittleness of metallic glasses.* **Lewandowski, J J, Wang, W H and Greer, A L.** 2005, Philosophical Magazine Letters, Vol. 85, p. 77.

122. *Elastic moduli of a ZrCuAlNi bulk metallic glass from room temperature to complete crystallisation by in situ pulse-echo ultrasonic echography.* **Keryvin, V, et al.** 2008, Journal of the Ceramic Society of Japan, Vol. 116, p. 851.

123. *Mechanical behavior of amorphous alloys.* **Schuh, C A, Hufnagel, T C and Ramamurty, U.** 2007, Acta Materialia, Vol. 55, p. 4067.

124. **Künzi, H U.** *In Glassy Metals II, Topics in Applied Physics.* [ed.] H. Beck and H.J. Güntherodt. New York : Springer, 1983. p. 169. Vol. 53.

125. *The mechanical properties of a glassy metal; Ni_3P.* **Ashby, M F, Nelson, A N and Centamore, R M A.** 1970, Scripta Metallurgica, Vol. 4, p. 715.

126. *Soft Transverse Phonons in a Metallic Glass.* **Golding, B, Bagley, B G and Hsu, F S L.** 1972, Physical Review Letters, Vol. 29, p. 68.

127. *The mechanical properties of palladium 20 a/o silicon alloy quenched from the liquid state.* **Masumoto, T and Maddin, R.** 1971, Acta Metallurgica, Vol. 19, p. 725.

128. *On the use of pair potentials to calculate the properties of amorphous metals.* **Weaire, D, et al.** 1971, Acta Metallurgica, Vol. 19, p. 779.

129. *Unconventional elastic properties, deformation behavior and fracture characteristics of newly developed rare earth bulk metallic glasses.* **Fornell, J, et al.** 2009, Intermetallics, Vol. 17, p. 1090.

130. *Structural aspects of elastic deformation of a metallic glass.* **Hufnagel, T C, Ott, R T and Almer, J.** 2006, Physical Review B, Vol. 73, p. 064204.

131. *Supersoftening of transverse phonons in $Zr_{41}Ti_{14}Cu_{12.5}Ni_{10}Be_{22.5}$ bulk metallic glass.* **Wang, W H, et al.** 2000, Physical Review B, Vol. 62, p. 25.

132. *Shear deformation of glassy metals: Breakdown of cauchy relationship and anelasticity.* **Suzuki, Y and Egami, T.** 1985, Journal of Non-Crystalline Solids, Vol. 75, p. 361.

133. *Enhanced mechanical properties in a Zr-based metallic glass caused by deformation-induced nanocrystallization.* **Fornell, J, et al.** 2010, Scripta Materialia, Vol. 62, p. 13.

134. *Relaxation and crystallization of $Zr_{41.2}Ti1_{3.8}Cu_{12.5}Ni_{10}Be_{22.5}$ bulk amorphous alloys.* **Rex, C, Tam, Y and Sheck, C H.** 2004, Materials Science and Engineering: A, Vol. 364, p. 198.

135. *Glass formation ability and mechanical properties of $Ti_{40}Cu_{40}Zr_{10}Ni_{10}$ alloy.* **Wang, J, et al.** 2008, Journal of Non-Crystalline Solids, Vol. 354, p. 3653.

136. *Work-hardening mechanisms of the Ti60Cu14Ni12Sn4Nb10 nanocomposite alloy.* **Concustell, A, et al.** 2009, Journal of Materials Research, Vol. 24, p. 3146.

137. *Fe-based bulk metallic glass matrix composite with large plasticity.* **Guo, S F, et al.** 2010, Scripta Materialia, Vol. 62, p. 329.

138. *Fe-based bulk glassy alloy composite containing in situ formed α-(Fe,Co) and $(Fe,Co)_{23}B_6$ microcrystalline grains.* **Shen, B L, Men, H and Inoue, A.** 2006, Applied Physics Letters, Vol. 89, p. 101915.

139. *Relationships between hardness, Young's modulus and elastic recovery in hard nanocomposite coatings.* **Musil, J, et al.** 2002, Surface and Coatings Technology, Vol. 154, p. 304.

140. *Wear resistance of experimental Ti-Cu alloys.* **Ohkubo, C, et al.** 2003, Biomaterials, Vol. 24, p. 3377.

141. *Quasi-static cyclic loadings induced inelastic deformation in a Zr-based bulk metallic glass under nanoindentation.* **Tekaya, A, et al.** 2009, Journal of Materials Science, Vol. 44, p. 4930.

142. *Localized deformation of a $Cu_{46.25}Zr_{45.25}Al_{7.5}Er_1$ bulk metallic glass.* **Yang, F, et al.** 2009, Journal of Physics D:Applied Physics, Vol. 42, p. 065401.

143. *Plasticity characteristic obtained by indentation.* **Milman, Y V.** 2008, Journal of Physics D: Applied Physics, Vol. 41, p. 074013.

144. *Corrosion: Understanding the basics.* **Davis, J R.** [ed.] Davis J.R. & Associates. Ohio 44073-0002 : ASM, Materials Park, 2000.

145. *Effects of surface finishing and dissolved oxygen on the polarization behavior of $Zr_{65}Al_{7.5}Ni_{10}Cu1_{7.5}$ amorphous alloy in phosphate buffered solution.* **Hiromoto, S, et al.** 2000, Corrosion Science, Vol. 42, p. 2167.

146. *Effects of nanoscale heterogeneity on the corrosion behavior of non-equilibrium alloys.* **Asami, K, et al.** 2001, Scripta Materialia, Vol. 4, p. 1655.

147. *The efect of microcrystallites in the amorphous matrix on the corrosion behavior of amorphous Fe-8Cr-P alloys.* **Im, B M, et al.** 1995, Corrosion Science, Vol. 37, p. 1411.

148. *The influence of heat treatment on the corrosion behaviour of amorphous melt-spun binary Mg–18 at.% Ni and Mg–21 at.% Cu alloy.* **Ong, M S, et al.** 2001, Materials Science and Engineering: A, Vol. 304, p. 510.

149. *Localized corrosion behavior of a zirconium-based bulk metallic glass relative to its crystalline state.* **Peter, W H, et al.** 2002, Intermetallics, Vol. 10, p. 1157.

150. *Investigation on corrosion of titanium/steel brazed joint.* **Elrefaey, A, Wojarski, L and Tillmann, W.** 2010, Mat-wiss u Werkstofftech, Vol. 41, p. 908.

151. *Electrochemical behavior of centrifuged cast and heat treated Ti–Cu alloys for medical applications.* **Osório, W R, et al.** 2010, Electrochimica Acta, Vol. 55, p. 759.

152. *Thermal and magnetic properties of bulk Fe-based glassy alloys prepared by copper mold casting.* **Inoue, A, Shinohara, Y and Gook, J S.** 1995, Materials Transactions JIM, Vol. 36, p. 1427.

153. *Ultra-high strength above 5000 MPa and soft magnetic properties of Co–Fe–Ta–B bulk glassy alloys.* **Inoue, A, et al.** 2004, Acta Materialia, Vol. 52, p. 1631.

154. *Structure and magnetic properties of amorphous and nanocrystalline* $Fe_{40}Co_{40}Cu_{0.5}Zr_9Al_2Si_4B_{4.5}$ *alloys.* **Mitra, A, et al.** 2004, Journal of Magnetism and Magnetic Materials, Vol. 278, p. 299.

155. *Nano-scratch behavior of a Zr-based bulk amorphous alloy.* **Wang, J G, et al.** 2000, Journal of Materials Research, Vol. 15, p. 913.

156. *Crystallization and magnetic properties of* $[(Fe,Co)_{0.75}Si_{0.05}B_{0.20}]_{94}Nb_6$ *metallic glasses.* **Li, R, et al.** 2009, Journal of Physics D, Vol. 42, p. 085006.

157. *Effect of minor Cu addition on phase evolution and magnetic properties of* $\{[(Fe_{0.5}Co_{0.5})_{0.75}Si_{0.05}B_{0.20}]_{0.96}Nb_{0.04}\}_{100-x}$ Cu_x *alloys.* **Li, R, Stoica, M and Eckert, J.** 2009, Journal of Physics: Conference Series, Vol. 144, p. 012042.

158. *Superhigh strength and good soft-magnetic properties of (Fe,Co)-B-Si-Nb bulk glassy alloys with high glass-forming ability.* **Shen, B L, Inoue, A and Chang, C T.** 2004, Applied Physics Letters, Vol. 85, p. 4911.

159. *Contact and rubbing of flat surfaces.* **Archard, J F.** 1953, Journal of Applied Physics, Vol. 24, p. 981.

160. *Surface films in tribology.* **Halling, J.** 1982, Tribologia, Vol. 1, p. 15.

161. *Applications of rapid solidification.* **Froes, F H and Carbonara, R.** 1988, Journal of Metals, Vol. 40, p. 20.

162. $Fe_{23}B_6$*-type quasicrystal-like structures without icosahedral atomic arrangement in an Fe-based metallic glass.* **Hirata, A, et al.** 2009, Physical Review B, Vol. 80, p. 140201.

163. *Nanocrystallization of complex* $Fe_{23}B_6$*-type structure in glassy Fe–Co–B–Si–Nb alloy.* **Hirata, A, et al.** 2008, Intermetallics, Vol. 16, p. 491.

164. *The effect of niobium alloying additions on the crystallization of a Fe–Si–B–Nb alloy.* **Zhang, Y R and Ramanujan, R V.** 2005, Journal of alloys and compounds, Vol. 403, p. 197.

165. *Structural variation of Fe-Nb-B metallic glasses during crystallization process.* **Imafuku, M, et al.** 2001, Scripta Materialia, Vol. 44, p. 2369.

166. *Crystallization behavior of $Fe_{62}Nb_{8-x}Zr_xB_{30}$ bulk amorphous alloy.* **Shapaan, M, et al.** 2004, Materials Science and Engineering A, Vol. 375, p. 789.

167. *Electronic structure, exchange interactions and Curie temperature of FeCo.* **MacLaren, J M, et al.** 1999, Journal of Applied Physics, Vol. 85, p. 4833.

168. *Temperature-dependent hyperfine interactions in Fe_2B.* **Murphy, K A and Hershikowitz, N.** 1973, Physical Review B, Vol. 7, p. 23.

169. *Cohesive energy, local magnetic properties, and Curie temperature of Fe_3B studied using the self-consistent LMTO method.* **Kong, Y and Li, F.** 1997, Physical Review B, Vol. 56, p. 3153.

170. *Exchange-spring magnet: a new material principle for permanent magnet.* **Kneller, E F and Hawing, R.** 1991, IEEE Transactions on Magnetics, Vol. 27, p. 3588.

171. *Structure and magnetic properties of metastable Fe-B phases.* **Barinov, V A, et al.** 2005, Physics of Metals and Metallography, Vol. 100, p. 456.

172. *Interplanar spacings of complex Fe-Ni phases in rapidly quenched Fe-Ni-Nb-B systems.* **Svec, P, et al.** 2009, Journal of Physics: Conference Series, Vol. 144, p. 012092.

173. *Crystallization behaviour of amorphous $Fe_{73.5}Cu_1Nb_3Si_{13.5}B_9$.* **Rixecker, G, Schaaf, P and Gonser, U.** 1992, Journal of Physics: Condensed Matter, Vol. 4, p. 10295.

174. *Mechanical properties of iron-based bulk metallic glasses.* **Gu, X G, Poon, S J and Shiflet, G J.** 2007, Journal of Materials Research, Vol. 22, p. 344.

175. *Critical Poisson ratio for room-temperature embrittlement of amorphous $Mg_{85}Cu_5Y_{10}$.* **Castellero, A, et al.** 2007, Philosophical Magazine Letters, Vol. 87, p. 383.

176. *Solid-state amorphization of Zr_3Al: evidence of an elastic instability and first-order phase transformation.* **Rehn, L E, et al.** 1987, Physical Review Letters, Vol. 59, p. 2987.

177. *Soft transverse phonons in a metallic glass.* **Golding, B, Bagley, B G and Hsu, F S L.** 1972, Physical Review Letters, Vol. 62, p. 68.

178. *Elastic and tensile behavior of nanocrystalline copper and palladium.* **Sanders, P G, Eastman, J A and Weertman, J R.** 1997, Acta Materialia, Vol. 45, p. 4019.

179. *The effects of grain size and porosity on the elastic modulus of nanocrystalline materials.* **Kim, H S and Bush, M B.** 1999, Nanostructured Materials, Vol. 11, p. 361.

180. *Formalism for the calculation of local elastic constants at grain boundaries by means of atomistic simulation.* **Kulge, M D, et al.** 1990, Journal of Applied Physics, Vol. 67, p. 2370.

181. *Nanocrystalline materials.* **Gleiter, H.** 1989, Progress in Materials Science, Vol. 33, p. 223.

182. *On the elastic moduli of nanocrystalline Fe, Cu, Ni, and Cu–Ni alloys prepared by mechanical milling/alloying.* **Shen, T D, et al.** 1995, Journal of Materials Research, Vol. 10, p. 2892.

183. *Processing dependence of Young's modulus of Ti-base nanostructured alloys.* **He, G, et al.** 2004, Solid State Communications, Vol. 129, p. 711.

184. *Interpretations of indentation size effects.* **Gerberich, W W, et al.** 2002, Journal of Applied Mechanics, Vol. 69, p. 433.

185. *The frictional component of the indentation size effect in low load microhardness testing.* **Li, H, et al.** 1993, Journal of Materials Research, Vol. 8, p. 1028.

186. *Indentation size effects in crystalline materials: a law for strain gradient plasticity.* **Nix, W D and Gao, H.** 1998, Journal of the Mechanics and Physics of Solids, Vol. 46, p. 411.

187. *A conventional theory of mechanism-based strain gradient plasticity.* **Huang, Y, et al.** 2004, International Journal of Plasticity, Vol. 20, p. 753.

188. *Deformation in a $Zr_{57}Ti_5Cu_{20}Ni_8Al_{10}$ bulk metallic glass during nanoindentation.* **Yang, F, et al.** 2007, Acta Materialia, Vol. 55, p. 321.

189. *Plasticity in nanocrystalline and amorphous metals: similarities at the atomic scale.* **Lund, A C and Schuh, C A.** 2004, MRS proceedings, Vol. 806, p. MM7.4.1.

190. *The Hall–Petch breakdown in nanocrystalline metals: A crossover to glass-like deformation.* **Trelewicz, J R and Schuh, C A.** 2007, Acta Materialia, Vol. 55, p. 5948.

191. *Evolution and microstructure of shear bands in nanostructured Fe.* **Wei, Q, et al.** 2002, Applied Physics Letters, Vol. 81, p. 1240.

192. *Formation, ductile deformation behavior and soft-magnetic properties of (Fe,Co,Ni)–B–Si–Nb bulk glassy alloys.* **Shen, B, Chang, Ch and Inoue, A.** 2007, Intermetallics, Vol. 15, p. 9.

193. *Super-high strength of over 4000 MPa for Fe-based bulk glassy alloys in* $[(Fe_{1-x}Co_x)_{0.75}B_{0.2}Si_{0.05}]_{96}Nb_4$ *system.* **Inoue, A, Shen, B L and Chang, C T.** 2004, Acta Materialia, Vol. 52, p. 4093.

194. *Evaluation of hardness-yield strength relationships for bulk metallic glasses.* **Zhang, H W, et al.** 2006, Philosophical Magazine Letters, Vol. 86, p. 333.

195. *Indentation of bulk metallic glasses: Relationships between shear bands observed around the prints and hardness.* **Keryvin, V.** 2007, Acta Materialia, Vol. 55, p. 2565.

196. *Cobalt-based bulk glassy alloy with ultrahigh strength and soft magnetic properties.* **Inoue, A, et al.** 2003, Nature Materials, Vol. 2, p. 661.

197. **Courtney, T H.** *Mechanical behavior of materials.* Singapore : McGraw-Hill Series in Materials Science and Engineering, 1990.

198. **Hultin-Stigenberg, A, Nilsson, J-O and Liu, P.** *Quasicrystalline precipitation hardened metal alloy and method of making. US Patent 5632826* 27 May 1997.

199. *On the significance of the H/E ratio in wear control: a nanocomposite coating approach to optimised tribological behaviour.* **Leyland, A and Matthews, A.** 2000, Wear, Vol. 246, p. 1.

200. *Yield point of metallic glass.* **Shimizu, F, Ogata, S and Li, J.** 2006, Surface and Coatings Technology, Vol. 54, p. 412.

201. *Structure and properties of Zr–Ta–Cu–Ni–Al bulk metallic glasses and metallic glass matrix composites.* **Ott, R T, et al.** 2003, Journal of Non-Crystalline Solids, Vol. 317, p. 158.

202. *Effect of tungsten additions on the mechanical properties of Ti-6Al-4V.* **Choe, H, et al.** 2005, Materials Science and Engineering A, Vol. 396, p. 99.

203. *Glass-Forming Ability and Thermal Stability of Ti-Zr-Cu-Pd-Si Bulk Glassy Alloys for Biomedical Applications.* **Shengli, Z, et al.** 2007, Materials Transactions, Vol. 48, p. 163.

204. . *Glass-forming ability and mechanical properties of Ti-based bulk glassy alloys with large diameters up to 1 cm.* **Zhu, S L, Wang, X M and A, Inoue.** 2008, Intermetallics, Vol. 16, p. 1031.

205. *Distinct plastic strain of Ni-free Ti-Zr-Cu-Pd-Nb bulk metallic glasses with potential for biomedical applications.* **Qin, F X, Wang, X M and Inoue, A.** 2008, Intermetallics, Vol. 16, p. 1026.

206. *Ductile Ti-based nanocrystalline matrix composites.* **Kühn, U, et al.** 2006, Intermetallics, Vol. 14, p. 978.

207. *The effect of Nb addition on mechanical properties, corrosion behavior, and metal-ion release of ZrAlCuNi bulk metallic glasses in artificial body fluid.* **Qiu, C L, et al.** 2005, Journal of Biomedical Materials Research A, Vol. 75, p. 950.

208. *Medium range ordering and its effect on plasticity of Fe-Mn-B-Y-Nb bulk metallic glass.* **Park, J M, et al.** 2010, Philosophical Magazine, Vol. 90.

209. *Distinct plastic strain of Ni-free Ti-Zr-Cu-Pd-Nb bulk metallic glasses with potential for biomedical applications.* **Qin, F X, Wang, X M and Inoue, A.** 2008, Intermetallics, Vol. 16, p. 1026.

210. . *A theory for amorphous viscoplastic materials undergoing finite deformations, with application to metallic glasses.* **Anand, L and Su, C.** 2005, Journal of the Mechanics and Physics of Solids, Vol. 53, p. 1362.

211. *Spaciotemporally inhomogeneous plastic flow of a bulk-metallic glass.* **Jiang, W H, et al.** 2008, International Journal of Plasticity, Vol. 24, p. 1.

212. *Fracture surface morphology of compressed bulk metallic glass-matrix-composites and bulk metallic glass.* **Kusy, M, et al.** 2006, Vol. 14, p. 982.

213. *Fracture mechanisms in bulk metallic glassy materials.* **Zhang, Z F, et al.** 2003, Physics Review Letters, Vol. 91, p. 045505.

214. *Effect of surface finishing of a Zr-based bulk metallic glass on its corrosion behavior.* **Gebert, A, Gostin, P F and Schultz, L.** 2010, Corrosion Science, Vol. 52, p. 1711.

215. *Copper corrosion inhibitors in near neutral media.* **Otmacic, H and Stupnisek-Lisac, E.** 2003, Electrochimica Acta, Vol. 48, p. 985.

216. *Kinetics and Mechanisms of Cu Electrodissolution in Chloride Media.* **Lee, H P and Nobe, K.** 1986, Journal of Electrochemical Society, Vol. 133, p. 2035.

217. **Donachie, M J.** Titanium: a technical guide. Materials Park, Ohio 44073-0002 : ASM international, 2000, Vol. chapter 13.

218. *Corrosion behavior of Zr-based bulk glass-forming alloys containing Nb or Ti.* **Raju, V R, et al.** 2010, Vol. 57, p. 173.

219. *Structural disordering in amorphous $Pd_{40}Ni_{40}P_{20}$ induced by high temperature deformation.* **de Hey, P, Sietsma, J and Van den Beukel, A.** 1998, Vol. 46, p. 5873.

220. *Dynamic softening and indentation size effect in a Zr-based bulk glass-forming alloy.* **Van Steenberge, N, et al.** 2007, Scripta Materialia, Vol. 56, p. 605.

221. *Size effects in micro- and nanoscale indentation.* **Manika, I and Maniks, J.** 2006, Acta Materialia, Vol. 54, p. 2049.

222. *Investigation of shear band evolution in amorphous alloys beneath a Vickers indentation.* **Zhang, H W, et al.** 2005, Acta Materialia, Vol. 53, p. 3849.

223. *A survey of instrumented indentation studies on metallic glasses.* **Schuh, C A and Nieh, T G.** 2004, Journal of Materials Research, Vol. 19, p. 46.

224. *The Mohr-Coulomb criterion from unit shear processes in metallic glasses.* **Lund, A C and Schuh, C A.** 2004, Intermetallics, Vol. 12, p. 1159.

225. *Atomistic simulation of shear localization in Cu-Zr bulk metallic glass.* **Ogata, S, et al.** 2006, Intermetallics, Vol. 14, p. 1033.

226. *Atomistic basis for the plastic yield criterion of metallic glass.* **Schuh, C A and Lund, A C.** 2003, Nature Materials, Vol. 2, p. 449.

227. *Spherical indentation response of metallic glasses.* **Patnaik, M N M, Narasimhan, R and Ramamurty, U.** 2004, Acta Materialia, Vol. 52, p. 3335.

228. *Evaluation of hardness-yield strength relationships for bulk metallic glasses.* **Zhang, W H, et al.** 2006, Philosophical Magazine Letters, Vol. 86, p. 333.

229. *A new modified expanding cavity model for characterizing the spherical indentation behaviour of bulk metallic glass with pile-up.* **Ai, K and Dai, L H.** 2007, Scripta Materialia, Vol. 56, p. 761.

230. *Formation of new Ti-based metallic glassy alloys.* **Ma, C, et al.** 2004, Materials Transactions, Vol. 45, p. 1802.

231. *A development of Ti-based bulk metallic glass.* **Kim, Y C, Kim, W T and Kim, D H.** 2004, Materials Science and Engineering A, Vol. 375, p. 127.

232. *Elastic constants and their pressure dependence of $Zr_{41}Ti_{14}Cu_{12.5}Ni_9Be_{22.5}C1$ bulk metallic glass.* **Wang, W- H, et al.** 1999, Applied Physics Letters, Vol. 74, p. 1803.

233. *Soft bulk metallic glasses based on cerium.* **Zhang, B, et al.** 2004, Applied Physics Letters, Vol. 53, p. 3849.

234. *A universal criterion for plastic yielding of metallic glasses with a $(T/Tg)^{2/3}$ temperature dependence.* **Johnson, W L and Samwer, K.** 2005, Physics Review Letters, Vol. 95, p. 195501.

235. *Intrinsic and extrinsic toughening of metallic glasses.* **Lewandowski, J J, Shazly, M and Nouri, A S.** 2006, Scripta Materialia, Vol. 54, p. 337.

236. *Difference in compressive and tensile fracture mechanisms of $Zr_{59}Cu_{20}Al_{10}Ni_8Ti_3$ bulk metallic glass.* **Zhang, Z F, Eckert, J and Schultz, L.** 2003, Acta Materialia, Vol. 51, p. 1167.

237. *Study of mechanical deformation in bulk metallic glass through instrumented indentation.* **Vaidyanathan, R, et al.** 2001, Acta Materialia, Vol. 49, p. 3781.

238. *Fracture of brittle metallic glasses: Brittleness or plasticity.* **Xi, X K, et al.** 2005, Physical Review Letters, Vol. 94, p. 125510.

239. *Metallic glasses as structural materials.* **Ashby, M F and Greer, A L.** 2006, Scripta Materialia, Vol. 54, p. 321.

240. *The frictional component of the indentation size effect in low load microhardness testing.* **Li, H, et al.** 1993, Journal of Materials Research, Vol. 8, p. 1028.

241. *Structural disordering in amorphous $Pd_{40}Ni_{40}P_{20}$ induced by high temperature deformation.* **de Hey, P, Sietsma, J and Van Den Beukel, A.** 1998, Acta Materialia, Vol. 46, p. 5873.

242. *Structural relaxation and plastic flow in amorphous $La_{50}Al_{25}Ni_{25}$.* **Van Aken, B, de Hey, B and Sietsma, J.** 2000, Materials Science and Engineering A, Vol. 278, p. 247.

243. *Thermal relaxation and high temperature creep of $Zr_{55}Cu_{30}Al_{10}Ni_5$ bulk metallic glass.* **Daniel, B S S, et al.** 2002, mechanics of time-dependent materials, Vol. 6, p. 193.

244. *Creation and annihilation of free volume during homogeneous flow of a metallic glass.* **Heggen, M, Spaepen, F and Feuerbacher, M J.** 2005, Journal of Applied Physics, p. 033506.

245. *Temperature rise at shear bands in metallic glasses.* **Lewandowski, J J and Greer, A L.** 2006, Nature Materials, Vol. 5, p. 15.

246. *Thermomechanical instability analysis of inhomogeneous deformation in amorphous alloys.* **Gao, Y F, Yang, B and Nieh, T G.** 2007, Acta Materialia, Vol. 55, p. 2319.

247. *Mean stress effects on flow localization and failure in a bulk metallic glass.* **Flores, K M and Dauskardt, R H.** 2001, Acta Materialia, Vol. 49, p. 2527.

248. *Characterization of free volume changes associated with shear band formation in Zr- and Cu-based bulk metallic glasses.* **Kanungo, B P, et al.** 2004, Intermetallics, Vol. 12, p. 1073.

249. *Analysis of indentation of pressure sensitive plastic solids using the expanding cavity model.* **Narasimhan, R.** 2004, Mechanics of Materials, Vol. 36, p. 633.

250. *Super plastic bulk metallic glasses at room temperature.* **Liu, Y H, et al.** 2007, Science, Vol. 315, p. 1385.

251. *Processing of bulk metallic glasses with high strength and large compressive plasticity in Cu50Zr50.* **Zhu, Z W, et al.** 2006, Scripta Materialia, Vol. 54, p. 1145.

252. *The effect of primary crystallizing phases on mechanical properties of Cu46Zr47Al7 bulk metallic glass composites.* **Jiang, F, et al.** 2006, Journal of Materials Research, Vol. 21, p. 2638.

253. *High strength bulk amorphous alloys with low critical cooling rates.* **Inoue, A.** 1995, Materials Transactions, Vol. 36, p. 886.

254. *Analysis of plastic strain and deformation mode of a Zr-based two-phase bulk metallic glass in compression.* **Chen, H M, et al.** 2009, Intermetallics, Vol. 17, p. 330.

255. *Shear striations and deformation kinetics in highly deformed Zr-based bulk metallic glasses.* **DallaTorre, F H, et al.** 2008, Acta Materialia, Vol. 56, p. 4635.

256. *Frictionless compression testing using load-applying platens made from porous graphite aerostatic bearings.* **El-Aguizy, T, et al.** 2005, Review of Scientific Instruments, Vol. 76, p. 075108.

257. *Heterogeneity of a Cu47.5Zr47.5Al5 bulk metallic glass.* **Kim, K B, et al.** 2006, Applied Physics Letters, Vol. 88, p. 051911.

258. *HRTEM analysis of nanocrystallization during uniaxial compression of a bulk metallic glass at room temperature.* **Deng, Y F, et al.** 2004, Vol. 98, p. 201.

259. *Effect of strain rate on the formation of nanocrystallites in an Al-based amorphous alloy during nanoindentation.* **Jiang, W H, Pinkerton, F E and Atzmon, M.** 2003, Journal of Applied Physics, Vol. 93, p. 9287.

260. *Ball milling-induced nanocrystal formation in aluminium-based metallic glasses.* **He, Y, Shiflet, G J and Poon, S J.** 1995, Acta Metallurgica et Materialia, Vol. 43, p. 83.

261. *Deformation-induced nanocrystallization and its influence on work hardening in a bulk amorphous matrix composite.* **Lee, J C, et al.** 2004, Acta Materialia, Vol. 52, p. 1525.

262. *Nanocrystal evolution in bulk amorphous Zr57Cu20Al10Ni8Ti5 alloy and its mechanical properties.* **Xing, L Q, et al.** 1998, Materials Science and Engineering: A, Vol. 241, p. 216.

263. *Strain induced martensite formation and its effect on strain hardening behavior in the cold drawn 304 austenitic stainless steels.* **Choi, J Y and Jin, W.** 1997, Scripta Materialia, Vol. 36, p. 99.

264. *Modeling deformation behavior of Cu–Zr–Al bulk metallic glass matrix composites.* **Pauly, S, et al.** 2009, Applied Physics Letters, Vol. 95, p. 101906.

265. *Ti-containing Zr based bulk amorphous/nanocrystalline composite alloy.* **Fan, C and Inoue, A.** 2000, Materials Transactions JIM, Vol. 41, p. 1467.

266. *Formation, thermal stability and mechanical properties of Cu-Zr-Al bulk glassy alloys.* **Inoue, A and Zhang, W.** 2002, Materials Transactions JIM, Vol. 43, p. 2921.

267. *Unusual glass-forming ability of bulk amorphous alloys based on ordinary metal copper.* **Xu, D, Duan, G and Johnson, W L.** 2004, Physical Review Letters, Vol. 92, p. 246604.

268. *Influence of casting temperature on microstructures and mechanical properties of $Cu_{50}Zr_{45.5}Ti_{2.5}Y_2$ metallic glass prepared using copper mold casting.* **Zhu, Z, et al.** 2009, Journal of Materials Research, Vol. 24, p. 3108.

269. *Microstructural heterogeneities governing the deformation of $Cu_{47.5}Zr_{47.5}Al_5$ bulk metallic glass composites.* **Pauly, S, et al.** 2009, Acta Materialia, Vol. 57, p. 5445.

270. *Unit cell detrmination in CuZr martensite by electron microscopy and X-ray diffraction.* **Schryvers, D, et al.** 1997, Scripta Materialia, Vol. 36, p. 1119.

271. *Influence of Al content on the microstructure and mechanical property of the $(Zr_2Cu)_{100-x}Al_x$ alloys.* **Qiu, F, et al.** 2009, Journal of Alloys and Compounds, Vol. 468, p. 195.

272. *Compressive and tensile properties of CuZrAl alloy plates containing martensitic phases.* **Wei, X F, et al.** 2009, Materials Science and Engineering: A, Vol. 517, p. 375.

273. *Plasticity-improved Zr–Cu–Al bulk metallic glass matrix composites containing martensite phase.* **Sun, Y F, et al.** 2005, Applied Physics Letters, Vol. 87, p. 051905.

274. *Deformation-induced martensitic transformation in Cu-Zr-(Al,Ti) bulk metallic glass composites.* **Pauly, S, et al.** 2009, Scripta Materialia, Vol. 60.

275. *Influence of Al content on the microstructure and mechanical property of the (Zr2Cu)100 − xAlx alloys.* **Qiu, F, et al.** 2009, Journal of Alloys and Compounds, Vol. 468, p. 195.

276. *Effect of microstructures on the compressive deformation and fracture behaviors of $Zr_{47}Cu_{46}Al_7$ bulk metallic glass composites.* **Fan, J T, et al.** 1996, Journal of Non-Crystalline Solids, Vol. 353, p. 4707.

277. *Microstructure and mechanical properties of Zr-Cu-Al bulk metallic glasses.* **Ma, W, et al.** 2007, Transactions of Nonferrous Metals Society of China, Vol. 17, p. 929.

278. *Nanoscale-twinning-induced strengthening in austenitic stainless steel thin films.* **Zhang, X, et al.** 2004, Applied Physics Letters, Vol. 84, p. 1096.

279. *Micro- and nanoindentation techniques for mechanical characterisation of materials.* **Jana, S, et al.** 2004, Materials Science and Engineering: A, Vol. 375, p. 1191.

280. *Depth dependent hardness variation in Ni-P amorphous film under nanoindentation.* **Zhang, B, Wang, W and Zhang, G P.** 2002, Materials Science and Technology, Vol. 22, p. 734.

281. *Investigation of shear band evolution in amorphous alloys beneath a Vickers indentation.* **Zhang, H, et al.** 2005, Acta Materialia, Vol. 53, p. 3849.

282. *Nanoindentation and microindentation of CuAlNi shape memory alloy.* **Crone, W C, Brock, H and Creuziger, A.** 2007, Experimental Mechanics, Vol. 47, p. 133.

283. *Apparent modulus of elasticity of near-equiatomic NiTi.* **Liu, Y and Xiang, H.** 1998, Journal of Alloys and Compounds, Vol. 270, p. 154.

284. *Nanoindentation and microindentation of CuAlNi shape memory alloy.* **Crone, W C, Brock, H and Creuziger, A.** 2007, Experimental Mechanics, Vol. 47, p. 133.